Lung deformation estimation using a hybrid image-based/biomechanics-based approach for the localization of pulmonary nodules during video-assisted thoracoscopic surgery

Pablo A. Alvarez

THÈSE DE DOCTORAT DE

UNIVERSITÉ DE RENNES 1

ÉCOLE DOCTORALE N° 601
Mathématiques et Sciences et Technologies de l'Information et de la Communication
Spécialité : *Signal, Image, Vision*

Par

Pablo A. ALVAREZ

Lung deformation estimation using a hybrid image-based/biomechanics-based approach for the localization of pulmonary nodules during video-assisted thoracoscopic surgery

Thèse présentée et soutenue à Rennes, le 9 novembre 2020
Unité de recherche : Laboratoire Traitement du Signal et de l'Image (LTSI), UMR Inserm 1099

Rapporteurs avant soutenance :

María J. Ledesma Carbayo	Professeure, Université Polytechnique de Madrid
Stéphane Cotin	Directeur de Recherche, INRIA, équipe MIMESIS, Strasbourg

Composition du Jury :

Présidente :	Su Ruan	Professeure, Université de Rouen
Examinateurs :	María J. Ledesma Carbayo	Professeure, Université Polytechnique de Madrid
	Stéphane Cotin	Directeur de Recherche, INRIA, équipe MIMESIS, Strasbourg
	Su Ruan	Professeure, Université de Rouen
	Matthieu Chabanas	Maître de Conférences, Université Grenoble-Alpes
Dir. de thèse :	Jean-Louis Dillenseger	Maître de Conférences (HdR), Université de Rennes 1
Co-dir. de thèse :	Yohan Payan	Directeur de Recherche, CNRS, Université Grenoble-Alpes

Invité(s) :

Simon Rouzé Praticien Hospitalier, CHU de Rennes

Résumé

Le cancer du poumon est la première cause de décès par cancer dans le monde, tant chez les femmes que chez les hommes. Chaque année, il représente plus de 18% de tous les décès dus au cancer et fait presque autant de victimes que les cancers de la prostate, du foie et du sein réunis. Cette mortalité élevée est principalement due à une détection tardive de la maladie, lorsque les traitements curatifs ne sont plus disponibles et que la survie des patients est très faible. Heureusement, la récente mise en œuvre des programmes de dépistage a augmenté les chances de détection précoce du cancer du poumon, de traitement curatif en temps utile et, en fin de compte, de survie des patients.

Néanmoins, sur l'ensemble des nodules pulmonaires détectés par les programmes de dépistage, seule une fraction est un cancer du poumon. Il est important d'établir un diagnostic précis de ces nodules, car cela permet de déterminer un plan de traitement approprié pour le patient. Bien que divers tests médicaux puissent aider à prédire une malignité, seule l'analyse histologique d'échantillons de nodules peut confirmer la présence d'un cancer et de son sous-type. Cependant, ces nodules sont généralement trop petits, trop profonds ou pas assez denses pour que les techniques de biopsie non chirurgicales (*e.g.* biopsie transthoracique par aiguille du ponction ou biopsie bronchoscopique) soient fiables. Par conséquent, dans de nombreux cas, une biopsie chirurgicale (*i.e.* retrait complet du nodule) mini-invasive par thoracoscopique vidéo-assistée (VATS), est la méthode préférée. En outre, cette résection chirurgicale des nodules pulmonaires est également la principale option de traitement à visée curative pour les patients atteints d'un cancer du poumon à un stade précoce. Bien que la lobectomie (*i.e.* la résection d'un lobe pulmonaire entier) par thoracotomie ouverte soit la procédure classique, la pratique clinique a évolué vers des techniques de résection moins invasives qui préservent mieux le tissu pulmonaire. En fait, il a été démontré que les petites résections non anatomiques (*i.e.* résections cunéiformes, *wedge resections* en anglais) par VATS pouvaient être réalisées sans aucun compromis sur le résultat clinique. En tant que tel, la VATS s'avère être un outil important pour la gestion précoce du cancer du poumon, tant au niveau du diagnostic que du traitement.

Cependant, pendant la VATS, les nodules pulmonaires sont difficiles à localiser, car ils ne sont souvent ni palpables, ni visibles à l'œil nu. Cette situation est aggravée par la très grande déformation subie par le poumon à cause d'un pneumothorax. En effet, lorsque le chirurgien insère l'espace intercostal pour y placer les trocarts nécessaires au placement de la caméra et des outils, il se crée des entrés d'air qui entraînent le

dégonflement du poumon. Si ce pneumothorax donne l'espace nécessaire pour les manœuvres chirurgicales, il induit une profonde déformation du poumon et un fort déplacement du nodule. Pour surmonter ce problème, différentes stratégies de localisation des nodules pulmonaires sont couramment utilisées dans la pratique clinique. La principale consiste à placer des marqueurs physiques (*e.g.* hameçons, teintures) dans le nodule pour faciliter sa localisation pendant la chirurgie. Cette procédure est réalisée sous guidage scanner X, scanner *cone beam* CT (CBCT) ou bronchoscopique, soit de façon préopératoire (intervention suivie du transfert du patient au bloc opératoire), soit de façon peropératoire (dans une salle d'opération hybride). Toutefois, cette procédure de marquage présente encore certaines limites, comme la possibilité de migration des marqueurs après le placement, la difficulté de placement à certains endroits anatomiques et diverses complications cliniques, notamment le pneumothorax, l'hémothorax et l'embolie. En outre, les procédures de placement de marqueurs préopératoires comportent des risques et un inconfort supplémentaires pour le patient en attendant son transfert en salle d'opération, sans mentionner la charge logistique liée à la coordination des procédures de localisation et de résection.

Le développement de techniques de localisation des nodules pulmonaires pour la VATS est toujours un domaine de recherche actif, avec des investigations en cours pour trouver des méthodes plus sûres, plus efficaces et plus fiables. Compte tenu des limites des stratégies de localisation actuelles, une procédure peropératoire ne nécessitant pas de marqueurs physiques externes est souhaitable. Dans ce contexte, une solution innovante pour la localisation peropératoire des nodules pulmonaires a été proposée par Rouzé et al. au CHU de Rennes. La méthode est basée sur la délimitation du nodule pulmonaire sur une image CBCT du poumon semi-dégonflé, acquise après un pneumothorax. Cette délimitation est ensuite projetée sur des images fluoroscopiques en tant que marqueur virtuel qui est utilisé pour guider la localisation du nodule pulmonaire. Une étude clinique réalisée sur 24 patients a démontré la faisabilité de cette approche. Cependant, bien que prometteuse, cette technique de localisation de nodule sans marqueur repose entièrement sur la visibilité du nodule pulmonaire dans l'image de CBCT, mais celle-ci peut être insuffisante dans de nombreux cas. En effet, le dégonflement du poumon dû au pneumothorax augmente la densité du parenchyme pulmonaire, ce qui diminue fortement le contraste d'intensité entre le nodule pulmonaire et le tissu environnant sur l'image CBCT, empêchant ainsi sa localisation.

Les nodules pulmonaires sont toujours visibles sur l'image scanner X préopératoire utilisées pour la planification du geste opératoire. L'idée principale de cette de Thèse est de fusionner, à l'aide de méthodes de recalage d'images, l'image scanner X préopératoire avec l'image CBCT peropératoire afin de compenser la déformation des poumons et ainsi d'estimer la position peropératoire des nodules pulmonaires. Ce recalage permettra non seulement de localiser les nodules qui ne sont pas directe-

ment visibles sur l'image CBCT, mais également, à termes, d'ouvrir la porte à des techniques de guidage chirurgical plus avancées (par exemple la réalité augmentée) qui pourraient être utiles à la pratique clinique actuelle.

Objectif de la thèse

L'objectif principal de cette thèse est de proposer une méthode de recalage d'image qui tient compte de la déformation du poumon pendant la VATS, afin de fournir une estimation de la position peropératoire des nodules pulmonaires. Cette méthode devra être intégré dans la stratégie de localisation des nodules pulmonaires développée au CHU de Rennes, en tant que mécanisme potentiel permettant d'atténuer les difficultés auxquelles cette méthode est actuellement confrontée.

Méthode de recalage pour la localisation peropératoire des nodules pulmonaires pendant la VATS

La déformation du poumon pendant la VATS peut être comprise comme le résultat de deux processus physiques de natures différentes. Le premier processus correspond au placement du patient sur la table d'opération. Lors de l'acquisition de l'image scanner X préopératoire, le patient est en décubitus dorsal, alors que sur la table d'opération le patient est en décubitus latéral. Ce changement de position entraîne une déformation de la cage thoracique et surtout un changement de l'orientation du corps par rapport à la gravité, ce qui provoque un déplacement et une déformation du poumon et des organes environnants sous l'effet de leur poids. Il est également à noter un relâchement du diaphragme dû à l'anesthésie avec pour conséquence un certain déplacement provoqué par le poids des organes abdominaux. Le second processus correspond au pneumothorax avec l'effondrement du poumon dans la cage thoracique. Cette thèse présente une première tentative de prise en compte de ces deux processus physiques, afin que la position du nodule pulmonaire puisse être projetée du cadre préopératoire au cadre chirurgical peropératoire. Cela a été réalisé en introduisant une image CBCT supplémentaire peropératoire du poumon avant le pneumothorax, ce qui a permis de décomposer le problème de recalage initial complexe en deux sous-problèmes plus faciles à traiter : le premier tenant compte de la déformation du changement de la pose du patient entre le scanner X préopératoire et son placement sur la table d'opération, et le second tenant compte de la déformation du pneumothorax. La méthodologie globale de la méthode de recalage proposée est présentée dans la figure 1.

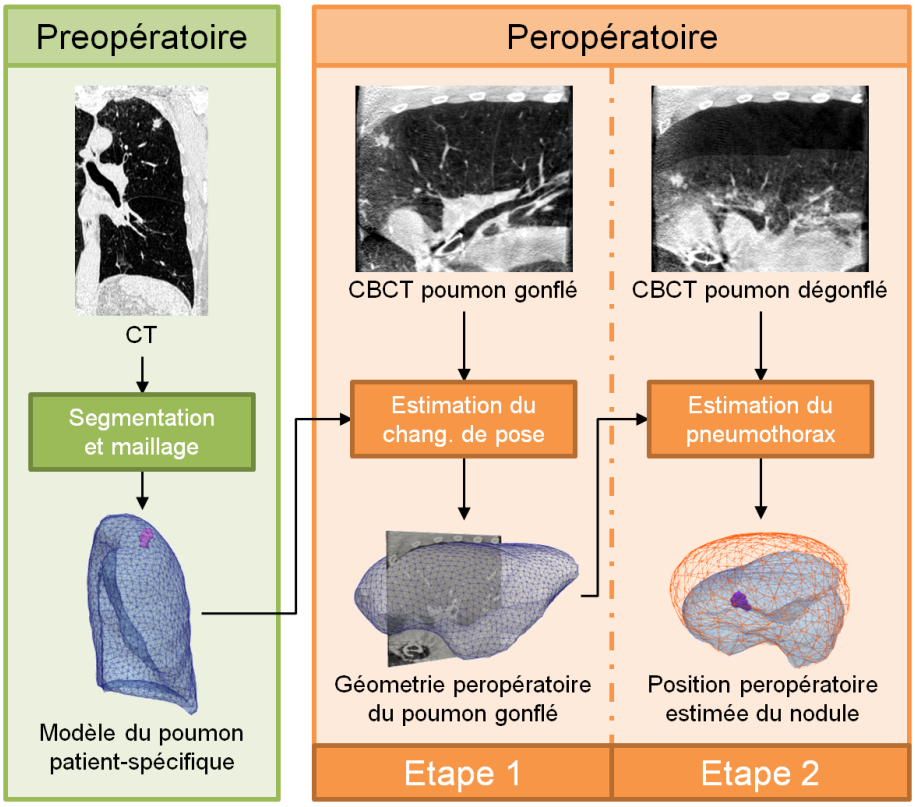

Figure 1 : Aperçu de la méthode de recalage proposée pour la localisation des nodules pulmonaires pendant la VATS. La méthode est composée de deux étapes : la première pour estimer la déformation du poumon due au changement de pose, et la deuxième pour estimer la déformation du poumon due au pneumothorax.

Estimation de la déformation du poumon due au changement de pose

L'objectif de cette première étape est d'estimer la configuration déformée du poumon complet après le changement de pose. Cette estimation fourni la géométrie peropératoire du poumon gonflé, qui est nécessaire pour l'estimation de la déformation du pneumothorax dans la deuxième partie. Il est important de souligner que les images peropératoires CBCT ne présentent qu'une vue partielle du poumon. Par conséquent, une méthode de recalage seulement basée sur les intensités des images ne serait pas suffisante, car seule une géométrie partielle du poumon pourrait être estimée. Par conséquent, une méthode hybride a été utilisée à la place, avec un recalage par intensité d'image pour estimer partiellement la déformation du poumon, et un modèle biomécanique poroélastique pour extrapoler cette déformation pour l'ensemble du poumon.

Estimation de la déformation du poumon due au pneumothorax

L'objectif de cette deuxième étape est d'estimer la configuration déformée du poumon après pneumothorax. La déformation du pneumothorax est modélisée à l'aide d'un modèle biomécanique poroélastique linéaire qui permet de prendre compte de l'évacuation de l'air lorsque le poumon se dégonfle. La géométrie du poumon gonflé résultant de l'estimation du changement de pose est utilisée comme configuration initiale pour la simulation du pneumothorax. Pour la phase fluide du modèle poroélastique (air), des conditions aux limites inspirées du processus d'expiration ont été définies, car elles correspondent naturellement à un processus du dégonflement de poumon. Pour la phase solide de ce modèle (parenchyme), des conditions de contact avec la cavité thoracique et le diaphragme sont utilisées, et des conditions limites de déplacement sont appliquées sur la face médiane pour tenir compte de la déformation du médiastin. Enfin, une formulation de problème inverse a été utilisée pour l'estimation des paramètres tissulaires, minimisant une fonction de coût basée sur une distance de surface à surface entre le modèle déformable et la surface pulmonaire dégonflée observée dans l'image CBCT peropératoire.

Contexte et financement

Cette thèse est le résultat d'une forte collaboration entre deux équipes de recherche, partenaires du projet national français «Laboratoire d'Excellence CAMI». D'une part, l'équipe IMPACT du laboratoire LTSI de l'Université de Rennes 1, avec une expérience dans les techniques de traitement d'images appliquées à l'assistance chirurgicale. D'autre part, l'équipe GMCAO du laboratoire TIMC-IMAG, Université de Grenoble-Alpes, avec une expérience dans les procédures médico-chirurgicales assistées par ordinateur. En outre, cinq mois (février 2018 - juin 2018) ont été passés au laboratoire *Biomechanical modeling laboratory* du *Vanderbilt Institute for Surgery and Engineering* (*VISE*), Université de Vanderbilt, Nashville, Tennessee, dans le cadre d'un programme de mobilité internationale.

De plus, cette thèse a été développée en parallèle avec la thèse de Sciences de Simon Rouzé (M.D.), chirurgien cardio-thoracique au CHU de Rennes, France, qui a initié le projet de recherche clinique sur la localisation peropératoire sans marqueurs guidée par la CBCT pour la VATS.

Le financement de cette thèse a été partagé par la Région Bretagne à travers des «Allocations de Recherche Doctorale» (ARED) et l'Agence Nationale de Recherche (ANR) à travers le cadre «Investissements d'Avenir Labex CAMI» (ANR-11-LABX-0004).

Structure du document

Ce manuscrit de thèse est divisé en sept chapitres et un annexe.

Le **Chapitre 4**, le **Chapitre 5**, le **Chapitre 6** et l'**Annexe A** ont tous été basés sur des publications présentées en conférences ou soumises à une revue internationale. Ces chapitres sont divisés en deux parties. La première partie reproduit le contenu de la publication sans modification. La seconde partie présente des méthodes et des résultats supplémentaires qui complètent le travail rapporté dans la publication. Afin de différencier clairement les deux parties, toutes les pages appartenant à une publication sont marquées par une bande verticale, comme celle qui se trouve à côté de ce paragraphe.

Le **Chapitre 1** fournit une description du contexte clinique dans lequel s'inscrit ce travail de thèse. Ce chapitre commence par donner un aperçu de l'anatomie et de la fonction pulmonaire. Ensuite, une vue d'ensemble sur le cancer du poumon et de sa gestion est présentée, en se focalisant plus sur la résection chirurgicale des nodules pulmonaires par VATS. Ensuite, les principales stratégies de localisation des nodules pulmonaires par VATS sont énumérées, la méthode de localisation peropératoire proposée au CHU de Rennes étant une solution alternative. Les principaux avantages et limites actuelles de ces méthodes de localisation sont discutés, ce qui conduit à la motivation principale de cette thèse.

Le **Chapitre 2** présente le contexte méthodologique des travaux développés dans cette thèse. Deux stratégies de compensation et d'analyse des déformations y sont brièvement décrites : celle du recalage d'images basé sur l'intensité et celle de la modélisation biomécanique. Ensuite, une revue de la littérature sur les méthodes de compensation des déformations pulmonaires est proposée, les méthodes étant classées en fonction de la stratégie utilisée.

Le **Chapitre 3** donne un aperçu global de la méthode de recalage proposée pour la localisation des nodules pulmonaires pendant la VATS et développée durant le travail de la Thèse, ainsi que des justifications des principaux choix méthodologiques. Pour ce faire, ce chapitre décrit tout d'abord les défis techniques à relever ainsi que les solutions proposées/possibles. Ensuite, le déroulement général de la méthode de recalage est présenté, ainsi que les données cliniques acquises pour sa validation, et la liste des principales investigations menées dans le cadre de cette thèse.

Le **Chapter 4** présente une caractérisation de la déformation pulmonaire résultant d'un changement de pose du patient entre les configurations préopératoires et peropératoires du patient pendant la VATS. Cette déformation a d'abord été estimée à l'aide d'une méthode de recalage basée sur l'intensité, puis a été quantifiée et caractérisée à l'aide d'indices de déformation issus de la littérature. Les résultats préliminaires de cette étude ont été présentés lors d'une conférence internationale :

P. Alvarez, M. Chabanas, S. Rouzé, M. Castro, Y. Payan, and J.-L. Dillenseger. Lung deformation between preoperative CT and intraoperative CBCT for thoracoscopic surgery : a case study. In *Medical Imaging 2018 : Image-Guided Procedures, Robotic Interventions, and Modeling*, page 40, Houston, United States, Mar. 2018. SPIE. ISBN 978-1-5106-1641-7. doi : 10.1117/12.2293938

Le **Chapitre 5** présente une première mise en œuvre de la méthode de recalage proposée pour la localisation des nodules pulmonaires. Pour faciliter cette mise en œuvre, les données cliniques ont été obtenues dans le contexte d'une biopsie par aiguille de ponction du poumon au lieu d'une intervention de VATS. Cela a permis de traiter des déformations pulmonaires très similaires à celles du VATS, tout en utilisant des données cliniques moins difficiles. Les résultats de cette étude ont été présentés lors d'une conférence internationale :

P. Alvarez, S. Narasimhan, S. Rouzé, J.-L. Dillenseger, Y. Payan, M. I. Miga, and M. Chabanas. Biphasic model of lung deformations for video-assisted thoracoscopic surgery (VATS). In *2019 IEEE 16th International Symposium on Biomedical Imaging (ISBI 2019)*, pages 1367–1371, Venice, Italy, 2019a. IEEE. ISBN 978-1-5386-3641-1. doi : 10.1109/isbi.2019.8759219

Le **Chapitre 6** présente la mise en œuvre finale de la méthode de recalage proposée pour la localisation des nodules pulmonaires pendant la VATS. Cette mise en œuvre s'appuie sur les travaux présentés dans les deux chapitres précédents afin d'étendre la méthode développée du contexte de la biopsie par aiguille de ponction du poumon au contexte de la VATS. Ce dernier est plus difficile en raison de la qualité des données cliniques et de la quantité de déformations pulmonaires. Les résultats de cette étude ont été soumis à une revue internationale et sont actuellement en cours de révision :

P. Alvarez, S. Rouzé, M. I. Miga, Y. Payan, J.-L. Dillenseger, and M. Chabanas. A hybrid image registration approach to markerless intraoperative nodule localization during video-assisted thoracoscopic surgery. *Medical Image Analysis*, submitted in April 2020

Le **Chapitre 7** fait le compte des principales contributions de ce travail de thèse et discute des lignes de recherche envisageables pour des développements futurs.

L'**Annexe A** évalue la méthode de recalage basé sur l'intensité introduit au chapitre 4 comme outil de localisation des nodules pulmonaires pendant la VATS. Cette étude permet d'illustrer la difficulté de la tâche à accomplir, et comment un algorithme classique basé seulement en des intensités d'image peut ne pas être suffisant pour construire une solution. Les résultats de cette étude ont été présentés lors d'une conférence internationale :

P. Alvarez, S. Rouzé, M. Chabanas, Y. Payan, and J.-L. Dillenseger. Image-based registration for lung nodule localization during VATS. In *Surgetica 2019*, Rennes, France, 2019

To my beloved parents and sister
for their unconditional love
that travels all distances

Acknowledgements

First of all, I would like to thank María J. Ledesma, associate professor at the *Universidad Politécnica de Madrid* and Stéphane Cotin, research director at INRIA and head of the MIMESIS team, for accepting to review this manuscript. I am also grateful to them and to Su Ruan, professor at the *Université de Rouen*, for participating in the jury of my thesis and for their interest in my work, which lead to very exciting discussions and interesting ideas.

I would like to express my sincere gratitude to my supervisors Jean-Louis Dillenseger, associate professor at the *Université de Rennes 1*, Yohan Payan, CNRS research director at the *Université Grenoble-Alpes*, and Matthieu Chabanas, associate professor at the *Université Grenoble-Alpes*. Their complementary expertise was fundamental for the accomplishment of this thesis, and they masterfully made it accessible to me in form of useful advice. I greatly thank them also for their kindness and encouragement throughout these four years.

I am deeply grateful to Simon Rouzé, cardiothoracic surgeon at the *CHU Pontchaillou*, without whom this research project would not have been born. Many thanks to him also for his role as my medical conscience, and his investment in acquiring and annotating the clinical data that was key for the development of this thesis.

I extend my special thanks to the people at the Vanderbilt Institute for Surgery and Engineering, from Vanderbilt University, where I spent 5 months for a mobility program. I am particularly grateful to professor Michael I. Miga and colleges from the Biomedical Modeling Laboratory for sharing with me their knowledge and methods on the poroelastic biomechanical model, which was central to my research.

I also truly thank the laboratory that so warmly hosted me during these four years, the LTSI. Not only did my stay there widen my knowledge, but it gave me the chance to meet many incredible people, many of which I now consider friends.

Many thanks to all my friends for their gracious company, it was a constant source of support and joyful experiences. In particular, I would like to express my profound gratitude to my dear friends Lara, Karim, Sandie and Margaux, along whom I have experienced some of my most pleasurable years.

I am also very grateful to Marcela Iregui, Eduardo Romero and Oscar Acosta, who saw in me the potential for becoming a researcher, and consequently, pushed me down this way and guided my initial steps.

Finally, I owe my deepest gratitude to my family, for all their love and support.

Table of Contents

List of Figures

List of Tables

Introduction

Lung cancer is the worldwide leading cause of cancer death among both women and men. Every year, it accounts for more than 18% of all cancer deaths, claiming almost as many lives as do prostate, liver and breast cancer combined. This high mortality is primarily caused by a late detection of the disease, when curative treatment is no longer available and patient survival is very low. Fortunately, the recent development of screening programs has increased the chances for early lung cancer detection, timely curative treatment, and ultimately, patient survival.

Nonetheless, of all pulmonary nodules detected through screening programs, only a fraction are lung cancer. It is important to establish an accurate diagnosis of these nodules, as it allows to determine an appropriate treatment plan for the patient. Although various medical tests may help in predicting for malignancy, only histological analysis of nodule samples can confirm the presence of cancer and its sub-type. However, these nodules are typically too small, too deep, or not dense enough for non-surgical biopsy techniques (*e.g.* transthoracic needle biopsy or bronchoscopic biopsy) to be reliable. Consequently, in many cases, surgical biopsy (*i.e.* complete removal of the nodule) through the minimally invasive video-assisted thoracoscopic surgery (VATS) is the preferred method. In addition, this surgical resection of pulmonary nodules is also the main treatment option with curative intent for patients with early stage lung cancer. Although lobectomy (*i.e.* removal of an entire lung lobe) through open thoracotomy is the classical procedure, the clinical practice has been evolving towards less invasive, better tissue-preserving resection techniques. In fact, it has been demonstrated that small non-anatomical resections (*i.e.* wedge resections) through VATS could be performed without any compromise in the clinical outcome. As such, VATS reveals as an important tool for early lung cancer management in both, diagnosis and treatment.

During VATS, however, pulmonary nodules are difficult to localize, as they are often neither palpable, nor visible to the naked eye. This is aggravated by the very large lung deformation resulting from pneumothorax (*i.e.* lung deflation caused by the entrance of air in the thoracic cavity), as the surgeon clears up space for surgical maneuvering. To overcome this problem, various nodule localization strategies are commonly used in clinical practice. The main approach consists in placing physical markers (*e.g.* hook-wires, micro-coils, dyes) in the nodule to facilitate its localization during surgery. This is carried out under CT, cone-beam CT (CBCT) or bronchoscopy guidance, either preoperatively (interventional procedure followed by patient transfer to the operating room) or intraoperatively (in a hybrid operating room). However,

there are still some limitations to this marking procedure, such as the possibility for marker migration after placement, the difficult placement at some anatomical locations and various clinical complications including pneumothorax, hemothorax and embolism. Furthermore, preoperative marker placement procedures bear additional risks and discomfort for the patient while he/she awaits for transfer to the operating room, not to mention the logistic burden of coordinating the localization and resection procedures.

The development of pulmonary nodule localization techniques for VATS is still an active area of research, with ongoing investigations towards safer, more efficient and more reliable methods. Considering the limitations of current localization strategies, an intraoperative procedure not requiring physical markers is desirable. In this context, an innovative solution for intraoperative pulmonary nodule localization has been proposed by Rouzé et al., at the Rennes University Hospital. The method is based on the delineation of the pulmonary nodule on a CBCT image of the semi-deflated lung, acquired after pneumothorax. This delineation is then projected into fluoroscopic images as a virtual marker serving for guidance. A clinical study performed on 24 patients demonstrated the feasibility of this approach. However, while promising, this markerless nodule localization technique relies entirely on the visibility of the pulmonary nodule in the CBCT image, which may be insufficient in many cases. Indeed, the lung deflation after pneumothorax increases the density of lung parenchyma, which in turn decreases the intensity contrast between the pulmonary nodule and the surrounding tissue in the CBCT image.

An important observation is that pulmonary nodules are always visible in the CT image that is used for surgical planning. Hence, it should be possible to integrate this preoperative CT image and the intraoperative CBCT image into an image registration framework, in order to compensate for lung deformation and estimate the intraoperative position of pulmonary nodules. This would not only help with the localization of the nodules that are not directly observable in the CBCT image, but would also open the door for more advanced surgical guidance techniques that could benefit the current clinical practice.

Thesis objective

The main objective of this thesis is to propose a registration framework that accounts for lung deformation during VATS, in order to provide an estimation of the intraoperative position of pulmonary nodules. This registration framework has to be integrated into the pulmonary nodule localization strategy developed at the Rennes University Hospital, as a potential mechanism to alleviate the challenges that this method currently faces.

Context and funding

This thesis is the result of a strong collaboration between two research teams, which are partners of the nation-wide french project "Laboratory of Excellence CAMI". On the one hand, the IMPACT team from the LTSI laboratory, University of Rennes 1, with experience in image processing techniques applied to surgical assistance. On the other hand, the GMCAO team from the TIMC-IMAG laboratory, University Grenoble-Alpes, with experience in computer assisted medical-surgical procedures.

In addition, 5-months (February 2018 - June 2018) were spent at the Biomechanical Modeling Laboratory of the Vanderbilt Institute for Surgery and Engineering (VISE), University of Vanderbilt, Nashville, Tennessee, within the context of an international mobility program.

Also, this thesis was developed in parallel to the Ph.D. thesis of Simon Rouzé (M.D.), cardio-thoracic surgeon at the Rennes University Hospital, Rennes, France, who initiated the clinical research project on markerless CBCT-guided VATS.

The funding for this thesis was shared by the *Région Bretagne* through its *Allocations de Recherche Doctorale* (ARED) framework and the *Agence National de Recherche* (ANR) through the framework *Investissements d'Avenir Labex CAMI* (ANR-11-LABX-0004).

Thesis outline

This thesis manuscript is divided into seven chapters and one appendix.

Chapter 4, **Chapter 5**, **Chapter 6** and **Appendix A** are all based from a manuscript. These chapters are each divided in two parts. The first part reproduces the content of the manuscript without modification. The second part presents additional methods and results that complement the work reported in the manuscript. In order to clearly differentiate the two parts, all pages belonging to a manuscript have been decorated with a vertical stripe, such as the one next to this paragraph.

Chapter 1 provides a description of the clinical context encompassing this thesis work. The chapter starts with an overview of lung anatomy and function. Then, an overall picture of lung cancer and lung cancer management is presented, with a special emphasis in surgical resection of pulmonary nodules through VATS. Following, the major strategies for pulmonary nodule localization for VATS are listed, with the intraoperative localization method proposed at the Rennes University Hospital as an alternative solution. The main advantages and current limitations of these methods are discussed, which lead to the main motivation of this thesis.

Chapter 2 introduces the methodological background of the work developed in this thesis. Therein, two strategies for deformation compensation and analysis are briefly

described: that of intensity-based image registration and that of biomechanical modeling. Then, a review of the literature for lung deformation compensation methods is proposed, with the methods being classified with respect to the strategy used.

Chapter 3 provides an overview of the proposed registration framework for pulmonary nodule localization during VATS, as well as justifications for the main methodological choices. This is done by first introducing the technical challenges that needed to be addressed, and the proposed/potential solutions. Then, the overall workflow of the registration framework is presented, as well as the clinical data collected for its validation, and the list of the main investigations carried out in this thesis.

Chapter 4 presents a characterization of the lung deformation resulting from a change of patient pose between the preoperative and the intraoperative settings in a VATS intervention. This deformation was first estimated using an intensity-based image registration framework, and was subsequently quantified and characterized using deformation indexes issued from the literature. The preliminary results of this study were presented in an international conference:

> **P. Alvarez**, M. Chabanas, S. Rouzé, M. Castro, Y. Payan, and J.-L. Dillenseger. Lung deformation between preoperative CT and intraoperative CBCT for thoracoscopic surgery: a case study. In *Medical Imaging 2018: Image-Guided Procedures, Robotic Interventions, and Modeling*, page 40, Houston, United States, Mar. 2018. SPIE. ISBN 978-1-5106-1641-7. doi: 10.1117/12.2293938

Chapter 5 presents a first implementation of the proposed registration framework for pulmonary nodule localization. To facilitate this implementation, the clinical data was obtained from the context of a lung needle-biopsy instead of a VATS intervention. This allowed dealing with lung deformation very similar to that of VATS, but with less challenging clinical data. The results of this study were presented in an international conference:

> **P. Alvarez**, S. Narasimhan, S. Rouzé, J.-L. Dillenseger, Y. Payan, M. I. Miga, and M. Chabanas. Biphasic model of lung deformations for video-assisted thoracoscopic surgery (VATS). In *2019 IEEE 16th International Symposium on Biomedical Imaging (ISBI 2019)*, pages 1367–1371, Venice, Italy, 2019a. IEEE. ISBN 978-1-5386-3641-1. doi: 10.1109/isbi.2019.8759219

Chapter 6 presents the final implementation of the proposed registration framework for pulmonary nodule localization during VATS. This implementation builds upon the work presented in the previous two chapters in order to extend the developed framework from the context of lung needle-biopsy to the context of VATS. This latter is more challenging because of the quality of clinical data, and the amount of lung deformation. The results of this study were submitted to an international journal, and are currently under review:

P. Alvarez, S. Rouzé, M. I. Miga, Y. Payan, J.-L. Dillenseger, and M. Chabanas. A hybrid image registration approach to markerless intraoperative nodule localization during video-assisted thoracoscopic surgery. *Medical Image Analysis*, submitted in April 2020

Chapter 7 reviews the main contributions of this thesis work and discusses possible lines of research for future developments.

Appendix A evaluates the intensity-based image registration framework introduced in Chapter 4 as a tool for pulmonary nodule localization during VATS. This study allows to illustrate the difficulty of the task at hand, and how a classical algorithm based on image intensity alone may not be sufficient for constructing a solution. The results of this study were presented in an international conference:

P. Alvarez, S. Rouzé, M. Chabanas, Y. Payan, and J.-L. Dillenseger. Image-based registration for lung nodule localization during VATS. In *Surgetica 2019*, Rennes, France, 2019

1 Clinical context

The objective of this chapter is to introduce the clinical problem that is addressed in this manuscript. First of all, the main notions of lung anatomy and function are provided, with emphasis in the physical mechanisms that allow human respiration. Then, an overview of lung cancer statistics and lung cancer management is given. Particular interest is accorded to the early detection of the disease, as well as the possible treatment options at this stage, which have been proven beneficial for patient survival. Finally, the video-assisted thoracoscopic surgery (VATS) is introduced as one of the main treatment options for early stage lung cancer. The advantages of this minimally invasive technique are discussed, as well as its main limitation: the need for pulmonary nodule localization. An overview of existing localization techniques is presented, with a focus on current trends in clinical practice. This chapter finishes by describing an alternative pulmonary nodule localization technique recently introduced at the Rennes University Hospital, whose improvement was the main motivation of this thesis work.

1.1 Lung anatomy and breathing

The main function of the lung is the exchange of respiratory gases. This exchange is performed by moving air in and out of the lungs by the process of breathing. The purpose of this section is to describe the process of breathing from a mechanical perspective. To that, an overview of the overall anatomy and function of lung structures is first provided, followed by the presentation of the breathing mechanisms. At the end of the section, the particular case of pneumothorax will be discussed.

1.1.1 Gross anatomy and function

The lung is the major organ of the respiratory system, whose main function is the exchange of oxygen and carbon dioxide with air from the atmosphere. The human body has two lungs located inside the thoracic cavity, one at each side of the body. The left and right lungs are separated by the mediastinum (the central compartment of the thoracic cavity), which contains the heart, the trachea, the great arteries and major veins, among other structures. Each lung possesses an interface to the mediastinum which is called hilum. The hilum is the only point of access into the lungs, and is crossed mainly by the major bronchi and the pulmonary arteries and veins. Each lung is surrounded by the thoracic wall at the apex (top) and costal surfaces, by the mediastinum at the medial (central) surface and by the diaphragm muscle at the

base. Since the heart lies to the left of the body, the left lung is comparatively smaller than the right lung to accommodate for the needed space.

The fissures separate each lung into smaller units called lobes. The left lung is divided by the oblique fissure into two lobes, namely the superior and inferior lobes. The right lung is divided by the horizontal and oblique fissures into three lobes, namely the superior, middle and inferior lobes (see Fig. 1.1). Each lung lobe is further divided into anatomically and functionally independent units called segments. As it will be described later in this chapter, this functional independence allows the surgical resection of isolated lung anatomical structures, with little impact to the remaining structures (Levitzky, 2007). The anatomical resections of an entire lung, lobe or segment, are respectively called pneumonectomy, lobectomy and segmentectomy.

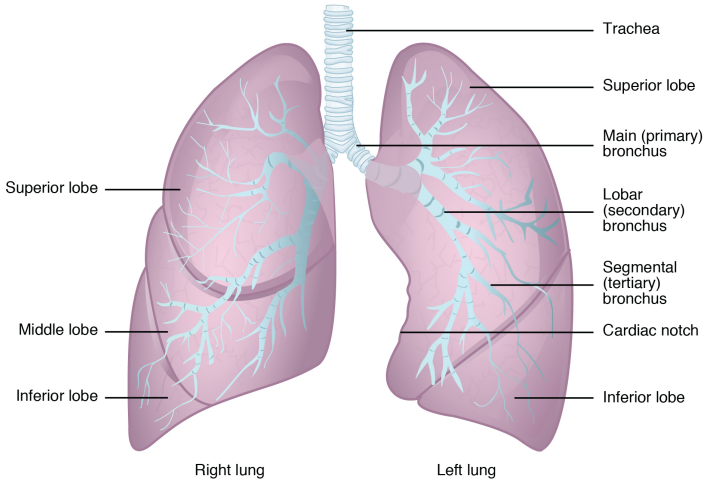

Figure 1.1: Coronal view of gross lung anatomy. The heart is located below the cardiac notch. Illustration taken from Anatomy and Physiology, OpenStax (2013).

The surfaces of lung and the thoracic cavity are lined with two thin membranes called pleurae, as illustrated in Fig. 1.2. The visceral pleura encloses the surface of each lung and penetrates deep within the fissures that separate the lobes. The parietal pleura covers the internal surface of the thoracic wall, the upper surface of the diaphragm and the mediastinum. For each lung, the two pleurae meet at the hilum, creating a potential space [1] called pleural cavity or pleural space. This space contains a small amount of serous liquid that is secreted from the pleurae and serves to lubricate their surfaces. This lubrication permits the pleurae to slide one against the other by reducing friction, hence preventing trauma during breathing.

1. In anatomy, a potential space is a space between two structures facing one each other, and being held together by pressure.

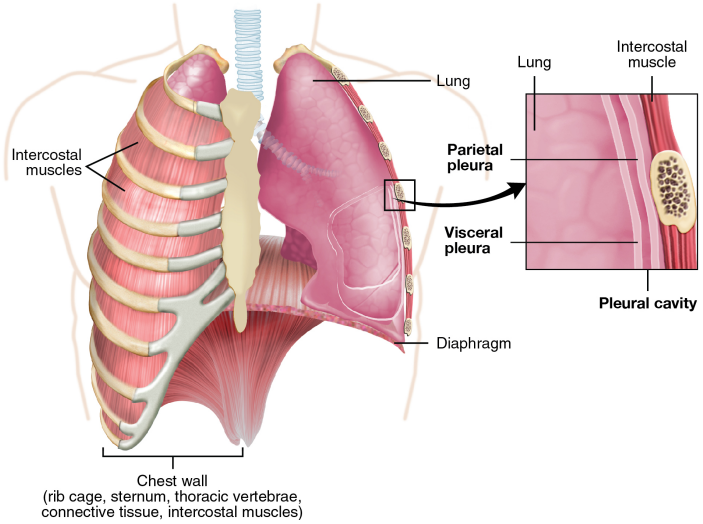

Figure 1.2: Pleural cavity and main lung structures. Illustration adapted from Anatomy and Physiology, OpenStax (2013).

Airways

Air is conducted from the atmosphere into the lungs within the airways. It enters the body at the mouth or nose and finishes inside alveoli, which are small balloon shaped structures where gas exchange takes place. Air gets later expelled out of the lungs also through the airways. The section of the airways that extends from the larynx and branches out from the trachea is called the bronchial tree. It is a fractal-like tubular structure of 23 branching generations. From the trachea (generation 0), it first divides into the left and right main bronchi before entering the lungs at the hilum. Each main bronchi is divided into lobar bronchi (secondary bronchi), which are in turn divided into segmental bronchi (tertiary bronchi). Further divisions follow, giving rise to even thinner and shorter structures called bronchioles. Alveoli start to appear on the walls of the smallest respiratory bronchioles, completely cover the subsequent alveolar ducts and are clustered in alveolar sacs at the end of the bronchial tree (see Fig. 1.3).

Gas exchange

The human body needs oxygen in order to break down foods that allow its normal functioning. It also produces carbon dioxide as a byproduct of metabolism, which needs to be expelled from the system. Gas exchange refers to the intake of oxygen and the elimination of carbon dioxide through the process of breathing. It happens within the numerous alveoli of lung parenchyma via diffusion.

The main pulmonary artery carries deoxygenated blood coming from the heart into the lungs. This main artery first divides into the right and left main pulmonary arteries, and branches down from there to the very small capillaries that surround alveo-

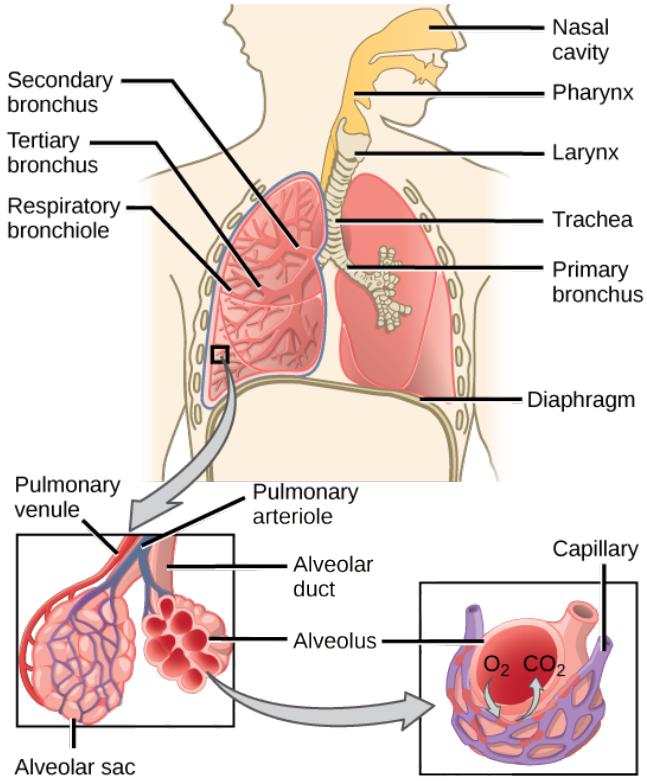

Figure 1.3: Overview of air transport and gas exchange. Illustration taken from Arteries and veins of the body, OpenStax (2013).

lar walls. The deoxygenated blood within these capillaries contains lower amounts of oxygen and higher amounts of carbon dioxide than the air inside alveoli. The differences in relative pressures allow gas diffusion to happen. This is, gas concentration between the air and blood balance out. As a result, the carbon dioxide of deoxygenated blood passes through alveolar walls into the the alveolus. Similarly, oxygen from air crosses alveolar walls into the bloodstream (see Fig. 1.3). This oxygenated blood flows from the capillaries to the pulmonary veins and into the the heart, where it gets pumped out to the rest of the body.

1.1.2 Mechanisms of breathing

Breathing, or ventilation, can be described as the movement of air into and out of the lungs. This airflow allows for gas exchanges to happen inside the numerous alveoli of lung parenchyma. Inhalation (the movement of air into the lungs) and exhalation (the movement of air out of the lungs) are the two main phases of a breathing cycle. These phases are dependent on the differences of pressure between the exterior and the interior of the lung, which are caused by the contraction and relaxation of the respiratory muscles.

Pressure relationships

Air, like other fluids, moves from a region of higher pressure to a region of lower pressure. Therefore, for airflow to exist, a pressure gradient between the exterior and the interior of the lungs must be established. In lung ventilation, three main pressures are of consideration: the atmospheric pressure; the pressure inside alveoli, called alveolar pressure and the pressure inside the pleural cavity, called intra-pleural pressure (see Fig. 1.4).

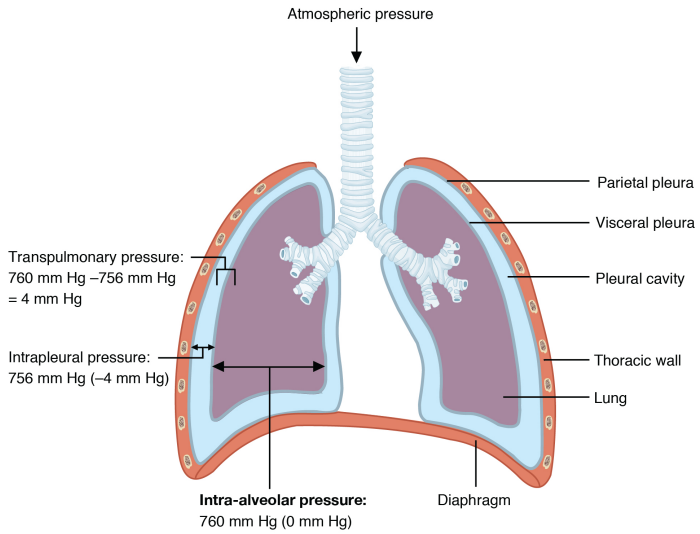

Figure 1.4: Principal respiratory pressures. Relative values with respect to atmospheric pressure are shown within parenthesis. Illustration taken from Anatomy and Physiology, OpenStax (2013).

Atmospheric pressure is the pressure within the atmosphere of Earth. It is approximately 760 mm Hg at sea level, and decreases with increasing elevation. During breathing, the atmospheric pressure remains relatively constant. Therefore, when discussing breathing mechanics, it is customary to express pressure values with respect to atmospheric pressure. That is, a pressure lower or higher than the atmospheric pressure is represented by positive and negative values respectively.

Alveolar pressure is the pressure of air inside alveoli. A difference between alveolar pressure and atmospheric pressure is what allows airflow to occur. Hence, alveolar pressure varies throughout the breathing cycle. It goes from negative during inhalation, to positive during exhalation, and it is zero when there is no airflow at the end of both phases.

The intra-pleural pressure is the pressure inside the pleural cavity. Like alveolar pressure, it also fluctuates throughout the breathing cycle. However, in normal conditions, intra-pleural pressure is always slightly negative (West, 2012), at approximately -4 mm Hg. This negative pressure is mainly caused by the mechanical interaction between the lung and the chest wall. Indeed, during breathing, these two structures

are constantly pulling each other in opposing directions. On the one hand, the lung parenchyma has a strong tendency to collapse into itself, which is caused by the inward elastic recoil of distended alveolar walls. On the other hand, the outward elastic recoil of the chest wall acts to expand the chest cavity. As a result, the chest wall holds the lung open, while at the same time, it gets pulled inwards by the lung.

In addition, the differences among the three pressures presented above are known as pressure gradients. There are three principal pressure gradients in lung ventilation: the transrespiratory pressure, the transpulmonary pressure and the transthoracic pressure. The transrespiratory pressure is the difference between the alveolar pressure and the atmospheric pressure. It is responsible for actual airflow into and out of the lungs. The transpulmonary pressure is the difference between the alveolar pressure and the intra-pleural pressure. It is responsible for holding the alveolar walls open during breathing, avoiding their collapse. The transthoracic pressure is the difference between the intra-pleural pressure and the atmospheric pressure. It represents the pressure needed to expand or contract the lungs and chest wall.

Mechanics of breathing

During breathing, the pressure within lung structures varies according to Boyle's law. This law states that the volume and pressure of a gas within a closed system under constant temperature are inversely proportional. That is to say that increasing the space that can be occupied by the gas results in a decrease of gas pressure, and vice-versa. Boyle's law is expressed as:

$$P_1 V_1 = P_2 V_2 \tag{1.1}$$

where P_1 and V_1 are the pressure and volume of the gas at the initial configuration; and P_2 and V_2 are those at the final configuration.

Changes in lung volume are then necessary in order to establish the pressure gradients required for airflow. However, alveoli (and hence the lung) are not capable of expanding themselves. They only expand passively in response to an increased distending pressure across the alveolar wall (Levitzky, 2007). This distending pressure is generated by the contraction of the respiratory muscles during breathing.

At the end of exhalation, all respiratory muscles are relaxed and pressure relationships are as depicted in Fig. 1.4. The alveolar pressure is zero, the intra-pleural pressure is negative and there is no airflow. From this resting state, a breathing cycle takes place: inhalation followed by exhalation to finally reach the initial resting state that prepares for the next cycle. A schematic representation of these inhalation and exhalation phases is provided in Fig. 1.5.

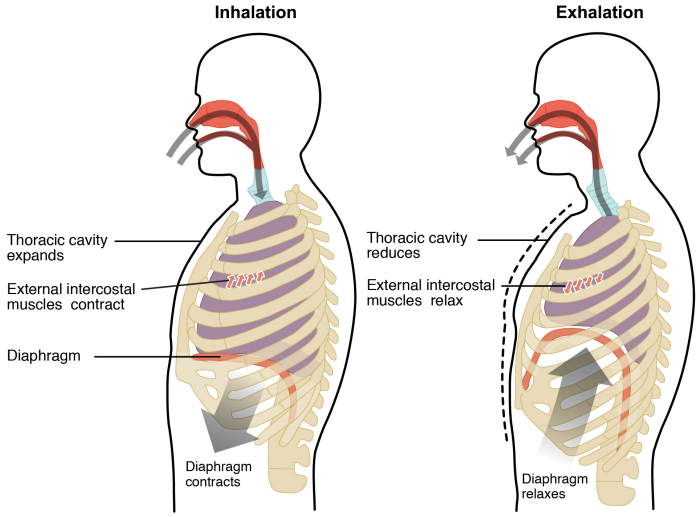

Figure 1.5: Inhalation and exhalation phases of breathing. Illustration taken from Anatomy and Physiology, OpenStax (2013).

Inhalation is an active process that involves the contraction of two groups of muscles: the diaphragm and the external intercostal muscles. On the one hand, the contraction of the diaphragm moves it away from the lung towards the abdominal cavity. On the other hand, the contraction of the external intercostal muscles pulls the rib cage upwards and outwards. As these muscles contract, the volume of the thoracic cavity increases and the intra-pleural pressure becomes more negative. This drop in intra-pleural pressure rises the transpulmonary pressure gradient, which in turn pulls the lung open. This pressure gradient is transmitted to the interior of the lung, expanding alveolar walls (Levitzky, 2007). The volume increase of alveoli decreases alveolar pressure, establishing a negative transrespiratory pressure gradient that allows air to enter into the lungs. As alveoli get filled in with air, alveolar pressure increases until it reaches zero again at the end of inhalation.

Exhalation is a passive process that consists in the relaxation of the muscles contracted during inhalation. As the diaphragm and the intercostal muscles come back to their resting positions, the volume of the thoracic cavity decreases. This reduces the transpulmonary pressure gradient that was pulling the lung open. Alveoli then start to recoil and decrease in volume, which rises alveolar pressure above atmospheric pressure. A positive transrespiratory pressure gradient is then established, and air starts to flow out of the lungs. The resting configuration is reached again once the alveolar pressure has decreased to zero at the end of exhalation.

The inhalation and exhalation processes described above are executed unconsciously during normal breathing. However, conscious forceful inhalation and exhalation are also possible if bigger breaths are necessary. These two active processes require the contraction of additional muscles that help in exaggerating volume changes of the

thoracic cavity. These additional muscles are located primarily in the neck, thorax and abdomen; and are called accessory respiratory muscles given their secondary role during normal breathing.

Pneumothorax

As mentioned earlier, alveoli have a strong tendency to collapse that is caused by the inward recoil of their distended walls. During breathing, the transpulmonary pressure gradient is always positive, pulling the lung outwards and avoiding its collapse. This is mainly due to the negative intra-pleural pressure.

Under certain circumstances (*e.g.* perforation of the thoracic cavity after trauma or during surgery), an abnormal pathway of air can make the pleural cavity get in direct communication with the atmosphere. Consequently, air from the atmosphere rushes into the pleural cavity until intra-pleural pressure reaches atmospheric pressure. In such scenario, the transpulmonary pressure gradient is no longer positive, making the outward pull at the lung surface to disappear and ultimately resulting in lung collapse. This condition is called pneumothorax. An illustration of a pneumothorax is provided in Fig. 1.6.

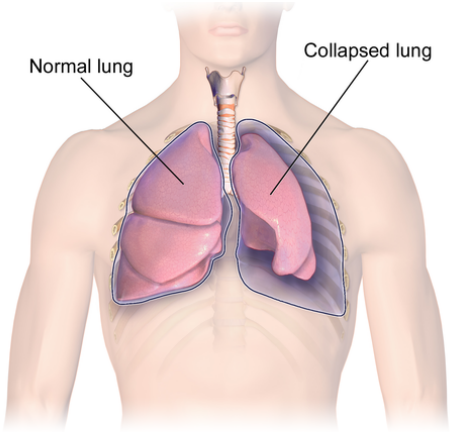

Figure 1.6: Illustration of a collapsed lung after pneumothorax. Illustration adapted from Blausen Medical (2014).

1.2 Lung cancer

Lung cancer is the worldwide leading cause of cancer death among both women and men (Bray et al., 2018). It accounts for more than 18% of all cancer deaths, claiming each year almost as many lives as do prostate, liver and breast cancer combined (see Fig. 1.7). In 2018, it is estimated that more than 2.1 million new lung cancer cases were diagnosed worldwide, and more than 1.8 million people died from the disease (Bray et al., 2018). In Europe, although tobacco regulation has helped decreasing

lung cancer incidence in men (Lortet-Tieulent et al., 2015), it is still considered one of the major global health problems (World Health Organization, 2019).

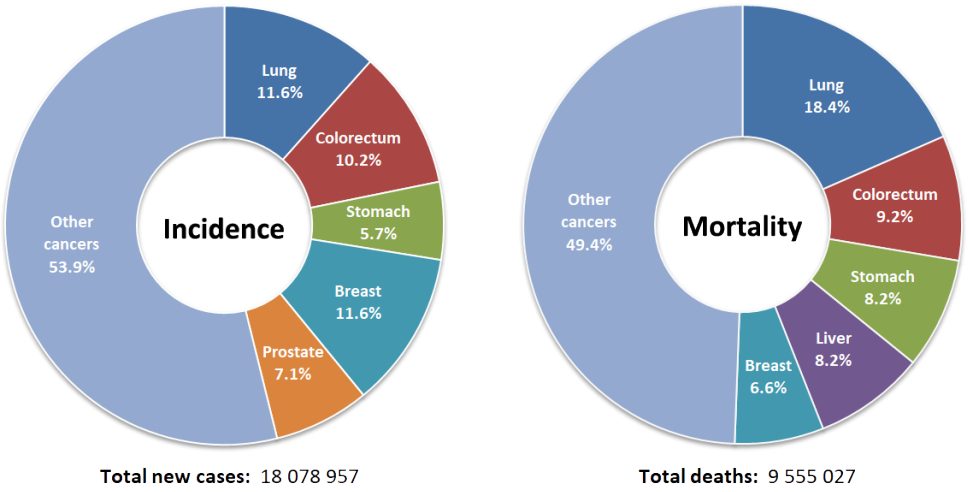

Figure 1.7: Estimated incidence and mortality rates for the 5 main cancer types in both men and women. This estimations were performed by Bray et al. (2018) for the year 2018.

In spite of the strong efforts towards better lung cancer management, patient survival following diagnosis of lung cancer is still pessimistic. A recent study by the American Cancer Society (Siegel et al., 2020) reported a 5-year survival rate [2] of 19% for lung cancer patients diagnosed from 2009 through 2015. This is in strong contrast with the significantly higher survival rates reported for other main cancer types, such as female breast cancer (62%) or prostate cancer (78%). The higher lung cancer mortality is largely explained by the generalized late detection of the disease, where curative treatment is no longer available (Spiro et al., 2007). It is well understood that patient survival and general prognosis are strongly dependent on the stage of lung cancer at diagnosis, being worst in advanced stages. Therefore, in order to improve the clinical outcome of lung cancer patients, early diagnosis is of paramount importance.

1.2.1 Early lung cancer detection

The early detection of lung cancer provides an opportunity for curative treatment, which ultimately results in higher survival probability. However, lung cancer patients are typically diagnosed after the onset of symptoms, where the cancer is already in an advanced stage (Buccheri, 2004). Currently, no curative treatment is available for advanced stages, and in the worst case scenario, the 5-year survival rate drops to only 5% (Siegel et al., 2020). In contrast, if timely detection and treatment are possible, the 5-year survival rate could improve significantly, up to 57% (Siegel et al., 2020). Con-

2. The 5-year survival rate is the ratio between the percentage of patients alive after five years of their diagnosis and the percentage of people of corresponding gender and age alive after five years.

sequently, considerable efforts have been put forward to develop screening programs that allow the early detection of the disease.

Screening programs

Several large studies have evaluated the efficacy of chest radiography for lung cancer screening (Manser et al., 2004; Melamed et al., 1984). This screening strategy was found to be potentially harmful to patients, without providing any significant reduction in mortality rates (Manser et al., 2004). Alternatively, low-dose CT (LDCT), providing more anatomical details, was also evaluated for lung cancer screening. Studies demonstrated that screening with LDCT increased the detection of early stage lung cancers with respect to chest radiographies (Henschke et al., 1999, 2001). However, the overall benefit for mortality from lung cancer was uncertain, and the increase in patient radiation and over-diagnosis raised concern.

Within this context, the National Lung Cancer Screening Trial (NLST) was developed to determine whether screening with LDCT could reduce mortality from lung cancer (The National Lung Screening Trial Research Team, 2011). The NLST is to date the largest of the many randomized trials conducted for lung cancer screening, including a total of 53,454 participants. The participants were randomly enrolled into one of two possible screening programs, following LDCT or chest radiography screening. The selection criteria aimed to include a population at high risk of developing lung cancer: a minimum of 30 pack-years of smoking history [3], age between 55 and 74 years, and, if former smoker, had quit whith the previous 15 years. The NLST study reported a 20% reduction in mortality from lung cancer in the LDCT group as compared to the chest radiography group. The results of the NLST study were complemented recently by the European screening trial NELSON (de Koning et al., 2020). This study, including a total of 15,792 participants, demonstrated a 26% reduction in mortality from lung cancer mortality with LDCT screening as compared to no screening. Based on these results, screening for lung cancer with LDCT is currently endorsed by several recognized scientific societies (Kauczor et al., 2015; Smith et al., 2015).

Current research focuses on improved inclusion criteria, personalized benefit-risk assessment and novel lung cancer predictive tools (Tanoue et al., 2015). Today, the implementation of screening programs is currently ongoing in cancer centers with appropriate infrastructure and expertise (Pirker, 2020).

3. A pack-year history measures the amount of tobacco a person has smoked over a long period of time. It is calculated by multiplying the number of packs of cigarettes per day by the number of years the person has smoked.

1.2.2 Lung cancer diagnosis and staging

Cancer diagnosis is achieved through a series of observations and tests including medical history, biopsies, laboratory tests, imaging tests and biomarker tests. Although the procedure may change from patient to patient, only histological analysis of tumor cells will determine the presence of cancer and its subtype (Dietel et al., 2016). Once lung cancer has been diagnosed, it is important to determine the stage of the disease, which is an estimation of the amount of cancer and its spread on the body. Diagnosis and staging allow medical doctors to prescribe the most appropriate treatment to patients, and provide an idea of their survival probability.

Non-Small Cell Lung Cancer (NSCLC) is the most common type of cancer and accounts for 80% - 85% of the cases. NSCLC groups together several cancer subtypes that differ in the type of cells at the origin of the cancer. The three main NSCLC subtypes are adenocarcinoma, squamus cell carcinoma and large cell carcinoma. NSCLC subtypes are grouped together because their management and patient outcomes are very similar.

Small Cell Lung Cancer (SCLC) accounts for the remaining 15% - 20% of lung cancer cases. SCLC exhibits aggressive behavior with rapid growth and early spread to distant sites. This type of cancer is almost exclusively associated to heavy smokers (Toh et al., 2007), and has been given its name after the smaller size of tumor cells under the microscope.

Lung cancer staging is carried out according to the 8th edition of the TNM Classification for Lung Cancer (Brierley et al., 2017). The TNM system allows for stratified staging of lung cancer, important for prognosis and treatment planning (International Agency for Research on Cancer, 2015). Although it can be used for staging both NSCLC and SCLC, it is generally not used for SCLC since it does not predict well for survival (International Agency for Research on Cancer, 2015). In the SCLC case, a simplified staging process differentiating limited and extensive (metastasized) cancer is often preferred.

TNM clinical classification

The TNM system is based on the evaluation of three key components: the extent of the primary **tumor**, the absence or presence and extent of regional lymph **node** metastasis, and the absence or presence of distant **metastasis** (Brierley et al., 2017).

The **tumor** is a pulmonary nodule that has been confirmed for cancer. Its extent refers to how large it has grown. **Metastasis** refers to cancer that has spread outside the primary tumor, and it is called distant metastasis if it affects distant organs. The lymph **nodes** are part of the immune system, and their function is to filter out harmful substances from the body. Lymph nodes are typically the first structures to be affected

by cancer metastasis. The three components of the TNM system are stratified as indicated in Table 1.1.

Table 1.1: The TNM system for cancer staging. Further subdivisions are possible if greater specificity is needed but are not included in this table. Adapted from TNM Classification of Malignant Tumours, 8th edition (Brierley et al., 2017).

Component	Grade	Description
T - Primary tumor	TX	Tumor cannot be assessed
	T0	No evidence of primary tumor
	Tis	Carcinoma in situ
	T1 - T4	Increasing size and/or local extent of primary tumor
N - Regional lymph nodes	NX	Regional lymph nodes cannot be assessed
	N0	No regional lymph node metastasis
	N1 - N3	Increasing involvement of regional lymph nodes
M - Distant Metastasis	M0	No distant metastasis
	M1	Distant Metastasis

Staging of NSCLC

Once the T, N, and M components have been determined, the information is combined in a process called stage grouping. The stage of the lung cancer gives the overall extent and severity of the disease. Stage 0 is the earliest of all possible stages, followed by stages I through IV. Further subdivisions are indicated using letters A to C along with the stage number. The higher the number and the letter of the stage, the larger the extent and the more advanced the cancer.

Staging of lung cancer is very complex, allowing each stage to be represented by various different combinations of the T, N and M components (American Joint Committee on Cancer, 2017). A minimal overview of the staging system is provided in Table 1.2.

1.2.3 Treatment strategies for NSCLC

The treatment plan for NSCLC is decided by a multidisciplinary team of medical experts. It is chosen based on the cancer stage, the cancer subtype and the suitability to the patient. In general, the earlier the cancer diagnosis, the better the possibilities of curative treatment. There are five principal ways to treat NSCLC: surgery, radiation therapy, chemotherapy, targeted therapy and immunotherapy. Surgery and radiation therapy correspond to localized treatment options, whereas the remaining three correspond to systemic treatment options. Depending on the situation, treatments may be administered in combination in order to improve patient outcomes.

Table 1.2: Overview of lung cancer staging, adapted from American Joint Committee on Cancer (2017). Note that the staging process is very complex, and only the main features are presented herein.

Stage	Subdivision	Description
Stage 0	-	This is called cancer in situ, meaning that the cancer has not grown into nearby tissues nor spread outside the chest cavity.
Stage I	IA, IB	Small tumors (less than 4 cm in the greatest direction) that have not spread to any lymph nodes and have not metastasized.
Stage II	IIA, IIB	Larger tumors (between 4 cm and 7 cm in the greatest direction) that have not spread to any lymph nodes and have not metastasized, or, small tumors (less than 4 cm in the greatest direction) that have spread to nearby lymph nodes and have not metastasized.
Stage III	IIIA, IIIB, IIIC	The cancer has spread within the chest but has not metastasized to other parts of the body. Multiple tumors can be found in the same lung and within surrounding structures (*e.g.* heart, mediastinum, bronchi).
Stage IV	IVA, IVB	The cancer has metastasized to the other lung or other structures of the body outside the chest cavity. At this stage, the size of the tumor and the compromise to lymph nodes is irrelevant.

Surgery

Surgical resection of the primary tumor is the preferred treatment when cancer is very localized and has not metastasized (Gould et al., 2013). This resection is performed either by open thoracotomy or by the minimally invasive video assisted thoracoscopic surgery (VATS). Several surgical gestures are available and the choice depends on the specifics of the cancer diagnosis and stage, as well as the overall clinical situation of the patient.

The surgical resection can be either anatomical or non-anatomical. Anatomical resections consist in the removal of a lung, lobe or segment, and are respectively referred to as pneumonectomy, lobectomy and segmentectomy. In current clinical practice, the lobectomy is the main treatment choice, allowing complete tumor resection while partially maintaining lung function (Yan et al., 2009). However, certain circumstances may require different resections. For instance, a pneumonectomy may be needed if the tumor is close to the mediastinum; or a segmentectomy may be needed if the patient cannot withstand the removal of a whole lobe because of poor lung function. Non-anatomical resections, called wedge resections, are also possible. The objective of a wedge resection is the removal of the tumor while maximizing lung function preservation.

In recent years, sublobar resections (*i.e.* segmentectomy and wedge resection) have gained interest of the scientific community because of their function-preserving capabilities. To date, the choice between lobar or sublobar resection appears to be established in favor of the smaller resections (Berfield and Wood, 2017). However, there is no consensus when choosing between segmentectomy or wedge resections, as the former are larger, technically more challenging resections; and the latter have been associated with higher rates of cancer recurrence (Berfield and Wood, 2017). However, some recent studies suggest that with appropriate negative margins, wedge resections could provide patient outcomes equivalent to those of traditional lobectomies for small pulmonary nodules (Mohiuddin et al., 2014; Wolf et al., 2017). Consequently, wedge resections are increasingly being adopted as the main surgical resection method for small pulmonary nodules, and they may become the standard in upcoming years.

Surgical resection is mainly prescribed with curative intent for NSCLC in stages I and II. It may be prescribed for localized tumors in stage III, and it is rarely prescribed in more advanced stages since the tumors are not resectable. Surgical resection may be precluded if the patient has poor cardiac function, poor lung function and or significant co-morbidities (Miller et al., 2019).

Radiation therapy

Radiation therapy, or radiotherapy, consists in the use of high energy x-rays to kill cancer cells. This treatment is often used after surgery (adjuvant radiotherapy) in order to eliminate any remaining cancer cell from the tissue. It can also be used to reduce the size of the tumor, before surgical resection (neoadjuvant radiotherapy) or as a palliative treatment. Like surgical resection, radiation therapy is a localized treatment, typically not prescribed if the cancer has metastasized. The most common mechanism to deliver radiation is by external-beam radiation therapy. With this approach, an external machine delivers high energy x-rays to the patient. Although this radiation is directed at the tumor, it passes through the body, causing inevitable damage to the surrounding structures. The objective is hence to optimize radiation delivery at the tumor, while sparing as much as possible healthy tissue. Radiation therapy can be used with curative intent for localized NSCLC if the tumors are not resectable. It is often used in combination with other treatment strategies.

Thermal ablation

Thermal ablation uses high/low temperature to destroy tumor cells. Radiofrequency ablation (RFA) is the most common technique, but more recently, microwave ablation (MWA) and cryotherapy have been proposed (Sabath and Casal, 2019). The heating (for RFA and MWA) or cooling (for cryotherapy) of the tumor is achieved using specialized needles, inserted via transthoracic access and CT guidance. Since the needle placement is not devoid of clinical complications, some researchers have proposed to deliver thermal ablation under bronchoscopy guidance (Palussière et al., 2017). Thermal ablation has been described as an alternative to radiation therapy, and may be prescribed with curative intent for inoperable patients.

Systemic treatment

The intake of medication for the treatment of lung cancer is known as systemic treatment. Three principal treatments can be differentiated: chemotherapy, targeted therapy and immunotherapy. Each one of these treatments uses different mechanisms to fight the cancer, as follows:

— **Chemotherapy** aims at the destruction of cancer cells, usually by keeping them from dividing and creating more cells. This treatment may cause damage to the healthy cells of the body and cause several side effects.

— **Targeted therapy** acts by targeting specific cancer genes or proteins, or the tissue environment that fosters cancer cell growth. This treatment focuses on fighting the cancer by limiting the damage to healthy cells.

— **Immunotherapy** acts by boosting the body's immune system, helping it to fight cancer growth.

Systemic treatments are typically prescribed in combination with surgery or radiation therapy as secondary treatment options, with the intent of augmenting the chances of curing the cancer. In metastatic NSCLC (stage IV), systemic treatments are used as the main treatment option in order to relieve the discomfort caused by cancer and lengthen patient's life. A combination of systemic treatments may be prescribed, and the specific choices depend on the patient's preference and/or applicability.

1.3 Video-Assisted Thoracoscopic Surgery (VATS)

The surgical resection of lung tumors is the mainline treatment for operable patients with early stage NSCLC. Tradionally, it is performed via open thoracotomy, requiring a large incision through one of more major muscles of the chest wall, as well as the use of a retractor to spread and hold the ribs apart (see Fig. 1.8 left). The procedure is very traumatic and often results in rib fracture and damage to intercostal nerves, leading to accute post-operative pain. Consequently, open thoracotomy has been described as the most painful of surgical procedures (Mesbah et al., 2016).

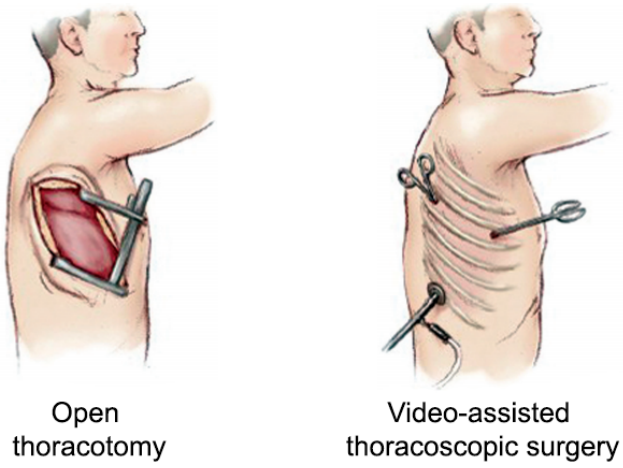

Figure 1.8: Comparison of surgical incisions in open thoracotomy and VATS

Recent decades have brought technological advancements allowing the development of minimally invasive surgical techniques. In the context of lung cancer management, it is the case for the video-assisted thoracoscopic surgery (VATS). In comparison to open thoracotomy, a VATS intervention uses considerably smaller incisions to access internal thoracic structures (see Fig. 1.8 right). Combining the use of a thoracoscope (small camera) and specialized surgical tools, surgeons can perform tumor resections while minimizing trauma. In fact, studies have reported results in favor of VATS interventions regarding perioperative complications, hospital stay, post-operative pain and quality of life (Al-Ameri et al., 2018; Bendixen et al., 2016). More importantly, it

has also been shown that VATS interventions provide similar clinical outcomes than traditional thoracotomies (Falcoz et al., 2015; Paul et al., 2014). Consequently, VATS interventions are increasingly replacing open thoracotomies as the default treatment option for operable lung cancer patients (Yan et al., 2013).

VATS is also an important diagnostic tool. Indeed, the advent of screening programs has increased the detection of pulmonary nodules with unknown histology. According to general clinical consensus, these nodules should be biopsed for diagnosis when suspected of malignancy (Gould et al., 2013). As mentioned earlier, this diagnosis is of paramount importance for appropriate treatment planning. However, nonsurgical biopsy techniques (*e.g.* transthoracic needle biopsy or bronchoscopic biopsy) still carry potential risks and are not applicable to all cases. More importantly, they may also be unreliable, specially for small, low-dense and/or deep nodules, for which a wedge resection through VATS is the preferred diagnostic method (Keating and Singhal, 2016).

1.3.1 Surgical procedure

A VATS intervention requires the active collaboration of a multidisciplinary team, including, but not limited to, a surgeon, an assisting surgeon, an anesthesiologist and a scrub nurse (Mehrotra and Arthur, 2019). Figure 1.9 illustrates the configuration of these specialists in a typical operating room setup. As depicted in the figure, during VATS, the patient lies to his/her side in lateral decubitus position, with one arm over the head and the operating lung at the top.

The specific VATS procedure depends very much on the health-care institution, the current clinical condition of the patient and the surgical procedure to be performed. However, in general, it involves the use of general anesthesia, artificial one-lung ventilation (OLV) and a triangular shaped three-port thoracic access (Hansen and Petersen, 2012; Mehrotra and Arthur, 2019). The overall procedure can be outlined as follows:

1. **General anesthesia.** The patient is placed on the operating table in supine position where general anesthesia is administered. This procedure typically includes the use of muscle relaxants (curare) to avoid spontaneous respiratory efforts (mainly diaphragmatic movement and coughing reflex). The muscle relaxant facilitates the setup of artificial OLV.
2. **Artificial lung ventilation and positioning.** An endotracheal tube, typically a double-lumen tube, is inserted in the patient's throat while in supine position. The tube is connected to a mechanical ventilator that provides controlled oxygenated airflow to the patient. The surgery is usually performed under OLV, meaning that only the non-operated lung contributes to breathing. The parameters of the mechanical ventilator and the placement of the endotracheal tube

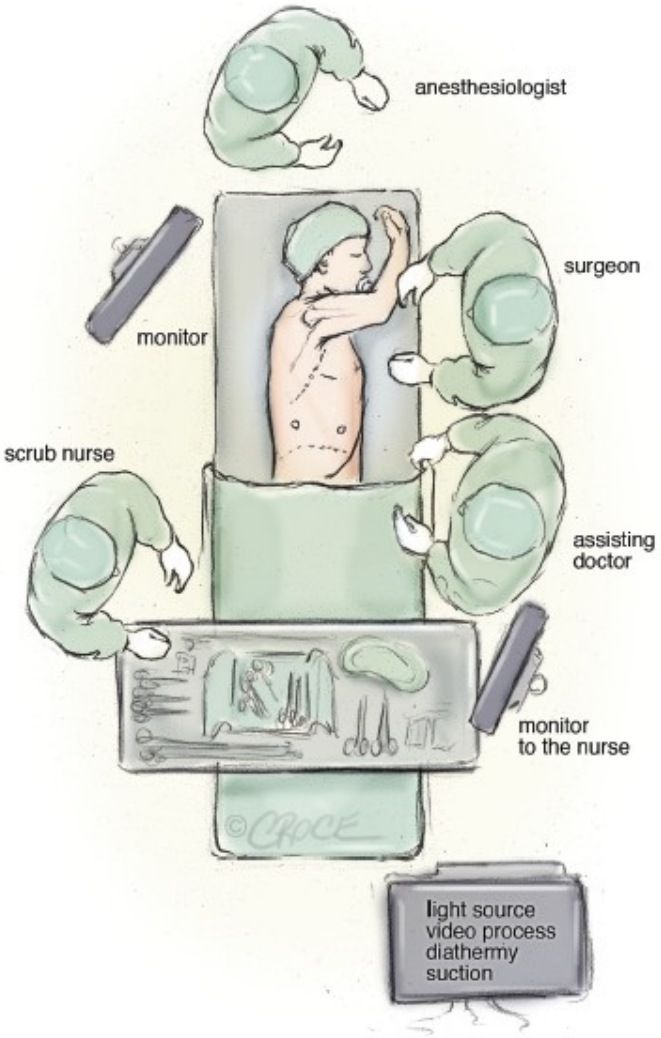

Figure 1.9: A typical operating room setup for VATS. Illustration taken from Hansen and Petersen (2012).

are carefully monitored to ensure adequate oxygen and carbon-dioxide levels. Finally, the patient is placed in lateral decubitus position, which is the operating position (see Fig. 1.9).

3. **Incisions and pneumothorax.** Access to the lung is typically achieved using three to four small incisions on the thoracic wall (surgical ports). These incisions are protected with plastic soft-tissue retractors and are configured in a triangular shape, allowing optimal use of the camera and surgical tools.

   The rupture of the thoracic wall disrupts the normal respiratory pressure gradients, causing a drop of the transpulmonary pressure gradient that results in pneumothorax (see Sec. 1.1.2). The resulting lung deflation creates space in the thoracic cavity that the surgeon uses for maneuvering during surgery. Total lung collapse may be avoided with a minimum positive transrespiratory pressure gradient applied from the mechanical ventilator.

4. **Resection.** After verification of appropriate patient setup, the surgeon proceeds to the surgical resection. The type of resection depends on the specific procedure to be performed. In general, the surgeon isolates the tissue to be removed (anatomical or non-anatomical) and uses surgical staples to cut it and suture. In particular, if a wedge resection is to be performed, localization of the pulmonary nodule might be required before resection. The resected specimen is placed in a special plastic bag, and is further extracted from the thoracic cavity through one of the surgical ports.

5. **Closing.** The patient is sutured, and a draining tube is placed on one of the surgical ports to allow the evacuation of any remaining air and/or secretions. The artificial lung ventilation is stopped once it has been verified that the patient is able to breath alone. The patient is placed in a post-operative care unit and is monitored closely until recovery.

If needed, the surgeon may enlarge one of the surgical ports in order to perform a traditional thoracotomy. This may become necessary if perioperative complications make the minimally-invasive intervention unfeasible or unsafe. This unplanned change in surgical technique is known as surgical conversion. Among the possible complications requiring surgical conversion, excessive bleeding due to vascular injury is the most common. Although non-negligible surgical conversion rates have been reported (*e.g* around 7% according to Puri et al. (2015)), they have been shown to decrease with surgical expertise (Vallance et al., 2017). Moreover, VATS interventions with unplanned surgical conversion appear to provide clinical outcomes that are no different than those with traditional open thoracotomy, which suggests that VATS should still be preferred even at the risk of surgical conversion (Subramanian and Puri, 2019).

1.3.2 Nodule localization for wedge resection

As mentioned earlier, during a wedge resection, pulmonary nodules are removed from the lung using non-anatomical cuts of tissue. This procedure naturally requires the localization of pulmonary nodules before resection, which has been typically performed by palpation and visual inspection. However, this manual localization technique becomes unreliable for small and/or deep nodules, since they are generally not palpable nor visible at the lung surface (Chao et al., 2018). This is especially the case for ground glass opacity (GGO) nodules, which can have very low density (GGO nodules are partly solid, partly sub-solid). Besides, finger palpation may also cause discomfort to the surgeon since his/her finger passing through a surgical port receives considerable pressure from the ribs. Furthermore, *a priori* estimations of the nodule position during surgery are hindered by the very large deformation suffered by the lung after pneumothorax. Nonetheless, failing to localize the nodules may ultimately result in unplanned surgical conversion with a rate as high as 54% (Suzuki et al., 1999). Consequently, the VATS clinical practice is evolving towards more reliable, more efficient and more practical localization techniques. This section presents an overall picture of the main pulmonary nodule localization strategies for VATS wedge resections.

Preoperative marker-placement localization

This technique consists in placing a distinctive marker inside or close to the nodule in order to facilitate its identification during surgery. The marker is inserted using a specialized needle under CT or broncoscopy guidance, for which an additional preoperative intervention is required. This intervention is minimally invasive, uses only local or no anesthesia, and is performed by an interventional radiologist in a CT interventional suit. Following marker placement, the patient is placed in a waiting room, before being transferred to the operating room. Three main marker types can be distinguished:

— **Hook-wires** might be the most commonly used method in current clinical practice. Nodule localization is achieved by hooking a long metallic wire to the nodule, which protrudes out of the lung and is visible during surgery. The hook-wire is inserted via transthoracic needle injection under CT guidance.

— **Microcoils** are small pieces of metal (generally platinum or gold) that are inserted into or close to the nodule by transthoracic needle injection under CT guidance. In comparison to hook-wires, microcoils are not directly seen from the exterior of the lung and require intraoperative fluoroscopy guidance for their localization.

— **Dyes** are also commonly used for nodule marking, and can be injected under either CT or broncoscopy guidance. According to the specific dye used, intraop-

erative nodule localization varies from visual inspection (*e.g.* methylene blue), fluoroscopy guidance (*e.g.* lipiodol) or radiation guidance (*e.g.* technetium 99).

Although high success rates have been reported for these nodule localization techniques (Chao et al., 2018; Keating and Singhal, 2016), significant disadvantages still prevail. For instance, hook-wires or microcoils have a potential for dislodgement or migration, which may occur during patient transfer to the operating room, or after pneumothorax or manipulation of the lung during surgery (Lin and Chen, 2016). Also, dyes might rapidly diffuse to lung parenchyma, or may result in dye/air embolism as they are often not water-soluble (Lin and Chen, 2016). Moreover, the use of transthoracic needle injections often results in complications such as pneumothorax or hemothorax, which are particularly cumbersome as the patient is under risk while waiting to be transferred to the operating room. The more the waiting time, the higher the discomfort for the patient and the higher the risk of complications (Chao et al., 2018). Consequently, although the optimal coordination of the preoperative marker-placement intervention and the VATS intervention may be challenging, it is of paramount importance.

Intraoperative image guided localization

To overcome the problems associated with preoperative localization procedures, intraoperative nodule localization has been proposed. This strategy uses imaging devices to localize pulmonary nodules directly in the operating room. The main proposed approaches are the following:

— **Intraoperative marker-placement** uses marker for pulmonary nodule localization as described previously, but takes place at the operating room immediately before surgery. Since intraoperative guidance is needed for marker placement, surgeons typically use C-arm imaging devices, as they provide cone-beam CT (CBCT) and fluoroscopy technology. For instance, Gill et al. (2015) have introduced the iVATS system that uses intraoperative CBCT images to place metallic fiducial markers, which are later localized under fluoroscopic guidance. Similar approaches exist, combining intraoperative CBCT guidance with either hook-wire (Zhao et al., 2016), dye (Yang et al., 2016), micro-coil (Lempel and Raymond, 2019) or double nodule marking (near-infrared and micro-coil marking, Chao et al. (2019)). With these intraoperative marker-placement techniques, the time at risk of the patient can be reduced without sacrificing localization success (Chao et al., 2018). However, although needle-induced pneumothorax or hemothorax are no longer of concern, heavier complications such as air/dye embolism may still happen.

— **Intraoperative ultrasonography** is a non-ionizing, portable and affordable imaging technology that has been proposed for the intraoperative localization of pul-

monary nodules. The feasibility of this method has been demonstrated, with pulmonary nodules identified as hyperechoic regions with hypoechoic shadows (Kondo et al., 2009; Sperandeo et al., 2019). However, this method assumes that the pulmonary nodules are visible in the ultrasound images, which may not be the case for some challenging nodules. For instance, the fuzzy borders and low density of GGO nodules could make them indistinguishable from normal lung parenchyma. Moreover, this method is also known to be difficult to learn and highly expert-dependent, which hinders its widely adoption. In addition, since any residual air in the lung leads to poor image quality, this localization technique must be performed on a fully deflated lung (after pneumothorax), which is unfeasible in some cases.

— **Near-Infrared imaging** uses fluorescent contrast agents that are administered systemically to the patient hours before surgery. These contrast agents bind to tumor cells, and are visible under near-infrared equipped thoracoscopes. This technique has been the subject of active research in recent years with promising results (Keating and Singhal, 2016; Predina et al., 2018). However, several questions remain open. For instance, the applicability to different patient populations and the binding of the contrast agent to different types of pulmonary nodules remain to be determined (Suda, 2018). In addition, issues such as the inability to detect deep pulmonary nodules (the deeper the nodule, the weaker the signal) or the detection of false positive nodules have been reported (Mao et al., 2017).

The major benefit of these localization strategies is that a single procedure is required for both localization and resection. This not only eliminates the logistic burden and patient discomfort associated to preoperative localization, but also reduces the time at risk for the patient as a transfer to the operating room is no longer necessary (Chao et al., 2018).

Intraoperative pulmonary nodule localization is a subject of active research. As each method has its advantages and limitations, establishing a gold standard will necessitate comparative clinical trials (Lin and Chen, 2016). However, it is worth highlighting that nodule localization techniques based on intraoperative imaging only are desirable, avoiding the complications and costs associated to preoperative localization and nodule marking procedures. In that regard, intraoperative ultrasound imaging is promising, but it still has limitations concerning image quality, nodule visibility and difficult interpretation. An alternative intraoperative imaging technique has been recently proposed for the localization of pulmonary nodules for VATS. This technique will be presented in the next section.

1.3.3 Intraoperative CBCT for pulmonary nodule localization during VATS

As an alternative to existing methods, a novel intraoperative localization strategy has been introduced at the Rennes University Hospital (Rouzé et al., 2016; Rouzé et al., 2018). The method requires a hybrid operating room equipped with a C-arm device, as the one illustrated in Fig. 1.10. Intraoperative CBCT images are acquired to help in the localization of pulmonary nodules, but, in contrast to the intraoperative CBCT-guided strategies discussed before, it does not require the use of any marker or contrast agent.

Figure 1.10: Hybrid operating room at the Rennes University Hospital. The C-arm is ready for a CBCT image acquisition of the patient, who lies on the operating table.

The VATS intervention is carried out following the standard procedure described previously in Sec. 1.3.1, with the exception of the nodule localization process, which is performed after the creation of surgical ports. A CBCT image is acquired once the lung has been deflated by the pneumothorax. However, the larger the pneumothorax, the denser the lung tissue becomes and the poorer the visibility of internal lung structures in the CBCT image. For this reason, oxygen is insufflated to the operating lung as to prevent its complete collapse. Then, the pulmonary nodule is localized by visual inspection of the image, and it is delineated using a dedicated image processing software. Figure 1.11 shows an example of a pulmonary nodule localized using this technique. The pulmonary nodule, the delineation, both lungs and the pneumothorax are visible in the figure.

Finally, the 3D reconstruction of the delineated nodule serves as an artificial marker that is localized under fluoroscopy guidance. This reconstruction is superposed onto fluoroscopic images with the surgical tools inside the thoracic cage, as shown in Fig.

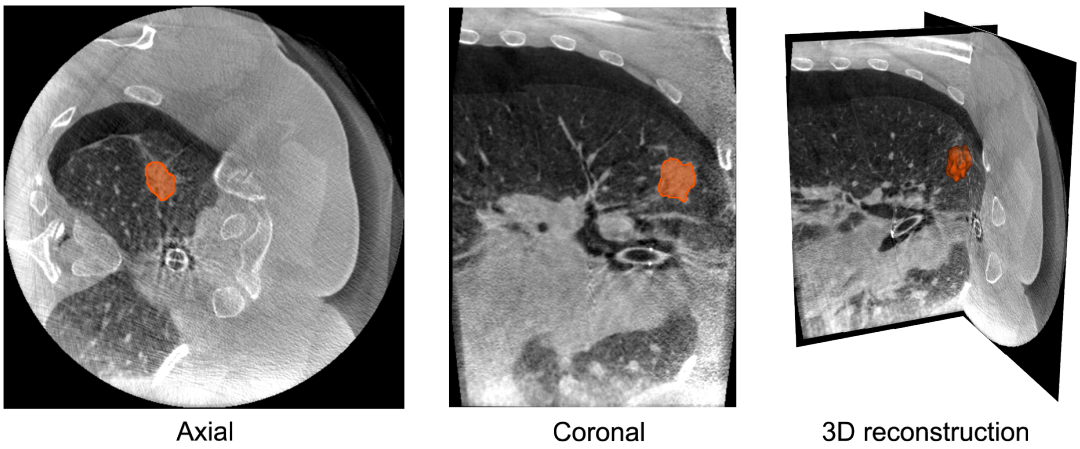

Figure 1.11: Manual delineation of a pulmonary nodule in an intraoperative CBCT image of a semi-deflated lung.

1.12. This mechanism provides the necessary spatial guidance for the surgeon to identify the section of the lung to be removed, which is resected immediately after.

The feasibility of this approach has already been demonstrated in a preliminary clinical study with promising results (Rouzé et al., 2016; Rouzé et al., 2018). Currently, there is ongoing research at the Rennes University Hospital to further evaluate its safety and efficacy.

Current challenges and motivation

The nodule localization method described above avoids using markers or contrast agents, which have both associated complications and non-negligible failure rates. However, some pulmonary nodules may still be very difficult to visualize in the intraoperative CBCT image. This is especially the case for GGO nodules, as the one illustrated in Fig. 1.13.

The visibility of the pulmonary nodule in the intraoperative CBCT image depends on the difference in density between the nodule and the surrounding parenchyma. Since the density of parenchyma increases with lung deflation, the larger the pneumothorax the more difficult it is to localize the nodules in the image. Even though artificial ventilation to the operating lung avoids total lung collapse and provides some control of the amount of pneumothorax, it is not possible to precisely regulate lung deflation, and heterogeneous localized airway collapse cannot be avoided. Moreover, lung structures in the intraoperative CBCT image are very largely deformed with respect to the preoperative CT image, which makes it difficult to take advantage of the known anatomical position of the nodule for its localization during surgery. Some of these difficulties can be observed in the example provided in Fig. 1.13.

In addition, the need for fluoroscopic guidance implies supplementary radiation dose

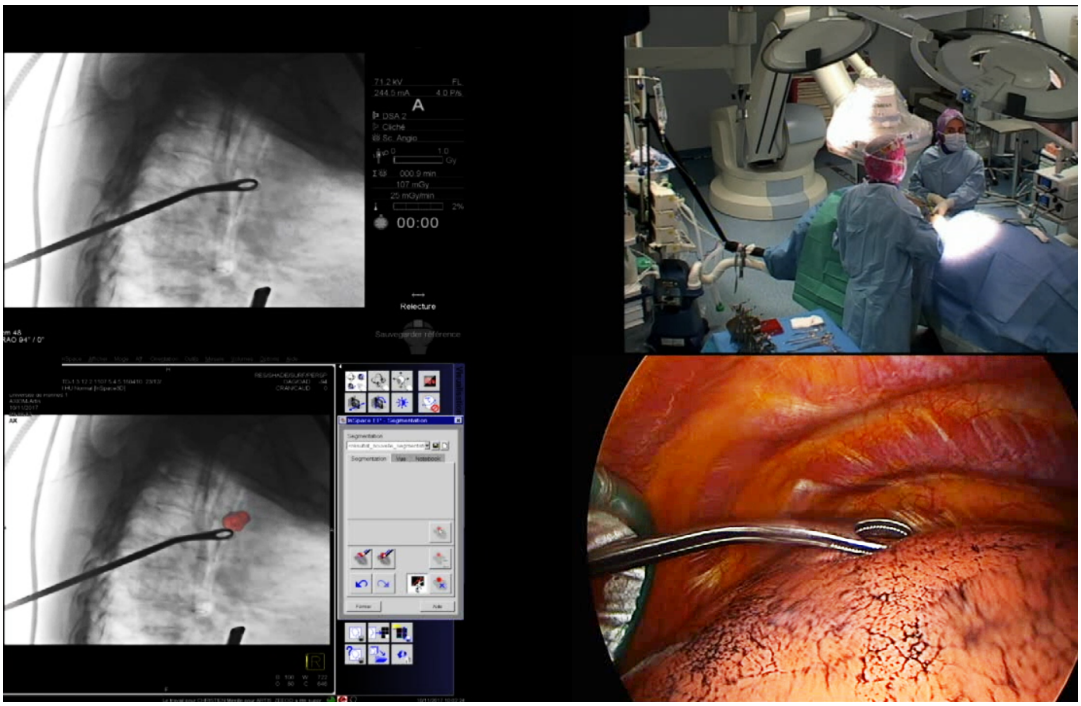

Figure 1.12: Intraoperative localization of a pulmonary nodule under fluoroscopic guidance. The 3D reconstruction of the delineated nodule is displayed in the fluoroscopic images to help the placement of surgical tools. The figure shows the original (top left) and augmented (bottom left) fluoroscopic, a view of the hybrid room during surgery (top right) and a view of lung from the endoscopic camera (bottom right).

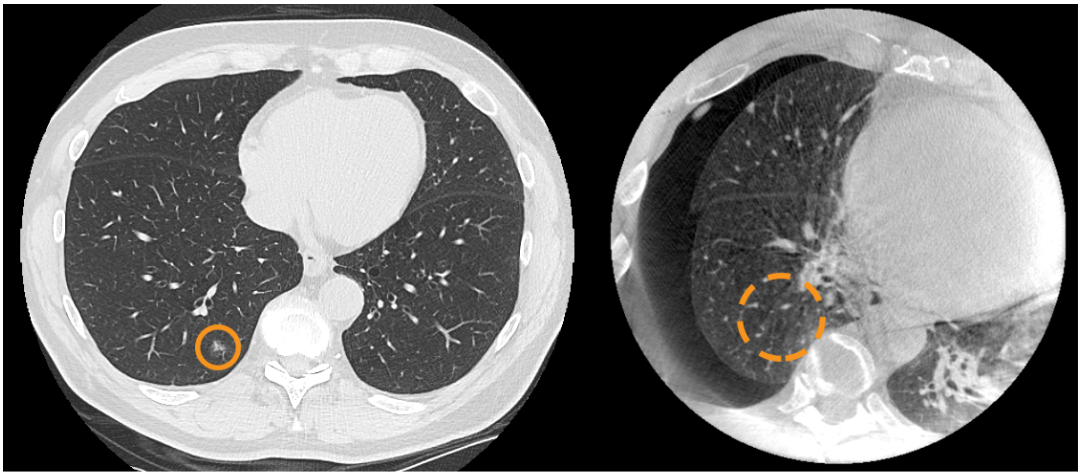

Figure 1.13: Comparison of GGO nodule visibility in preoperative and intraoperative images. Full-line and hashed-line circles indicate that the position of the nodule is known and unknown, respectively. The visibility of the nodule in the intraoperative CBCT image is not sufficient to allow its localization.

for the patient, but also for the surgical team. Indeed, this guidance relies on the position of the surgical tools and the 3D reconstructed pulmonary nodule in the fluoroscopic images to localize the resection zone. The surgeon and assistant surgeon need to stay close to the patient during fluoroscopy acquisitions, and therefore, receive radiation dose. The importance of this issue becomes clear in the long term by considering multiple fluoroscopic images during multiple localization procedures. It should be recalled that this limitation is intrinsic to the fluoroscopic guidance, and hence various pulmonary localization strategies are of concern (*e.g.* micro-coils, indocyanine-green dye). Ultimately, a virtual reality localization system would remove the need for fluoroscopic localization, and therefore reduce the radiation dose for the patient and the surgical team.

An important remark is that the position of the pulmonary nodule is always known in the preoperative images. Moreover, even though the nodule itself may not be visible in the intraoperative images, these images provide useful structural information about the actual state of the lung during surgery. For instance, the surface of the deflated lung, the main bronchi, as well as the main arteries and veins are visible. In some cases, even the fissures separating the lobes are partially visible (see Fig. 1.13). Consequently, it should be possible to integrate these observations into a deformation compensation algorithm, in order to estimate the intraoperative position of pulmonary nodules for cases where they are not directly observable. This is the main premise that motivated the works developed during this thesis.

Deformation compensation algorithms, in combination with lung imaging techniques, have the potential to improve the efficiency of the diagnosis, treatment-planning, and intervention guidance of lung diseases (McClelland et al., 2013). In the context of this thesis, they can help in the intraoperative localization of pulmonary nodules during VATS. The next chapter deals with the main methodological aspects of such algorithms and provides an overview of the literature in the context of lung deformation compensation.

2 Lung motion compensation: background and related works

In the previous chapter, it has been established that the combination of intraoperative imaging and lung motion compensation methods could prove useful for the intraoperative localization of pulmonary nodules during VATS. This chapter has the purpose of presenting a methodological background for lung motion compensation and a review of the literature. As it will be discussed herein, mainly two methods are used in lung motion compensation: intensity-based image registration methods and biomechanical modeling methods. An introduction to these methods is then necessary, and will be provided at the beginning of the chapter. Following, the main works on lung motion compensation will be presented, which will allow the introduction of the methodology developed during this thesis.

2.1 Intensity-based image registration

Image registration is an active research field, important in the area of medical imaging. Various methods exist with many different applications. Comprehensive reviews in medical image registration can be found in (Hill et al., 2001; Oliveira and Tavares, 2012; Sotiras et al., 2013). In the context of lung motion compensation, methods based on image-intensity are the most common (see for example (Murphy et al., 2011)), and the general framework will be introduced in this section.

2.1.1 Medical image

A medical image provides a discrete visual representation of the structure or function of some part of the body. Several imaging modalities are used in clinical practice for the acquisition of medical images, with Computed Tomography (CT) scanners, Magnetic Resonance Imaging (MRI) scanners and Ultrasound (US) scanners being the most common. The image is composed of a n-dimensional array of unit elements called voxels, which are accommodated in a finite rectangular grid of non-overlapping regions (see Fig. 2.1). To simplify, only images in 3 dimensions will be discussed in the remaining of this section, but the notions are the same for other dimensions.

Each voxel is associated to a discrete numeric quantity called image intensity, which results from quantizing the signal measured from the imaging device. The range of possible image intensity values as well as their physical interpretation are dependent on the imaging modality. For instance, intensity values may correspond to acoustic

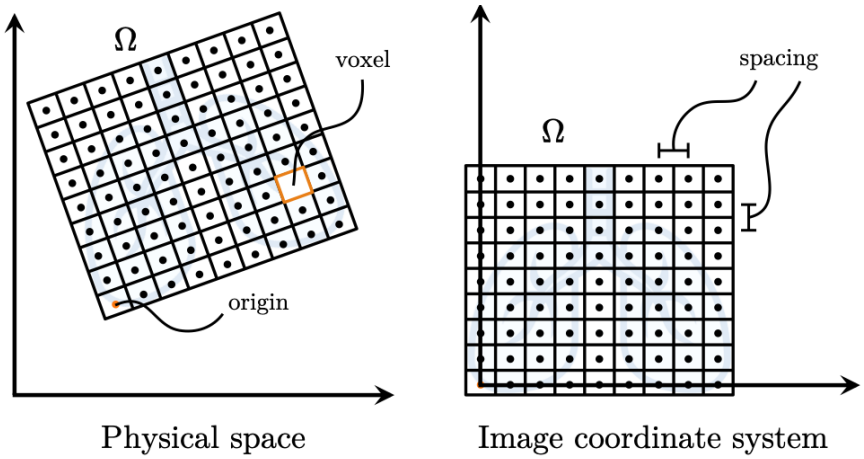

Figure 2.1: Illustration of a medical image in two dimensions. The position of voxel centers is illustrated with black circles. The bounds of the voxel array determine the domain of definition $\boldsymbol{\Omega}$.

impedance (B-mode Ultrasound), amount of water and fat content (Magnetic Resonance Imaging) or radiodensity (Computed Tomography).

The bounds of the voxel array determine the domain $\boldsymbol{\Omega} \subset \mathbb{R}^3$ in which the image is defined, which is a subspace of some world coordinate system. This coordinate system is also called the physical space. Each voxel has a center that is associated to a position $\boldsymbol{x} \in \boldsymbol{\Omega}$ in the physical space. The position of the first voxel in the physical space determines the origin of the image. The coordinate system whose origin is at the image origin and whose axes are aligned with the voxel array is called the image coordinate system. The world coordinate system and the image coordinate system are related by the image origin and a rotation matrix that represents image orientation.

A useful interpretation is to consider an image I as a mapping of voxel center positions $\boldsymbol{x}$ to image intensities: $I : \boldsymbol{x} \mapsto I(\boldsymbol{x})$.

2.1.2 Registration framework

Image registration refers to the process of spatially aligning two medical images. One of the images, called the *moving image* I_m, is deformed so that it aligns with the other image, the *fixed image* I_f. Although each image is defined in its own domain, they both share the same physical space: $\boldsymbol{\Omega}_m \subset \mathbb{R}^3$, and $\boldsymbol{\Omega}_f \subset \mathbb{R}^3$, respectively. The two images usually represent the same object under different configurations, moments of time or with different imaging modalities. As such, the registration process consists in finding a spatial transformation $\boldsymbol{T}$ that maps points in the *fixed image* I_f to homologous points in the *moving image* I_m, *i.e.* $\boldsymbol{T} : \boldsymbol{\Omega}_f \mapsto \boldsymbol{\Omega}_m$. In many cases, $\boldsymbol{T}$ is also described in terms of a displacement field $\boldsymbol{u}$, such that: $\boldsymbol{T}(\boldsymbol{x}) = \boldsymbol{x} + \boldsymbol{u}(\boldsymbol{x})$. A schematic representation of the registration process is provided in Fig. 2.2.

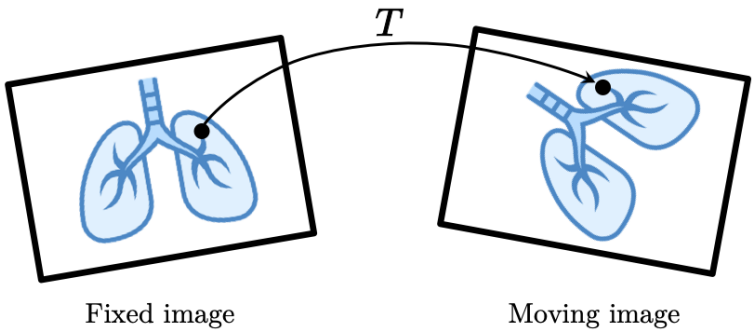

Figure 2.2: Spatial mapping in image registration. The transformation $\boldsymbol{T}$ is defined from the *fixed image* to the *moving image*.

The registration process is commonly expressed as an optimization problem in which a cost function $\mathcal{C}$ (also called energy function) is minimized with respect to $\boldsymbol{T}$, which can be formulated as:

$$\hat{\boldsymbol{T}} = \arg\min_{\boldsymbol{T}} \mathcal{C}\left(I_f, I_m \circ \boldsymbol{T}\right) \tag{2.1}$$

where $\hat{\boldsymbol{T}}$ is the estimated transformation, $I_m \circ \boldsymbol{T}$ is the *moving image* after being deformed by $\boldsymbol{T}$, and $\arg\min$ represents the optimization process with respect to $\boldsymbol{T}$.

In order to evaluate the quality of the transformation $\boldsymbol{T}$, a measure of difference or similarity between the two images I_f and $I_m \circ \boldsymbol{T}$ is required. The objective being that after registration, the measure of difference is minimal, or, the measure of similarity is maximal. In intensity-based image registration, both measures are commonly termed as similarity metric or similarity measure (Hill et al., 2001). In addition, the registration process is generally ill-posed, as there is no unique transformation $\boldsymbol{T}$ that maximizes the similarity metric. Consequently, constraints may be applied over $\boldsymbol{T}$ as to improve the behavior of the cost function $\mathcal{C}$, or to ensure a physically plausible transformation $\boldsymbol{T}$. With these considerations, the cost function $\mathcal{C}$ can be written as:

$$\mathcal{C}\left(I_f, I_m \circ \boldsymbol{T}\right) = -\mathcal{S}\left(I_f, I_m \circ \boldsymbol{T}\right) + \gamma \mathcal{P}(\boldsymbol{T}) \tag{2.2}$$

where $\mathcal{S}$ is the similarity metric, $\mathcal{P}$ is a penalty term devised to ensure the regularity of $\boldsymbol{T}$, and γ is a parameter weighting similarity against regularity.

Several options exist for each one of the components appearing in Eqs. (2.1) and (2.2). In each case, the appropriate choice is dependent on the type of medical images at hand, as well as the desired application. The following subsections provide further details regarding the transformation $\boldsymbol{T}$ and the similarity metric $\mathcal{S}$, which are the most relevant components concerning this manuscript.

Transform

The transformation $\boldsymbol{T}$ maps voxel positions from the *fixed image* domain to the *moving image* domain, so that the objects represented by those images are in alignment. However, the direction in which $\boldsymbol{T}$ is defined may seem contradictory, as it is the *moving image* and not the *fixed image* who gets deformed. The reason for this has to do with the computation of the deformed *moving image* ($I_m \circ T$) at the end of the registration process. In fact, the mapped positions $\boldsymbol{T}(\boldsymbol{x})$ generally do not correspond with voxel centers in the *moving image*, and hence, do not have associated intensity values. In practice, this issue is solved by using image interpolation: for each voxel position $\boldsymbol{x}$ in the *fixed image* domain $\boldsymbol{\Omega}_f$, calculate the value of the deformed *moving image* by interpolating the *moving image* at the mapped position $\boldsymbol{T}(\boldsymbol{x})$. On the contrary, if the transformation $\boldsymbol{T}$ was defined from the *moving* to the *fixed* image, there would be holes in the deformed *moving image*, as there is no guarantee that all voxels in the *fixed image* will be mapped to from the *moving image* (see (Schwarz, 2007, Sec. 3.2)).

In order to solve the optimization problem in Eqs. (2.1) and (2.2), different representations can be used for the transformation $\boldsymbol{T}$. The choice of the specific representation is problem-dependent, and the compromise between computational efficiency and richness of description plays an important role. Two main categories are usually distinguished in the literature: parametric and non-parametric transformations.

Parametric transformations: these transformations rely on a model, depending on a (typically small) set of parameters, which fully describes $\boldsymbol{T}$. The simplest transformation in this category is the so-called rigid-body transformation, with a total of 6 parameters: 3 for translation and 3 for rotation. More degrees of freedom can be allowed by introducing scaling (similarity transformation) and shearing (affine transformation) parameters in the transformation model. These transformation models are most of the time used for the registration of bony structures, as they undergo little to none deformation. However, the soft tissue deformation cannot be accurately represented with such simple transformation models.

Registration of soft tissue can be handled with transformation models that allow non-linear, localized deformation. Such transformation models are termed non-rigid, elastic or curved transformations. Parametric non-rigid transformation models optimize for displacements on a set of control points, and calculate the complete displacement field $\boldsymbol{u}$ using interpolation. For instance, the free-form-deformation (FFD) method uses control points defined on a regular lattice completely overlying the *fixed image*. It is typically used in conjunction with B-Spline functions for the interpolation of the displacement field (Rueckert et al., 1999). The main advantage of this method is that computation of the displacement field at any point depends only on a small set of neighboring control points, as the interpolation functions have compact support. This allows modeling highly local deformations in a computationally-efficient

manner. Another commonly used method is the thin-plate splines (TPS), in which control points can be placed arbitrarily in the physical space. This allows more flexibility, but requires all control points for the computation of the displacement field at a given point. Because of this, TPS transformations are generally less efficient than FFD transformations.

Non-parametric transformations: these transformations are also non-rigid transformations used for registering soft tissue deformation. In comparison with the parametric transformations, however, the displacement at each voxel position has to be found independently during optimization. The most commonly used approach in this category is the Demons algorithm (Thirion, 1998). It was conceived originally as an iterative algorithm, with attraction forces (*i.e.* displacement estimates) being computed at each iteration from image intensity gradients, and then being smoothed out using a Gaussian kernel. It has been shown, however, that a formulation similar to that given in Eq. (2.1) can be adopted (Vercauteren et al., 2007). The Demons algorithm has gained interest of the community as it has been shown to be very efficient, and various improvements have been proposed (Vercauteren et al., 2009; Wang et al., 2005). However, as every displacement vector may change independently from its neighbors during optimization, careful constraints should be enforced to the displacement field as to avoid physically implausible deformation.

Similarity metric

Different similarity metrics can be used to measure the quality of alignment during registration. Their use is problem-dependent, as each one has underlying assumptions that should be met for the registration process to work. Commonly, similarity metrics are classified with respect to the intended application: mono-modal or multi-modal image registration (Sotiras et al., 2013, Sec. III).

Mono-modal registration: in mono-modal registration, both images have been acquired using the same imaging modality. Under the hypothesis that the same objects and features appear with the same intensity values in both images, the mean of squared-distances (MSD) or the mean of absolute-differences (MAD) can be used to measure image similarity. However, such hypothesis may not be sufficient in some circumstances. For instance, different calibration parameters, different reconstruction techniques (*e.g.* CT - CBCT registration) or some physical processes (*e.g.* varying lung density during breathing) may result in large intensity differences between the images. In such cases, the normalized cross-correlation (NCC) and related similarity metrics may be more appropriate, as they only require a linear relationship between image intensities (Kim and Fessler, 2004).

Multi-modal registration: in multi-modal registration, the intensity values between both images may not be directly related as they typically represent different physical

quantities (*e.g.* CT - MRI registration). Instead of direct intensity associations, similarity metrics for multi-modal registration are based on information theory. As such, no assumptions are made for the intensity values between the images. The most commonly used similarity metric is the mutual information (MI) (Pluim et al., 2003). It is based on the computation of the marginal and joint entropy of the images, and measures the quantity of information one image has about the other. Several modifications have been proposed to the original similarity metric, with normalization (Studholme et al., 1999) and region-based computation (Studholme et al., 2006) being some examples.

Typically, the computation of the similarity metric is not performed over the whole image domains, but rather on a region of interest (ROI) enclosing the anatomical structures to be registered. This ROI can be manually or automatically segmented in one of both images, and then be used to define the voxels that will contribute in the computation of the similarity metric. This not only allows to better drive the registration process (*e.g.* if only the lungs are to be segmented in CT images of the whole chest), but it may even become necessary when registering structures with sliding interfaces.

2.2 Biomechanical modeling

Biomechanical models, issued from the field of continuum mechanics, allow to represent the physical and/or physiological behavior of tissue in the form of mathematical models. Using this representation, the tissue is considered to be a continuum delimited by a given geometry, governed by physical laws that ensure its mechanical coherence, and subject to specific conditions that induce its deformation. Several biomechanical models have been used in the context of lung motion compensation, and the general aspects for their mathematical description are provided in this section. For reference, a more complete and comprehensive description of these same aspects can be found in (Lai, 1993; Mase, 2009; Reddy, 2008).

2.2.1 Description of motion

Let us consider a material body $\mathcal{B}$ with known geometry and constitution in a three dimensional euclidean space $\mathbb{R}^3$. This body $\mathcal{B}$ can be understood as a collection of infinitesimal units called particles, each one occupying a unique position $\mathbf{X}$. For a given instant of time, the specification of position for all particles is said to determine the configuration of $\mathcal{B}$. The configuration of $\mathcal{B}$ at the instant $t = 0$, is called the initial configuration. The configuration of $\mathcal{B}$ at the instant t is called the current configuration. The analysis of motion and deformation is done with respect to one specific reference configuration, which is commonly assumed to be the initial configuration.

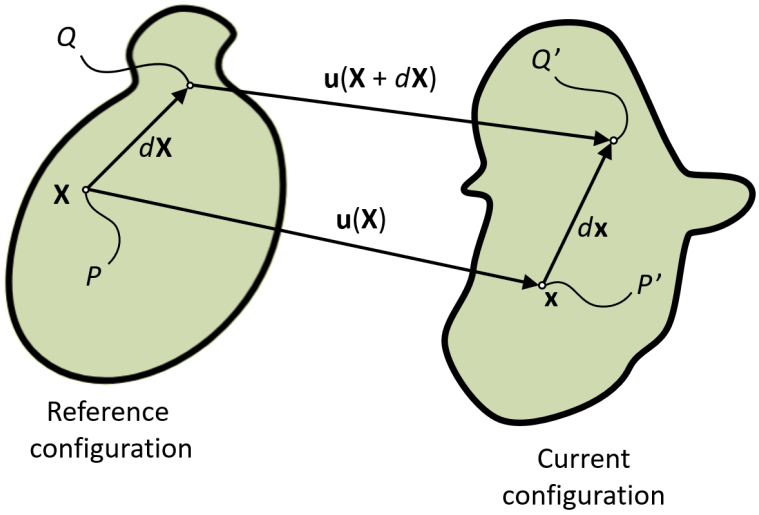

Figure 2.3: Reference and current configurations of a body subject to deformation.

Suppose that $\mathcal{B}$ has deformed after the application of loads. In such situation, the particle with reference position $\mathbf{X}$ is now at position $\mathbf{x}$ in the current configuration. This process is illustrated in Fig. 2.3. The position in the reference and current configurations of the particle are related by the displacement field $\mathbf{u}(\mathbf{X})$

$$\mathbf{u}(\mathbf{X}) = \mathbf{x} - \mathbf{X} \tag{2.3}$$

2.2.2 Deformation and strain

Deformation occurs when the relative distances among particles in the reference configuration are not conserved in the current configuration. One of the key quantities in the analysis of deformation is the deformation gradient tensor, noted by $\mathbf{F}$, which describes the relationship between a differential material line $d\mathbf{X}$ before deformation to its counterpart differential material line $d\mathbf{x}$ after deformation.

Let us consider a particle P with position $\mathbf{X}$ in the reference configuration. Using the relation provided by Eq. (2.3), the position of P in the current configuration (P') is expressed as

$$\mathbf{x} = \mathbf{X} + \mathbf{u}(\mathbf{X}) \tag{2.4}$$

Consider now a neighboring particle Q whose position with respect to P in the reference configuration is given by the differential relation $\mathbf{X} + d\mathbf{X}$. The position of Q in the current configuration (Q') is thus given by

$$\mathbf{x} + d\mathbf{x} = \mathbf{X} + d\mathbf{X} + \mathbf{u}(\mathbf{X} + d\mathbf{X}) \tag{2.5}$$

where the differential vector $d\mathbf{X}$ in the reference configuration gets mapped to $d\mathbf{x}$ in the current configuration. Using the principles of differential calculus and subtract-

ing Eq. (2.4) from Eq. (2.5), the following relation can be obtained:

$$d\mathbf{x} = d\mathbf{X} + \mathbf{u}(\mathbf{X} + d\mathbf{X}) - \mathbf{u}(\mathbf{X}) = d\mathbf{X} + (\nabla \mathbf{u}) d\mathbf{X} \tag{2.6}$$

where $\nabla \mathbf{u}$ is a second-order tensor called displacement gradient, and corresponds to the derivative of the displacement field $\mathbf{u}(\mathbf{X})$ with respect to $\mathbf{X}$. The right hand side of Eq. (2.6) can be factorized such that the equation becomes

$$d\mathbf{x} = \mathbf{F}\, d\mathbf{X} \tag{2.7}$$

where $\mathbf{F}$ is the deformation gradient tensor, which corresponds to

$$\mathbf{F} = \mathbf{I} + \nabla \mathbf{u} \tag{2.8}$$

As can be seen in Eq. 2.7, the deformation gradient tensor relates the differential vectors $d\mathbf{X}$ and $d\mathbf{x}$, and provides a measure of local deformation at every position $\mathbf{X}$. If $\mathbf{F}$ does not depend on $\mathbf{X}$ (*i.e.* it is constant), it is said that the deformation is homogeneous. On the other hand, if $\mathbf{F}$ is a function of $\mathbf{X}$, it is said that the deformation is inhomogeneous, as the particles deform differently according to their position. It should be noted that $\mathbf{F}$ is assumed to represent physically plausible deformation. Consequently, it is a bijective mapping between the reference and current configurations, and hence Eq. 2.7 implies that

$$d\mathbf{X} = \mathbf{F}^{-1}\, d\mathbf{x} \tag{2.9}$$

An important quantity issued from $\mathbf{F}$ is its determinant, which is called Jacobian of motion and is denoted by $J = \det \mathbf{F}$. The Jacobian of motion is a measure of volume change between the reference and current configurations. Realistic deformation is obtained only for positive values of J, and it may correspond to volume reduction ($J < 1$), volume conservation ($J = 1$) or volume expansion ($J > 1$).

The deformation gradient tensor $\mathbf{F}$ fully describes the deformation state of a body $\mathcal{B}$. Although it is translation invariant, it is not rotation-invariant. However, both translation and rotation-invariance are desirable, as rigid-body movement does not alter relative distances among particles, and hence, should not alter the measure of deformation. The deformation gradient tensor $\mathbf{F}$ can be used to derive other tensors that are invariant to rigid body movement, as introduced below.

Cauchy-Green deformation tensors

The Cauchy-Green deformation tensors describe the relationship of squared local distances between the reference and current configurations and vice versa. Consid-

ering the particles P and Q introduced above, their squared distance in the reference and current configurations is given respectively by

$$(dL)^2 = d\mathbf{X} \cdot d\mathbf{X} \tag{2.10}$$

$$(dl)^2 = d\mathbf{x} \cdot d\mathbf{x} \tag{2.11}$$

Using the relationship provided in Eq. (2.7), Eq. (2.11) becomes

$$\begin{aligned}(dl)^2 &= (\mathbf{F}\, d\mathbf{X}) \cdot (\mathbf{F}\, d\mathbf{X}) \\ &= (\mathbf{F}\, d\mathbf{X})^T (\mathbf{F}\, d\mathbf{X}) \\ &= d\mathbf{X}^T\, \mathbf{F}^T\, \mathbf{F}\, d\mathbf{X} \\ &= d\mathbf{X}^T\, \mathbf{C}\, d\mathbf{X}\end{aligned} \tag{2.12}$$

where $\mathbf{C}$ is the right Cauchy-Green deformation tensor, which corresponds to

$$\mathbf{C} = \mathbf{F}^T\, \mathbf{F} \tag{2.13}$$

Likewise, taking into consideration Eq. (2.9), it can be obtained that

$$(dL)^2 = d\mathbf{x}^T\, \mathbf{b}^{-1}\, d\mathbf{x} \tag{2.14}$$

where $\mathbf{b}$ is the left Cauchy-Green deformation tensor, which corresponds to

$$\mathbf{b} = \mathbf{F}\, \mathbf{F}^T \tag{2.15}$$

If the deformation gradient tensor $\mathbf{F}$ is orthogonal, then $\mathbf{C} = \mathbf{F}^T\, \mathbf{F} = \mathbf{I}$, and $\mathbf{b} = \mathbf{F}\, \mathbf{F}^T = \mathbf{I}$. This means that there is no deformation between the reference and current configurations, and the length of the differential material lines is conserved, *i.e.* $(dL)^2 = (dl)^2$. In this case, $\mathbf{F}$ represents a rigid-body motion.

Green-Lagrange strain tensor and infinitesimal strain tensor

The Green-Lagrange strain tensor describes the changes in squared lengths that occur from the reference to the current configuration. Consider again the differential vector $d\mathbf{X}$ and its deformed version $d\mathbf{x}$, as well as the respective squared lengths $(dL)^2$ and $(dl)^2$. Using the Eqs. (2.11) and (2.12), a change in squared length with respect to the reference configuration is written as

$$\begin{aligned}(ds)^2 - (dS)^2 &= d\mathbf{X}^T\, \mathbf{C}\, d\mathbf{X} - d\mathbf{X}^T d\mathbf{X} \\ &= d\mathbf{X}^T (\mathbf{C} - \mathbf{I}) d\mathbf{X} \\ &= 2\, d\mathbf{X}^T\, \mathbf{E}\, d\mathbf{X}\end{aligned} \tag{2.16}$$

where $\mathbf{E}$ is the Green-Lagrange strain tensor, which corresponds to

$$\mathbf{E} = \frac{1}{2}(\mathbf{C} - \mathbf{I}) \tag{2.17}$$

In comparison with the previously introduced deformation tensors, the Green-Lagrange strain tensor is zero when no deformation is present, *i.e.* $\mathbf{E} = \mathbf{0}$. It is typically described in terms of the displacement gradient $\nabla\mathbf{u}$, which gives

$$\begin{aligned} \mathbf{E} &= \frac{1}{2}(\mathbf{C} - \mathbf{I}) = \frac{1}{2}(\mathbf{F}^T\,\mathbf{F} - \mathbf{I}) \\ &= \frac{1}{2}((\mathbf{I} + \nabla\mathbf{u})^T\,(\mathbf{I} + \nabla\mathbf{u}) - \mathbf{I}) \\ &= \frac{1}{2}((\nabla\mathbf{u}) + (\nabla\mathbf{u})^T + (\nabla\mathbf{u})^T(\nabla\mathbf{u})) \end{aligned} \tag{2.18}$$

where the relationships from Eqs. (2.8), (2.13) and (2.17) have been used.

When the displacements $\mathbf{u}$ are very small (*i.e.* the assumption of "small deformations"), it is possible to neglect the second-order terms in the Green-Lagrange strain tensor, which results in

$$\mathbf{E} \approx \boldsymbol{\varepsilon} = \frac{1}{2}(\nabla\mathbf{u} + \nabla\mathbf{u}^T) \tag{2.19}$$

where $\boldsymbol{\varepsilon}$ is the infinitesimal strain tensor, also called linear strain tensor or small-deformation tensor.

2.2.3 Stress

So far, different ways to measuring the deformation of a body have been considered, without paying attention to the forces that may cause such deformation. These forces may be of two forms: body forces and surface forces. Body forces act throughout the volume of the body and do not require contact between its particles for being transmitted. The forces induced by gravity or by an electromagnetic field are examples of body forces. Body forces are typically expressed in terms of force per unit mass or force per unit volume. Surface forces, on the other hand, are forces that act upon a surface of the body, may it be real or imaginary. The forces emerging on the outer surface of two bodies when pressed one against each other (contact forces), or those emerging at the interior of a body while it resists being deformed are both examples of surface forces. These forces are designated by stress, or traction, and are expressed in terms of force per unit area.

Stress vector

Consider a body subject to arbitrary surface and body forces. Suppose that there is a cross-sectional surface $\mathcal{S}$ with normal unit vector $\mathbf{n}$, which passes through an arbitrary internal point P. The body is divided into two parts, one at each side of $\mathcal{S}$,

which are designated by I and II respectively. When considering I as a free body, its action upon II generates a force $\Delta\mathbf{f}$ distributed on a small area $\Delta\mathcal{S}$ of $\mathcal{S}$ that contains P, as depicted in Fig. 2.4. The Cauchy stress principle states that on the limit as the area $\Delta\mathcal{S}$ shrinks to zero around P, the net force at P depends uniquely on $\mathbf{n}$ and is defined by

$$\lim_{\Delta\mathcal{S}\to 0}\frac{\Delta\mathbf{f}}{\Delta\mathcal{S}}=\frac{d\mathbf{f}}{d\mathcal{S}}=\mathbf{t}^{(\mathbf{n})} \tag{2.20}$$

where $\mathbf{t}^{(\mathbf{n})}$ is called the stress vector at P on $\mathcal{S}$.

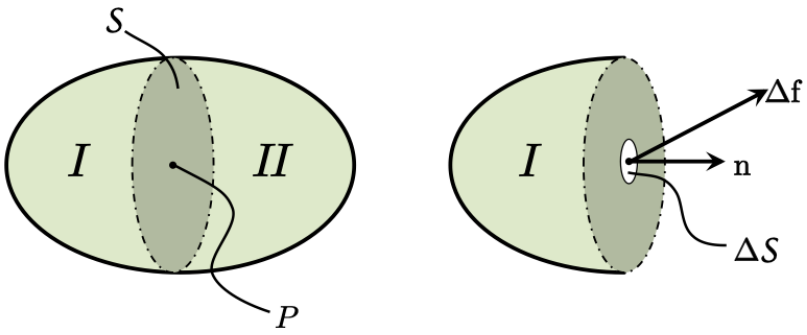

Figure 2.4: A body divided into two parts by a cross-sectional surface $\mathcal{S}$. The action of I upon II generates a force $\Delta\mathbf{f}$ distributed in a small area $\Delta\mathcal{S}$ centered at P.

Considering II also as a free body acting upon I, Newton's law of action and reaction states that there should be a stress vector at the same point P on the same surface $\mathcal{S}$ with opposite unit normal vector $-\mathbf{n}$ that is equal in magnitude and opposite to that defined in Eq. (2.20)

$$\mathbf{t}^{(\mathbf{n})}=-\mathbf{t}^{(-\mathbf{n})} \tag{2.21}$$

By definition, for each point inside the body, there is an infinite number of stress vectors, each one associated to one of the infinite number of possible cross-sectional surfaces. However, it is more convenient to describe the stress state of a point in the body as depending only on its position.

Stress tensor

Consider a small portion of the body in the shape of a tetrahedron with vertex at an arbitrary point P and base ABC perpendicular to an arbitrary normal unit vector $\mathbf{n}$, as the one illustrated in Fig. 2.5. An euclidean coordinate system of mutually orthogonal bases $\mathbf{e}_1$, $\mathbf{e}_2$ and $\mathbf{e}_3$ is chosen, so that the three faces of the tetrahedron BPC, CPA, APB are aligned with the coordinate planes, and the unit normal vector $\mathbf{n}$ can be expressed as $\mathbf{n}=n_1\,\mathbf{e}_1+n_2\,\mathbf{e}_2+n_3\,\mathbf{e}_3$.

If the area of the base ABC is designated as dA, then the areas of the remaining three

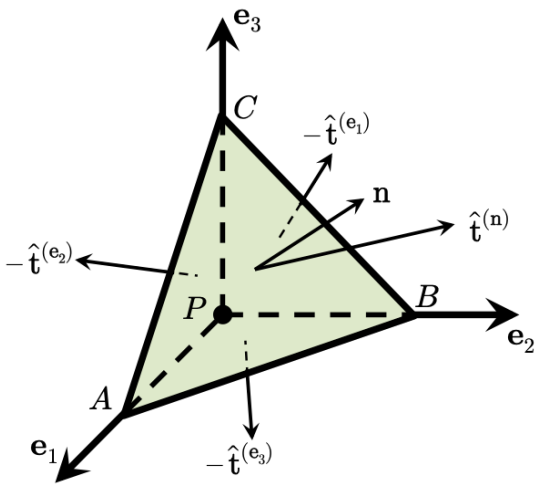

Figure 2.5: Free-body diagram of a tetrahedron having its vertex at a point P.

faces are respectively

$$\begin{aligned} dA_1 &= n_1 dA, \quad \text{for } BPC \\ dA_2 &= n_2 dA, \quad \text{for } CPA \\ dA_3 &= n_3 dA, \quad \text{for } APB \end{aligned}$$

Assuming that the tetrahedron is in equilibrium, the sum of all forces acting on it should be zero. Considering the relationship for the areas defined above, this is expressed by

$$\hat{\mathbf{t}}^{(\mathbf{n})}\, dA - \hat{\mathbf{t}}^{(\mathbf{e}_1)}\, n_1\, dA - \hat{\mathbf{t}}^{(\mathbf{e}_2)}\, n_2\, dA - \hat{\mathbf{t}}^{(\mathbf{e}_3)}\, n_3\, dA + \rho\, \hat{\mathbf{f}}\, dV = \mathbf{0} \tag{2.22}$$

where $\hat{\mathbf{t}}^{(\cdot)}$ is the average force acting on a face of the tetrahedron, ρ is the density of the material, $\hat{\mathbf{f}}$ the average body force acting throughout the body and dV the volume of the tetrahedron.

Let us designate h as the height of the tetrahedron, corresponding to the perpendicular distance between P and the base. The volume of the tetrahedron dV can be then be expressed in terms of the area of the base dA by $dV = (dA\, h)/3$, so that Eq. (2.22) becomes

$$\hat{\mathbf{t}}^{(\mathbf{n})} - \hat{\mathbf{t}}^{(\mathbf{e}_1)}\, n_1 - \hat{\mathbf{t}}^{(\mathbf{e}_2)}\, n_2 - \hat{\mathbf{t}}^{(\mathbf{e}_3)}\, n_3 + \frac{1}{3}\, \rho\, \hat{\mathbf{f}}\, h = \mathbf{0} \tag{2.23}$$

Now, on the limit as the height h of the tetrahedron reduces to zero, the average forces on each face become stress vectors at P, which leads to

$$\mathbf{t}^{(\mathbf{n})} = \mathbf{t}^{(\mathbf{e}_1)}\, n_1 + \mathbf{t}^{(\mathbf{e}_2)}\, n_2 + \mathbf{t}^{(\mathbf{e}_3)}\, n_3 \tag{2.24}$$

which can be rewritten as

$$\mathbf{t}^{(\mathbf{n})} = \boldsymbol{\sigma}\,\mathbf{n} \tag{2.25}$$

where $\boldsymbol{\sigma}$ is a second-order tensor called the Cauchy's stress tensor, and Eq. (2.25) is known as the Chauchy's stress formula.

The Cauchy's stress tensor is a property of the body that is independent to any unit vector normal $\mathbf{n}$. The stress state of the body is fully determined by a tensor field bounded by the body's geometry: it is possible to calculate a stress tensor for any given point in any given direction.

2.2.4 Elasticity

In order to describe the behavior of a body subject to loading, a relationship between the forces applied to this body (stress) and the resulting deformation (strain) must be established. Such a relationship is given the name of constitutive law or constitutive equation. The derivation of a constitutive law requires the formalization of a number of assumptions about the specific behavior and constitution of the material. In the study of soft tissue deformation, one common assumption is that the material is elastic: the stress in the material is a unique function of strain and the material completely recovers its original shape upon release of the applied loading. In the following, the three constitutive laws that are mostly used for lung motion description and compensation are introduced.

Linear elasticity

This is the simplest of all constitutive laws, and assumes that the relationship between stress and strain is linear. This assumption, however, is only suitable for the study of small deformations, as increasingly higher resistance to deformation may occur with higher stress. In consequence, this law is typically expressed in terms of the infinitesimal strain tensor $\boldsymbol{\varepsilon}$ as

$$\boldsymbol{\sigma} = \mathbf{c}\boldsymbol{\varepsilon} \tag{2.26}$$

where $\mathbf{c}$ is a fourth-order tensor, usually called stiffness tensor or elasticity tensor.

Equation (2.26) is known as the generalized Hook's law, as it is analogous to Hook's spring law. The stiffness tensor contains a total of 81 coefficients (it is a linear mapping between the 9 components of $\boldsymbol{\sigma}$ and the 9 components of $\boldsymbol{\varepsilon}$), which represent properties inherent of the body under study. However, it can be shown that only 21 of these coefficients are independent. Furthermore, only two coefficients are needed for the particular case of isotropic materials. In such case, Eq. (2.26) is reduced to

$$\boldsymbol{\sigma} = 2\mu\boldsymbol{\varepsilon} + \lambda \mathrm{tr}(\boldsymbol{\varepsilon})\mathbf{I} \tag{2.27}$$

where μ and λ are called Lamé constants.

The Lamé constants are commonly written in terms of the Young's Modulus E and Poisson's ratio ν through the relations

$$\lambda = \frac{E\nu}{(1+\nu)(1-2\nu)}, \quad \text{and} \quad \mu = \frac{E}{2(1+\nu)} \tag{2.28}$$

The Young's Modulus (E), also called modulus of elasticity, corresponds to the material's ability to resist deformation. On the other hand, the Poisson's ratio (ν) represents the material's ability to preserve its volume with deformation (compressibility). These two parameters could be determined for each material by experimentation.

Hyper-elasticity

Hyper-elastic constitutive laws describe stress-strain relationships as being non-linear. This allows to represent the increasing resistance to deformation coming from increasing stress. They do not make any assumptions on the amount of deformation undergone by the body under study, thus being more adequate for modeling large deformations than linearly-elastic constitutive laws. Hyper-elastic models rely on the existence of a strain energy density (W) which is a function of the deformation gradient tensor $\mathbf{F}$, such that

$$\boldsymbol{\sigma} = \frac{1}{J}\frac{\partial W}{\partial \mathbf{F}}\mathbf{F}^T \tag{2.29}$$

Poroelasticity

Poroelasticity models (Biot, 1941; Verruijt, 2013) assume that a single body is composed of two coexisting media: a solid, porous structure that is assumed to be elastic, and an incompressible fluid that moves within the pores of the solid structure. The total stress applied to the material is carried out partly by the fluid and partly by the solid structure. The hydrostatic pressure of the fluid inside the pores generates tensile/compressive stresses that cause deformation of the whole medium. It is assumed that the total stress on the porous medium can be decomposed as the sum of the stress carried by the solid structure and the stress carried by the fluid. This is known as the principle of effective stress and is described by

$$\boldsymbol{\sigma}_t = \boldsymbol{\sigma}_e - \alpha p \boldsymbol{I} \tag{2.30}$$

where $\boldsymbol{\sigma}_t$ and $\boldsymbol{\sigma}_e$ are the Cauchy stress tensors for total and effective stresses, respectively, and p is the hydrostatic pore pressure. The parameter α is called the Biot-Willis coefficient, and describes the amount of bulk volume change that is explained by a pore pressure change under constant stress.

The definition of the effective stress $\boldsymbol{\sigma}_e$ depends upon the mechanical behavior assumed for the solid medium. Both linear and non-linear stress-strain relationships (as those described in the previous sections) can be used in poroelastic constitutive laws. Since the porous medium is composed of two phases, its density may also be defined in terms of its constituent densities as

$$\rho = (1 - \phi)\rho_s + \phi\rho_f \tag{2.31}$$

where ρ_s and ρ_f are the densities of the solid and fluid media, respectively, and ϕ is the porosity of the whole medium (the fraction of the volume of pores over the total volume).

In a porous medium, the fluid flows through the pores according to Darcy's law. This law proposes a relationship between the instantaneous flow rate $\boldsymbol{q}$ of an incompressible fluid through a porous medium, and the hydrostatic pressure drop over a given distance ∇p , which is expressed by

$$\boldsymbol{q} = -\frac{\kappa}{\mu_f}\nabla p \tag{2.32}$$

where κ is the intrinsic permeability of the porous medium (the ability of the porous medium to allow fluid to pass through it) and μ_f the dynamic viscosity of the fluid.

The changes in strain of the solid medium are related to the changes in hydration level by the storage equation, which is defined by

$$\nabla \cdot \boldsymbol{q} + S\frac{\partial p}{\partial t} = -\alpha\frac{\partial \epsilon}{\partial t} \tag{2.33}$$

where S is the storativity parameter and $\epsilon = \partial u_x/\partial x + \partial u_y/\partial y + \partial u_z/\partial z = \nabla \cdot \boldsymbol{u}$ is the volumetric strain. The storativity parameter S may be understood as the amount of fluid that can be forced into the porous medium while maintaining a constant bulk volume.

The term to the right hand of Eq. (2.33) expresses the time rate of change of dilatation/contraction of the solid structure and how that affects fluid mass transport. For instance, if the pores are considered to be totally saturated with fluid, a negative rate of volumetric strain will shrink the porous material and immediately squeeze fluid out (interstitial pressure raises). On the contrary, if the pores are not fully saturated with fluid, the rate of volumetric strain does not have an instantaneous effect on the distribution of pore pressure.

Finally, an important consideration is the evacuation of fluid from the porous medium. According to Eq. (2.33), the fluid can flow through the porous medium following variations in hydrostatic pressure and in strain rate of the solid structure, and it can

be eventually evacuated from the porous medium at the boundary (by means of boundary conditions). However, in structures such as the lung, the fluid is evacuated through an intricate network of conducts (airways) distributed throughout the whole body. Although this fluid evacuation may be modeled explicitly (see the works by Berger et al. (2015) and Pozin et al. (2017)), it may as well be modeled implicitly. For instance, Chen et al. (2011) introduced a source term into the storage equation in order to account for fluid evacuation (in the context of brain modeling). As such, the fluid is allowed to sink inside the porous medium, hence approximating the fluid exchange happening at the small conducts. This is achieved by modifying Eq. (2.33), such that it becomes

$$\nabla \cdot \boldsymbol{q} + S\frac{\partial p}{\partial t} = -\alpha\frac{\partial \epsilon}{\partial t} - \kappa_b(p - p_c) \tag{2.34}$$

with $-\kappa_b(p - p_c)$ being the source term allowing for fluid evacuation. In the context of modeling lung deformation, the parameters κ_b and p_c represent the intrabronchi permeability and the intrabronchi pressure, respectively.

2.3 Related works in lung deformation compensation

The lung is a very soft, highly deformable organ in constant motion and deformation due to breathing, heart beats, and body movements. A wide variety of lung image registration techniques based on image intensity, biomechanical models, or hybrid approaches have been developed to compensate for lung deformation. These techniques were proposed mainly in the context of respiratory motion, with tomographic images typically acquired by pairs at both the end inhalation and the end of exhalation, or during the entire breathing cycle through 4DCT. This thesis work, however, deals with the compensation of lung deformation occurring during VATS using intraoperative CBCT imaging.

Breathing deformation and VATS deformation have different orders of magnitude, and are caused by different factors. For instance, during normal breathing, lung deformation results from the contraction and relaxation of respiratory muscles that in turn induce volumetric changes (see Sec. 1.1.2). Furthermore, the pleural space allows the lungs and the thoracic cavity to slide one against the other almost independently. On the other hand, during VATS, lung deformation results from various causes: the patient's change of pose; the muscle relaxants (curare) needed for surgery; and the pneumothorax. The change of patient's pose (observed in tomographic images from the preoperative and the intraoperative settings) entails a change in the direction of gravity with respect to the patient, which deforms the lung and other chest organs. The muscle relaxant administered with general anesthesia distends the diaphragm muscle, which in turn gets pushed upwards (*i.e.* towards the

apex) by the weight of the abdominal organs. The pneumothorax, resulting from the insertion of surgical ports, induces very large lung deflation that also leads to deformation of the mediastinum. The combination of these factors results in lung deformations that are considerably larger during VATS than during breathing.

2.3.1 Intensity-based image registration methods

Besides large lung deformation, sliding motion against the thoracic cage is widely known to be one of the major challenges encountered when dealing with intensity-based elastic registration of the lung parenchyma. In practical terms, the deformations of the lung and surrounding structures are constrained at the interface in the normal direction, but move almost freely in the tangential direction. However, most transformation models used in medical image registration assume a continuous displacement field that can not model this sliding effect (Maintz and Viergever, 1998; Sotiras et al., 2013).

Several authors have introduced methods for taking into account sliding interfaces for lung registration. Anatomical segmentations can be used to independently register the structures at the interface (Rietzel and Chen, 2006). With this technique, classical image registration algorithms can be used with little to none modification. However, gaps or overlaps may appear at the interface as a result of the independent registration. One solution consists in using a boundary-matching penalty method so that the interfaces are tied together. Wu et al. (2008) proposed to dilate the segmentations after a masking procedure to enforce the alignment of the interface. Another strategy is based on decomposing the deformation field at the interface into normal and tangential components. Sliding motion can be preserved by applying regularization on the normal component (Schmidt-Richberg et al., 2012), or by using a composite transformation with a shared normal component but independent tangential components (Delmon et al., 2013). The main drawback of these methods is the need for anatomical segmentations. Indeed, these segmentations are time-consuming to extract manually or may be inaccurate if extracted automatically, especially for pathological lungs or low contrast images.

In order to overcome the maksing issue, other works have proposed alternative methods that do not require prior anatomical segmentations. Ruan et al. (2009) presented a regularization strategy that discriminates the divergence and the curl of the deformation field separately. The authors are able to preserve sliding motion by allowing large shearing while penalizing other forms of non-smooth deformation. Another technique consists in using several layers of supervoxels (*i.e.* groups of neighboring voxels with similar intensities) connected using minimum spanning trees (Heinrich et al., 2016). The deformation field is enforced to be smooth across edge connections via regularization. However, non-connected supervoxels are allowed to be registered

independently, hence preserving sliding motion.

2.3.2 Biomechanical model-based methods

Another approach for lung deformation compensation is the use of biomechanical models describing the lung's behavior. The Finite Element Method (FEM) is commonly used to obtain numerical solutions to the underlying equations. For instance, Zhang et al. (2004) proposed a Finite Element (FE) deformable model of the lung reconstructed at the end of exhalation to simulate lung expansion motion. The thoracic cage surface at the end of inhalation was included in the formulation as frictionless contact conditions that constrained lung expansion. A uniformly distributed negative surface pressure was applied to the deformable model until it filled the thoracic cage. A similar approach to lung expansion motion was proposed by Werner et al. (2009). The authors performed a study on 12 lung tumor patients and evaluated how changing tissue parameters affect the estimated deformations. The results suggested that if tissue homogeneity was considered, changing tissue parameters could only produce marginal perturbations in lung deformation, since it was mainly dictated by the limiting geometry of the thoracic cage. Another study investigated the effect of tissue heterogeneity while modeling lung expansion (Ilegbusi et al., 2014). The elasticity modulus was estimated locally using an inverse non-invasive method. In average, the obtained values decreased with proximity to the diaphragm. The authors showed that the history of deformation as well as its spatial distribution were different when considering heterogeneous versus homogeneous material properties. Other authors have also investigated the use of non-constant, non-uniformly distributed negative surface pressures to produce lung expansion. Eom et al. (2010) computed negative pressure values from patient-specific Pressure-Volume (P-V) curves calculated from 4DCT data. With this approach, the authors were able to simulate lung deformation for the whole breathing cycle. The FE deformation predictions were more accurate than simple linear interpolation between end expiration and end inspiration deformations. Fuerst et al. (2015) automatically divided the lung surface in disjoint contact zones. The negative pressure applied at the surface was then differentiated for each contact zone, the specific values being found through an inverse problem formulation. Although the authors used homogeneous material properties, the results suggested an improvement of the deformation estimation thanks to the heterogeneous surface pressures, which are able to account for the lack of heterogeneous material properties.

Several works have also approached lung deformation estimation during breathing as a contraction motion. Al-Mayah et al. (2008) proposed a deformable model of the lung and surrounding structures reconstructed at the end of inhalation. Surface displacements from the end inhalation to the end exhalation phases were found using a mesh morphing method. These displacements were imposed as boundary condi-

tions to the inner surface of the thoracic cage, which is in direct contact with the deformable lung model. Interactions between the lung and thoracic cage was modeled via frictionless contact, which allowed the integration of lung sliding. This study was further extended to investigate the effects of contact friction at the lung interface (Al-Mayah et al., 2009) or heterogeneous material properties (Al-Mayah et al., 2010), as well as the influence of linear and non-linear elasticity constitutive laws (Al-Mayah et al., 2011). These studies led to the development of the biomechanical model-based deformable image registration framework Morfeus for treatment planning and accurate target delineation during external radiation therapy. Recently, Velec et al. (2017) validated the accuracy of a commercial version of Morfeus on tomographic and MR images of the thorax, prostate and liver of 74 patients, with validation errors measured in the range of the image spacing.

All the methods reported above model the lung parenchyma as a single elastic continuum. In reality, the volume occupied by the lung is composed of not only the parenchyma but also a great quantity of air that is stored inside the airways and alveoli. External forces exerted by the respiratory muscles allow the inhalation or exhalation of air from the lung, ultimately resulting in tissue deformation. Following this interpretation, the lung can be modeled as a porous medium composed of two coexisting physical domains: a solid domain (*i.e.* the parenchyma) and a fluid domain (*i.e.* the air flowing inside the lung). Physical laws governing the behavior of such porous medium constitute the theory of poroelasticity, which has been previously used to model breathing deformation. For instance, Ilegbusi et al. (2012) proposed a poroelastic model to simulate lung deformation throughout a complete breathing cycle. Boundary conditions for the fluid and solid domains consisted in a time varying positive pressure and a fixed support, respectively. The authors reported realistic deformations including a hysteresis deformation effect when accouting for heterogeneous material properties. Gravity was later added in the loads which improved the accuracy of the predicted deformation (Seyfi Noferest et al., 2018). Berger et al. (2015) also proposed a dynamic poroelastic model of the lung tightly coupled with an airway network modeling the airways. The authors presented a comprehensive description of their model and introduced its applicability to normal and physiological breathing using varying airflow resistance and local elasticity. Physiologically realistic global measurements were reported.

2.3.3 Hybrid methods

Lung deformation compensation methods using intensity-based image registration methods or biomechanical models have both advantages and disadvantages. Intensity-based methods are limited by the reduced quality of intraoperative images and the need for complex regularization strategies for realistic motion estimation. On the other hand, good results on a voxel-by-voxel basis, especially for internal structures,

can be obtained if images of adequate quality are available. Regarding biomechanical models, limits mostly come from the uncertainties on boundary conditions needed for realistic lung motion simulations, the high variance in tissue constitutive parameters that could be difficult to estimate accurately, or the compliance of computational requirements with clinical practice. However, when compared with intensity-based methods, biomechanical models are able to work with less data since the underlying biophysical representation naturally constrains the solution space. In addition, as these are naturally boundary valued problems, their resolution is quite compatible with environments where primarily only surface information is available. Also, approaches that use modeled physical and physiological phenomena may provide insight into understanding disease and its effects on lung behavior. The hypothesis of hybrid methods is that combining the two strategies allows to compensate for their individual limitations.

Hybrid methods for lung deformation estimation have already been investigated in previous works. Li et al. (2008) used intensity-based image registration to estimate a deformation field from end of exhalation to end of inhalation breathing phases. Dirichlet boundary conditions (*i.e.* imposed displacements) were then computed by interpolating the deformation field on the surface nodes of a deformable FE lung mesh. A similar approach was employed by Tehrani et al. (2015), who used Demons image registration to estimate surface displacement boundary conditions at several moments of the breathing cycle. In addition, the authors studied the effects of tissue parameters and non-linear elasticity laws on tumor displacement estimation accuracy, reporting best results under non-linear elasticity assumptions.

Other studies have used intensity-based image registration to reduce residual errors resulting from biomechanical model motion estimation. For example, Samavati et al. (2015) used the Morfeus platform to estimate lung contraction between end of inhalation and end of exhalation. The estimated deformation was then refined using nonrigid image-intensity registration between the warped end of inhalation image and the target end of exhalation image, which lead to improved estimation accuracy. Han et al. (2017) applied the same methodology to lung expansion deformation estimation during breathing. The authors compared their approach to only intensity-based or only biomechanical-model based image registration, and also evaluated the influence of tissue parameters, contact friction and tissue heterogeneity. Their results suggest better performance of hybrid approach with respect to intensity or biomechanical models alone, but a performance similar to intensity-based approaches that account for sliding motion. The uncertainty of model parameters was accounted for by the refinement image-intensity step, allowing the use of simplified assumptions for the biomechanical models in hybrid approaches.

Finally, in the context of lung deformation compensation for VATS, very few works

have been proposed. Uneri et al. (2013) carried out a preliminary study using CBCT images of an inflated and deflated ex-vivo pig lung. Although the authors did not use biomechanical modeling, a hybrid approach was implemented combining surface morphing and nonrigid intensity-based image registration. The reported results were promising, but the applicability to clinical practice remains to be determined, since the quality of real intraoperative VATS images is potentially lower than the quality of the images used by the authors, and the amount of pneumothorax deformation is not under control. More recently, Nakao et al. (2019) proposed a surface-based shape model of lung deflation validated on lungs of Beagle dogs. The authors provided inter-subject statistical analysis of lung deformation on a population of 10 animals. However, validation results were reported only for surface landmarks, and its applicability to internal lung deformation remains to be investigated. To date, these studies are the only ones within the VATS context, but are limited to animal specimens in non-clinical conditions.

2.3.4 Summary

In this section, the state-of-the-art for lung deformation compensation methods was presented. Although there is plenty of research in the context of deformation during breathing, very few works have been proposed in the context of deformation during VATS. Indeed, as explained in Chapter 1, surgical resection of pulmonary nodules has seen a paradigm shift to minimally invasive, tissue-preserving techniques, which only recently benefit from the use of intraoperative images. As a result, the problem of lung deformation compensation for pulmonary nodule localization during VATS has been barely addressed by the scientific community, with only some notable exceptions (Nakamoto et al., 2007; Nakao et al., 2019; Uneri et al., 2013).

Recent studies have shown that hybrid approaches have the ability to deal with the restrictions of intensity-based or biomechanical model-based registration approaches in a complementary manner. This could be specially useful for the compensation of lung deformation during VATS, as bad-quality images and unknown boundary conditions, external loading and tissue properties need to be handled.

3 Challenges, method overview and clinical data

The previous two chapters have introduced the general clinical and methodological contexts encompassing the works presented in this manuscript. The overall objective of this thesis was the development of a registration framework for lung deformation compensation, as a tool for pulmonary nodule localization for VATS. This chapter provides an overview of the proposed registration framework, which corresponds to the main contribution of this thesis work. The chapter starts by listing the principal technical challenges to be addressed, which provides the context for introducing the methodological choices that were made. Following, an overview of the registration framework is presented, and the clinical data that was acquired for its validation is described. Finally, the last section provides a summary of the main investigations carried out during this thesis.

3.1 Technical challenges and methodological choices

The current surgical VATS workflow, described in Sec. 1.3.3, has been proposed only very recently (Rouzé et al., 2016; Rouzé et al., 2018). Consequently, developing a registration framework that accounts for lung deformation in such a surgical workflow needs to overcome various technical challenges that have not been addressed previously in the literature. Indeed, although some authors have proposed registration approaches for pulmonary nodule localization during VATS, these are either based on simplified surgical workflows in animal studies (Nakao et al., 2019; Uneri et al., 2013), or do not account for internal lung deformation and are based on surface features only (Nakamoto et al., 2007; Nakao et al., 2019).

This section introduces the main technical challenges and presents how they were addressed in this thesis. For illustration purposes, some of the problems associated to these challenges are pointed out in Fig. 3.1, over a CBCT image of the deflated lung that was acquired according to the current clinical VATS workflow.

3.1.1 Challenge of CBCT images

The acquisition processes for the CT and CBCT images differ significantly. On the one hand, CBCT images require less irradiation than CT images (Kalender and Kyriakou, 2007), which is beneficial for the patient but not without detriment of the resulting image quality. On the other hand, the projection and reconstruction strategies are also different, with larger 2D flat detectors for the CBCT images (cone beam) instead of

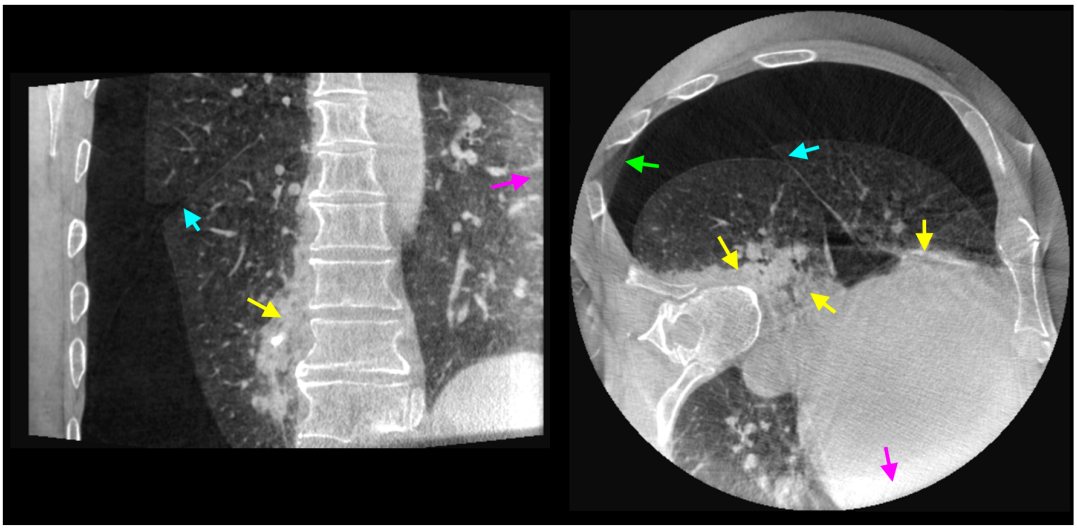

Figure 3.1: Coronal and axial slices of a CBCT image of the deflated lung illustrating some of the technical challenges. The large deformation induced by the pneumothorax is clearly visible. The arrows indicate localized atelectasis (yellow), cupping artifacts (magenta), image reconstruction artifacts (green) and lobe sliding (cyan). The CBCT image only provides a partial view of the lung.

line 1D detectors for the CT images (fan beam). These larger 2D detectors allow faster acquisitions, but suffer from higher image intensity scattering, and introduce cupping, aliasing, and truncation artifacts (Kalender and Kyriakou, 2007; Schulze et al., 2011). Furthermore, parenchyma densification and atelectasis can also be observed under large lung deformations, which decreases even more the contrast among internal lung structures and between the lung parenchyma and surrounding structures. Finally, only a partial view of the lung is available within the CBCT images due to the limited FOV of the scanner. All these problems (some of them illustrated in Fig. 3.1) hinder the interpretation of these images, as well as their automatic processing for intensity-based image segmentation and registration . In this thesis, the challenge of CBCT images was handled in two ways:

Image preprocessing: The cupping, truncation and reconstruction artifacts significantly modify intensity values in the CBCT images, which leads to poor-performing intensity-based image processing algorithms. In this thesis, the CBCT images were pre-processed with an in-house artifact reduction algorithm (see Sec. 6.5).

Semi-automatic/manual segmentation: Automatic segmentation of lung structures in CBCT images is a challenging problem in itself, especially with the lung deflated by pneumothorax. Since this thesis was focused in solving a registration problem rather than a segmentation problem, automatic segmentation was not

addressed, and semi-automatic or even manual approaches were used instead. However, it is expected that automatic segmentation methods could be developed in the future.

3.1.2 Challenge of large lung deformation

In the current VATS clinical workflow, two structural images of the lung are used for localizing pulmonary nodules (see Sec.1.3.3): a preoperative chest CT with the patient in supine position, and an intraoperative CBCT of the deflated lung (*i.e.* after pneumothorax) with the patient in lateral decubitus position. Between the two acquisitions, the lung undergoes very large deformation. Finding a transformation that aligns these two images (*i.e.* solving the registration problem) requires not only dealing with such large deformation, but also with the challenges associated to the CBCT image that were discussed in the previous section (see Fig. 3.1). Up until now, this registration problem has not been directly addressed in the literature. The closest example is the work carried out by Uneri et al. (2013), in which CBCT images of the inflated and deflated lung of porcine specimens were registered in order to account for lung deformation. In comparison to this thesis, the authors did not study real VATS clinical cases and used images of the complete lung, both in lateral decubitus position. In this thesis, the registration problem was approached differently, and the large lung deformation was addressed in two ways:

Two registration sub-problems: Lung deformation during VATS may be understood as a result of two physical processes. The first process corresponds to a change of the patient pose from supine to lateral decubitus, which alters the orientation of the body with respect to gravity and causes weight to deform the lung and surrounding organs. The second process corresponds to the pneumothorax, which causes lung deflation and deformation of other chest structures. This thesis presents a first attempt to account for both physical processes, so that the position of the pulmonary nodule can be projected from the preoperative setting into the intraoperative surgical setting. This was achieved by introducing an additional intraoperative CBCT image of the lung after the change of pose but before pneumothorax, which allowed to decouple the original registration problem into two smaller, more tractable sub-problems: the first accounting for the change of pose deformation, and the second accounting for the pneumothorax deformation.

Hybrid approach to lung registration: As discussed in the previous chapter, lung deformation compensation could be addressed using intensity-based image registration methods, biomechanical model-based methods, or hybrid methods combining both (see Sec. 2.3.3). However, the large lung deformation may be too difficult to deal with using only intensity-based methods or only biome-

chanical model-based methods. Indeed, on the one hand, using intensity-based methods only would require sophisticated mechanisms to deal with the challenging CBCT images, and preliminary investigations carried out in that direction deemed unsatisfactory (see Appendix A). On the other hand, using biomechanical model-based methods only would require a validated model of lung deformation in the context of VATS, as well as appropriate boundary conditions, which are both unknown to date. Consequently, in this thesis, a hybrid approach was considered to be the most appropriate. Moreover, this goes in accordance with the literature in lung deformation compensation, where hybrid approaches have been found helpful in solving challenging registration problems (see Sec. 2.3.3).

3.1.3 Challenge of modeling lung deformation

The lung is a very soft, highly deformable organ in constant motion and deformation due to breathing, heart beats, and body movements. Although various biomechanical models have been proposed in the literature for the study of this deformation (see Sec. 2.3.2), to date, neither of these has been evaluated in the context of change of patient pose or pneumothorax during VATS. Consequently, in principle, the boundary conditions and tissue parameters reported in those studies may not be applicable to the registration problem addressed in this thesis, since the physical processes causing lung deformation are inherently different. Moreover, the observed lung deformation (and hence the tissue parameters and the boundary conditions) is likely to be patient- and intervention-specific. In this thesis, the challenge of modeling lung deformation was handled in the following ways:

The lung as a poroelastic medium: Various biomechanical models have been used to account for lung deformation. For the most part, these models represent the lung as a single elastic medium, and both linearly-elastic and hyperelastic constitutive laws have been used for that purpose (Al-Mayah et al., 2011). However, in reality, a large amount of volume inside the lung is occupied by air, and it is the air-tissue interaction that ultimately causes lung deformation. Although this aspect has been obviated in many works modeling breathing deformation, it was considered essential in this thesis for modeling pneumothorax deformation, which is driven principally by air evacuation. Consequently, this air-tissue interaction was modeled via a poroelastic biomechanical model with allowance for air evacuation. A first order approximation using linear-strain theory was adopted, which facilitated the formulation and implementation, while allowing investigating the feasibility of the approach.

Image registration to boundary conditions: Intensity-based image registration has proven useful in the estimation of boundary conditions for biomechanical mod-

els in breathing deformation compensation (Li et al., 2008; Tehrani et al., 2015). This approach consists in imposing the observed displacement (issued from the intensity-based image registration process) as a partial solution to the biomechanical simulation (boundary conditions). This allows to exploit the image information that is available/measurable while leaving to the biomechanical model the estimation of the overall deformation. This approach was used in this thesis to estimate boundary conditions for the solid phase of the poroelastic biomechanical model.

Inverse problem formulation for patient-specific simulation: The amount of pneumothorax observed during VATS could differ significantly from patient to patient. This entails a difference in lung deformation, which can be modeled using different tissue parameters. These parameters, however, are unknown in advance. Therefore, in this thesis, an inverse problem formulation was adopted in order to estimate the tissue parameters required to simulate each clinical case. This formulation used an objective function based on a data-driven criteria within an unconstrained optimization framework. The criteria corresponded to a surface-to-surface distance, between the simulated deformation and the observed deformation in the CBCT image.

3.1.4 Challenge of clinical compatibility

Naturally, the pulmonary nodule localization tool has to be designed and developed to be compatible with the surgical workflow. This introduces restrictions on the amount of manual interaction needed, as well as the time required for the execution of the localization method. However, this thesis was focused primarily in developing and studying the feasibility of a registration framework as a nodule localization tool during VATS, for which some compromises had to be made with respect to the clinical compatibility. Nonetheless, the numerous perspectives discussed in the following chapters would allow future improvements to the proposed registration framework, which will help ensuring its clinical compatibility.

3.2 A hybrid registration framework to markerless intraoperative pulmonary nodule localization during VATS

The intraoperative localization of pulmonary nodules during VATS was addressed as a deformation compensation problem, for which a hybrid registration framework combining intensity-based image registration and biomechanical modeling techniques was developed. The registration framework consists of two phases that estimate lung deformation resulting from change of patient pose (*Phase 1*) and pneumothorax (*Phase 2*), respectively. Each phase corresponds to a registration problem, firstly between the preoperative CT and the intraoperative CBCT of the inflated lung, and secondly be-

tween the intraoperative CBCTs of the inflated and deflated lung. A composition of the estimated deformations produced a displacement field that was used to estimate the position of the pulmonary nodule in the CBCT image of the deflated lung. The overall methodology is depicted in Fig. 3.2.

The proposed registration framework implements the solutions to the technical challenges that were discussed in the previous section. The overall registration framework constitutes the main contribution of this thesis, and its implementation the main result. The characteristics of the framework are briefly discussed in this section, but a more comprehensive description will be provided later in Chapter 6.

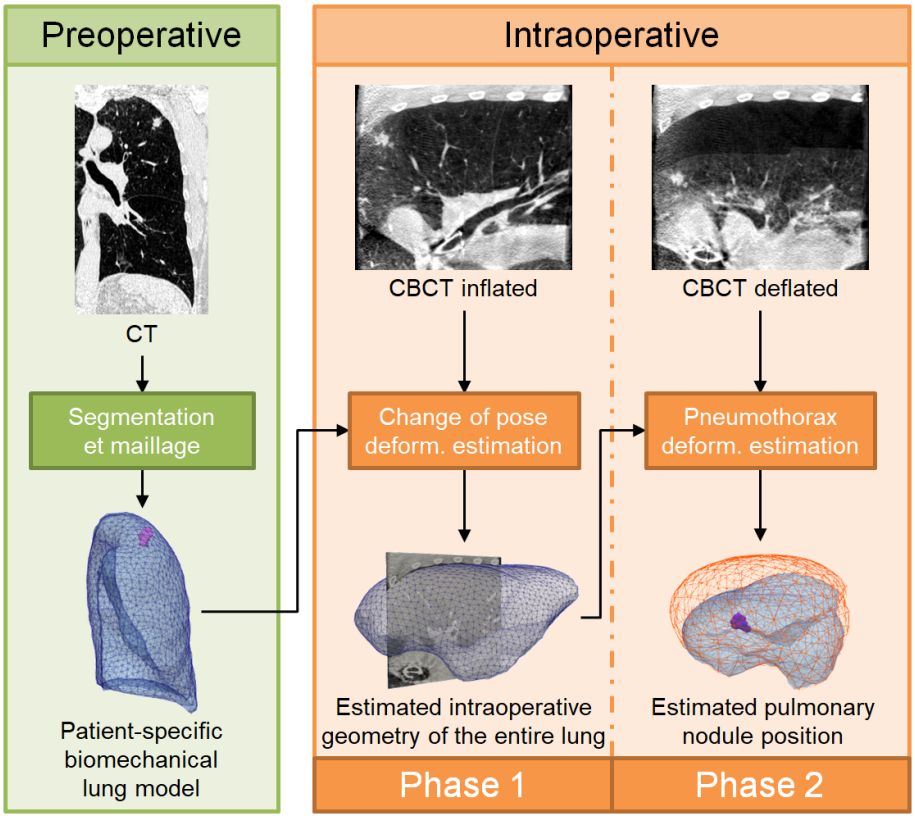

Figure 3.2: Overview of the proposed registration framework for pulmonary nodule localization during VATS. The framework is composed of two phases that respectively estimate the change of pose deformation and the pneumothorax deformation.

3.2.1 Phase 1: estimation of change of pose deformation

The objective of *Phase 1* was to estimate the deformed configuration of the complete lung after change of pose and before pneumothorax. This estimation provided the intraoperative geometry of the inflated lung, which was required for the estimation of pneumothorax deformation in *Phase 2*. It should be emphasized that intensity-based image registration alone would not be sufficient, as only a partial view of

the lung is available in the CBCT images, and consequently, only a partial geometry can be estimated. Therefore, a hybrid registration framework was used instead, with intensity-based image registration for partially estimating lung deformation, and a linear poroelastic biomechanical model for extrapolating that deformation to the complete lung.

3.2.2 Phase 2: estimation of pneumothorax deformation

The objective of *Phase 2* was to estimate the deformed configuration of the lung after the pneumothorax. The pneumothorax deformation was modeled using a linear poroelastic biomechanical model with allowance for air evacuation. The geometry of the inflated lung resulting from *Phase 1* was used as the initial configuration for the pneumothorax simulation. For the fluid phase (air), boundary conditions inspired from the process of exhalation were prescribed, as these naturally correspond with lung deflation. For the solid phase (parenchyma), contact conditions with the thoracic cavity and the diaphragm were included, and boundary conditions were applied at the medial face to account for hilum deformation. Finally, an inverse problem formulation was used for the estimation of tissue parameters, minimizing an objective function based on a surface-to-surface distance from the deformable model to the observed deflated lung surface.

3.3 Clinical data

As part of this thesis project, the current clinical workflow (see Sec. 1.3.3) was modified to introduce an intraoperative CBCT acquisition before pneumothorax, with the lung fully inflated and the patient in lateral decubitus position. A total of 6 patients were enrolled in the study, all with single pulmonary nodules scheduled for resection via VATS at the Rennes University Hospital. The study counted with the approval of the local ethics committee (2016-A01353-48 35RC16_9838) and of the patients, who gave informed consent prior surgery.

3.3.1 Clinical dataset

Three tomographic images were acquired for each patient: a preoperative CT and two intraoperative CBCTs. The preoperative CT is the standard diagnosis image. It provides a complete view of the lung with the patient in supine position. The CBCT images were acquired with a C-arm system (Artis Zeego, Siemens Healthcare, Germany) after general anesthesia, with the patient on the operating table, in lateral decubitus position. The first CBCT image was acquired just before the creation of surgical ports, with the target lung still inflated. The second CBCT image was acquired after pneumothorax, with the target lung deflated. In contrast to the preoperative CT image, these two CBCT images provide only a partial view of the lung. Details for

the CT and CBCT acquisitions are provided in Table 3.1. Coronal slices for all three images and the corresponding patient positions are shown in Fig. 3.3.

Table 3.1: Details for image acquisitions in the in-house VATS clinical workflow.

	CT	CBCT
Acquisition	Preoperative	Intraoperative
Patient position	Supine	Lateral decubitus
Lung state	Inflated	Inflated / Deflated
Lung view	Complete	Partial
Spacing (mm)	$0.97 \times 0.97 \times 0.8$	$0.48 \times 0.48 \times 0.48$
Size	$512 \times 512 \times 337$ †	$512 \times 512 \times 354$

†The number of slices in the cranio-caudal direction varies among cases and only the median is reported. However, for all cases, the complete lung anatomy is visible in the image.

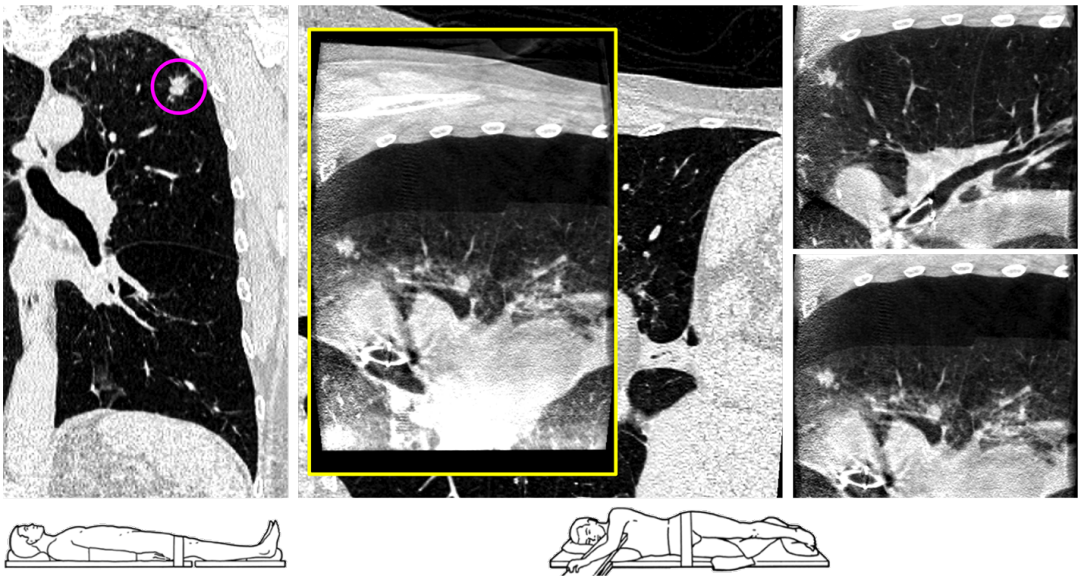

Figure 3.3: Coronal slices of structural tomographic images acquired for a VATS intervention. Left: preoperative CT image with the patient in supine position. Right: intraoperative CBCT images of the inflated (top) and deflated (bottom) lung with the patient in lateral decubitus position. Middle: superposition of the preoperative CT image rigidly registered to the intraoperative CBCT image of the deflated lung. The FOV of the CBCT image (outlined in yellow) only provides a partial view of the lung. The pulmonary nodule is encircled in the preoperative CT image and is visible in all other images.

All patients were intubated with a double-lumen tube (Bronchocath, Mansfield, MA, USA), which allowed independent ventilation of the operated and non-operated lungs. The amount of lung deflation was controlled to ensure enough space for maneuvering during surgery, while avoiding a total collapse of the lung that would heavily deteriorate the image quality. This was achieved by controlling gas insufflation for two distinct mechanisms. The first mechanism consisted in insufflating oxygen into

the operated lung through the lumen of the tube, which corresponds to the current surgical workflow (see Sec. 1.3.3). The second mechanism consisted in insufflating pressurized CO_2 into the thoracic cavity through airtight trocars [1]. The second mechanism was used only for one of the patients (Case 5, see Table 3.2) as an alternative to the first mechanism. It should be noted that neither of both mechanisms allows full control of pneumothorax, and excessive or too limited lung deflation cannot always be avoided.

3.3.2 Anatomical landmarks for validation

For validation purposes, paired anatomical landmarks were manually placed on the three tomographic images by the expert thoracic surgeon who performed all VATS interventions. These landmarks were distributed among vessel and airway bifurcations in the CBCT image of the deflated lung, and were then localized in the other two images. However, the pneumothorax was so pronounced for one of the clinical cases (Case 6) that no anatomical landmarks could be identified in the corresponding CBCT image of the deflated lung. For this case, the landmarks were placed only on the other two images. The study characteristics for each clinical case are summarized in Table 3.2.

Table 3.2: Study characteristics for the 6 clinical cases considered. The pneumothorax was controlled using two mechanisms: insufflation of oxygen into the operated lung through the intubation tube; or insufflation of CO_2 into the thoracic cage through airtight trocars. The number of validation landmarks depends on the visibility of lung structures in the images.

Case	Operated lung	Pneumothorax	# landmarks
1	Left	Air	27
2	Right	Air	40
3	Right	Air	46
4	Right	Air	23
5	Left	CO_2	23
6	Right	Air	48 †

†No landmarks were available for the deflated lung because of very poor visibility of internal structures.

Finally, the spatial distribution of anatomical landmarks is depicted for two clinical cases in Fig. 3.4. Although in principle the anatomical landmarks should cover as much of lung volume as possible, this was impossible because of the reduced FOV in the CBCT images. In addition, the restrictions of image quality were difficult to surpass in some cases and further reduced the spatial extent of these landmarks, notably near the periphery of the lung, where partial volume effects were more pronounced.

1. Airtight trocars, in contrast to the soft tissue retractors used in the current surgical protocol, do not allow air to pass into the thoracic cavity. The pneumothorax is created with the injection of pressurized CO_2 into the thoracic cavity. This is the procedure used in other minimally invasive procedures such as laparoscopy, where the internal organs do not retract naturally.

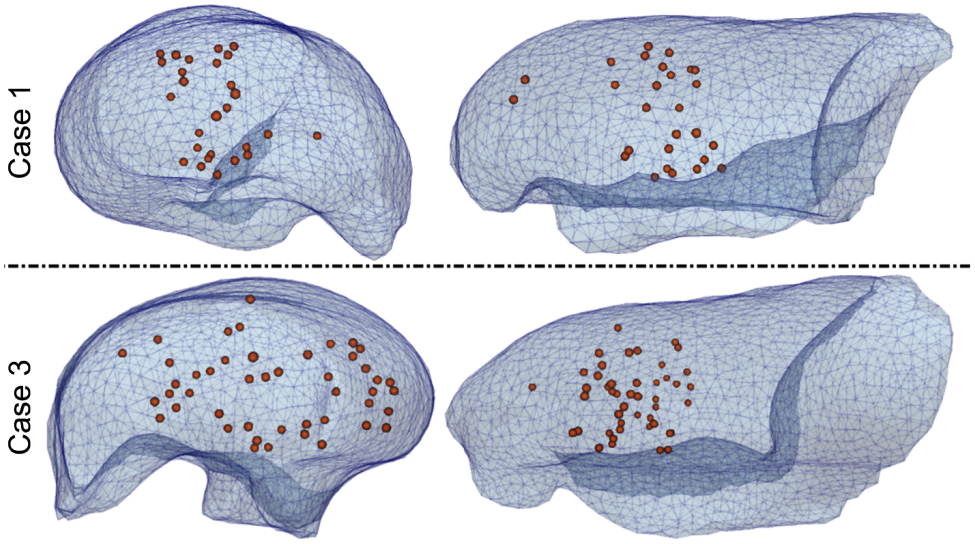

Figure 3.4: Spatial distribution of anatomical landmarks within the lung in the preoperative configuration.

3.4 Summary of the main investigations

The hybrid registration framework presented in this chapter is the result of three main studies that were carried out during this thesis. These studies progressively addressed the main challenges discussed above, and provided contributions to the problem of pulmonary nodule localization during VATS. These studies are discussed in the remaining chapters of this thesis, and are briefly introduced below:

In **Chapter 4**, the lung deformation between the preoperative CT and the intraoperative CBCT of the inflated lung is estimated using intensity-based image registration, and subsequently quantified and characterized using deformation indexes taken from the literature. In this study, all the clinical cases presented above were taken into account. The first preliminary results were presented in an international conference:

> **P. Alvarez**, M. Chabanas, S. Rouzé, M. Castro, J.-L. Dillenseger, and Y. Payan. Lung deformation between preoperative CT and intraoperative CBCT for thoracoscopic surgery: a case study. In *Medical Imaging 2018: Image-Guided Procedures, Robotic Interventions, and Modeling*, page 40, Houston, United States, 2018. ISBN 978-1-5106-1641-7 978-1-5106-1642-4. doi: 10.1117/12.2293938

In **Chapter 5**, a first implementation of the proposed hybrid registration framework is developed in the context of needle-biopsy, which involves dealing with lung deformation very similar to that of VATS but with less challenging clinical data. The clinical data used for this study (and only this study) is different from that presented in this chapter, and it will be described in Chapter 5. The results of this study were presented in an international conference:

P. Alvarez, S. Narasimhan, S. Rouzé, J.-L. Dillenseger, Y. Payan, M. I. Miga, and M. Chabanas. Biphasic model of lung deformations for video-assisted thoracoscopic surgery (VATS). In *2019 IEEE 16th International Symposium on Biomedical Imaging (ISBI 2019)*, pages 1367–1371, Venice, Italy, 2019a. IEEE. ISBN 978-1-5386-3641-1. doi: 10.1109/isbi.2019.8759219

In **Chapter 6**, the final implementation of the proposed hybrid registration framework is presented. This implementation extends and adapts the registration framework introduced in Chapter 5, such that it applies to the context of VATS. The resulting framework corresponds the main contribution of this thesis work. In this study, all clinical cases except for Case 6 were used for validation, as anatomical landmarks were not available for this case. The results were submitted to an international journal, and are currently under review:

P. Alvarez, S. Rouzé, M. I. Miga, Y. Payan, J.-L. Dillenseger, and M. Chabanas. A hybrid image registration approach to markerless intraoperative nodule localization during video-assisted thoracoscopic surgery. *Medical Image Analysis*, submitted in April 2020

4 Characterization of lung deformation after a change of patient pose during VATS

Foreword

The lung undergoes very large deformation from the preoperative configuration to the intraoperative, surgical configuration. As introduced in Chapter 3, this deformation may be understood as the result of a change of patient pose (from supine to lateral decubitus) followed by a pneumothorax. To date, the few works on lung deformation compensation for VATS either only account for pneumothorax deformation (Nakao et al., 2019; Uneri et al., 2013), or approximate the change of pose deformation using a simple rigid body transformation (Nakamoto et al., 2007). However, even though the change of patient pose probably entails more than rigid body motion, until now, little is known about its effects on lung the deformation.

The study presented in this chapter aims at quantifying and characterizing the lung deformation induced by the change of patient pose from the preoperative to the intraoperative configuration. This investigation had the purpose of identifying patterns of deformation, in case simple rules could be employed to compensate for the change of pose deformation. This study was inspired by the work of Amelon et al. (2011), in which deformation measures are used to characterize lung breathing deformation.

The first part of this chapter reproduces the initial investigation, which was presented in an international conference:

> **P. Alvarez**, M. Chabanas, S. Rouzé, M. Castro, J.-L. Dillenseger, and Y. Payan. Lung deformation between preoperative CT and intraoperative CBCT for thoracoscopic surgery: a case study. In *Medical Imaging 2018: Image-Guided Procedures, Robotic Interventions, and Modeling*, page 40, Houston, United States, 2018. ISBN 978-1-5106-1641-7 978-1-5106-1642-4. doi: 10.1117/12.2293938

The second part of this chapter extends the work to include multiple cases, a more thorough characterization of lung deformation, as well as some methodological improvements.

Article: Lung deformation between preoperative CT and intraoperative CBCT for thoracoscopic surgery: a case study

Abstract: Video-Assisted Thoracoscopic Surgery (VATS) is a promising surgical treatment for early-stage lung cancer. With respect to standard thoracotomy, it is less invasive and provides better and faster patient recovery. However, a main issue is the accurate localization of small, subsolid nodules. While intraoperative Cone-Beam CT (CBCT) images can be acquired, they cannot be directly compared with preoperative CT images due to very large lung deformations occurring before and during surgery. This paper focuses on the quantification of deformations due to the change of positioning of the patient, from supine during CT acquisition to lateral decubitus in the operating room. A method is first introduced to segment the lung cavity in both CT and CBCT. The images are then registered in three steps: an initial alignment, followed by rigid registration and finally non-rigid registration, from which deformations are measured. Accuracy of the registration is quantified based on the Target Registration Error (TRE) between paired anatomical landmarks. Results of the registration process are on the order of 1.01 mm in median, with minimum and maximum errors 0.35 mm and 2.34 mm. Deformations on the parenchyma were mesured to be up to 14 mm and approximately 7 mm in average for the whole lung structure. While this study is only a first step towards image-guided therapy, it highlights the importance of accounting for lung deformation between preoperative and intraoperative images, which is crucial for the intraoperative nodule localization.

4.1 Introduction

Lung cancer remains as the worldwide leading cause of cancer death for both women and men (Jemal et al., 2011; Stewart and Wild, 2014). Such a high mortality is related to the late detection of the disease, where curative treatements are normally not available and the 5-year survival rate lies between 6% and 18% (Siegel et al., 2016; Stewart and Wild, 2014). However, screening programs performed on patients at risk have demonstrated that survival rates might be significantly increased if diagnosis and treatement are performed at early stages (Henschke et al., 1999; The National Lung Screening Trial Research Team, 2011). In such scenarios, surgical resection of malignant nodules is prescribed to patients. The treatement is performed via either open thoracotomy or video-assisted thoracoscopic surgery (VATS), the latter being the least invasive method with better and faster patient recovery (McKenna and Houck, 2005).

Even if preoperative CT images are used for planning VATS intervention, intraoperative localization of lung nodules is still challenging in many cases. This is particulary true when the nodules to be resected are small, sub-solid or deep within the

parenchyma (Gould et al., 2013). The cause of this problem is the anatomical disparity between the intraoperative and preoperative configurations, as a consequence of large lung deformations present during surgery. These lung deformations can be mainly associated to two different sources: on the one hand, the patient position is changed from supine in preoperative CT acquisition to lateral decubitus in the operating room, which affects the way gravity influences internal organs. On the other hand, for the comfortable manipulation of the lung during surgery, the surgeon creates space inside the thoracic cage by allowing air getting into the intrapleural space. This phenomenon, known as a pneumothorax, produces a total collapse of the lung towards the mediastinum that modifies internal lung structures.

Thanks to its low dose radiation and fast acquisition time, intraoperative Cone-Beam CT (CBCT) imaging could guide the localization of challenging nodules during a VATS intervention (Rouzé et al., 2016; Uneri et al., 2013). Nonetheless, lung structures are more difficult to see in CBCT images given the reduced image quality when compared to CT images. In addition, the intensity contrast between lung nodules and lung's parenchyma is decreased as a consequence of the deformation induced by the pneumothorax. In fact, the parenchyma becomes denser due to lung deflation. This is particularly problematic for the localization of low density lung nodules also referred as Ground Glass Opacities (GGO). A possible solution to this problem might be the superposition of preoperative CT information (*e.g.* segmentation of nodules and other important structures) with the intraoperative CBCT image, via an image registration procedure. However, the existence of large lung deformations makes such a task a real challenge.

This paper focuses on the quantification of the deformations induced by the change of the patient position between preoperative and intraoperative configurations during a VATS intervention. Understanding these deformations might be an important factor towards the development of an efficient image-guided surgery procedure. A non-rigid registration method is proposed for the superposition of preoperative CT and intraoperative CBCT lung structures. The resulting geometrical transformation is then used to quantify the deformations needed to achieve such superposition. To the best of our knowledge, no study has ever tried to quantify the lung deformations occurring during a VATS intervention, even before pneumothorax.

4.2 Materials and Methods

4.2.1 Data

The work herein presented is a feasibility study performed on one clinical case only. In this context, a wedge resection was prescribed to the patient for a solitary nodule of approximately 13 millimeters in diameter. The VATS surgical intervention was done

at the Rennes University Hospital, Rennes, France. This study was approved by the local ethics committee and the patient gave informed consent prior to the procedure.

The study consisted of the acquisition of two tomographic images: a preoperative CT, where the patient is in supine position and was instructed to hold his breath during the capture (end of inspiration cycle); and an intraoperative CBCT where the patient is in lateral decubitus position under sedation and mechanical ventilation. No surgical action was done before the CBCT acquisition, so that the patient's lung could be imaged in a fully inflated state, *i.e.* witouth pneumothorax.

Figure 4.1 shows an axial view of the images. Although the nodule is here clearly visible in both modalities, it is worth mentioning that it might not be the case, particularly for GGO nodules. While nodule visibility in intraoperative images plays an important role in image guided thoracic surgery, it is not relevant for the purposes of this work.

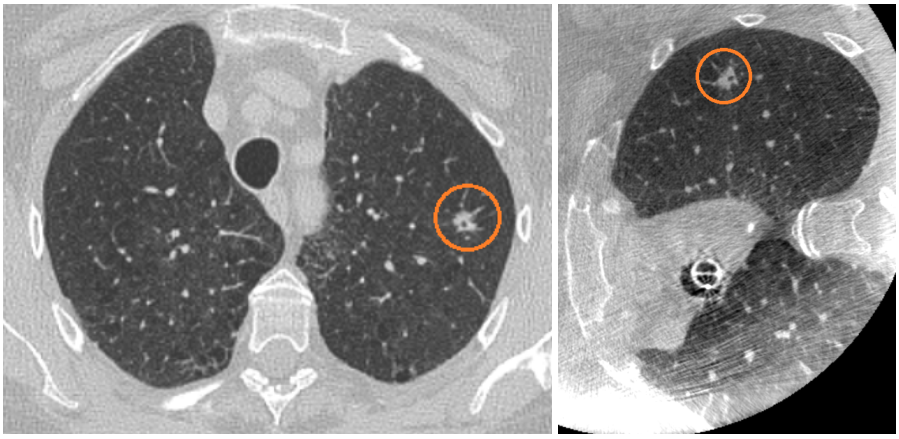

Figure 4.1: Slices in approximately the same transversal plane for preoperative CT (supine position) and intraoperative CBCT (lateral decubitus position). The nodule is encircled in orange. The change of configuration from preoperative to intraoperative configurations is clearly visible.

4.2.2 Segmentation

Segmentation of the lung parenchyma was achieved using an own modified version of Chest Imaging Platform, an open source library for image processing and analysis of chest CTs (Estepar et al., 2015). The method is based on a thresholding approach that exploits the differences in intensity of voxels inside and outside the lungs, which resulted in a segmentation containing both lungs and airways. A 3D Iterative Region Growing approach was used to segment only the primary airway branches, which were then removed from the previously obtained lung's segmentation. This allowed the separation of the two lungs, to extract the affected lung by using connected component analysis and *a priori* information on the position. Finally, morphological op-

erations where applied to fill in holes and smooth irregular boundaries that were present mostly towards the mediastinum.

Given the reduced quality of the CBCT image, the aforementioned segmentation procedure was only used on the preoperative CT image. However, a similar approach using morphological eroding operations instead of airways extraction was applied to the CBCT to obtain a rough segmentation of the intraoperative lung. This latter is not accurate, and hence it is only used for the initialization of the registration workflow.

4.2.3 Registration

The registration process aims to account for lung deformations that occur after a change in patient position before and during a VATS intervention. A registration workflow composed of three steps is proposed: (1) initial alignment, (2) rigid registration and (3) non-rigid registration.

Initial alignment

As discussed before, preoperative and intraoperative images were taken under different configurations. Hence, the position of such images in the physical space is non-overlapping. To compensate for this misalignment, the centroids of the lung segmentations were superposed by translating the preoperative CT image. In addition, the change of orientation of the lung was assumed to be of approximately 90 degrees on the axial plane, so a rotation of this amount was also applied.

Rigid registration

Once the images were roughly aligned, an image-based rigid registration process was performed. The idea was to find a geometrical transformation that maximized image correspondence without introducing local deformations. This rigid registration step is of great importance since it affects directly the latter measurement of local deformations. Although different sources of information could be used to drive such registration (*e.g.* spine and ribs, airway tree, etc.), emphasis was made on structural information of the parenchyma. So, the optimization of a similarity metric estimated over the gray level information contained inside the lung mask was performed, disregarding the rest of the information on the image.

The procedure was accomplished using the multi-resolution image registration techniques implemented in the Elastix toolbox (Klein et al., 2010). Normalized Mutual Information was used as a similarity metric, with an Adaptive Stochastic Gradient Descent optimization process. For each iteration, a set of 3000 paired random points were extracted inside the lung's segmentation and were used for the computation of the similarity metric. Several image resolutions were necessary to allow the algorithm to account for large displacements.

Non-rigid registration

The last step of the registration workflow consists of maximizing image correspondence by allowing local deformations. Any non-rigid registration procedure is characterized by the similarity metric, the optimization method and the elastic transformation model. For the first two components, as for the rigid registration step, the Normalized Mutual Information similarity metric estimated on samples over the lung's parenchyma, along with an Adaptive Stochastic Gradient Descent optimizer were used. B-Splines were chosen as the elastic transformation model. Over-deformation was avoided by restricting the degrees of freedom of the transformation, *i.e.* reducing the amount of control points. For that, a grid spacing of 16 mm in the highest resolution was chosen, which was found empirically to be large enough to allow fine deformations but also small enough to avoid over-registration. Elastix toolbox was again used to accomplish this task, by taking the rigidly registered image as the starting point.

4.3 Results

An illustration of the qualitative results obtained after applying the proposed registration workflow is presented in Figure 4.2. Image misalignment is represented using a complementary color approach. After the initial alignment and rigid registration steps, there is an overall good overlap of the lung's parenchyma (left). This can be particularly appreciated towards the lateral and posterior parts of the lung contour. However, important misalignments still remain towards the medial and anterior parts of the lung, since they can not be recovered without allowing local deformations. These misalignments mainly disappear after the final non-rigid registration step (middle). The lung contours are now better matched and disparities on internal structures are recovered.

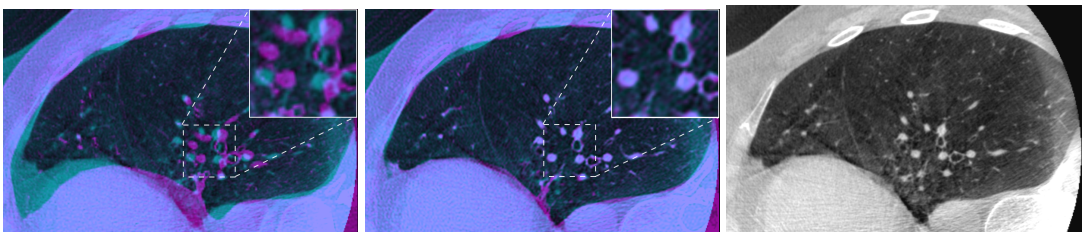

Figure 4.2: Axial view of the lung. Left: CT-CBCT image overlap after rigid registration. Middle: CT-CBCT image overlap after non-rigid registration. Right: target intraoperative CBCT image.

Before the quantification of local lung deformations, a quantitative evaluation of the registration accuracy had to be performed. For that, the Target Registration Error (TRE) between a set of 51 paired anatomical landmarks was calculated. These land-

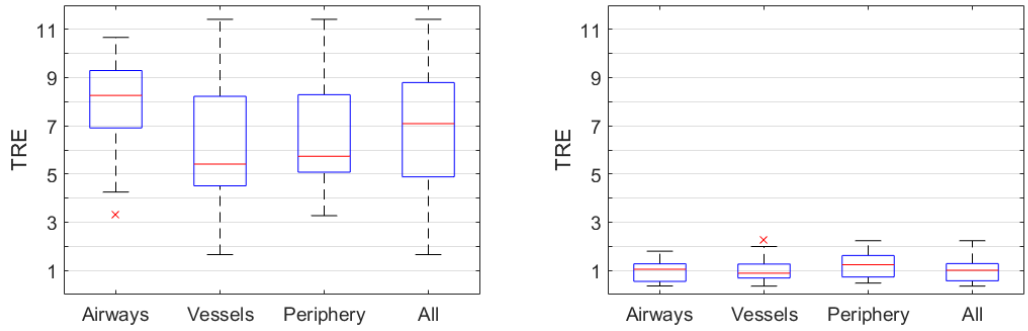

Figure 4.3: Target Registration Errors (TRE) in millimeters for different landmark groups before and after non-rigid registration.

marks were manually placed by an expert thoracic surgeon both in CT and CBCT, during a single session. Instructions were given so that the spatial distribution was as homogeneous as possible, covering the whole lung. Three landmark groups could be identified: 20 landmarks on airway bifurcations, 30 landmarks on vessel bifurcations and 14 landmarks towards the periphery of the lung, where the distance to the surface is lower than 18 mm. Additionally, another landmark was placed inside the nodule. Figure 4.3 presents the TREs obtained before and after the non-rigid registration procedure was applied.

The spatial distribution of the anatomical landmarks can be seen in Figure 4.4. Emphasis was given to the set of peripheral landmarks, which was the group where the remaining TREs were the highest. It is clear from the figure that misalignments of anatomical landmarks existing after rigid registration were successfully recovered after non-rigid registration, when local deformations of the lung were taken into account.

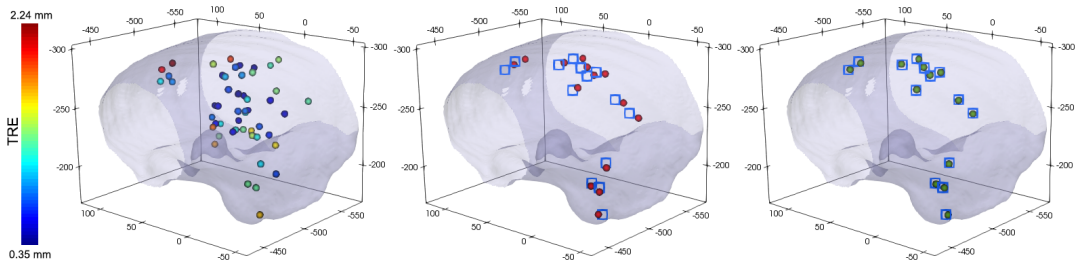

Figure 4.4: Spatial distribution of the whole set of landmarks. Left: Color map representation of the TREs after non-rigid registration, for all landmarks. Middle: Set of preoperative periphery landmarks (red spheres) after rigid registration compared to intraoperative periphery landmarks (blue squares). Right: Set of preoperative periphery landmarks (green spheres) after non-rigid registration compared to intraoperative periphery landmarks (blue squares).

Finally, the magnitude of the deformation field obtained after non-rigid registration

is depicted in Figure 4.5. Two anatomical planes are used to illustrate how such deformation is distributed throughout the parenchyma. In addition, the normalized histogram of deformations present on the whole lung volume is also presented.

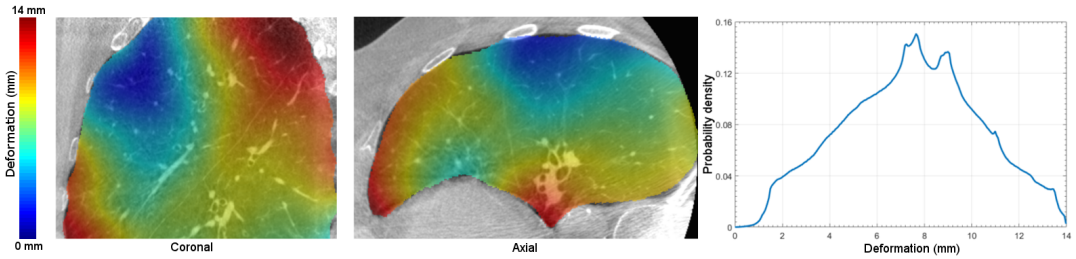

Figure 4.5: Left: color mapped local deformations in millimeters for coronal and axial views of the lung. Right: the normalized histogram of local deformations in millimeters for the whole lung volume.

4.4 Discussion

As for the segmentation of the lung, the proposed procedure was straightforward on the preoperative CT and produced a smooth binary mask of the lung's parenchyma. For the CBCT, however, the reduced image quality did not allow the same results. The modified segmentation procedure was then applied, and even if it could not completely recover the whole lung structure, the result was sufficient to estimate the lung's centroid required for the initialization of the registration workflow.

With respect to image registration, the TREs obtained after rigid registration only where on the order of 7 mm, with better aligned landmarks near the vessels and lung periphery (~ 6 mm) than near the airways (~ 8 mm). A significant error reduction was achieved after non-rigid registration. In fact, median values of TREs for all landmark groups where reduced to 1.04 mm, 0.89 mm and 1.24 mm for airways, vessels and peripheral landmarks, respectively. In particular, a TRE reduction from 7.3 mm to 0.4 mm was observed for the the landmark placed inside the nodule. It is important to note that after non-rigid registration, the largest TREs are located in the lung's periphery. Lung structures are the smallest in this regions, hence Partial Volume Effects (PVE) in the image are more important. As a result, the registration algorithm has more trouble finding correspondences, which produces larger misalignments. Overall, a median TRE of 1.01 mm was obtained for the whole set of landmarks after non-rigid registration, with a minimum of 0.35 mm and a maximum of 2.24 mm. Since the majority of the TREs are around 1.01 mm (see Figure 4.3), one can conclude that the resulting registration is accurate, since the errors are on the order of image spacing.

Regarding the magnitude of the deformations, experimental results showed non-negligible measurements with maximum values around 14 mm, in different areas.

However, a special remark has to be made with respect to the anatomical interpretation of these deformations' locations. Although the measured deformations were here the highest near the apex and anterior parts of the lung (see Figure 4.5), this does not necessarily mean that these regions are the most affected by the change of configuration before the VATS intervention. In fact, the measurement of local deformations is highly sensitive to the initial alignment and rigid registration steps: a minimization of these local deformations in some regions of the lung will necessarily result in an increase in others. Hence, since there is anatomically no fixed point in the chest, deformations between the lung's areas are always relative. Other results would have been obtained with different initial geometrical transformations. However, the relative differences would remain similar.

To conclude, it is clear that important, non-uniform deformations of the lung occur between the pre- and intraoperative configurations. They are caused by a change of the patient pose, breathing mechanics and how gravity affects internal structures. Only a non-rigid registration procedure can cope with these local deformations, to obtain a perfect match between preoperative CT and intraoperative CBCT images.

4.5 Conclusion

This paper presents a registration workflow that was used to measure lung deformations resulting from changes between preoperative and intraoperative configurations during a VATS intervention. Registration accuracy was measured using TREs on a set of 51 paired anatomical landmarks, obtaining a median error of 7.09 mm after rigid registration, which was significantly reduced to 1.01 mm after non-rigid registration. Deformations throughout the lung where measured to be of maximum 14 mm ($\sim$ 7 mm in average) on different regions of the lung.

Experimental results highlighted the importance of accounting for lung deformations during VATS, since it will be necessary for transforming information extracted from preoperative images to the intraoperative setting. This will be of particular importance for the localization of lung nodules, which might be not visible through intraoperative imaging when their density or size is considerably low.

Future work includes the study of lung deformations on a dataset of several cases. Also, the analysis of the deformation under different rigid initialization approaches might be of interest for the identification of deformed lung regions. Finally, special focus must be brought to the correction of deformations induced by the pneumothorax that will allow the prediction of nodule displacement during VATS, which is the long-term goal of this work.

Acknowledgment

The work presented in this article was partially supported by the *Région Bretagne* through its *Allocations de Recherche Doctorale* (ARED) framework and by the French National Research Agency (ANR) through the frameworks *Investissements d'Avenir Labex CAMI* (ANR-11-LABX-0004) and *Infrastructure d'Avenir en Biologie et Santé* (ANR-11-INBS-0006).

Additional methodological aspects, results and discussion

The preliminary study presented in this chapter provides a first insight into lung deformation during the change of patient position. The displacement field obtained after non-rigid registration of the preoperative CT and intraoperative CBCT images was locally varying, with an average displacement of approximately 7 mm. These measurements were validated using TREs computed on a set of 51 paired anatomical landmarks, with a median error of 1.01 mm after non-rigid registration. The displacement measurements were clearly not negligible, and demonstrate the importance of taking into account lung deformation from the change of patient position. Several aspects were investigated after publication of the first preliminary study. This section first describes the new methodological aspects introduced, and then presents new findings obtained in a multiple-case study.

Additional methodological aspects

In order to improve the accuracy of the proposed registration framework, two modifications were considered. Firstly, a rigid-body initialization strategy that generalizes to multiple patients. Secondly, an intensity masking procedure that allows to better account for sliding lung motion during registration. Also, in order to provide a more thorough characterization of lung deformation, additional measurements extracted from the literature were considered. The two improvements to the registration framework and the additional deformation measurements are described bellow.

Rigid-body initialization using the spine

As mentioned earlier, the displacement measurements are sensible to the rigid-body initialization. In the literature, bony structures are typically used for this initialization, as they undergo little to none deformation (Hartkens et al., 2003). In the context of lung registration, the ribs move and rotate with respiratory movements, and the spine may be subject to deformation with the change of patient position. For these reasons, neither of those structures were used for rigid-body initialization in the study presented above, where intensity information of internal lung structures was preferred. However, such initialization may result in an underestimation of lung deformation, and deformation patterns may be difficult to generalize for several patients, as each one would be initialized differently. Moreover, a closer look to rigid registration using the spine as the reference shows that within the FOV of the CBCT image, the spine remains rigid for the most part, as shown in Fig. 4.6. As such, the remaining works of this thesis document assumed very few deformation of the spine among changes of configuration of the lung.

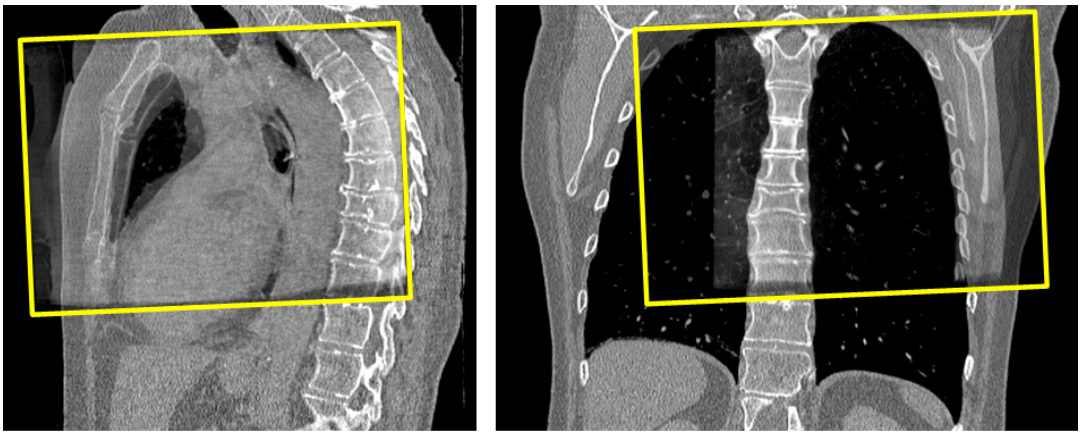

Figure 4.6: Result of change of pose rigid registration using the spine as the reference. The FOV of the intraoperative CBCT image of the inflated lung is indicated with yellow contours. The CBCT image is superimposed over the CT image within this FOV. It can be observed that the spine undergoes little to none deformation.

Accounting for sliding motion

The registration accuracy was better for airways and vessel landmarks (average TREs of 0.44 mm and 0.89 mm respectively) than for peripheral landmarks (average TREs of 1.24 mm). Although this miss-registration in the periphery may be partially explained by partial-volume effects, it can also be caused by the sliding motion of lung parenchyma against the thoracic cavity. Indeed, the parametric B-Spline transformation model used assumes a continuous displacement field, which is not well suited to represent such sliding motion. This is a well known problem in lung registration literature, and several methods have been proposed to deal with it, mainly through regularization schemes (Delmon et al., 2013; Schmidt-Richberg et al., 2012) and anatomical segmentations (Vandemeulebroucke et al., 2012; Wu et al., 2008).

In the remaining of this chapter and later in this thesis (Chapter 6, Appendix A), sliding motion was taken into account using the method of sub-anatomical registration proposed by Wu et al. (2008). The method independently registers sliding structures by selectively masking image intensities with anatomical segmentations of lung parenchyma in both images.

However, although the automatic segmentation of lung parenchyma is straightforward in the preoperative CT image (see Sec. 4.2.2), it remains challenging in the intraoperative CBCT image (lower signal-to-noise ratio, reconstruction artifacts, limited FOV). As both segmentations are needed, a semi-automatic approach based on image registration was implemented for the segmentation of lung parenchyma in the CBCT image. A first registration step was performed as described previously in Sec. 4.2.3. Then, an estimation of the intraoperative CBCT lung segmentation was achieved by

warping the preoperative CT segmentation with the resulting transformation. The result was further processed using morphological operations and manually adjusted in poorly segmented regions. The manual adjustments were necessary notably for the lung contours near the border of the FOV of the CBCT image, where reconstruction artifacts are not uncommon. An illustration of a manually corrected segmentation is provided in Fig. 4.7. This semi-automatic process avoids the highly time-consuming manual segmentation, and hence, it was used in the remaining of this thesis for the segmentation of the inflated lung in the intraoperative CBCT image.

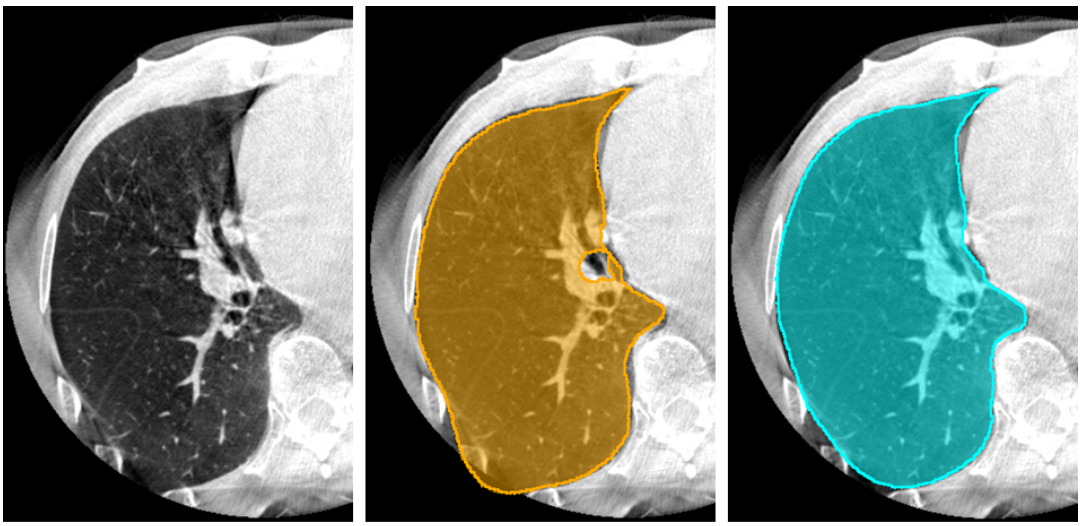

CBCT inflated lung | Estimated segmentation (warped after registration) | Final segmentation (manually adjusted)

Figure 4.7: Lung segmentation in CBCT image of the inflated lung. A reconstruction artifact in the CBCT image results in a poorly segmented region after warping that is manually corrected in the final segmentation.

After the segmentation of the lung parenchyma, the images were registered using the sub-anatomical registration process proposed by Wu et al. (2008). First, the CT and CBCT images were masked using the corresponding lung segmentation. The voxels lying outside these masks were replaced with a constant HU value below the range of possible parenchyma values (*i.e.* below -1000 HU, corresponding to air). The similarity metric was computed using the masks after being extended 5 mm using morphological dilation. By extending the masks, points lying outside the lung in the *fixed* image (intraoperative CBCT image) are registered to the same intensity values in the *moving* image (preoperative CT image), which also lie outside the lung. Moreover, matching outside points has no cost in terms of the similarity metric, which results in the registration process to be guided mostly by the information within the lung. As a result, this process minimizes the misalignment error of the internal lung structures while allowing sliding at the lung interface. In the remaining of this thesis, the registration of CT/CBCT lung images was carried out using this method.

Measures of deformation

In addition to characterizing tissue displacement, it is also interesting to analyze the local variations of lung deformation. During deformation, the lung changes its volume and overall shape in ways that are generally region-specific. These variations are related to the constitution of lung tissue and the loading applied to it. Local deformation changes during breathing have been reported in previous studies (Amelon et al., 2011), and the measurements have been used as estimates of local lung function (Du et al., 2013; Patton et al., 2018). However, to date, no study has reported local changes of lung deformation during change of patient pose.

Two measures of local deformation are herein considered. The first measure is the Jacobian of motion (J), introduced in Sec. 2.2.2, which provides information of local volume change. The second measure is the Anisotropy Deformation Index (ADI), introduced by Amelon et al. (2011), which provides information of shearing stretch. These two measurements are extracted from the deformation gradient tensor, which is computed from the displacement field (see Sec. 2.2.2). Here, the displacement field results from the process of intensity-based image registration.

To recall, the deformation gradient tensor $\mathbf{F}$ relates line segments in a reference configuration to a deformed configuration:

$$d\mathbf{x} = \mathbf{F}\, d\mathbf{X} \tag{4.1}$$

Here, the reference and deformed configuration correspond to the lung configurations before and after change of pose respectively. A physically plausible deformation assumes that $\mathbf{F}$ has an inverse. As such, $\mathbf{F}$ can then be decomposed in a purely rotation tensor $\mathbf{R}$ and a purely stretching tensor $\mathbf{U}$ using the theorem of polar decomposition:

$$\mathbf{F} = \mathbf{R}\,\mathbf{U} \tag{4.2}$$

The rotation tensor $\mathbf{R}$ can be factored out by multiplying $\mathbf{F}$ with its transpose $\mathbf{F}^T$

$$\begin{aligned} \mathbf{F}^T\,\mathbf{F} &= (\mathbf{R}\,\mathbf{U})^T\,(\mathbf{R}\,\mathbf{U}) \\ &= \mathbf{U}^T\,\mathbf{R}^T\,\mathbf{R}\,\mathbf{U} \\ &= \mathbf{U}^T\,\mathbf{U} = \mathbf{C} \end{aligned} \tag{4.3}$$

with $\mathbf{C}$ being the right Cauchy-Green deformation tensor introduced previously in Sec. 2.2.2.

The eigenvalues of $\mathbf{U}$, noted $\lambda_i, i \in \{1, 2, 3\}$, are known as principal stretches. From the relation in Eq. (4.3), the values λ_i can be calculated as the square roots of the eigenvalues of $\mathbf{C}$. The two measures of deformation herein studied are determined

from the principal stretches by

$$J = \det(\mathbf{F}) = \lambda_1\lambda_2\lambda_3 \quad , \quad \text{ADI} = \sqrt{\left(\frac{\lambda_1 - \lambda_2}{\lambda_2}\right)^2 + \left(\frac{\lambda_2 - \lambda_3}{\lambda_3}\right)^2} \tag{4.4}$$

Both measures have values ranging from zero to infinity. In the case of J, they correspond to volume contraction ($J < 1$), volume preservation ($J = 1$) and volume extension ($J > 1$). In the case of ADI, higher values indicate larger relative differences among principal stretches and hence larger deformation anisotropy. Perfect isotropic deformation (*i.e.* $\lambda_1 = \lambda_2 = \lambda_3$) results in zero ADI.

Additional results: a deformation study with multiple clinical cases

The initial investigation presented in the first part of this chapter was further extended to a total of 6 clinical VATS cases. All cases belong to the same clinical study previously described in Sec. 3.3. The preoperative CT and intraoperative CBCT images were registered for all clinical cases, taking into account the improved initialization and registration protocols discussed in the previous sections. The resulting TRE distributions are presented in Fig. 4.8.

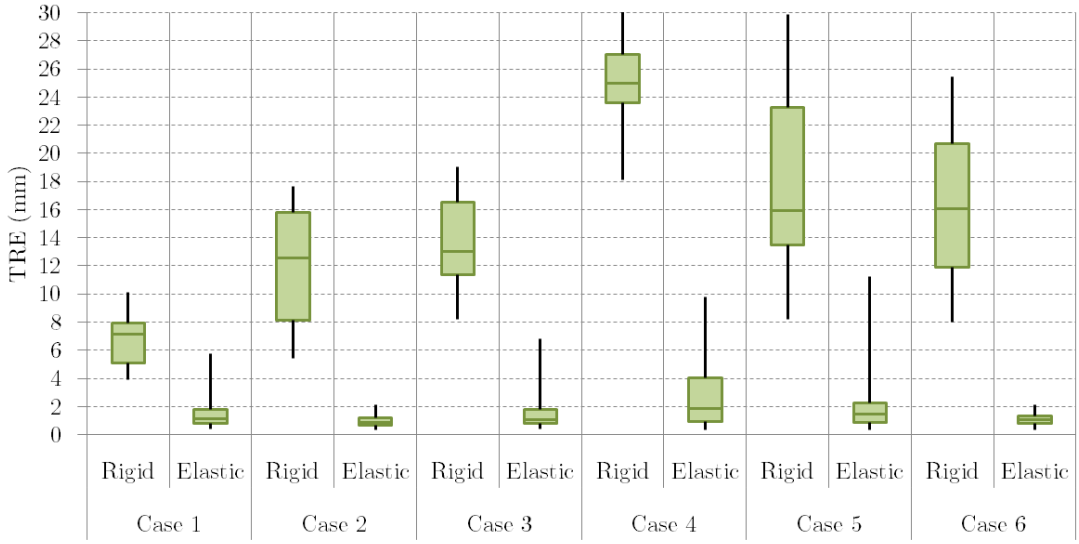

Figure 4.8: TRE distributions for change of pose rigid and elastic registration for all clinical cases. The bounds of the box represent the 25$^{\text{th}}$ and 75$^{\text{th}}$ percentile; the horizontal line inside the box represents the median; and the error bars extend from the 2$^{\text{th}}$ to 98$^{\text{th}}$ percentile.

The average ($\pm$ standard deviation) TRE after rigid registration were 6.8 mm ($\pm$ 1.8 mm), 12.1 mm ($\pm$ 4.0 mm), 13.5 mm ($\pm$ 3.2 mm), 25.8 mm ($\pm$ 4.9 mm), 18.0 mm ($\pm$ 6.9 mm), and 16.3 mm ($\pm$ 5.1 mm), for each clinical case respectively. These errors were reduced after elastic to 1.5 mm ($\pm$ 1.4 mm), 1.0 mm ($\pm$ 0.5 mm), 1.6 mm ($\pm$ 1.4 mm), 2.8 mm ($\pm$ 2.7 mm), 2.7 mm ($\pm$ 3.3 mm), and 1.1 mm ($\pm$ 0.4 mm), for each clinical

case respectively. Although very large differences in initial alignment were observed among clinical cases, average TREs below 2 mm were consistently obtained after elastic registration. The average error correction ranged between 78% (Case 1) and 93% (Case 6). This level of accuracy was considered sufficient for the purpose of characterizing lung deformation.

The spatial distributions for displacement, displacement magnitude, J and ADI are illustrated for Case 4 in Fig. 4.9, and for Case 6 in Fig. 4.10.

In both cases, the displacement field near the diaphragm indicates upward movement. This was the expected behavior, since the diaphragm gets pushed by the weight of the abdominal organs after anesthesia. Also, the displacement field indicates important movement in the direction of gravity (from the ribs to the spine). The magnitude of displacement is larger near the diaphragm in both cases, and decreases with proximity to the spine and the apex. Concerning J, the distribution fluctuates smoothly with no specific regional preference, with the exception of a hot-spot at the posterior tip of the lung for both cases, which is most likely explained by registration artifacts. The average J value in both cases is below 1, indicating overall volume contraction. In the case of ADI, higher values appear near the lung fissures in both cases, which corroborates the findings presented by Amelon et al. (2011). This is explained by lung lobes sliding one against the other, and the impossibility of the transformation model used to represent such discontinuities in the displacement field.

To further investigate regional deformation, the lobes were segmented for each clinical case with the open source Chest Imaging Platform (Estepar et al., 2015). The distributions of deformation measurements for the entire lung and its individual lobes are shown for the displacement magnitude in Fig. 4.11, for J in Fig. 4.12, and for ADI in Fig. 4.13. It is important to notice that since the FOV of the CBCT image contains only a portion of each patient's lung, it was not possible to quantify deformation for the entire lung. Consequently, deformation patterns exposed by the distribution of deformation measurements should be interpreted carefully, as they may be affected by a sample bias effect.

The average displacement magnitude among cases was very heterogenous, ranging approximately from 5 mm to 24 mm. Very large displacements of more than 30 mm were observed for Case 4 and Case 5. This amount of displacement is even larger than that of respiratory motion (*e.g.* Delmon et al. (2013) reported average displacement ranging from 3.9 mm to 15.0 mm for anatomical landmarks of 16 patients), especially considering that diaphragm motion could not be fully measured herein. In addition, larger displacement was consistently observed for the middle right lobe across cases ($p < .001$, two-sample independent t-test). A possible physical interpretation could be derived from the position of this lobe, as it is both far from the attachments to the spine and in contact with the diaphragm. As gravity and diaphragm movement are

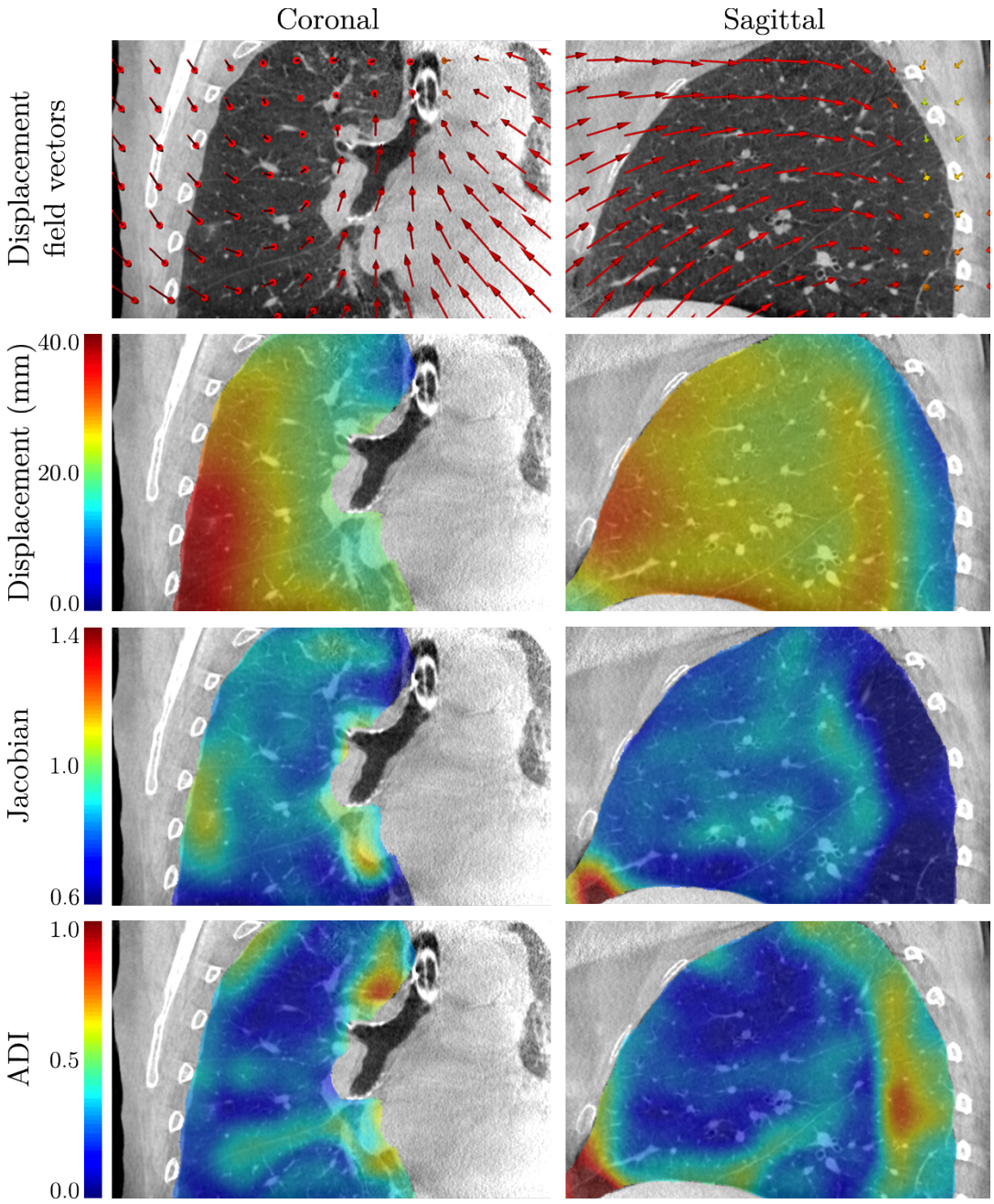

Figure 4.9: Sagittal and coronal slices showing spatial distribution of estimated deformation measurements for Case 4. The arrows (first row) represent actual displacement field vectors, subsampled on a regular grid of 20 mm of spacing.

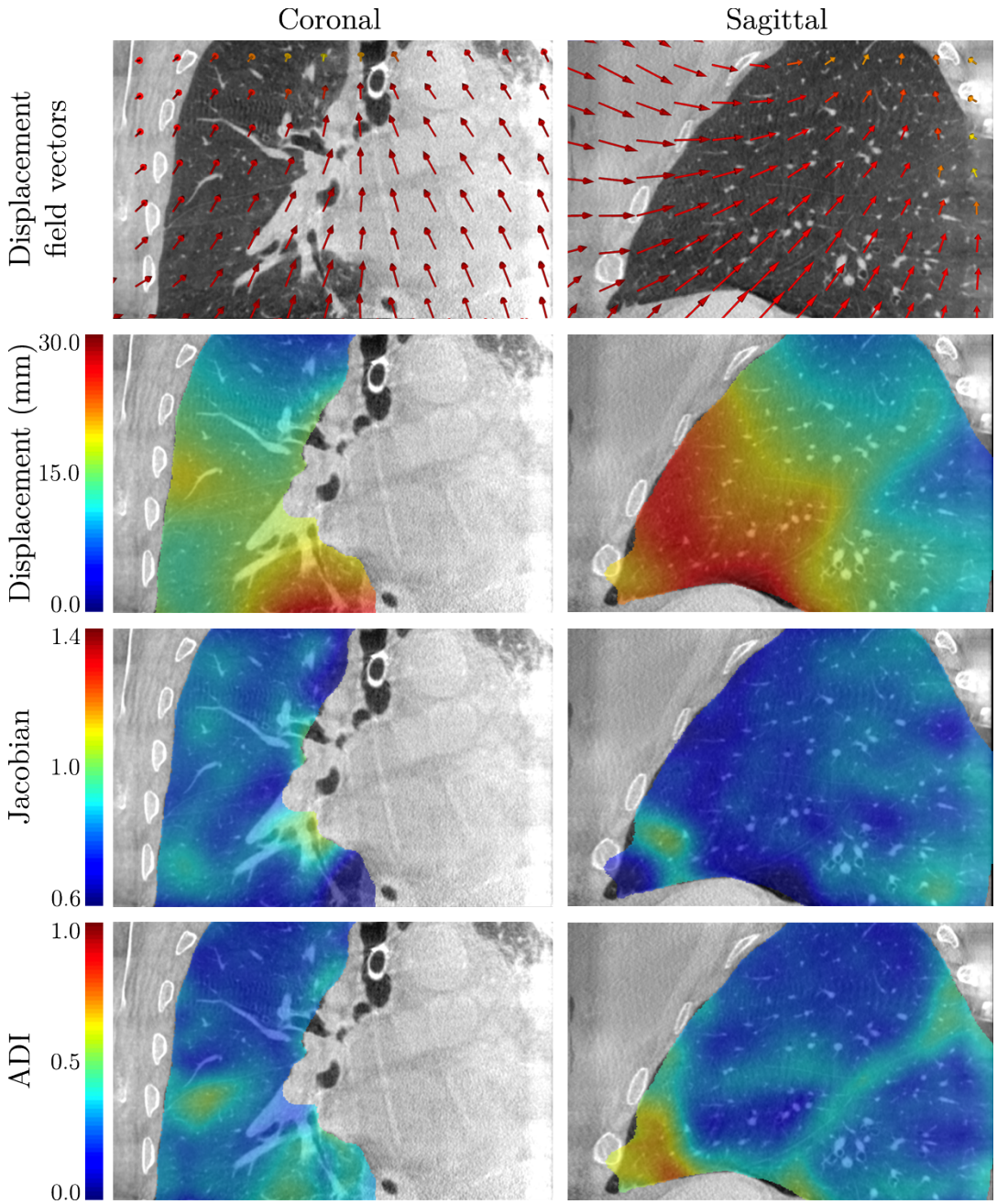

Figure 4.10: Sagittal and coronal slices showing spatial distribution of estimated deformation measurements for Case 6. The arrows (first row) represent actual displacement field vectors, subsampled on a regular grid of 20 mm of spacing.

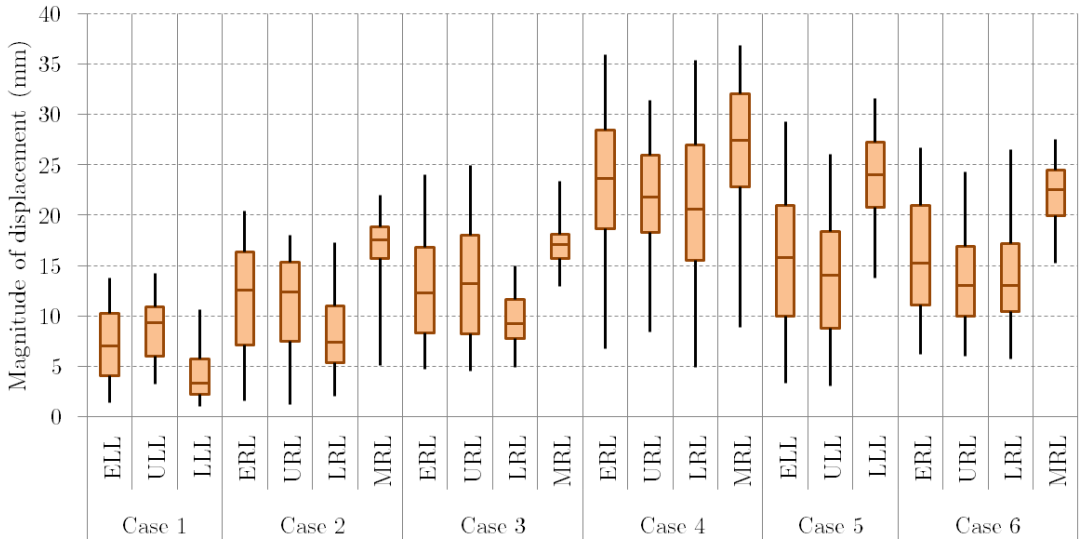

Figure 4.11: Distributions of estimated displacement magnitude for all clinical cases. For each case, the distribution of the entire lung and individual lobes are shown. The following notation is used: entire left lung (ELL), upper left lobe (ULL), lower left lobe (LLL), entire right lobe (ERL), upper right lobe (URL), lower right lobe (LRL) and middle right lobe (MRL). The bounds of the box represent the 25^{th} and 75^{th} percentile; the horizontal line inside the box represents the median; and the error bars extend from the 2^{th} to 98^{th} percentile.

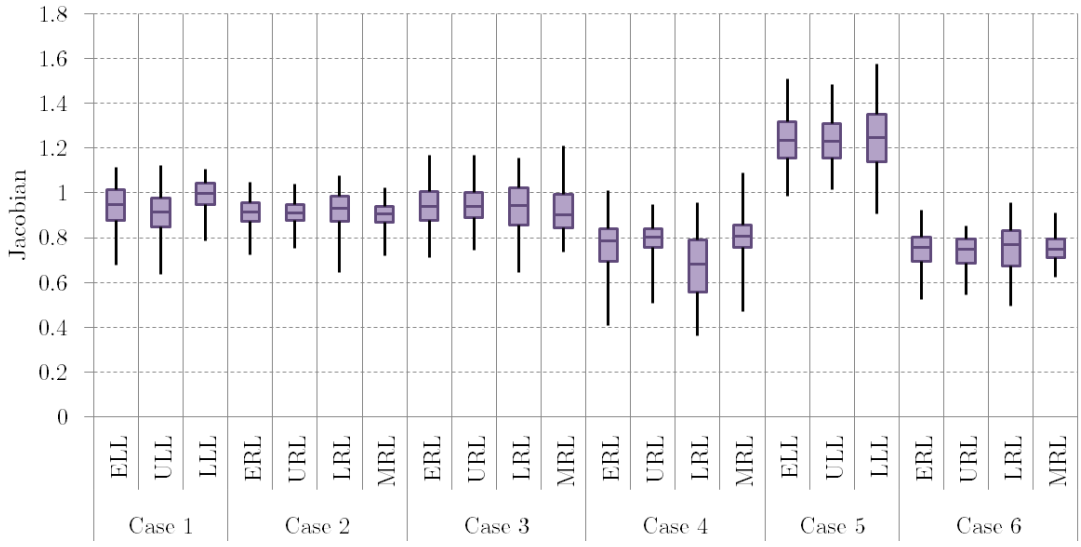

Figure 4.12: Distributions of estimated J for all clinical cases. For each case, the distribution of the entire lung and individual lobes are shown. The following notation is used: entire left lung (ELL), upper left lobe (ULL), lower left lobe (LLL), entire right lobe (ERL), upper right lobe (URL), lower right lobe (LRL) and middle right lobe (MRL). The bounds of the box represent the 25^{th} and 75^{th} percentile; the horizontal line inside the box represents the median; and the error bars extend from the 2^{th} to 98^{th} percentile.

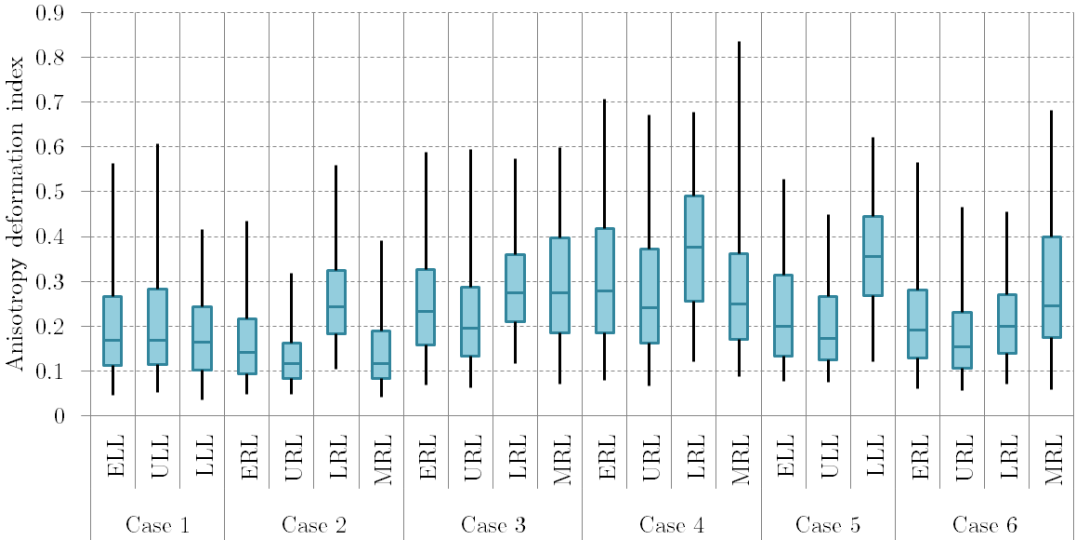

Figure 4.13: Distributions of estimated ADI for all clinical cases. For each case, the distribution of the entire lung and individual lobes are shown. The following notation is used: entire left lung (ELL), upper left lobe (ULL), lower left lobe (LLL), entire right lobe (ERL), upper right lobe (URL), lower right lobe (LRL) and middle right lobe (MRL). The bounds of the box represent the 25^{th} and 75^{th} percentile; the horizontal line inside the box represents the median; and the error bars extend from the 2^{th} to 98^{th} percentile.

the two main causes of deformation, the middle right lobe is heavily affected by both, whereas roughly speaking, the lower right lobe is mostly affected by the diaphragm and the upper right lobe is mostly affected by gravity (see Figs. 4.9 and 4.10).

No significant differences were observed in J values across lung lobes for all clinical cases. Across clinical cases, it fluctuated around 0.9 for cases 1 to 3 and around 0.8 for cases 4 and 6, an indication of generalized volumetric contraction. Case 5 had significantly higher J values than all other cases ($p < .001$, two-sample independent t-test). The average value for this case was above 1.0, an indication of generalized volumentric expansion. In addition, it is interesting to note that this was the only case were curare was not administered with anesthesia, as airtight trocars in combination with pressurized CO_2 were used to generate the required pneumothorax during surgery (see Sec. 3.3). As such, the diaphragm remains contracted, holding the weight of the abdominal organs, and staying in its natural position (*i.e.* it does not move upwards). The resulting deformation is then inherently different than for the other clinical cases, as the external loading is different. Unfortunately, no clinical case with the same surgical workflow was available to confirm these findings.

Finally, although some significant differences were found for ADI values across lobes, they were not consistent for all clinical cases. In addition, as ADI values are higher for sliding interfaces, the distributions are sensitive to the ratio of sampled voxels

and voxels at the interface. This ratio can change among patients as an expression of anatomical differences, but it can also change with the amount of volume per lobe within the FOV of the CBCT image. It can be said, however, that the measured values were relatively low throughout the analyzed lung volume, and across clinical cases, *i.e.* below 0.5 for the most part. These values were equal or lower than those previously reported by Amelon et al. (2011)(between 0.2 and 2.5), suggesting less anisotropic deformation during change of pose than during breathing.

General conclusion

The study presented in this chapter provided a characterization of lung deformation from the preoperative to the intraoperative conditions, as the patient undergoes a change of pose. Measurements of deformation were computed from a displacement field, which was automatically calculated using a registration framework with allowance for sliding motion. Very large displacement was observed, with average values approximately ranging from 5 mm to 24 mm, which are larger than those reported in the breathing lung literature. Analysis of the displacement field suggested that the diaphragm upward movement and the change in direction of gravity with respect to the patient were the main factors causing lung deformation. Values of ADI were higher at sliding interfaces, confirming the findings of previous studies. Also, J values below unity were observed in general, indicating volumetric lung contraction. This had a remarkable exception in one clinical case for which intraoperative setup was different than for the others. This study also provided valuable insights and methods that were useful for the development of the works presented in the subsequent chapters.

5

A hybrid registration framework for lung deformation compensation after change of pose and pneumothorax: an initial investigation

Foreword

In the context of transthoracic needle biopsy of pulmonary nodules, one of the main complications after the procedure is a pneumothorax. The management of this complication often requires a follow-up low-dose CT (LDCT) image acquisition of the affected lung, with the patient in lateral decubitus position. Therefore, with respect to the CT standard diagnosis image, this LDCT image provides structural information of the lung after being deformed by a change of patient pose and a pneumothorax, namely, with lung deformation very similar to that of VATS. In contrast to the CBCT images used in the current clinical workflow (see Sec. 3.3), this LDCT image provides a complete view of the deflated lung, without the various artifacts affecting image quality. As such, these transthoracic needle biopsy images allow the study of lung deformations present during VATS, but with better quality clinical data.

The study presented in this chapter aims at evaluating the feasibility of a hybrid image-based and biomechanics-based registration framework to compensate for lung deformation after change of pose and pneumothorax. The image-based components are based on the work presented in Chapter 4. The biomechanics-based components use a linear poroelastic (biphasic) model of the lung with allowance for air evacuation (see Sec. 2.2.4). This model was considered the most appropriate for simulating a pneumothorax, since it is primarily caused by air flowing out of the lung. The first-order approximation allowed an initial study of suitable material properties and boundary conditions, but non-linearity may be taken into account later.

The initial investigation was developed during a mobility program in the Department of Biomechanical Engineering, Vanderbilt University, Nashville, USA, in collaboration with professor Michael Miga, who has extensive experience with biomechanical modeling, and particularly, with linear poroelastic models with allowance for fluid evacuation.

The first part of this chapter reproduces this initial investigation, which was presented in an international conference:

P. Alvarez, S. Narasimhan, S. Rouzé, J.-L. Dillenseger, Y. Payan, M. I. Miga, and M. Chabanas. Biphasic model of lung deformations for video-assisted thoracoscopic surgery (VATS). In *2019 IEEE 16th International Symposium on Biomedical Imaging (ISBI 2019)*, pages 1367–1371, Venice, Italy, 2019a. IEEE. ISBN 978-1-5386-3641-1. doi: 10.1109/isbi.2019.8759219

The second part of this chapter presents additional results concerning the distribution of material properties, which were studied after the initial publication, as well as supplementary discussions and perspectives of the work.

Article: Biphasic model of lung deformations for Video-Assisted Thoracoscopic Surgery (VATS)

Abstract: Intraoperative localization of small, low-density or deep lung nodules during Video-Assisted Thoracoscopic Surgery (VATS) is a challenging task. Localization techniques used in current practice require an additional preoperative procedure that adds complexity to the intervention and might yield to clinical complications. Therefore, clinical practice may benefit from alternative, intraoperative localization methods. We propose a nonrigid registration approach for nodule localization. Our method is based on a biomechanical model of the lung, where lung parenchyma is represented as a biphasic medium. Preliminary results are promising, with target registration errors reduced from 28.39 mm to 9.86 mm in median, and to 3.68 mm for the nodule in particular.

5.1 Introduction

Surgical resection of lung nodules via Video-Assisted Thoracoscopic Surgery (VATS) is one of the treatments available for early stage lung cancer. In comparison to open thoracotomy, this minimally invasive procedure reduces the length of hospitalization and minimizes post-operative complications (Falcoz et al., 2015). However, at the beginning of the procedure, the insertion of surgical ports and the artificial ventilation applied only on the contralateral lung, allow air to flow into the intrapleural space. This abnormal air inflow, known as pneumothorax, induces a collapse of the lung towards the hilum, and, therefore large anatomical deformations. As a result, the intraoperative localization of small, deep or low-density nodules becomes considerably difficult (Gould et al., 2013).

In current practice, localization techniques rely on preoperative procedures for nodule marking, generally involving the placement of hookwires or dyes under CT fluoroscopy (Keating and Singhal, 2016). However, these procedures not only increase the cost and complexity of care, but also occasionally lead to serious complications (Park et al., 2017). As an alternative, several groups have recently proposed localization methods based on intraoperative imaging only, for example, Cone Beam CT (CBCT) (Rouzé et al., 2016) or Ultrasound (Wada et al., 2015). While promising, these methods rely entirely on nodule visibility in the images, which may be insufficient. For instance, the fuzzy borders and low-density of ground glass opacity nodules could make them indistinguishable, especially considering the increased density of the collapsed lung. A potential solution to address this limitation could be nonrigid image registration, to transfer information from the preoperative CT to the deformed intraoperative configuration.

Many studies have addressed the registration of lung images, with methods based on

image intensity (Murphy et al., 2011), biomechanical models (Al-Mayah et al., 2010; Seyfi Noferest et al., 2018) or a combination of both (Han et al., 2017). The purpose of these methods is to compensate for the lung deformations during normal breathing, mainly for conformational radiation therapy. However, lung deformations are considerably larger during VATS (Alvarez et al., 2018), which increases the difficulty of the registration problem. To the best of our knowledge, only one study has proposed the use of nonrigid image registration in the context of VATS using CBCT images of a pig lung (Uneri et al., 2013).

In this preliminary work, we propose to compensate for lung deformation using a nonrigid image registration approach guided by a biomechanical model of the lung. Using clinical data with deformations consistent to those of VATS, we modeled the lung as a biphasic medium and estimated its deformation via finite element modeling. The main objective was to evaluate the capacity of the model to estimate lung deformations during VATS. We intend to use this approach as an intraoperative nodule localization strategy for VATS.

5.2 Materials and Methods

5.2.1 Data

This retrospective study was conducted on a single clinical case. After a CT image was acquired, the patient had a needle biopsy of a solitary nodule located in his left lung. During this procedure, the patient developed a pneumothorax that was later detected with a post-interventional Low Dose CT (LDCT) image. Although this clinical case is not a VATS intervention, the resulting lung deformation is approximately the same. Specifically, there is a change of patient pose from supine during the CT imaging to lateral decubitus during the LDCT imaging, as well as a pneumothorax (Fig. 5.1).

Several structures were manually segmented from these images: the airway tree, lung parenchyma and nodule from the CT image; and the deflated lung parenchyma, thoracic cage, and nodule from the LDCT image.

5.2.2 Finite element model

In this work, the biphasic model proposed in (Miga et al., 1999) was used to represent the lung. This model is based on Biot's theory of soil consolidation (Biot, 1941), and has been previously used for brain shift compensation (Sun et al., 2014). The governing equations are:

$$\nabla \cdot (G\nabla \mathbf{u}) + \nabla \frac{G}{(1-2\nu)}(\nabla \cdot \mathbf{u}) - \nabla p = -\rho \mathbf{g} \quad (5.1)$$

$$-\nabla \cdot (k\nabla p) + k_c(p - p_c) = 0 \quad (5.2)$$

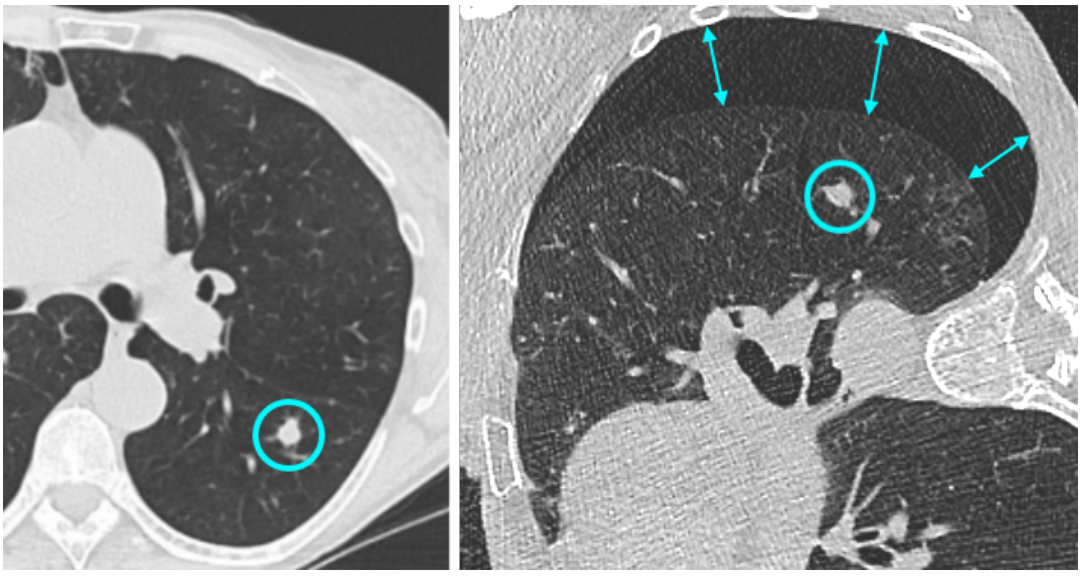

Figure 5.1: Left lung containing a solid, solitary nodule, indicated with a circle. Left: Axial cut of the CT image with the patient in supine position. Right: Axial cut of the LDCT image after pneumothorax with the patient in lateral decubitus position. The pneumothorax is indicated by arrows.

where $\mathbf{u}$ is the displacement vector, p is the interstitial pressure, ν is the Poisson's ratio, G is the shear modulus defined by $\frac{E}{2(1+\nu)}$ with E as Young's modulus, ρ is a density measure defined by $(\rho_f - \rho_s)$ with ρ_f and ρ_s as the density of the fluid and solid phases respectively, $\mathbf{g}$ is the gravitational unit vector, k_c is the bronchi permeability, p_c is the internal bronchi pressure and k the hydraulic conductivity. In addition, we should note that the interchange of air between the lung parenchyma and small bronchi has been approximated by lumping these exchange-effects using the organ-wide distributed term $k_c(p-p_c)$. It allows the simulation of air evacuation from small-scale lower bronchi structures distributed throughout the lung parenchyma, therefore producing local volume changes.

5.2.3 Geometry reconstruction

Using CGAL library (www.cgal.org), two finite element meshes of the lung with four-node-tetrahedral elements were generated (Fig. 5.2). The first mesh (L_{ct}) was generated from the lung parenchyma segmented in the CT image. The second mesh (L_{ldct}) was generated from the the thoracic cage segmented in the LDCT image. For the latter, the underlying assumption is that the original shape of the lung (*i.e.* before pneumothorax) matches the shape of the thoracic cage.

5.2.4 Material properties

As shown in previous studies, the lung parenchyma is highly heterogeneous (Seyfi Nofer-est et al., 2018). The Young's modulus E, for instance, is considered to be lowest near

the diaphragm and highest near the hilum. Similarly, we have made the approximation that the hydraulic conductivity k decreases significantly with the distance from the main airways. The natural anatomic structure of the lung with its decreasing bronchi diameter scale would result in a more restricted exchange, or a lower hydraulic conductivity.

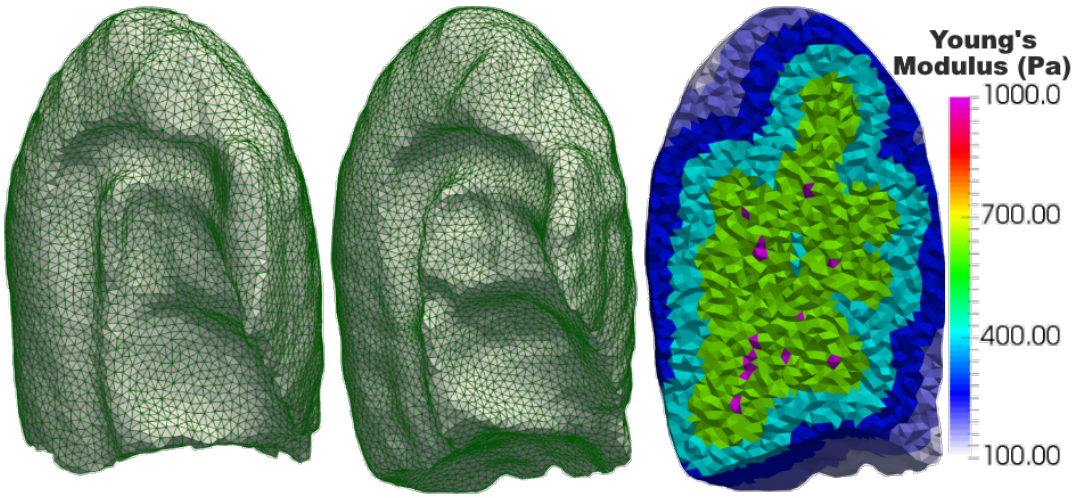

Figure 5.2: Left: Tetrahedral mesh of lung parenchyma from the CT image (L_{ct}). Middle: Tetrahedral mesh of the thoracic cage from the LDCT image (L_{ldct}). Right: Example of mesh stratification on L_{ldct} and the corresponding values of Young's modulus E ($E_{min} = 0.1$ kPa and $E_{max} = 1$ kPa).

Similar to the hydraulic conductivity, we have adopted a distance-to-airway dependence with Young's modulus. As the arrangement of bronchi cartilage rings and subsequent structural elements is present, an approximation of tissue heterogeneity is proposed to decrease Young's modulus with increasing distance from these structures. We have used distance ranges of approximately 15 mm (0 - 15 mm, 15 - 30 mm, etc.) to vary the Young's modulus as an exponential function of this distance (Fig. 2 right). This relationship is represented by:

$$E(d) = \alpha e^{-\gamma d} + \beta \tag{5.3}$$

where d is the distance to the airway tree and γ is the decay constant. Constants α and β are computed based on fit values of E_{min} and E_{max} such that $E(d_{min}) = E_{max}$ and $E(d_{max}) = E_{min}$. An analogous exponential function was used for the hydraulic conductivity k, based on fit values of k_{min} and k_{max}.

5.2.5 Initial alignment

Before nonrigid deformation, registration to a common reference frame was performed. We aligned the spine from the CT and LDCT images using rigid body registration guided by Mutual Information. This procedure was performed with the help

of the multi-resolution, image-based registration techniques implemented in Elastix toolbox (Klein et al., 2010).

5.2.6 Deformation compensation strategy

The deformation experienced by the lung from the CT configuration to the LDCT configuration might be understood as a combination of three interdependent events: (1) a change in the direction of gravity and its effects on internal structures; (2) a change in patient pose that affects the position and shape of the lung; and (3) the deflation of the lung as a result of pneumothorax. The true deformation is an intricate combination of the individual deformations resulting from each one of these events. In this preliminary study, we explored the feasibility of a linear biomechanical model to estimate these lung deformations. The three deformations were estimated independently before being superposed to produce the final post-pneumothorax registered CT image.

Deformations (1) and (2) dealt with the estimation of the pre-pneumothorax anatomy of the lung in the LDCT image configuration. Deformation (3) used the previously estimated anatomy to calculate the deformation associated with only the pneumothorax. It is worth mentioning that our approach does not employ a moving grid from stage to stage so geometric nonlinearities are neglected. We should also note that no hereditary approach accounting for strain history has been implemented. Rather, in this preliminary work, we have estimated each condition from a single mesh pose and deformation was a simple linear combination of deformation modes.

Gravity compensation

The direction of gravity with respect to the patient is different in the CT and LDCT configurations. We compensated for this difference by first estimating a gravity-free state of the lung in the CT configuration, and then recomputing the effects of gravity in the LDCT configuration. For the gravity-free state, the deformation was computed on L_{ct} by applying a body force with the magnitude of gravity, but in the opposite direction, *i.e.* the right hand side of Eq. (5.1) becomes positive.

Tissue parameters were assigned as described in section 5.2.4, using empirically-found values within the range suggested in (Seyfi Noferest et al., 2018). The fluid medium was disregarded during the simulation to compute this deformation. In addition, nodes on the boundaries of the parenchyma were allowed to slide along the surface, while assuming no friction between the visceral and parietal pleurae.

Change of pose compensation

Notable deformation is introduced in the thorax after the change of patient pose (Alvarez et al., 2018). We used a surface matching strategy to compensate for this de-

formation, where displacements were imposed on surface nodes of L_{ct} to match the surface of L_{ldct}.

First, the borders of the thoracic cage of the CT and LDCT images were matched using a BSpline-based Free-Form Deformation (FFD) registration algorithm guided by Mutual Information, as implemented in Elastix toolbox (Klein et al., 2010). From this, we obtained a displacement map describing the deformation necessary to align the surface of L_{ct} to that of L_{ldct}. Then, we imposed displacements on each node of the surface of L_{ct}, according to the displacement map computed previously. Material properties were designated as in the previous step.

Pneumothorax compensation

We modeled the pneumothorax as being caused by differences in pressure between the surface and the interior of the parenchyma. The fluid mass conservation law associated with equation (5.2) allows for the evacuation of the fluid phase (air) via the bronchi and the subsequent volumetric contraction of tissue.A positive pressure (5 cm H_2O) was assigned to the surface nodes of L_{ldct}, while remaining nodes had a no-flux boundary condition. Bronchi permeability was addressed with k_c and p_c, with pressure p_c equals to zero inside the airways. Additionally, the deflation of the lung is constrained by the boundaries of the thoracic cage. Therefore, we assigned slip conditions to the nodes in contact with the thoracic cage, as visualized in the LDCT image.

Since, to the best of our knowledge, the material properties used in the governing equations have never been established for the pneumothorax, we approximated these values using the trust-region nonlinear optimization method implemented in MATLAB. The 7 parameters being fit for in this inverse model were: E_{max}, E_{min}, k_{max}, k_{min}, γ, ρ and k_c. We iteratively minimized the difference between our model-estimated deformation and the true deformation measured in the LDCT image. More specifically, we used a measure of surface-to-surface proximity between the current(model) and target (LDCT) deformations as the indicator of deformation optimality. That is, we minimized the objective function Ω defined as:

$$\Omega = \frac{1}{N}\sum_{i=1}^{N}\left(\mathbf{x}_{d,i} - \mathbf{x}_{t,i}, \mathbf{n}_{t,i}\right)^2 \tag{5.4}$$

where N is the number of deformed surface points, $\mathbf{x}_{d,i}$ is an indexed deformed-surface point, $\mathbf{x}_{t,i}$ is the corresponding closest target-surface point, $\mathbf{n}_{t,i}$ is the normal of the target surface on $\mathbf{x}_{t,i}$, and $(\cdot,\cdot)$ is the inner product operator. The objective function Ω is a variant of the point-to-point distance that takes into account the local shape of the target surface. We clarify that $\mathbf{x}_d$ comes from the surface of L_{ldct} after simulation, and $\mathbf{x}_t$ comes from the surface of the deflated lung, in the LDCT image.

Deformation superposition

The computed deformations were superposed to obtain the post-pneumothorax registered CT image. First, deformations (1) and (2) were added on every node of L_{ct}. The resulting deformation field was used to warp the CT image into the pre-pneumothorax, LDCT configuration. Then, this synthetic image was warped again using deformation (3) on L_{ldct} to produce the final post-pneumothorax registered CT image.

5.3 Experimental results

Our approach was validated using Target Registration Errors (TRE) on a set of 22 paired anatomical landmarks. Twenty-one of those landmarks were localized in clearly identifiable airway and vessel bifurcations, covering a large portion of the lung volume. Finally, an additional landmark was defined in the center of the lung nodule.

Figure 5.3 collects the resulting TREs after three different levels of deformation compensation. First, we applied the rigid initial alignment only, which provides an order of magnitude for the deformation. Then, we applied the pneumothorax compensation step only, to evaluate the relevance of accounting for the gravity and the change of pose. Finally, we evaluated our whole deformation compensation strategy.

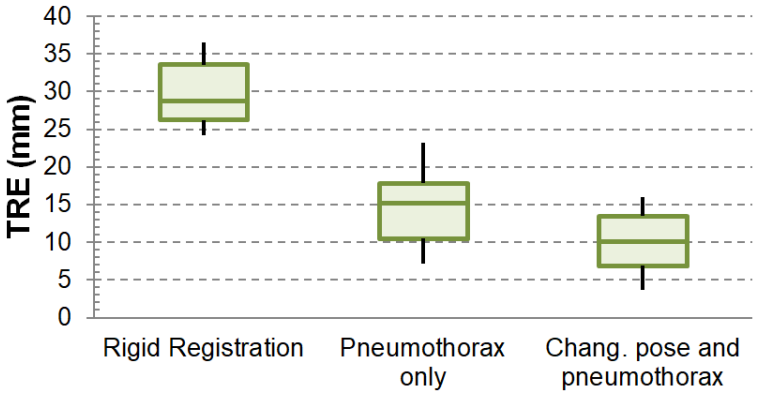

Figure 5.3: TREs after three levels of deformation compensation.

A graphical representation of the spatial distribution of post-deformation anatomical landmarks is depicted in Fig. 5.4. Each landmark is displayed with a color indicating final TRE. In particular, the landmark positioned in the nodule had a TRE of 28.39 mm after initial alignment, 8.06 mm after correcting for the pneumothorax only, and 3.64 mm after applying the whole deformation compensation strategy.

Finally, the parameters found in the optimization procedure were as follows: $E_{max} = 0.94$ kPa, $E_{min} = 0.14$ kPa, $k_{max} = 1.7 \times 10^{-12}$ m^{3}s/kg, $k_{min} = 1.5 \times 10^{-13}$ m^{3}s/kg, $\gamma = 0.28$, $\rho = 165.96$ kg/m^3 and $k_c = 2.51 \times 10^{-9}$ Pa/s.

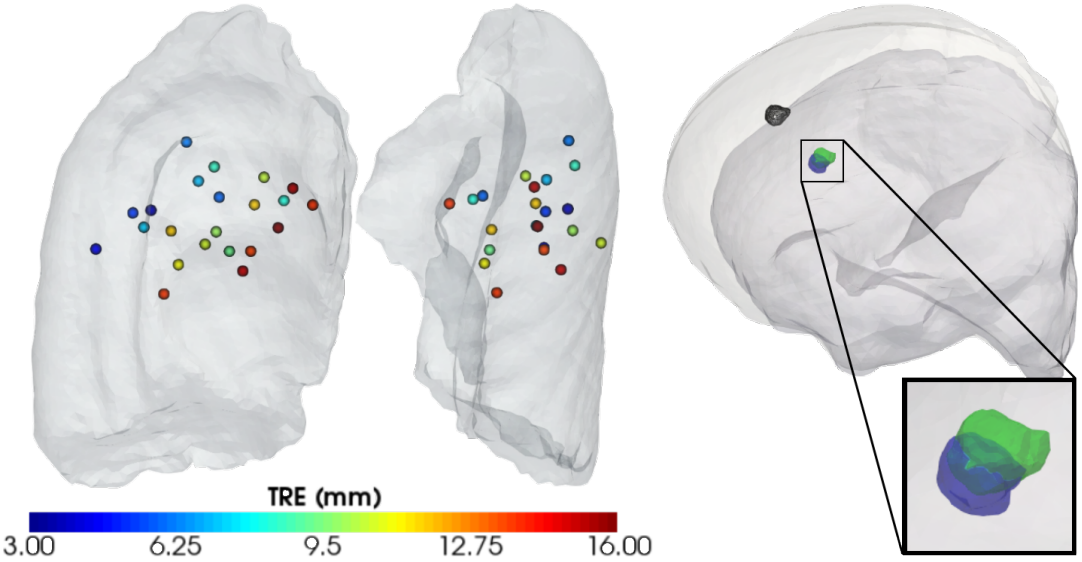

Figure 5.4: Left: Spatial distribution of post-deformation landmarks represented with a color code indicating TREs. Right: 3D reconstructions of the ground truth tumor (in blue), deformation compensated tumor (in green) and rigidly transformed tumor (in black). The surfaces represent L_{ldct} before and after simulation of pneumothorax.

5.4 Discussion and conclusion

Preliminary results suggest that our proposed nonrigid registration approach could compensate for lung deformations occurring during VATS. The reported TREs are promising, considering that the necessary negative margins for nodule resection in VATS are approximately 15 mm (Mohiuddin et al., 2014). In addition, we have also shown the importance of accounting for the change of pose of the patient, and gravity. To that end, it is interesting to note that our preliminary linear superposition of the three deformations resulted in improvements in terms of TRE.

As tissue parameters of the lung are patient-dependent, we did not know the property values required to induce the pneumothorax deformation. For this reason, we used optimization as the tool to estimate these tissue parameters, which ultimately dictated the required deformation. The found values were consistent with previous studies (Dumpuri et al., 2007; Seyfi Noferest et al., 2018). We could then use these values to test the ability of the proposed model to reproduce the lung deformation occurring during VATS.

Future work will include validating our method with more clinical data, to reflect varying degrees of pneumothorax and different nodule locations. Also, the registration approach will have to be adapted for intraoperative CBCT images, by dealing with partial lung anatomy and increased image noise.

Acknowledgments

This work was supported by the *Région Bretagne* through its *Allocations de Recherche Doctorale* (ARED) framework; the French National Research Agency (ANR) through the frameworks *Investissements d'Avenir Labex CAMI* (ANR-11-LABX-0004) and *Infrastructure d'Avenir en Biologie et Santé* (ANR-11-INBS-0006); and the National Institutes of Health - NINDS grant R01NS049251.

Additional results and discussion

This chapter presented a first lung deformation compensation framework, in which image processing and biomechanical modeling techniques were combined. The very large lung deformation observed from the CT image (supine position) to the LDCT image (lateral decubitus position) was approximated using a deformation superposition approach, where the deformations caused by gravity, change of pose, and pneumothorax were estimated independently. In reality, lung deformation is caused by an intricate mixture of the three phenomena, and is governed by the complex dynamics of the lung and surrounding structures. To date, such complex dynamics cannot be modeled directly as they are not completely understood: unknown patient-specific material properties, unknown external loads, unknown stress-free condition, *etc*. In that regard, the functional approach herein proposed is valuable, as it provides means to approximate the solution of a very complex problem by solving three smaller, more tractable sub-problems. Moreover, the results suggest the feasibility of this approach, as the better estimations were obtained with the composition of the three approximated deformations.

Some aspects of the proposed approach are worth of a more detailed analysis. For instance, it is unclear whether using heterogeneous material properties with the linear poroelastic lung model is effective in the current context. Also, the contact conditions used at the lung surface have some implications in lung deformation that have not yet been discussed. Finally, the accuracy and efficiency of the inverse problem formulation necessitate further improvements, which reveals various perspectives. These three aspects will be discussed in the following.

Additional results: an evaluation of tissue heterogeneity

Previous works on lung-deformation modeling generally assume homogeneous material properties (see for example the works by Fuerst et al. (2015) and Tehrani et al. (2015)). However, it has been shown that lung parenchyma exhibits an elastic response that can be spatially heterogeneous (Hasse et al., 2018; Santhanam et al., 2010). Nonetheless, the spatial distribution of heterogeneous material properties is patient-specific, and its estimation remains difficult to date. For that reason, the study presented in this chapter included an approximation of heterogeneous material properties using a functional varying with distance to the airway tree.

As can be seen in Fig. 5.2, the Young's Modulus was varying along distance ranges of approximately 15 mm from the airway tree. However, such discretization may introduce deformation artifacts due to discontinuities at the interfaces between layers, which can be avoided by using a continuous function of distance instead. Moreover, thinner airways are expected to be softer than thicker airways, as there is less cartilage covering their surface. As airway thickness decreases with depth, the distance

from an airway to the inlet may provide an approximation to airways' thickness, and hence provide an estimation of airways' stiffness. These factors were taken into account to improve the spatial distribution of Young's Modulus, as illustrated to the right of Fig. 5.5.

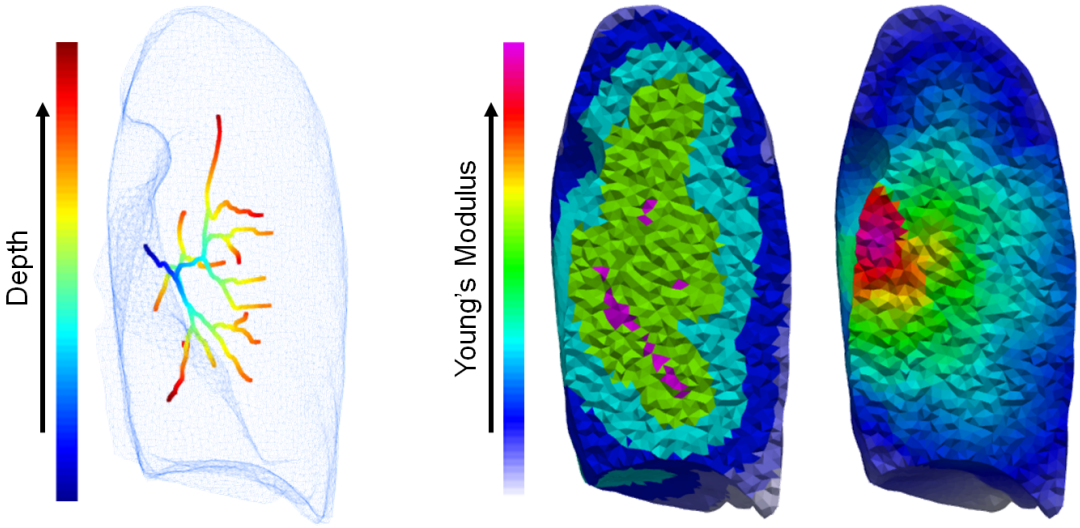

Figure 5.5: Depth of airways and continuous stiffness approximation. The left figure illustrates the skeleton of the airway tree and the evolution of depth at each point. The right figure shows the heterogeneous distribution of Young's Modulus by layers (as previously presented in this chapter) and by taking into account distance to airways and and airway's depth.

To complement the results provided by the initial study presented above, the pneumothorax deformation compensation was repeated using homogeneous and heterogeneous (with layers and continuous variations) Young's Modulus. The objective of this experimentation was to provide further insights in the impact of tissue heterogeneity in deformation compensation. The results are provided in Fig. 5.6.

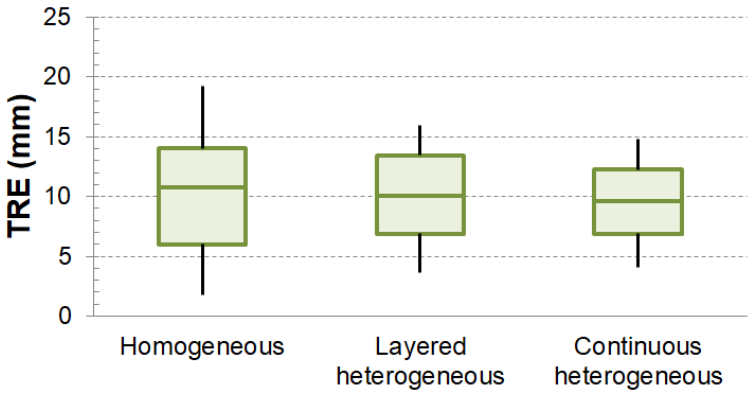

Figure 5.6: Comparison of deformation compensation results with homogeneous and heterogeneous Young's Modulus. The two different heterogeneous distributions are illustrated in Fig. 5.5.

Although differences in minimal and maximal values among TRE distributions can be appreciated in Fig. 5.6, the median differences were not statistically significant (minimum $p > .38$, non-parametric Wilcoxon signed rank test). This could be caused by the simplified poroelastic biomechanical model, the chosen boundary conditions or even the assumptions made for tissue heterogeneity. For studying the feasibility of the proposed deformation compensation approach, these results suggest that a homogeneous assumption for the material properties might be sufficient, as median TREs after deformation compensation would be similar to those obtained with heterogeneous material properties. However, the benefit of taking into account material heterogeneity will have to be re-evaluated if further improvements on the constitutive law or boundary conditions are studied.

In addition, a limitation of the heterogeneous material properties herein used is the need for an airway tree segmentation. This would not represent a problem if such segmentation is performed automatically or before surgery, but it will be incompatible with the VATS protocol if it has to be manually performed during surgery as this is greatly time consuming. Alternatively, the automatic generation of a structure with spatial properties similar to that of the real airways could be used to avoid segmentation. Such approach has been used in the literature in the context of respiratory motion (Berger et al., 2015; Pozin et al., 2017), and its value in the context of VATS could be evaluated in future work.

Contact conditions

In the study presented in this chapter, nodal/tangential contact conditions were used to simulate sliding friction-less contact between the deformable lung and the thoracic cavity. These conditions allow tangential displacement while enforcing zero normal displacement for the surface nodes where they are prescribed. The major advantage of this approach is its efficiency, as only Dirichlet boundary conditions are necessary for each node at the contact surface (in a rotated coordinate system, local to each node). However, it requires to determine beforehand the surface nodes that should remain in contact at the end of the simulation, which seems difficult since it is simulation dependent. Although a priori information can be used to try to list such contact nodes (*e.g.* the medial face of the lung cavity, as was used in the study herein presented), it still remains impractical. Furthermore, it may also be inaccurate, as prescribing too many or too few surface nodes with nodal/tangential contact conditions may result in deformation artifacts. These issues could be resolved by using more realistic contact conditions that are deformation dependent, and are calculated iteratively during solving. This, however, would come with significantly higher computational cost and potential convergence issues, since such contact conditions are highly nonlinear.

Inverse problem formulation

The model parameters required to approximate the observed lung deflation observed were estimated through an inverse problem formulation, in which a surface-to-surface distance was used to measure data misfit. It should be noted that the final deformation is predicted by the linear poroelastic model only (with the parameters found by optimization), and hence, the resulting accuracy is limited by the degrees-of-freedom of the model. Although so far promising results have been obtained for one clinical case (TREs of approximately 10 mm in median), it is likely that an improved model would be necessary to reach the desired accuracy (TREs below 5 mm).

At least two mechanisms could be evaluated to improve the accuracy of the proposed deformation compensation framework. The first mechanism deals with linear poroelastic model. Indeed, it is expected that including non-linearity in the strain tensor (Seyfi Noferest et al., 2018), or using a non-linear stress-strain relationship (Berger et al., 2015) would improve the deformation estimation. The second mechanism deals with the intraoperative data used to drive the deformation. Regardless of the constitutive law used, a perfect surface-to-surface match after deformation compensation is unlikely. The current approach only provides a min-least-squares approximation to surface displacement, which may be insufficient for some cases. To alleviate such misfit error, point-to-surface projection based on shape features could be calculated (Nakao et al., 2019), and incorporated as relaxed imposed displacements to help constrain surface deformation (Morin et al., 2017).

Another consideration of the inverse problem formulation is its computation time. Among the several factors affecting computation time, the number of parameters to be estimated is relevant to this discussion. The higher the number of parameters to be estimated, the higher the computation time required. In the study herein presented, 7 parameters were estimated in total. However, it is expected that not all parameters contribute the same way in the cost function, and the total number may be reduced. For instance, it was suggested in a previous section that homogeneously distributed material properties could be sufficient, in which case the number of parameters is reduced from 7 to 4. A sensitivity analysis could provide further insights on the contribution of each parameter, but it was out of the scope of this thesis. Finally, the computation time may also be significantly decreased using model reduction or machine learning approaches (Mendizabal et al., 2020). Currently, each simulation takes about two or three minutes to run in a local computer (Intel Core i7-6820 2.7 GHz, 32GB RAM), with a total optimization time of approximately seven hours ($\approx$ 170 simulations) in the heterogeneous case, and three hours ($\approx$ 70 simulations) in the homogeneous case. Reducing the simulation time below 1 second, as in the work by Mendizabal et al. (2020), could result in total optimization time in the order of minutes, which would remain compatible with the clinical workflow.

General conclusion

In this chapter, a preliminary study towards lung deformation compensation during VATS was presented. The method relied on a hybrid approach, where the deformations induced by gravity, patient's change of pose and pneumothorax were estimated independently before being combined to predict the total lung deformation observed from the CT to the LDCT image. A linear poroelastic model predicted lung deformation at each phase. In the gravity and change of pose estimation phases, intensity-based image registration allowed the computation of boundary conditions for the solid phase of the poroelastic model. In the pneumothorax estimation phase, an inverse problem formulation allowed the estimation of tissue parameters necessary to reproduce as close as possible the observed intraoperative lung deflation. The major limits of this approach were discussed, and potential further research directions were provided. This first registration framework was conceived with a clinical case of transthoracic needle biopsy, for which lung deformation is very similar to that during VATS. The next chapter deals with the adaptation of the same approach for a real VATS context, where CBCT images are available with partial views of the lung only and significantly reduced image quality.

6

A hybrid registration framework for lung deformation compensation during VATS

Foreword

In this chapter, the hybrid registration framework introduced in Chapter 5 is improved and adapted from the context of transthoracic needle biopsy to the context of VATS. The methodological changes introduced here were driven by two primary factors: a change in the clinical data, and a change in the clinical workflow that affects lung deformation.

With respect to the intraoperative data, two CBCT images are used here (after change of pose and after pneumothorax) instead of only one LDCT image (after a change of pose with pneumothorax). On the one hand, besides image quality, the main difficulty was the partial view of the lung in the CBCT images. As a result, intensity-based image registration can only provide a partial estimation of the boundary conditions for the change of pose. On the other hand, the CBCT image of the lung before pneumothorax provides information that was unavailable in the LDCT image. As such, the effects of gravity during change of pose can be estimated directly using intensity-based image registration, hence reducing the amount of deformation estimation phases from three (first implementation) to two (final implementation).

With respect to lung deformation, the use of anesthesia and curare in the VATS surgical workflow induces large diaphragm displacement that is not present in the context of needle biopsy. Moreover, the lung deformation caused by the pneumothorax also entails deformation of the thoracic cavity, especially at the medial face (hilum). This had to be taken into account before the inverse problem formulation, as this inverse problem was designed to estimate pneumothorax deformation for the lung only.

The first part of this chapter reproduces a manuscript that was submitted to the international journal *Medial Image Analysis*:

> **P. Alvarez**, S. Rouzé, M. I. Miga, Y. Payan, J.-L. Dillenseger, and M. Chabanas. A hybrid image registration approach to markerless intraoperative nodule localization during video-assisted thoracoscopic surgery. *Medical Image Analysis*, submitted in April 2020

The second part of this chapter provides further discussion and perspectives with respect to the investigations presented in the other chapters of this thesis.

Article: A hybrid image registration approach to markerless intraoperative nodule localization during video-assisted thoracoscopic surgery

Abstract: The resection of small, low-dense or deep lung nodules during video-assisted thoracoscopic surgery (VATS) is surgically challenging. Nodule localization methods in clinical practice typically rely on the preoperative placement of markers, which may lead to clinical complications. We propose a markerless lung nodule localization framework for VATS based on a hybrid method combining intraoperative cone-beam CT (CBCT) imaging, free-form deformation image registration, and a poroelastic lung model with allowance for air evacuation. The difficult problem of estimating intraoperative lung deformations is decomposed into two more tractable subproblems: (i) estimating the deformation due the change of patient pose from preoperative CT (supine) to intraoperative CBCT (lateral decubitus); and (ii) estimating the pneumothorax deformation, *i.e.* a collapse of the lung within the thoracic cage. We were able to demonstrate the feasibility of our localization framework with a retrospective validation study on 5 VATS clinical cases. Average initial errors in the range of 22 to 38 mm were reduced to the range of 4 to 14 mm, corresponding to an error correction in the range of 63 to 85%. To our knowledge, this is the first markerless lung deformation compensation method dedicated to VATS and validated on actual clinical data.

6.1 Introduction

Lung cancer is the leading cause of cancer death among both men and women, making up more than 18% of all cancer deaths (Bray et al., 2018). The high mortality of lung cancer is associated with its asymptomatic nature that hinders its early detection, diagnosis and treatment. However, the advent of screening programs with low-dose computed tomography (CT) have significantly increased patient survival (Henschke et al., 1999; The National Lung Screening Trial Research Team, 2011). Surgical resection is considered one of the best curative treatments for patients with early-stage lung cancer. Historically, lung lobectomy (*i.e.* the removal of entire lung lobes) through open thoracotomy was the chosen protocol. Within the last decades, clinical practice has evolved towards less invasive, better tissue preserving techniques. For instance, minimally-invasive video-assisted thoracoscopic surgery (VATS) has proven to yield equivalent clinical outcomes while improving patient care, and decreasing both the length of hospitalization and post-operative complications (Falcoz et al., 2015). In parallel, the interest for smaller, non-anatomic resections (known as wedge resections) has arisen for small nodules as a substitute to lung lobectomy. Although no consensus has been reached yet, studies suggest that the use of appropriate neg-

ative margins during wedge resections could provide patient outcomes equivalent to those of traditional lobectomies (Mohiuddin et al., 2014; Wolf et al., 2017). However, this shift from lung lobectomy to wedge resection through minimally-invasive VATS has introduced new surgical challenges. For instance, thoracic incisions to insert surgical instrument break the pressure equilibrium in the intrapleural space and cause air to flow into the thoracic cage. This abnormal air inflow, known as a pneumothorax, induces very large tissue deformation by collapsing the lung towards the hilum. While this voluntary induced pneumothorax is required to create surgical workspace, it significantly impairs the intraoperative localization of lung nodules, especially for small nodules that are generally not visible to the naked eye nor palpable through thoracoscopic instruments (Chao et al., 2018). Failing to localize lung nodules during VATS may ultimately result in unplanned surgical conversion to open thoracotomy, with a conversion rate as high as 54% reported in some studies (Suzuki et al., 1999). Therefore, several nodule localization strategies are commonly used in clinical practice. The main approach consists in placing fiducial markers in the nodule to facilitate its intraoperative localization. This nodule marking generally requires an additional preoperative procedure, just before surgery, to typically place hookwires, micro-coils, or dyes under fluoroscopy guidance (Keating and Singhal, 2016). Despite the high success rates reported for these nodule localization techniques (Chao et al., 2018), the risk of marker migration is still non negligible and the patient is subject to additional radiation exposure. Furthermore, the optimal coordination of the two procedures (*i.e.* preoperative localization and surgical resection) may become a logistic burden, while the patient is at risk during the transfer from the CT suite to the operating room.

To overcome the problems associated with preoperative localization procedures, intraoperative nodule localization has been proposed. This strategy relies on intraoperative imaging to guide nodule-marker placement immediately before surgery, generally in a hybrid operating room. For instance, Gill et al. (2015) have introduced the iVATS system that uses a C-arm to localize nodules placing metal fiducial markers under fluoroscopy guidance. Other groups have implemented similar approaches combining intraoperative CT guidance with either hook-wire (Zhao et al., 2016), dye (Yang et al., 2016), or double nodule marking (Chao et al., 2019). Chao et al. (2018) showed that these intraoperative localization techniques were associated with decreased time at risk but increased time in the operating room, without any significant difference in clinical outcomes with respect to preoperative localization.

Another intraoperative localization paradigm consists in markerless approaches. The idea is to use intraoperative imaging on the patient under operating conditions, namely, after the insertion of surgical ports and the induction of pneumothorax. This allows to localize the nodule immediately before its surgical resection. Several authors have proposed to use intraoperative ultrasound for the localization of lung nodules

(Kondo et al., 2009; Rocco et al., 2011; Wada et al., 2015). In these images, nodules can be identified as hyperechoic regions with hypoechoic shadows (Kondo et al., 2009). However, this strategy is highly expert-dependent and requires a fully deflated lung, which is in many cases unfeasible. Another method has been introduced by Rouzé et al. (2016) in a hybrid operating room. A Cone Beam CT (CBCT) image of the semi-deflated lung is used for the localization and delineation of the nodule. This delineation is then registered to intraoperative fluoroscopic images that are used for guidance. A clinical study performed on 8 patients demonstrated the feasibility of this approach. While promising, all these intraoperative markerless approaches rely entirely on the nodule visibility in the images, which may be limited in many cases by the reduced quality and contrast of intraoperative images. For instance, the fuzzy borders and low-density of ground glass opacity (GGO) nodules could make them indistinguishable from normal parenchyma in a low-contrast CBCT or US image. To overcome this limitation, we believe that image registration techniques can be used to bring preoperative surgical planning information into the intraoperative setting.

Image registration has been previously used to compensate for lung deformation to improve the efficiency of medical lung imaging in the diagnosis, treatment-planning, and guided intervention of lung diseases (McClelland et al., 2013). Several registration methods have been proposed based on image intensity (Murphy et al., 2011), biomechanical models (Al-Mayah et al., 2010; Seyfi Noferest et al., 2018), or a combination of both (Han et al., 2017). The applicability of these methods is currently restricted to lung breathing motion, mainly for conformational radiation therapy. However, lung deformation is considerably larger during VATS (Alvarez et al., 2018) which increases the difficulty of the registration problem. To our knowledge, only a handful of works have addressed the problem of lung nodule localization during VATS through image registration (Alvarez et al., 2019a; Uneri et al., 2013). This paper presents a novel method to address this problem, evaluated for the first time on actual VATS clinical cases.

The contributions of this work can be summarized as follows: (i) we propose a markerless approach for lung nodule localization during VATS that is based on intraoperative CBCT imaging and image registration techniques; (ii) we propose a hybrid registration method combining intensity-based and biomechanics-based image registration; (iii) we specifically take into account lung deformation resulting from the patient's change of pose, the pneumothorax, the diaphragm movements, and the hilum deformation during the surgical procedure; and (iv) we evaluate our method on 5 retrospective clinical cases of patients that underwent wedge resection through VATS.

The remaining of this document is organized as follows: Sec. 6.2 presents an overview of existing methods for lung deformation estimation. Sec. 6.3 exposes the general

workflow of our proposed approach. Sec. 6.4 describes the poroelastic biomechanical model used in our simulations. Secs. 6.5, 6.6 and 6.7 then present the different steps involved in our registration method. Results and discussion are presented in Sec. 6.8, followed by final concluding remarks in Sec. 6.10.

6.2 Related works

The lung is a very soft, highly deformable organ in constant motion and deformation due to breathing, heart beats, and body movements. A wide variety of lung image registration techniques based on image intensity, biomechanical models, or hybrid approaches have been developed to compensate for lung motion. These techniques were proposed mainly for breathing motion compensation, with tomographic images typically acquired by pair at both the end inhalation and the end of exhalation, or during the entire breathing cycle through 4DCT. In this study, our interest is the compensation of lung deformation occurring during VATS using intraoperative CBCT imaging. Breathing deformation and VATS deformation have different orders of magnitude, the latter being significantly larger. Causes of these lung deformation differ with the context. During normal breathing, lung deformation results from the contraction and relaxation of respiratory muscles that induce volumetric changes. Since the lung parenchyma and the thoracic cage can move independently, sliding motions between these structures can be observed. The intraoperative lung configuration results from different sources of deformation, mostly the patient pose, the insertion of surgical ports, and the general anesthesia. The insertion of surgical ports induces a pneumothorax that deflates the lung parenchyma and deforms the hilum. General anesthesia also relaxes the diaphragm muscle which therefore moves upwards (*i.e.* towards the apex), pushed by the weight of abdominal organs. The combination of these factors with the reduced quality of intraoperative CBCT images make the compensation of lung deformation for nodule localization during VATS a real challenge.

6.2.1 Intensity-based image registration methods for lung deformation compensation

Besides large lung deformation, sliding motion against the thoracic cage is widely known to be one of the major challenges encountered when dealing with intensity-based elastic registration of the lung parenchyma. In practical terms, the deformations of the lung and surrounding structures are constrained at the interface in the normal direction, but move almost freely in the tangential direction. However, most transformation models used in medical image registration assume a continuous deformation field that can not model this sliding effect (Maintz and Viergever, 1998; Sotiras et al., 2013).

Several authors have introduced methods for taking into account sliding interfaces for lung registration. Anatomical segmentations can be used to independently register the structures at the interface (Rietzel and Chen, 2006). With this technique, classical image registration algorithms can be used with little to none modification. However, gaps or overlaps may appear at the interface as a result of the independent registration. One solution consists in using a boundary-matching penalty method so that the interfaces are tied together. Wu et al. (2008) proposed to dilate the segmentations after a masking procedure to enforce the alignment of the interface. Another strategy is based on decomposing the deformation field at the interface into normal and tangential components. Sliding motion can be preserved by applying regularization on the normal component (Schmidt-Richberg et al., 2012), or by using a composite transformation with a shared normal component but independent tangential components (Delmon et al., 2013). The main drawback of these methods is the need for anatomical segmentations. Indeed, these segmentations are time-consuming to extract manually or may be inaccurate if extracted automatically, especially for pathological lungs or low contrast images. In order to overcome this issue, other works have proposed alternative methods that do not require prior anatomical segmentations. Ruan et al. (2009) presented a regularization strategy that discriminates the divergence and the curl of the deformation field separately. The authors are able to preserve sliding motion by allowing large shearing while penalizing other forms of non-smooth deformation. Another technique consists in using several layers of supervoxels (*i.e.* groups of neighboring voxels with similar intensities) connected using minimum spanning trees (Heinrich et al., 2016). The deformation field is enforced to be smooth across edge connections via regularization. However, non-connected supervoxels are allowed to be registered independently, hence preserving sliding motion.

In a previous preliminary study, we applied the methods proposed by Wu et al. (2008) to register two intraoperative CBCT images of the undeformed and deformed lung acquired during a VATS intervention (Alvarez et al., 2019b). We managed to obtain reasonable alignment of the lung surface, but insufficient alignment of the internal structures. To our knowledge, no other study has addressed the same problem using intensity-based image registration only.

6.2.2 Biomechanical model-based methods for lung deformation compensation

Another approach for lung deformation compensation is the use of biomechanical models describing the lung's behavior. The Finite Element Method (FEM) is commonly used to obtain numerical solutions to the underlying equations. For instance, Zhang et al. (2004) proposed a Finite Element (FE) deformable model of the lung reconstructed at the end of exhalation to simulate lung expansion motion. The thoracic

cage surface at the end of inhalation was included in the formulation as frictionless contact conditions that constrained lung expansion. A uniformly distributed negative surface pressure was applied to the deformable model until it filled the thoracic cage. A similar approach to lung expansion motion was proposed by Werner et al. (2009). The authors performed a study on 12 lung tumor patients and evaluated how changing tissue parameters affect the estimated deformations. The results suggested that if tissue homogeneity was considered, changing tissue parameters could only produce marginal perturbations in lung deformation, since it was mainly dictated by the limiting geometry of the thoracic cage. Another study investigated the effect of tissue heterogeneity while modeling lung expansion (Ilegbusi et al., 2014). The elasticity modulus was estimated locally using an inverse non-invasive method. In average, the obtained values decreased with proximity to the diaphragm. The authors showed that the history of deformation as well as its spatial distribution were different when considering heterogeneous versus homogeneous material properties. Other authors have also investigated the use of non-constant, non-uniformly distributed negative surface pressures to produce lung expansion. Eom et al. (2010) computed negative pressure values from patient-specific Pressure-Volume (P-V) curves calculated from 4DCT data. With this approach, the authors were able to simulate lung deformation for the whole breathing cycle. The FE deformation predictions were more accurate than simple linear interpolation between end expiration and end inspiration deformations. Fuerst et al. (2015) automatically divided the lung surface in disjoint contact zones. The negative pressure applied at the surface was then differentiated for each contact zone, the specific values being found through an inverse problem formulation. Although the authors used homogeneous material properties, the results suggested an improvement of the deformation estimation thanks to the heterogeneous surface pressures, which are able to account for the lack of heterogeneous material properties.

Several works have also approached lung deformation estimation during breathing as a contraction motion. Al-Mayah et al. (2008) proposed a deformable model of the lung and surrounding structures reconstructed at the end of inhalation. Surface displacements from the end inhalation to the end exhalation phases were found using a mesh morphing method. These displacements were imposed as boundary conditions to the inner surface of the thoracic cage, which is in direct contact with the deformable lung model. Interactions between the lung and thoracic cage was modeled via frictionless contact, which allowed the integration of lung sliding. This study was further extended to investigate the effects of contact friction at the lung interface (Al-Mayah et al., 2009) or heterogeneous material properties (Al-Mayah et al., 2010), as well as the influence of linear and non-linear elasticity constitutive laws (Al-Mayah et al., 2011). These studies led to the development of the biomechanical model-based deformable image registration framework Morfeus for treatment planning and accu-

rate target delineation during external radiation therapy. Recently, Velec et al. (2017) validated the accuracy of a commercial version of Morfeus on tomographic and MR images of the thorax, prostate and liver of 74 patients, with validation errors measured in the range of the image spacing.

All the methods reported above model the lung parenchyma as a single elastic continuum. In reality, the volume occupied by the lung is composed of not only the parenchyma but also a great quantity of air that is stored inside the airways and alveoli. External forces exerted by the respiratory muscles allow the inhalation or exhalation of air from the lung, ultimately resulting in tissue deformation. Following this interpretation, the lung can be modeled as a porous medium composed of two coexisting physical domains: a solid domain (*i.e.* the parenchyma) and a fluid domain (*i.e.* the air flowing inside the lung). Physical laws governing the behavior of such porous medium constitute the theory of poroelasticity, which has been previously used to model breathing deformation. For instance, Ilegbusi et al. (2012) proposed a poroelastic model to simulate lung deformation throughout a complete breathing cycle. Boundary conditions for the fluid and solid domains consisted in a time varying positive pressure and a fixed support, respectively. The authors reported realistic deformations including a hysteresis deformation effect when accouting for heterogeneous material properties. Gravity was later added in the loads which improved the accuracy of the predicted deformation (Seyfi Noferest et al., 2018). Berger et al. (2015) also proposed a dynamic poroelastic model of the lung tightly coupled with an airway network modeling the airways. The authors presented a comprehensive description of their model and introduced its applicability to normal and physiological breathing using varying airflow resistance and local elasticity. Physiologically realistic global measurements and dynamic were reported.

To our knowledge, no biomechanical model has ever been proposed to compensate for intraoperative deformation during VATS. As mentioned before, deformation during VATS can be significantly larger than during breathing, primarily because of the pneumothorax. The parenchyma deflation observed following a pneumothorax is caused by air getting out of the lung. Using elasticity models to represent this kind of deformation may be oversimplifying, since the loss of air mass (*i.e.* air escaping from the lungs) would be modeled as large tissue strain, which is unrealistic given the amount of volume change. A poroelasticic model could instead be better suited to separate the deformation of the two different media, which would allow to model the air-tissue coupling in a macro-scale and cost-effective manner, as well as to simulate air loss from the fluid phase.

6.2.3 Hybrid methods for lung deformation compensation

Lung deformation compensation methods using intensity-based image registration methods or biomechanical models have both advantages and disadvantages. Intensity-based methods are limited by the reduced quality of intraoperative images and the need for complex regularization strategies for realistic motion estimation. On the other hand, good results on a voxel-by-voxel basis, especially for internal structures, can be obtained if images of adequate quality are available. Regarding biomechanical models, limits mostly come from the uncertainties on boundary conditions needed for realistic lung motion simulations, the high variance in tissue parameters that could be difficult to estimate accurately, or the compliance of computational requirements with clinical practice. However, when compared with intensity-based methods, biomechanical models are able to work with less data since the underlying biophysical representation naturally constrains the solution space. In addition, as these are naturally boundary valued problems, their resolution is quite compatible with environments where primarily only surface information is available. Also, approaches that use modeled physical and physiological phenomena may provide insight into understanding disease and its effects on lung behavior. The hypothesis of hybrid methods is that combining the two strategies allows to compensate for their individual limitations.

Hybrid methods for lung deformation estimation have already been investigated in previous works. Li et al. (2008) used intensity-based image registration to estimate a deformation field from end of exhalation to end of inhalation breathing phases. Dirichlet boundary conditions (*i.e.* imposed displacements) were then computed by interpolating the deformation field on the surface nodes of a deformable FE lung mesh. A similar approach was employed by Tehrani et al. (2015), who used Demons image registration to estimate surface displacement boundary conditions at several moments of the breathing cycle. In addition, the authors studied the effects of tissue parameters and non-linear elasticity laws on tumor displacement estimation accuracy, reporting best results under non-linear elasticity assumptions.

Other studies have used intensity-based image registration to reduce residual errors resulting from biomechanical model motion estimation. For example, Samavati et al. (2015) used the Morfeus platform to estimate lung contraction between end of inhalation and end of exhalation. The estimated deformation was then refined using nonrigid image-intensity registration between the warped end of inhalation image and the target end of exhalation image, which lead to improved estimation accuracy. Han et al. (2017) applied the same methodology to lung expansion deformation estimation during breathing. The authors compared their approach to only intensity-based or only biomechanical-model based image registration, and also evaluated the influence of tissue parameters, contact friction and tissue heterogeneity. Their results

suggest better performance of hybrid approach with respect to intensity or biomechanical models alone, but a performance similar to intensity-based approaches that account for sliding motion. The uncertainty of model parameters was accounted for by the refinement image-intensity step, allowing the use of simplified assumptions for the biomechanical models in hybrid approaches.

Finally, Uneri et al. (2013) carried out a preliminary study using CBCT images of an inflated and deflated ex-vivo pig lung. Although the authors did not use biomechanical modeling, a hybrid approach was implemented combining surface morphing and nonrigid intensity-based image registration. The reported results were promising, but the applicability to clinical practice remains to be determined, since the quality of real intraoperative VATS images is potentially lower than the quality of the images used by the authors, and the amount of pneumothorax deformation is not under control. More recently, Nakao et al. (2019) proposed a surface-based shape model of lung deflation validated on Beagle lungs. The authors provided inter-subject statistical analysis of lung deformation on a population of 10 animals. However, validation results were reported only for surface landmarks, and its applicability to internal lung deformation remains to be investigated. To our knowledge, these studies are to date the only ones within the VATS context, but are limited to animal specimens in non-clinical conditions.

In a preliminary study, we recently proposed a hybrid approach to account for pneumothorax related lung deformations (Alvarez et al., 2019a). This method was evaluated on a retrospective clinical case of needle biopsy with pneumothorax complication, using a preoperative CT of the inflated lung and a postoperative low-dose CT of the deflated lung. The present work complements our deformation compensation approach and propose its adaption to actual intraoperative CBCT images acquired during VATS interventions.

6.3 Method Overview

From the preoperative, routinely acquired structural chest CT image to the intraoperative surgical conditions, the lung undergoes very large deformation. This deformation may be understood as a combination of two main factors: (i) a change of the patient pose from supine to lateral decubitus, which changes the orientation of the body and hence the influence of gravity on internal structures; and (ii) the pneumothorax, which induces lung and hilum deformation. Accounting for these two sources of deformation at once is a nontrivial task. To reduce the complexity of this challenge, we thus introduced a functional approach that treats each source of deformation independently in two sequential phases. The lung deformation caused by the change of patient pose was first estimated, followed by the one resulting from the pneumothorax. Intraoperative CBCT images at each phase provided structural

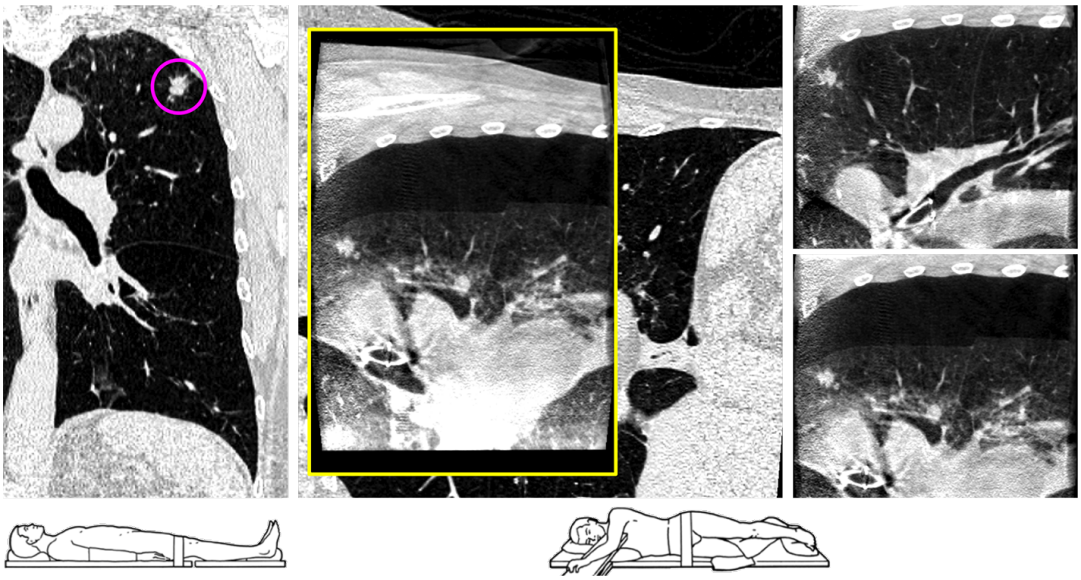

Figure 6.1: Left: preoperative CT image with the patient in supine position. Right: intraoperative CBCT images of the inflated (CBCT_{inf}) and deflated (CBCT_{def}) lung with the patient in lateral decubitus position. Middle: superposition of the preoperative CT image rigidly registered to the intraoperative CBCT_{def} image. The FOV of the CBCT_{def} image (outlined in yellow) only provides a partial view of the lung. The nodule is encircled in the preoperative CT image and is in this visible in all other images.

information of the deformed lung, which was integrated into our hybrid nonrigid registration framework. In total, three anatomical images were used in this study: a preoperative CT image containing the whole lung of the patient in supine position (CT), and two intraoperative CBCT images of the patient in lateral decubitus position. The two CBCT images provide a partial view of the inflated lung before pneumothorax (CBCT_{inf}) and the deflated lung after pneumothorax (CBCT_{def}), respectively. It should be noted that only the preoperative CT image is currently used in the medical protocol of a VATS intervention. Figure 6.1 shows the three images for one clinical case.

The overall methodology proposed in this work is depicted in Fig. 6.2. A patient-specific biomechanical lung model was first built from the preoperative CT image before the intervention. As a first approximation, we considered the lung as a single unified structure. The three or two lobes of a right or left lung, respectively, were then not modeled separately. A poroelastic constitutive law was chosen to represent both the parenchyma and the air flow within the lung.

The first stage of our process, later referred as *Phase 1*, estimates the deformation associated to the patient change of pose. Nonrigid intensity-based image registration was performed between the CT and CBCT_{inf} images to compute the deformation within the field of view (FOV) of the CBCT_{inf} image. The biomechanical model was

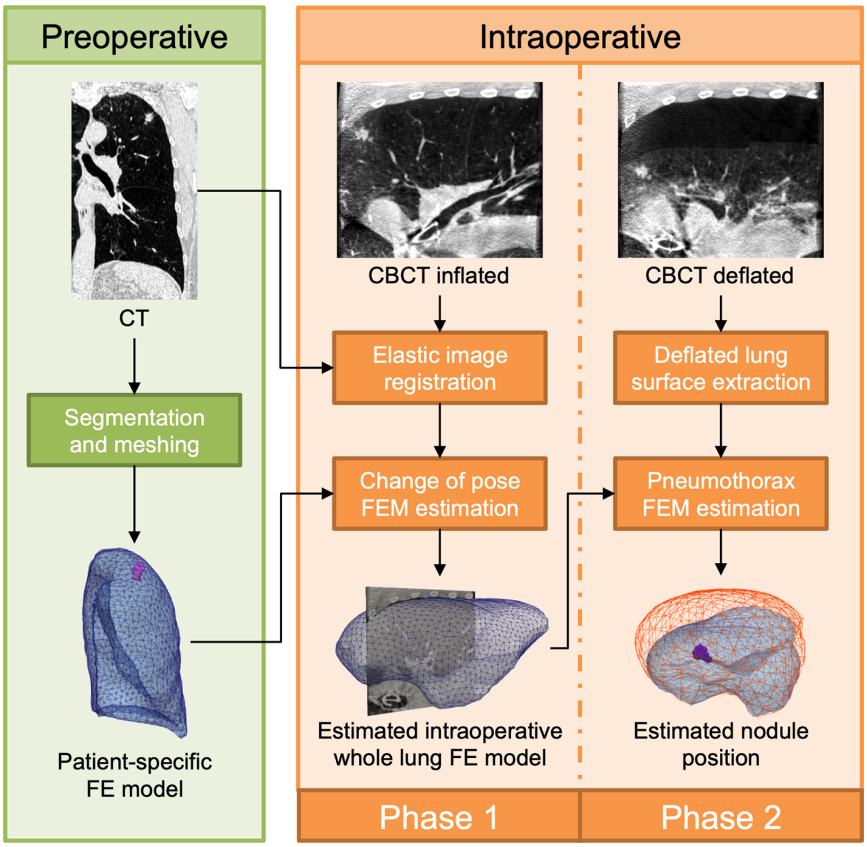

Figure 6.2: Overview of the proposed nodule localization framework. The process is split into two stages, *Phase 1* and *Phase 2*, that respectively estimate the change of pose deformation then the pneumothorax deformation.

then used extrapolate this deformation to the whole extent of the lung, including portions that are not visible in CBCT_{inf}. This estimation of the whole lung geometry will allow to define proper boundary conditions in the next phase, which would not be possible with only the lung portion included in the CBCT_{inf} FOV. After this *Phase 1*, that will be detailed in Sec. 6.6, the complete intraoperative lung geometry before pneumothorax is thus estimated.

The second stage of our method, *Phase 2*, estimates the deformation induced by the pneumothorax. Surface information of the deflated lung was first extracted from the CBCT_{def} image, while also evaluating the associated deformation of the hilum. An inverse problem was then iteratively solved, using biomechanical simulations, to identify the model parameters that minimize a distance between the lung model and the CBCT_{def} inputs. At the end of this process the final pneumothorax deformation is applied to the preoperative CT image, which provides an estimation of the intraoperative lung nodule position. *Phase 2* of our methodology will be described in Sec. 6.7.

6.4 Poroelastic model of the lung

The physical laws governing the poroelastic material used in this work were first introduced in Biot's theory of 3D soil consolidation (Biot, 1941, 1955). The total stress in the porous material is carried partly by the fluid and partly by the solid structure. The hydrostatic pressure of the fluid inside the pores generates tensile/compressive stresses that cause deformation of the whole medium. It is assumed that the total stress on the porous medium can be decomposed as the sum of the stress carried by the solid structure and the stress carried by the fluid (Verruijt, 2013). This is known as the principle of effective stress and is described by the expression

$$\boldsymbol{\sigma}_t = \boldsymbol{\sigma}_e - \alpha p \boldsymbol{I} \tag{6.1}$$

where $\boldsymbol{\sigma}_t$ and $\boldsymbol{\sigma}_e$ are the stress tensors for the total and effective stresses, p is the hydrostatic pore pressure and $\boldsymbol{I}$ is the second-order identity tensor. The parameter α is the Biot-Willis coefficient that describes the amount of bulk volume change that is explained by a pore pressure change under constant stress.

The definition of the effective stress tensor $\boldsymbol{\sigma}_e$ depends upon the mechanical behavior assumed for the solid medium. In this work, we used a first order approximation assuming the theory of linear elasticity. We hypothesized that most of the deformation is caused by the fluid medium, thus the solid medium was modeled as linearly elastic (*i.e.* assuming small deformations for this solid medium). The solid medium was also considered as isotropic. It should be noted that more elaborate fluid-solid interaction non-linear models are possible and this work represents a linearization of considerably complex physics as a first step in understanding the potential of a model-based approach. Following these assumptions, the effective stress $\boldsymbol{\sigma}_e$ (known as the Cauchy stress tensor in the framework of linear elasticity) is related to the deformation tensor $\boldsymbol{\varepsilon}$ by the Hooke's constitutive equation

$$\boldsymbol{\sigma}_e = \lambda \, tr(\boldsymbol{\varepsilon}) \boldsymbol{I} + 2\mu \boldsymbol{\varepsilon} \tag{6.2}$$

where λ and μ are the Lamé constants that characterize the tissue's response to stress. These Lamé constants can also be written in terms of the Young's Modulus E and Poisson's ratio ν through the relations

$$\lambda = \frac{E\nu}{(1+\nu)(1-2\nu)} \qquad \mu = \frac{E}{2(1+\nu)} \tag{6.3}$$

The strain tensor $\boldsymbol{\varepsilon}$ of Eq. (6.2) is defined in terms of tissue displacements $\boldsymbol{u}$ as

$$\boldsymbol{\varepsilon} = \frac{1}{2}(\nabla \boldsymbol{u} + \nabla \boldsymbol{u}^T) \tag{6.4}$$

This corresponds to the definition of the infinitesimal strain tensor, where second-order terms are neglected. This is a first-order geometrical approximation of tissue deformation.

Mechanical equilibrium is reached when stresses within the porous medium are in balance with external loads. If inertial forces are not considered and the only external force is gravity, the total stress tensor $\boldsymbol{\sigma}_t$ must then satisfy the equilibrium equation

$$\nabla \cdot \boldsymbol{\sigma}_t + \rho \boldsymbol{g} = \mathbf{0} \tag{6.5}$$

where ρ is the density of the porous medium and $\boldsymbol{g}$ is the gravitational acceleration vector. Since the porous medium is composed of two phases, its density may also be defined in terms of its constituent densities as

$$\rho = \rho_s(1 - \phi) + \phi\rho_f \tag{6.6}$$

where ρ_s and ρ_f are the densities of the solid and fluid media, respectively, and ϕ is the porosity of the whole medium.

An additional equation is needed in order to complete the description of the continuum. In Biot's theory of consolidation, the fluid flows through the pores according to Darcy's law. This law proposes a relationship between the instantaneous flow rate $\boldsymbol{q}$ of an incompressible fluid through a porous medium, which is expressed by the equation:

$$\boldsymbol{q} = -\frac{\kappa}{\mu_f}\nabla p \tag{6.7}$$

where κ is the intrinsic permeability of the porous medium and μ_f the dynamic viscosity of the fluid. The conservation of fluid and solid mass is expressed by the storage equation:

$$\nabla \cdot \boldsymbol{q} + S\frac{\partial p}{\partial t} = -\alpha\frac{\partial \epsilon}{\partial t} \tag{6.8}$$

where S is the storativity parameter and $\epsilon = \partial u_x/\partial x + \partial u_y/\partial y + \partial u_z/\partial z = \nabla \cdot \boldsymbol{u}$ is the volumetric strain.

The term to the right hand of Eq. (6.8) expresses the time rate of change of dilatation/contraction of the solid matrix and how that affects the nature of fluid mass transport. For instance, if we consider the pores to be totally saturated with fluid, a negative rate of volumetric strain will shrink the porous material and immediately squeeze fluid out of the pores by means of raising interstitial pressure. Such fully saturated porous medium is modeled by choosing the parameters $\alpha = 1$ and $S = 0$. On the contrary, if the pores are not fully saturated with fluid, the rate of volumetric strain does not have an instantaneous effect on the distribution of pore pressure. This is represented by the second term of Eq. (6.8) being nonzero, which results in a delay on the transferal of volumetric strain to net fluid flow. The storativity parameter S is

also understood as the amount of fluid that can be forced into the porous medium while maintaining a constant bulk volume. Eq. (6.8) is in essence a mass conservation law that relates changes in volumetric strain of the solid medium to changes in hydration level.

Animal studies were carried out by Miga et al. in order to evaluate the applicability of a poroelastic model to brain shift deformation compensation. The authors extracted *in vivo* measurements of displacement and interstitial pressure of interstitial fluid within the context of two separate deformations sources, an expanding mass represented by a balloon catheter (Paulsen et al., 1999), and a temporal piston-delivery system (Miga et al., 2000). The objective was to determine the accuracy of the poroelastic model to compensate for the main bulk brain deformation under surgically realistic loads. The results reported in those studies in conjunction with more recent follow-up studies (Narasimhan et al., 2018) suggest that deformation and interstitial pressure gradients measured from tissue can be predicted reasonably well using relatively simple boundary conditions on the poroelastic model. Another remarkable finding found in the human environment was that sources of brain deformation were identified that involved significant fluid exchange with the parenchymal space as a result of hyperosmotic agents (Chen et al., 2011). This exchange is very similar to the evacuation occurring in the collapsing lung here. Based on that work, the additional source term was employed into Eq. (6.8) to represent this fluid evacuation dynamic, so that the storage equation is rewritten as

$$\nabla \cdot \boldsymbol{q} + S\frac{\partial p}{\partial t} = -\alpha\frac{\partial \epsilon}{\partial t} - \kappa_b(p - p_c) \tag{6.9}$$

with $-\kappa_b(p - p_c)$ being the source term allowing for fluid evacuation. The parameter κ_b represents intrabronchi permeability. The parameter p_c represents the pressure at the interior of the anatomical structures that allow fluid evacuation. In this present work, p_c corresponds to intrabronchi pressure. It can be seen from Eq. (6.9) that fluid evacuation (*i.e.* fluid sinking) occurs for positive values of $\kappa_b(p - p_c)$. This modified version of the poroelastic equations was used to estimate brain shift deformation (Dumpuri et al., 2007; Sun et al., 2014), and more recently yielded promising results to estimate lung pneumothorax deformation (Alvarez et al., 2019a).

Finally, Eqs. (6.5) and (6.9) fully describe the dynamic behaviour of a poroelastic material with allowance for fluid evacuation. However, computing the transition from the undeformed configuration to the equilibrium configuration is not necessary in our context. Instead, we only seek to estimate the deformation once the lung has settled after the pneumothorax. Consequently, computing only the equilibrium configuration is sufficient. We then implemented the steady-state version of the poroelastic

equations previously presented, simplified as:

$$\nabla \cdot \boldsymbol{\sigma}_e - \alpha \nabla p + \rho \boldsymbol{g} = \mathbf{0} \tag{6.10}$$

$$-\nabla \cdot \left(\frac{\kappa}{\mu_f} \nabla p \right) + \kappa_b (p - p_c) = 0 \tag{6.11}$$

The solution to these equations was computed using a FEM formulation implemented on the open source library *GetFEM* (`http://getfem.org/`). Tissue parameters and boundary conditions prescribed for each simulation will be described in Sec. 6.7.2.

6.5 Preprocessing of the CBCT images

CBCT scanners produce image reconstruction artifacts as any other conventional CT scanner. However, the acquisition of the CT and CBCT images differ on the projection data used, namely 1D for the CT (fan-beam) and 2D for the CBCT (cone beam). The 2D projection strategy relies on larger detectors that allow the CBCT scanner to have a better spatial resolution and reduced irradiation dose (Kalender and Kyriakou, 2007). These are desirable features that make the CBCT scanner portable and OR-compatible. However, the benefits come in detriment of the image quality, since the larger detector suffers from higher image intensity scattering (Schulze et al., 2011), and the particular mechanics of the acquisition process introduces cupping, aliasing and truncation artifacts (Kalender and Kyriakou, 2007; Schulze et al., 2011). The presence of these artifacts will deteriorate the performance of any processing algorithm based on Hounsfield unit (HU) values. We thus proposed to pre-process CBCT images before our registration method.

Two artifacts affect HU values: the truncation artifact that appears when the imaged object is larger than the scanner FOV (Lehr, 1983), and the cupping artifact due to scatter radiation. As a result, the reconstructed images presents an overestimation of HU values near the circular border of the FOV and an underestimation of HU values towards the center of the FOV. In this work, we assumed the reconstructed image to be the sum of real HU values and artifact effects. We modeled these artifact effects via a piece-wise linear function that is circular symmetric with respect to the cranio-caudal axis (*i.e.* the rotation axis of the CBCT scanner) and constant across axial slices. The shape of this function was designed empirically by observing CBCT images. The artifact-corrected images were obtained by subtracting the modeled artifacts to the reconstructed images.

In addition to HU artifacts, reconstruction errors are also present at the superior and inferior borders of the FOV, in the cranio-caudal direction. These errors are caused by projection data missing in several projections of the whole gauntry rotation, as well as beam scattering and aliasing. As a consequence, the reconstructed image is severely

distorted in these regions, where structural information is almost completely lost. We observed that this effect is present in the axial slices of the first and last 12 mm of the image approximately. For all the processing algorithms described in subsequent sections, we did not take into account the information contained in these slices.

6.6 Phase 1: Estimation of the change of pose deformation

This section describes the *Phase 1* processes of the general workflow presented in Fig. 6.2. The aim is here to estimate the geometry of the whole lung in intraoperative condition from the CBCT_{inf} scan, just before the pneumothorax is induced. These *Phase 1* processes are schemed in Fig. 6.3. First, a deformation field was computed between the preoperative CT and intraoperative CBCT_{inf} images, via intensity-based image registration. This registration process involved both a rigid and a nonrigid transformation, as well as a masking procedure that permitted sliding motion at the lung interface. The computed deformation field then defined imposed displacement boundary conditions to a biomechanical model of the lung, to extrapolate the whole lung deformation.

6.6.1 Image-based change of pose estimation

The following subsections describe the intensity-based image registration of the preoperative CT and intraoperative CBCT_{inf} images, as illustrated on top of Fig. 6.3.

Segmentation of CT structures

The lung parenchyma was segmented using an own modified version of Chest Imaging Platform (`https://chestimagingplatform.org/`), an open source library for image processing and analysis of chest CTs. A threshold-based approach was used for the segmentation of air-like voxels in the preoperative CT volume. This provided an initial segmentation containing both lungs and the airways. Connected component analysis was then applied on an axial slice located at approximately 40 mm from the top of the initial segmentation for the automatic detection of a voxel inside the trachea. This voxel was used as a starting seed of a 3D region growing algorithm that segmented the trachea and the first airway branches. The resulting airways segmentation was removed from the initial air-like voxels segmentation, to isolate the lung of interest. The result was manually adjusted to include the areas of the hilum that remained under-segmented. Finally, morphological closing was applied to the lung segmentation to fill in the remaining wholes and to smooth out the contours.

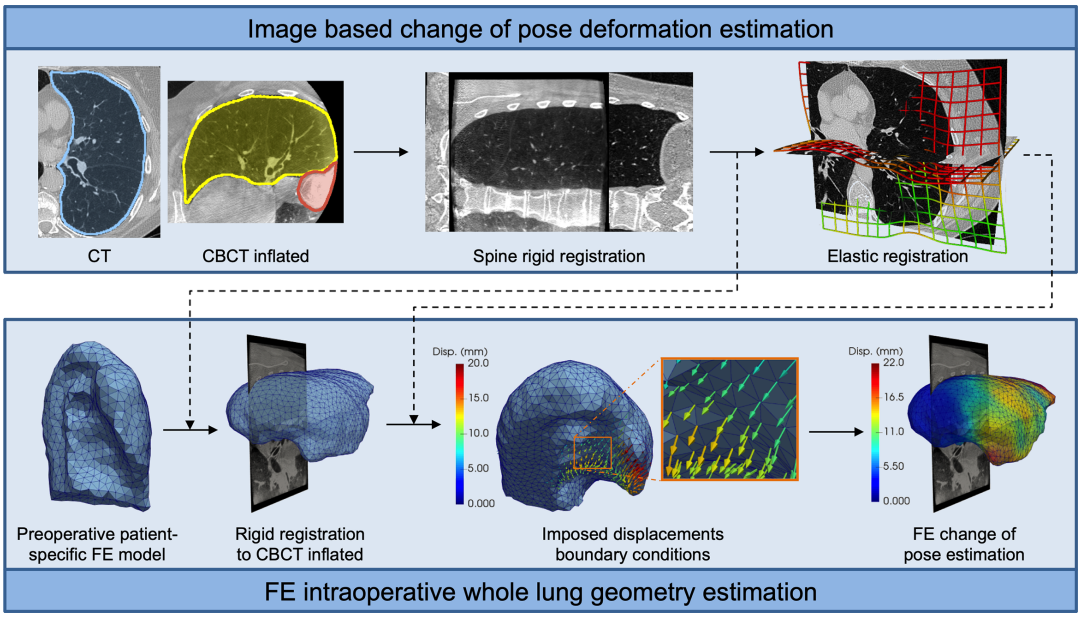

Figure 6.3: Schematic diagram of the *Phase 1* process to estimate the change of pose deformation. The top block illustrates the image-based registration of the preoperative CT and intraoperative CBCT$_{inf}$ images. After rigidly registering the spine, an elastic registration based on anatomical segmentations of the lung is carried out. The bottom block concerns the estimation of the complete lung geometry after the change of pose deformation. The previously computed deformation field is transferred as imposed displacements boundary conditions on a FEM model. This model extrapolates the deformation to the whole extent of the lung, including regions that are not within the FOV of the CBCT$_{inf}$ image.

Segmentation of the CBCT$_{inf}$ structures

The CBCT artifacts and noise, combined with the deformed lung morphology after the patient change of pose, make the automatic segmentation of the lung in CBCT images very challenging. The segmentation algorithm used on the preoperative CT indeed performed poorly on the CBCT$_{inf}$ image. We thus implemented a semi-automatic growing method, initialized by the CT segmentation and propagating in the CBCT$_{inf}$ image. This propagation was based on an elastic image registration process very similar to the one described in Sec. 6.6.1 and 6.6.1. To avoid redundancy, we refer the reader to those sections for details on the registration process. After registration, the preoperative lung segmentation was warped with the resulting deformation field and the resulting segmentation was manually adjusted to correct for poorly-segmented regions.

The spine was also semi-automatically segmented. First, a line profile crossing the spine was computed. Then, a minimal Region of Interest (ROI) containing the whole spine was determined using the spatial derivative of intensities on the line profile. After thresholding the image intensities within the ROI, a connected component anal-

ysis and morphological operations yielded the final spine segmentation.

Rigid registration of the spine

The CT and CBCT$_{inf}$ images are defined in non-overlapping reference frames, as they were acquired by distinct scanners with the patient in a different pose (supine and lateral decubitus, respectively). An initial rigid transformation between the two images is thus necessary before considering any local deformations. In this study, we hypothesized that the spine's curvature is minimally affected by the change of pose, and we thus used this structure as the reference for the rigid registration.

The rigid registration process was carried out with the Elastix toolbox (Klein et al., 2010), with the preoperative CT as the *moving* image and the intraoperative CBCT$_{inf}$ as the *fixed* one. A Normalized Correlation Coefficient (NCC) similarity metric was computed over a series of 2000 image points randomly pooled from the spine segmentation. Since the NCC metric uses image intensities and vertebrae resemble significantly one another, a single spine landmark was manually selected to initialize the transformation and avoid shifting in the spine's direction. The optimal transformation parameters were found using the adaptive stochastic gradient descent optimization algorithm.

Elastic registration

The elastic registration process, again using the NCC similarity metric, was based on the sub-anatomical registration approach proposed by Wu et al. (2008). This approach independently registers sliding structures by selectively masking image intensities with anatomical segmentations. First, we masked the CT and CBCT$_{inf}$ images using the lung segmentations. The voxels lying outside these masks were replaced with a constant HU value below the range of possible parenchyma values (*i.e.* below -1000 HU, corresponding to air). The lung mask in the intraoperative CBCT$_{inf}$ image was extended by 5 mm using morphological dilation, and the set of points used to compute the NCC metric were pooled from this extended mask. By extending the mask, points lying outside the lung in the *fixed* image are registered to the same intensity values in the *moving* image, which also lie outside the lung. In addition, matching outside points has no cost in terms of the similarity metric, which results in the registration process to be guided mostly by the information within the lung. As a result, this process minimizes the misalignment error of the internal lung structures while allowing sliding at the lung interface.

Large deformations were accounted for using a multi-resolution Free Form Deformation (FFD) strategy, with a B-Splines transformation model parameterized on a regular grid in the *fixed* image domain (*i.e.* CBCT$_{inf}$). A total of 5 incremental grid resolutions were used, where the increments were calculated by factors of two. The

finest resolution had a regular grid size of 16 mm. The adaptive stochastic gradient descent algorithm was used for the optimization process.

The result of this registration process is a non-rigid deformation field that maps all points of the *fixed* image (CBCT_{inf}) domain to the *moving* image (rigidly registered CT) domain. Thanks to the multi-grid, multi-resolution transformation model, the spatial Jacobian of the deformation field is positive throughout the whole domain (Choi and Lee, 1999). This ensures the invertibility of the deformation field, which is important to later compute imposed displacement boundary conditions.

6.6.2 Extrapolation of the deformation to the entire lung

The deformation field obtained in the previous step provides a first estimation of the change of pose deformation, but is limited to the FOV of the CBCT_{inf} image. A FEM model was then used to extrapolate this deformation to the entire lung, especially in the lung apex and/or the diaphragm area that are usually at least partially not visible. The hypothesis is that the unknown deformation in these regions can be estimated by means of mechanical forces that emerge to counter external loads applied in the middle of the lung (*i.e.* inside the FOV). In other words, deformation in unknown regions is estimated by finding a state of mechanical equilibrium after imposing the partially known deformation. Note that we did not try to simulate the very complex mechanisms of the patient change of pose; we have so far no means of estimating the actual external and body loads of this complex phenomenon. Instead, we simply tried to functionally estimate the entire lung deformation for the practical purposes of intraoperative surgical guidance.

The following subsections describe the FE extrapolation process which main steps are illustrated at the bottom of Fig. 6.3.

FE mesh generation

The geometry of the lung was meshed from the preoperative lung segmentation using CGAL library (`https://www.cgal.org/`). This FE mesh consisted of approximately 27000 first order tetrahedral elements with an average size of 8 mm.

Computation of imposed displacements

The FEM boundary conditions were computed from the rigid transformation and the deformation field described previously in Sec. 6.6.1. First, the patient-specific preoperative FE mesh was rigidly registered to the intraoperative setting using the rigid transformation parameters. Then, we calculated the deformation associated to every node of the mesh lying within the bounds of the change of pose deformation field. The deformation field at every node position was inverted using the iterative algorithm proposed by Crum et al. (2007), to define the displacement from the rigidly

registered CT domain to the CBCT$_{inf}$ domain. As a result, we obtained a set of displacement vectors that can be used as nodal boundary conditions in a FE simulation. In the following, we will refer to these boundary conditions as imposed displacements.

FE estimation of the change of pose

The lung was modeled as an homogeneous and isotropic medium, governed by the biphasic constitutive laws described by Eqs. (6.10) and (6.11). We here hypothesized that the change of pose deformation is mainly caused by gravity and contacts between the lung and its surrounding moving structures. Thus, effects of the fluid phase on this deformation were assumed to be negligible at this stage, which implies no fluid flow throughout the whole domain and fluid mass conservation.

For the fluid phase, we prescribed homogeneous Dirichlet boundary conditions of pressure on the whole lung surface ($p = 0$), with the intrabronchi permeability parameter κ_b set to zero to ensure mass conservation. For the solid phase, imposed displacement were applied to surface nodes as Dirichlet boundary conditions, while ensured on nodes inside the mesh via Lagrange multipliers. The remaining nodes were left unconstrained.

Since imposed displacements boundary conditions enforce the final deformation, tissue parameters have little influence on the final equilibrium state. Thus, we simply used the parameters of the pneumothorax estimation phase described in Sec. 6.7.2.

6.7 Phase 2: Estimation of the pneumothorax deformation

This section describes the second stage of the general workflow presented in Fig. 6.2. The pneumothorax deformation was estimated using a pipeline based on an inverse formulation, as illustrated in Fig. 6.4. This inverse formulation fitted the lung biomechanical model to the real intraoperative deflated state observed in the CBCT$_{def}$ image. The nodule position was then updated by warping the preoperative CT with the change of pose deformation and then the simulated pneumothorax deformation.

6.7.1 Intraoperative data processing

The intraoperative CBCT$_{inf}$ and CBCT$_{def}$ images can be in misalignment, because the patient may had to be moved between the two scans so that the surgeon could better perform the thoracic incisions. We thus rigidly registered these images using the rigid spine as a reference. The resulting transformation served to align the FE extrapolated lung model with the CBCT$_{def}$ image. Afterwards, this image was processed to extract the surface of the deflated lung and to estimate the hilum deformation after pneumothorax.

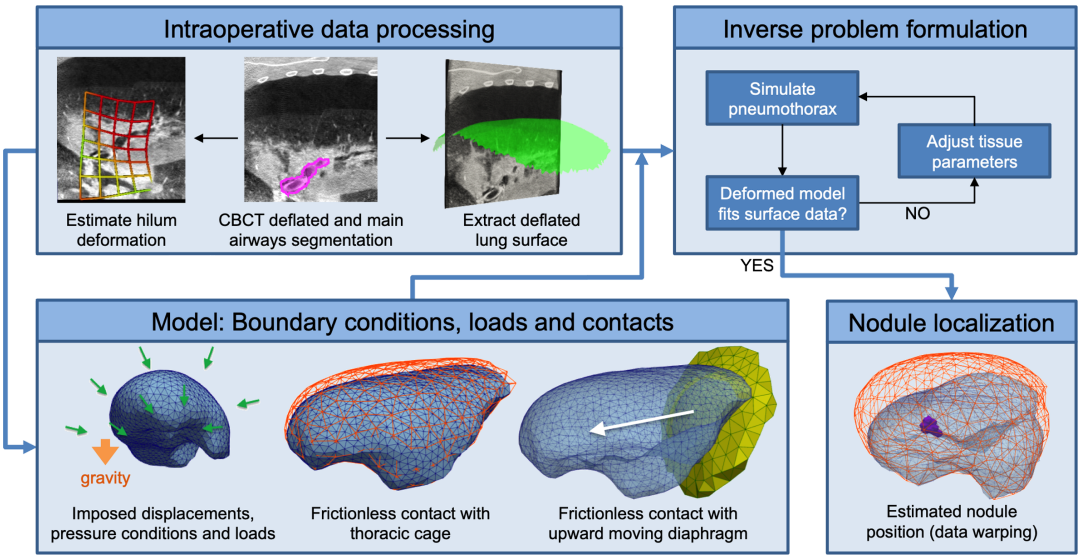

Figure 6.4: Schematic diagram of the *Phase 2* stage to estimate the pneumothorax deformation. Intraoperative images are processed to segment the surface of the deflated lung, and to compute a deformation field approximating the hilum deformation between CBCT_{inf} and CBCT_{def}. An inverse problem based on FE simulations estimated the pneumothorax deformation. Tissue parameters were optimized until the simulated model best fits the intraoperative data. Finally, the intraoperative nodule position is obtained by warping the undeformed position with the simulated pneumothorax deformation.

Segmentation of the deflated lung surface

The lung deflation process causes the complete collapse of some airways branches and alveoli. This condition, known as atelectasis, locally increases the density of the lung parenchyma making its boundary with other soft tissues barely distinguishable in some regions. Therefore, automatically segmenting the deflated lung is extremely challenging. Since providing an automatic method was out of the scope of this paper, we decided to segment this surface manually. In this study, only the external surface of the deflated lung is considered.

A set of about 300 points were manually placed over the CBCT_{def} image along the surface of the deflated lung. The distance among points varied with the local curvature of the deflated surface, ranging roughly from 10 mm to 30 mm. Then, we used MeshLab (Cignoni et al., 2008) to reconstruct a triangular surface from these points. First, the convex-hull of the point cloud provided an initial estimation of the surface. Then, this initial surface was re-sampled with the Poisson disk sampling algorithm (Corsini et al., 2012) to obtain a homogeneous point resolution. Finally, a refined surface mesh was reconstructed from the sampled point cloud using the ball-pivoting algorithm (Bernardini et al., 1999). It is worth noting that because of the convex-hull algorithm, details of independent lobe deformation were averaged. This goes in ac-

cordance with our single structure assumption for representing the lung anatomy.

Estimation of the hilum deformation

During pneumothorax, the hilum deforms in the same direction as the lung deflates. The extent of this deformation is intervention-dependent and unknown *a priori*. In addition, regions of the lung parenchyma closest to the hilum are often totally collapsed by the pneumothorax. The image intensity of the hilum and the collapsed parenchyma become nearly indistinguishable. For these reasons, in this study, we used the deformation of the main airways as a surrogate for the hilum deformation. We estimated this airways deformation by means of intensity-based image registration. First, the three main level airways were semi-automatically segmented from the CBCT_{def} image. This segmentation was extended by 5 mm using morphological dilation in order to ensure the inclusion of airway contours (see purple contours on Fig. 6.4). Elastic registration between the rigidly registered CBCT_{inf} and the CBCT_{def} images was then performed using the NCC similarity metric computed over the airways segmentation. The resulting deformation field was used as an estimation of the hilum deformation.

6.7.2 Simulation of the pneumothorax

At the end of exhalation phase of a breathing cycle, no air flows into or out of the lung. At this moment, the internal lung pressure is equal to the external atmospheric pressure. This is explained by a perfect equilibrium between the inward recoil of the alveoli and the outward recoil of the chest wall, which is possible thanks to the negative pressure ($\approx$ -5 cm H_2O relatively to the atmosphere) in the intrapleural space (Levitzky, 2007). As illustrated in Fig. 6.5, the pneumothorax phenomenon may be understood as a disruption of this natural state of equilibrium. Specifically, the rupture of the parietal pleura resulting from surgical thoracic incisions allows the entrance of air into the intrapleural space (or the forceful inflow of gas, if airtight trocars are used). As a result, this pressure in the intrapleural space is no longer negative, which produces a lost of balance between the outward recoil of the chest wall and the inward recoil of the alveoli. Without the negative pressure in the intrapleural space, the lung parenchyma is no longer pulled out by the thoracic cavity, resulting in the shrinking effect observed during a pneumothorax.

We decided to model the pneumothorax deformation using a functional approach. First, the lack of outward recoil from the chest wall was represented by a positive pressure on the lung surface of 5 cm H_2O relative to the atmosphere. This fixed hydrostatic pore pressure, corresponding to the transmural pressure, was applied as Dirichlet boundary conditions on all surface nodes of the FE mesh, for the fluid phase only ($p = 5$ cm H_2O). Second, the inward recoil of the alveoli was modeled by fluid

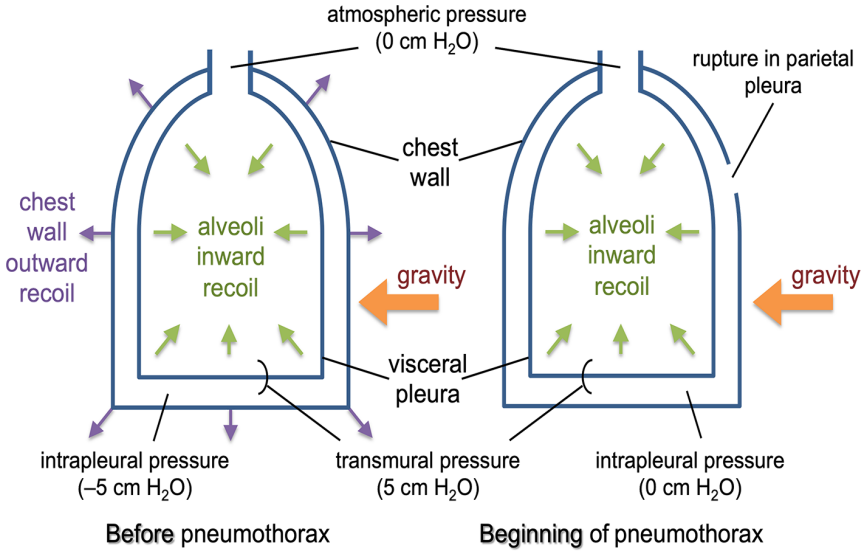

Figure 6.5: Schematic representation of the pneumothorax phenomenon. Left, the state of the lung at end of expiration. The lung is at equilibrium and no airflow is present. Right, the rupture in the parietal pleura makes the intrapleural negative pressure vanish which voids the outward recoil from the chest wall. The transmural pressure and the inward recoil of the alveoli produce the lung deflation observed during a pneumothorax.

evacuation. In the constitutive law of the fluid represented by Eq. (6.9), this evacuation of fluid from the system is modeled by a nonzero value for the evacuation term $\kappa_b(p - p_c)$. Using these two conditions, internal pore pressure gradients were generated in the fluid phase during simulations. These gradients induced volumetric stresses in the porous medium, which resulted in the desired pneumothorax tissue contraction.

Boundary conditions and loads

For the fluid phase, all surface nodes were prescribed with a fixed pressure condition of 5 cm H_2O, whereas remaining nodes were left with the natural no-flux boundary condition. As for the solid phase, nodes inside the main airways were constrained with imposed displacements coming from the estimation of the hilum deformation. Remaining nodes were left with the natural stress-free boundary condition. Finally, a gravitational load was applied to the whole porous medium in the lateral to medial direction (horizontal axis in the CBCT_{def} image).

Contact with the thoracic cage

Frictionless contact conditions were used to simulate the deforming lung sliding along the parietal pleura, *i.e.* the inner surface of the thoracic cavity. This surface corresponds to the outer surface of the initial FE lung mesh, before simulation, that was re-sampled with a coarser mean triangle size of approximately 20 mm. This re-

sampled surface, later referred as the contact surface, was assumed rigid throughout the simulations. Node-to-node frictionless contact conditions were prescribed on all surface nodes of the FE lung model, excluding the nodes with imposed displacement boundary conditions. These contact conditions restrict the deformation of the lung, and can be expressed using the following inequality constraints:

$$g(\boldsymbol{x}) \geq 0 \tag{6.12}$$

$$\sigma_n(\boldsymbol{x}) \leq 0 \tag{6.13}$$

$$g(\boldsymbol{x})\,\sigma_n(\boldsymbol{x}) = 0 \tag{6.14}$$

where $g(\boldsymbol{x})$ is the gap distance between the contact surface and the deformable surface at the material point $\boldsymbol{x}$; and $\sigma_n(\boldsymbol{x})$ is the applied normal contact force at the material point $\boldsymbol{x}$.

The gap distance is calculated as $g(\boldsymbol{x}) = g_0(\boldsymbol{x}) + \boldsymbol{u}(\boldsymbol{x}) \cdot \boldsymbol{v}$, where $\boldsymbol{v}$ is the inward pointing normal of the contact surface, $g_0(\boldsymbol{x})$ is the initial gap distance before deformation, and $\boldsymbol{u}(\boldsymbol{x})$ is the displacement vector. The distance $g(\boldsymbol{x})$ is thus negative when there is penetration of the deformable surface into the contact surface. The term $\sigma_n(\boldsymbol{x})$ is a shorthand notation for $(\boldsymbol{\sigma}(\boldsymbol{x})\,\boldsymbol{n}) \cdot \boldsymbol{n}$, the projection of the Cauchy traction at the material point $\boldsymbol{x}$ onto the outward pointing normal $\boldsymbol{n}$.

The Eqs. (6.12) to (6.14) correspond to Signorini's conditions. The relation expressed in Eq. (6.12) represents a condition of impenetrability, while Eq. (6.13) states that the contact forces must always be compressive. The complementary condition in Eq. (6.14) allows contact forces to be generated only during contact (*i.e.* $g(\boldsymbol{x}) = 0$).

Contact with the upward moving diaphragm

During surgery, the use of curare (a muscle relaxant) relieves tension in the diaphragm that then deforms under the pressure from abdominal organs. This deformation is transferred to the lung parenchyma which moves upwards towards the apex. Although this phenomenon is clinically observed for all patients, those with higher indices of obesity undergo larger diaphragm displacement.

During intraoperative imaging, the position of the diaphragm is not always in the FOV of the CBCT images.We thus introduced an additional contact surface representing the diaphragm that can push the lung model upwards during the FE simulations. This diaphragm contact surface was initialized as the lower surface of the initial FE lung mesh, before simulation, that was re-sampled with a coarser mean triangle size of approximately 20 mm. Since the position of this diaphragm surface was unknown in the intraoperative CBCT images, we defined its position with an additional parameter d_{diaph}. The surface is allowed to move towards the apex along the principal axis of the lung's geometry, which was computed using Principal Component Anal-

Table 6.1: Material properties and their values during pneumothorax simulations. The last three parameters are patient and intervention specific and varied within the reported range during an optimization process.

Parameter	Value	Units
E	550	Pa
ν	0.35	-
α	1.0	-
ρ_s	700	kg / m^3
ρ_f	1.205	kg / m^3
κ	2.75×10^{-17}	m^2
μ_f	1.83×10^{-5}	Pa·s
p_c	0	Pa
$\boldsymbol{g}$	9.81	m / s^2
ϕ	$[0.00\ ,\ 0.93]$	-
κ_b	$[1.83 \times 10^{-19}\ ,\ 1.83 \times 10^{-9}]$	1 / Pa·s
d_{diaph}	$[15 \times 10^{-3}\ ,\ 40 \times 10^{-3}]$	m

ysis (PCA) on the mesh nodes. d_{diaph} represent the distance, along the vertical axis, between the current diaphragm position and its initial position. This displacement was included in the parameters to be optimized by our inverse problem formulation, with a minimum value of 15 mm defined empirically by clinical observation.

Material properties

The lung tissue was considered as an isotropic and homogeneous poroelastic continuum. An important characteristic of our pneumothorax modeling approach is the allowance of air evacuation. We hypothesized that during pneumothorax air exchanges happen at the level of small bronchi, resulting in air being transported out of the porous medium through the airways. These exchange effects were approximated by an organ-wide distributed term $\kappa_b(p - p_c)$ that allowed the simulation of air evacuation (Eq. (6.9)). In addition, we hypothesized that tissue porosity may change from patient to patient according to his/her response to general anesthesia and mechanical ventilation, and the amount of atelectasis. The values for tissue porosity and intra-bronchi permeability are unknown for every particular surgery, and were then included in the parameters to be optimized by our inverse problem formulation. For the remaining material properties, values and ranges reported in previous studies were chosen (Alvarez et al., 2019a; Seyfi Noferest et al., 2018; Sun et al., 2014). Table 6.1 collects the values used during the pneumothorax simulations.

6.7.3 Inverse problem formulation

The amount of pneumothorax deformation observed during a VATS intervention is patient and intervention dependent. This difference in deformation can be translated

as different values for specific model parameters. Since these values are unknown in advance, we proposed to estimate them using an inverse problem formulation. The goal was to simulate several pneumothorax deformations and to optimize the parameters until the model best reproduces the observed intraoperative deformation.

The trust-region non-linear optimization method was used to solve the inverse problem. The cost function was defined as a surface-to-surface distance between the lung deflated surface, segmented from the CBCT$_{def}$ image (*c.f.* Sec. 6.7.1), and the simulated lung deformed surface. Formally, we solved the following problem:

$$\arg\min_{\boldsymbol{\theta}} \ \Omega(\boldsymbol{\theta}) = \frac{1}{N}\sum_{i=1}^{N} \|\boldsymbol{p}_i - \boldsymbol{q}_i(\boldsymbol{\theta})\|^2 \tag{6.15}$$

where $\boldsymbol{\theta}$ is a set of tissue parameters and Ω the surface-to-surface distance. N is the total number of nodes in the target surface segmented in CBCT$_{def}$, $\boldsymbol{p}_i$ is an indexed node of that surface and $\boldsymbol{q}_i(\boldsymbol{\theta})$ is its corresponding closest node on the surface of the deformed FE mesh.

Since the optimization may be highly sensitive to initialization, we repeated the process three times with a different initialization parameter vector $\boldsymbol{\theta}_0$. Values were each time randomly generated from realizations of uniform distributions with empirically-defined ranges (see Table 6.1). In this study all three simulations were always consistent, and only the first simulation results were reported in the results section.

6.7.4 Nodule localization

Tissue parameters ($\boldsymbol{\theta}$) that solve the optimization problem defined in Eq. (6.15) produce the lung deformation that more closely approaches the intraoperative observed lung surface. The associated deformation field is defined on a spatial domain bounded by the FE mesh, and can be computed at any point by means of barycentric interpolation. This interpolation was used to warp the preoperative CT, which provided an estimation of the nodule position after pneumothorax.

6.8 Results

This section presents and comments the quantitative and qualitative findings from this study. The clinical dataset used for validation is first described, followed by the evaluation of the deformation estimated after the change of pose (*Phase 1*) and pneumothorax (*Phase 2*).

Table 6.2: Study characteristics for each clinical case. The pneumothorax was controlled following two techniques: mechanical control of air inflow into the lung through the intubation tube; or pressurized insufflation of CO_2 into the thoracic cage through airtight trocars. The number of validation landmarks depends on the visibility of lung structures in the images.

Case	Operated lung	Pneumothorax	# landmarks
1	Left	Air	27
2	Right	Air	40
3	Right	Air	46
4	Right	Air	23
5	Left	CO_2	23

6.8.1 Clinical dataset

Our retrospective study included five patients with single pulmonary nodules detected by CT examination. All were enrolled for a VATS wedge resection guided by intraoperative CBCT imaging. The experimental protocol was based on the work introduced by Rouzé et al. (2016). This protocol was extended to include two CBCT acquisitions instead of one, before and after induction of the pneumothorax. This study was realized at Rennes University Hospital (France) under the approval of the local ethics committee (2016-A01353-48 35RC16_9838). All patients signed an informed consent prior to the procedure.

Preoperative CT is the standard diagnostic image and was acquired with the patient in supine position. Both CBCT images were acquired with a C-arm system (Artis Zeego, Siemens Healthcare, Germany) after general anesthesia, with the patient in lateral decubitus position. The first CBCT image ($CBCT_{inf}$) was acquired just before the creation of surgical incisions, with the target lung still inflated. The second CBCT image ($CBCT_{def}$) was acquired after pneumothorax, with the target lung deflated. The amount of lung deflation had to be controlled to provide enough space for maneuvering during surgery, while avoiding a total collapse of the lung.

All patients were intubated with a double lumen tube (Bronchocath, Mansfield, MA, USA) which allows independent ventilation of the operated and non-operated lungs. For the image acquisitions, lung deflation was controlled using two mechanisms. For patients 1 to 4, air flew naturally into the thoracic cavity through the thoracic incisions. The lung deflation was controlled by insufflating oxygen into the operated lung through the lumen of the tube. For patient 5, airtight trocars were used and CO_2 was insufflated into the thoracic cavity. The lung deflation was controlled by modulating the CO_2 pressure.

For validation purposes, paired anatomical landmarks were manually placed on the CT, $CBCT_{inf}$and $CBCT_{def}$ images. This was performed by a single rater, the expert thoracic surgeon who performed all the VATS interventions. A total of 23 to 45 land-

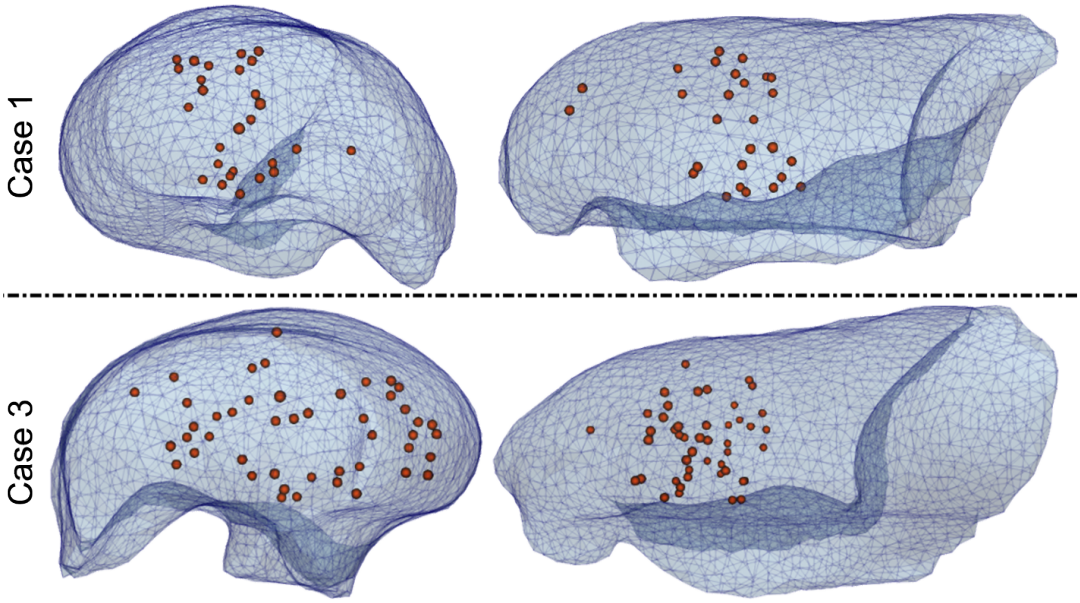

Figure 6.6: Spatial distribution of anatomical landmarks within the lung FE mesh reconstructed from the preoperative CT image.

marks were placed for each patient. These landmarks were distributed among vessel and airway bifurcations in the most complex image, *i.e.* the CBCT$_{def}$ image, and then were localized in the CBCT$_{inf}$ and CT images. The validation was based on Target Registration Errors (TRE) computed as the distance between corresponding landmarks after deformation compensation. Differences among TRE distributions were tested with the non parametric Wilcoxon signed rank test, with a confidence level of 5%. The study characteristics for each clinical case are detailed in Table 6.2.

Landmark positions are illustrated in two representative cases in Fig. 6.6. Since these anatomical landmarks are used for validation, their positions should be distributed inside the lung parenchyma as homogeneously as possible. However, the restrictions of the image quality were difficult to surpass and reduced the spatial distribution of these landmarks in some cases. Notably, structures of medium-size and below that are clearly visible in the preoperative CT image were impossible to locate in the CBCT$_{def}$ image. It is clear from Fig. 6.6 that validation can only be performed for regions of the lung inside the FOV of the CBCT scans. Notably, regions of the apex and diaphragm do not contain any landmarks.

6.8.2 Results: Phase 1, estimation of the change of pose

The change of pose deformation estimation relies heavily on the computation of a deformation field through intensity based image registration. The accuracy of this deformation field was evaluated with TRE distributions computed from the landmarks of the preoperative CT and intraoperative CBCT$_{inf}$ images. Figure 6.7 depicts the obtained TRE distributions for all clinical cases. First, rigid registration provided

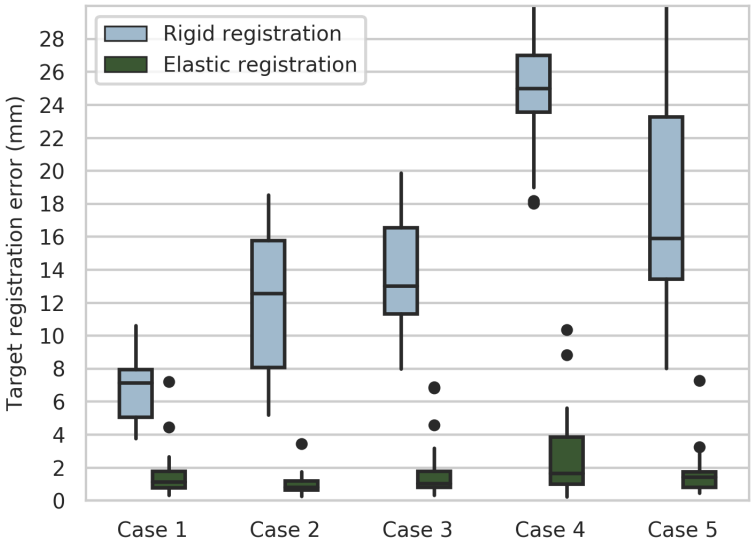

Figure 6.7: TRE distributions for rigid and elastic registration between the preoperative CT and intraoperative CBCT$_{inf}$ (*Phase 1*, change of pose).

an insight on the amount of deformation induced by the change of patient pose. We could observe large deformations, with the main structures in major miss-alignment. We obtained mean ($\pm$ standard deviation) TREs of 6.8 mm ($\pm$1.9 mm), 12.1 mm ($\pm$4.1 mm), 13.5 mm ($\pm$3.2 mm), 25.8 mm ($\pm$5.0 mm), and 18.0 mm ($\pm$7.1 mm) for cases 1 to 5, respectively. These errors are even larger than those reported for respiratory motion in the lung registration literature (*e.g.* a mean error of 8.4 mm reported by Delmon et al. (2013)). After elastic registration, TREs were significantly reduced to mean values of 1.5 mm ($\pm$1.4 mm), 1.0 mm ($\pm$0.5 mm), 1.6 mm ($\pm$1.4 mm), 2.7 mm ($\pm$2.7 mm), 1.6 mm ($\pm$1.4 mm), respectively. This registration accuracy is comparable to the one reported in studies for lung breathing motion compensation (Murphy et al., 2011).

Fig. 6.8 depicts the results obtained after rigid and elastic registration. Coronal slices of the registered CT and intraoperative CBCT$_{inf}$ images were superposed to show the quality of registration on two representative clinical cases. It can be observed that internal structures were within reasonable alignment, as suggested by the obtained TRE distributions. Also, lung contours were well aligned thanks to the masking approach used during registration. However, we found poorly-registered regions near the rim of the CBCT$_{inf}$ images, where the lung is incomplete because of the limited FOV of the scanner and where reconstruction artefacts were present (*e.g.* Case 1). Furthermore, localized atelectasis also reduced the registration quality, since voxel intensities drastically differed between images in the affected regions (*e.g.* Case 4). These registration errors may be under-represented in the TRE distributions of Fig. 6.7 given the difficult landmark placement in these regions. However, we consider that the achieved registration accuracy is sufficient for the purpose of estimating the com-

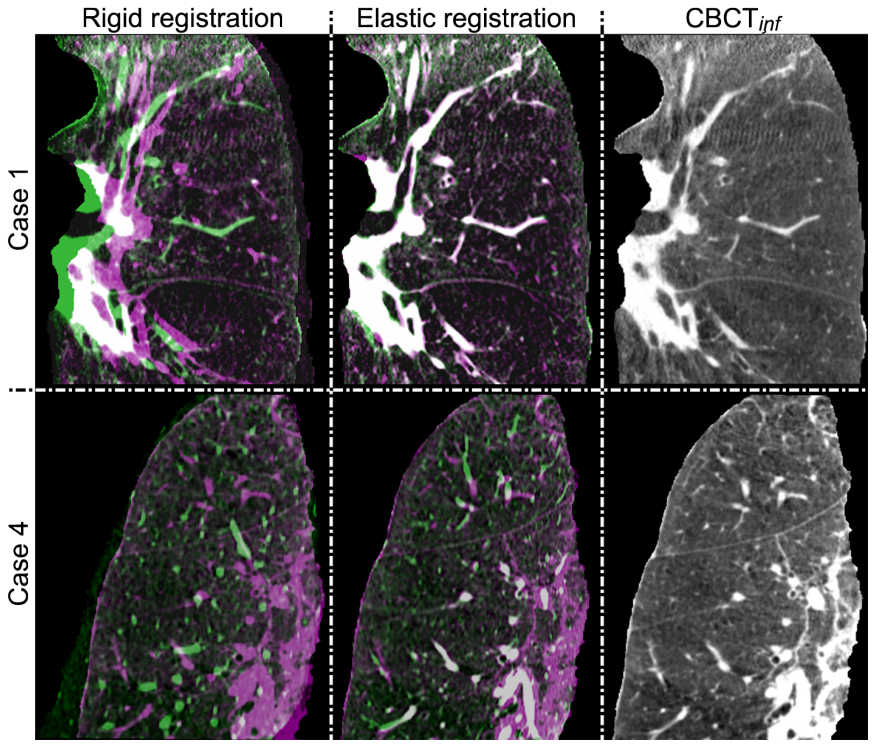

Figure 6.8: Qualitative results of rigid and elastic registration between the preoperative CT (green) and intraoperative CBCT$_{inf}$ (magenta) images. Coronal slices are shown for two representative cases. The target CBCT$_{inf}$ image in gray-scale is shown in the far right column.

plete lung geometry after the change of pose.

Due to the lack of landmarks outside the FOV of the CBCT images, it was not possible to directly evaluate the quality of the complete lung geometry after FEM extrapolation. Nonetheless, the benefit of this extrapolation approach was assessed in comparison to a baseline rigid registration approach, and the results are presented later in Sec. 6.8.4.

6.8.3 Results: Phase 2, estimation of the pneumothorax

The solution to the inverse problem formulation was used to warp the CBCT$_{inf}$ landmarks with barycentric interpolation. The TRE distributions were computed using these deformed landmarks and the ground truth CBCT$_{def}$ landmarks. To illustrate our contribution, the errors that would be obtained without a deformation compensation method were also estimated in two ways. First, TREs between the rigidly registered CT and CBCT$_{def}$ images were computed. This corresponds to the errors expected when the CBCT$_{inf}$ image is not available and only a rigid transformation of the preoperative data to the intraoperative setting is possible. Second, TREs were computed between the rigidly registered CBCT$_{inf}$ and CBCT$_{def}$ images. These would be the expected errors when estimating the nodule position directly from the CBCT$_{inf}$

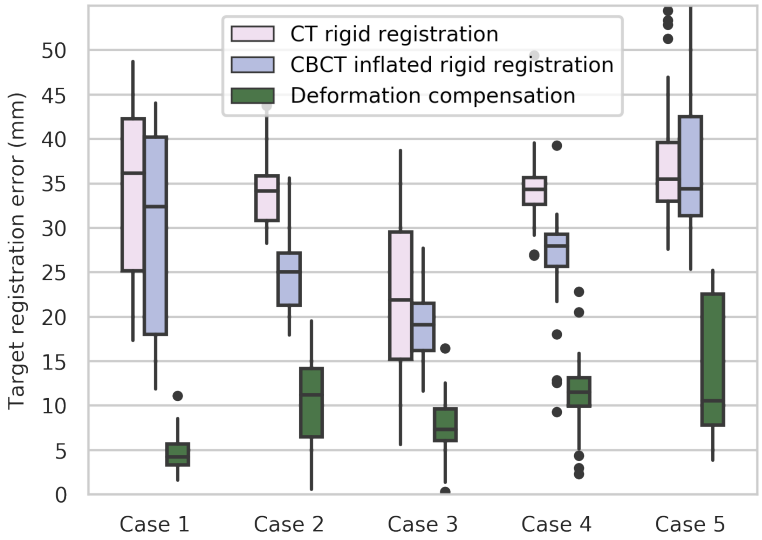

Figure 6.9: TRE distributions for our complete deformation compensation framework, alongside the errors expected without deformation compensation. These latter distributions correspond to rigidly registering the preoperative CT with the CBCT_{inf} and CBCT_{def} images, respectively.

image, without compensating for the pneumothorax deformation. These TRE distributions are presented for all clinical cases in Fig. 6.9.

Figure 6.9 first puts in evidence the large lung deformation that occurs during a VATS procedure. After rigid registration of the preoperative CT and intraoperative CBCT_{def} images, we obtained mean TREs of 33.8 mm ($\pm$10.1 mm), 34.1 mm ($\pm$3.7 mm), 22.0 mm ($\pm$8.9 mm), 34.4 mm ($\pm$4.6 mm), and 37.9 mm ($\pm$8.2 mm) for cases 1 to 5, respectively. Likewise, mean TREs after rigid registration of the CBCT_{inf} and CBCT_{def} images were 28.7 mm ($\pm$11.6 mm), 24.6 mm ($\pm$4.0 mm), 19.5 mm ($\pm$4.0 mm), 25.9 mm ($\pm$6.8 mm), and 37.7 mm ($\pm$8.8 mm). This deformation is considerably larger than both breathing and change of pose deformations. Except for Case 5, larger deformations were obtained from rigidly registering the preoperative CT image instead of the CBCT_{inf} image (maximum $p = .018$). This result corroborates that the change of patient pose does have an influence in lung deformation during VATS. Also, it is clear from Fig. 6.9 that our deformation compensation framework is able to account for a considerable amount of this intraoperative deformation. Indeed, mean TREs were reduced to 4.9 mm ($\pm$2.2 mm), 10.3 mm ($\pm$5.2 mm), 7.5 mm ($\pm$3.3 mm), 11.2 mm ($\pm$4.9 mm), and 14.3 mm ($\pm$7.5 mm), respectively, which corresponds to a correction of 85%, 70%, 68%, 68%, and 63% (71% in mean) of the initial error without compensation. Specifically, the nodule localization errors were 8.4 mm, 13.4 mm, 9.9 mm, 11.6 mm and 10.2 mm, respectively.

Figure 6.10 illustrates quantitative results for two clinical cases. It can be observed that the surfaces of the deformed FE meshes were close to the intraoperative de-

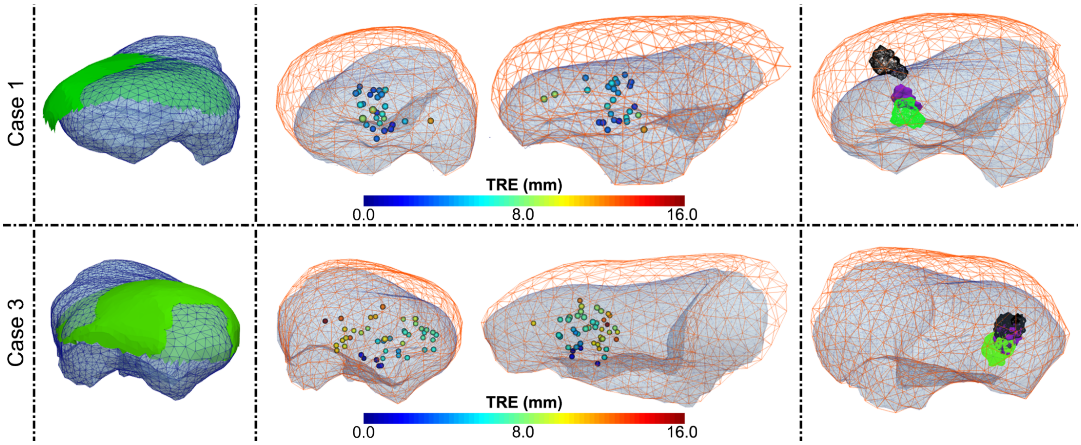

Figure 6.10: Qualitative results of our deformation compensation framework for two clinical cases. Left: final deformed lung FE mesh superposed over the extracted deflated lung surface (in green). Middle: Registered landmark errors, deformed FE lung mesh and thoracic cage contact surface. Right: Initial nodule position (wireframe, black surface), ground truth nodule position (wireframe, green surface) and predicted nodule position (solid, purple surface).

flated surfaces without fitting them perfectly. This is a consequence of the chosen simplified approach to model the complex lung deformation. For instance, the constant fluid pressure boundary conditions generated highly symmetrical and homogeneous lung deformation, given that the contribution of the fluid medium to total stress is purely volumetric. This symmetry was only constrained by the shape of the estimated lung geometry (*i.e.* the deformable FE mesh and contact surfaces) and the direction of gravity, which may be oversimplifying. For Case 2, lobes also deform very independently from each other, which is currently not taken into account for modeling pneumothorax deformation. Finally, it can also be observed in Fig. 6.10 that the landmarks with the lowest registration errors were those closest to the hilum. These better results in the hilum area can be explained by the hilum deformation estimation step, which was based on intensity-based registration of the main airways.

The tissue parameters obtained from our inverse problem formulation are listed in Table 6.3. The optimization process resulted in values for the intrabronchi permeability (κ_b) and tissue porosity (ϕ) that were consistent with a previous study (Alvarez et al., 2019a). As for the diaphragm upward displacement (d_{diaph}), we could observe that besides Case 1, a value of 15 mm was found for all clinical cases. This value corresponds to the lower bound of the range specified during optimization, meaning that a higher diaphragm displacement only increased the distance from the FE deformed mesh and the target intraoperative deflated lung surface in these clinical cases.

The complete deformation compensation framework allows the warping of the preoperative CT image with the FE deformed meshes issued from *Phase 1* and *Phase 2*.

Table 6.3: Tissue parameters estimated from our inverse problem optimization approach: intrabronchi permeability (κ_b), tissue porosity (ϕ), and diaphragm upward displacement (d_{diaph}).

Case	κ_b (1 / Pa s)	ϕ (unitless)	d_{diaph} (m)
1	14.44×10^{-9}	0.56	20.41×10^{-3}
2	95.31×10^{-9}	0.79	15.00×10^{-3}
3	2.61×10^{-9}	0.82	15.00×10^{-3}
4	1.23×10^{-9}	0.37	15.00×10^{-3}
5	37.29×10^{-9}	0.64	15.00×10^{-3}

This warped CT image is shown in Fig. 6.11 along with the preoperative CT, CBCT$_{inf}$ and CBCT$_{def}$ images, for two representative cases (results for all cases are available in the online supplementary materials [1].). Color contours are used to illustrate the changing shape of the FE lung mesh through the deformation compensation stages: before change of pose (cyan), after change of pose (orange), and after change of pose and pneumothorax (purple). It can be observed that the diaphragm is completely out of the FOV of both CBCT images for Case 1, and is only barely visible in the CBCT$_{def}$ image for Case 2. Also, the cranio-caudal misalignment between both CBCTs can be very important, as seen for Case 2, reducing significantly the overlap between the intraoperative images. In terms of deformation compensation, it can be observed for Case 1 that the estimated deflated lung surface is well aligned with the CBCT$_{def}$ deflated surface. Also, the cranio-caudal height of the oblique fissure fits well with its actual position. These results are consistent with the mean TRE measured below 5 mm. For Case 2, however, the estimated deformation is clearly poorer. In this highly complex case, the lung lobes deformed independently during pneumothorax, inducing the opening of both fissures and a highly heterogeneous lung deflation. Furthermore, atelectasis was significant in the lower lobe, causing it to deflate more than the other two lobes. While the mean TRE is reduced from 34 mm to 10 mm, the estimated deformed lung is too regular in comparison with its actual shape. While our compensation framework seems promising for several cases, further investigations will be necessary for such complex deformations.

6.8.4 Variants of the method

The relevance of the main components of our deformation compensation framework was investigated using variant implementations presented in this section.

Influence of the change of pose and hilum estimation

Three variants of our method were implemented to assess the influence of the change of pose and hilum deformation estimation processing steps:

1. The supplementary materials are included in the second part of this chapter, under the section Additional qualitative results

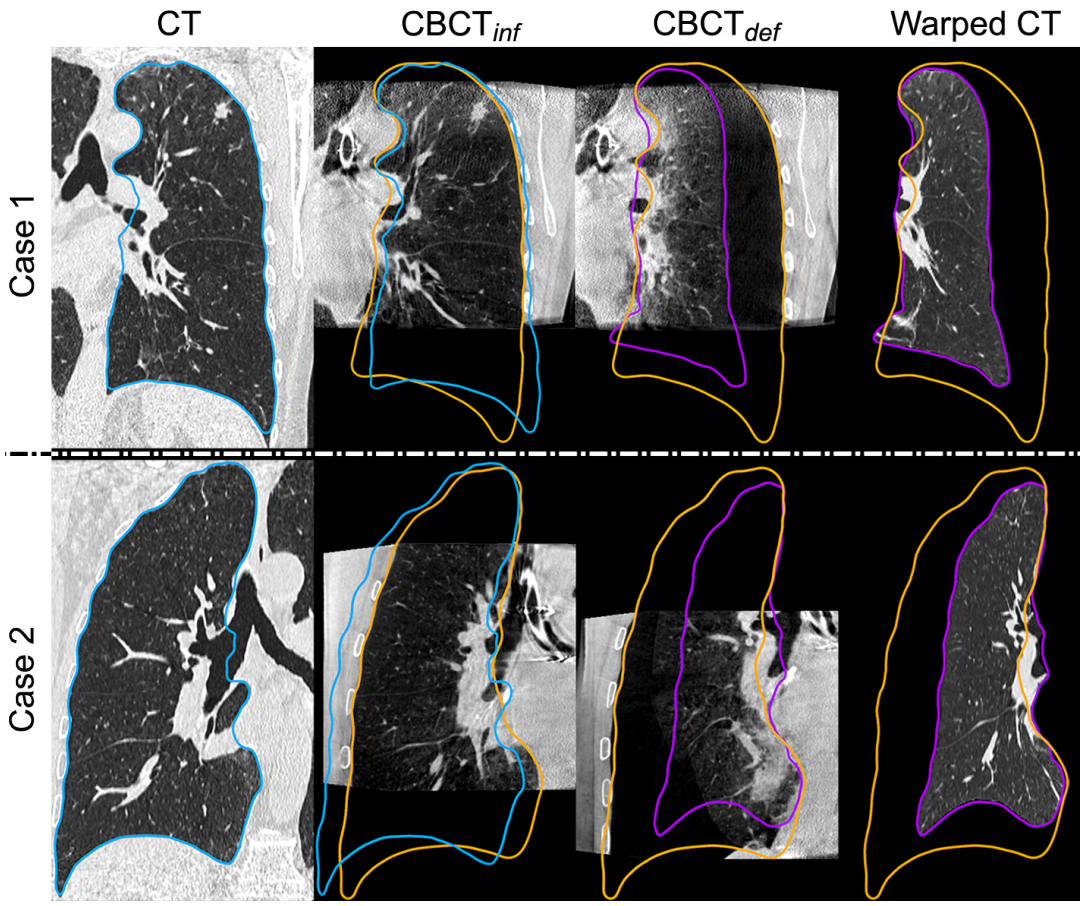

Figure 6.11: Qualitative results of our deformation compensation framework for two representative cases. The CT and CBCT$_{inf}$ images are rigidly registered to the CBCT$_{def}$ image. Coronal slices of exactly the same region of interest are shown for all images. The color contours illustrate the position of the FE mesh at the beginning of *Phase 1* (cyan) and *Phase 2* (orange), as well as at the end of *Phase 2* (purple).

(A) *No change of pose*: neither the change of pose deformation nor the hilum deformation between the CBCT$_{inf}$ and CBCT$_{def}$ images were taken into account. The preoperative CT image was simply rigidly registered to the CBCT$_{def}$ image using the spine as the reference, as in Sec. 6.6.1. The transformed lung segmentation was used to generate the lung FE mesh and to define contact surfaces. Boundary conditions were prescribed as in Sec. 6.7.2, with the exception of the imposed displacements in the airway inlet that were replaced with fixed boundary conditions ($\boldsymbol{u} = \mathbf{0}$).

(B) *No hilum deformation*: the change of pose deformation was taken into account but the hilum deformation between both CBCT images was not compensated. Since no deformation field mapping the airways before and after pneumothorax was available, fixed boundary conditions were applied at the airway inlet ($\boldsymbol{u} = \mathbf{0}$). The remaining boundary conditions, intraoperative geometry and con-

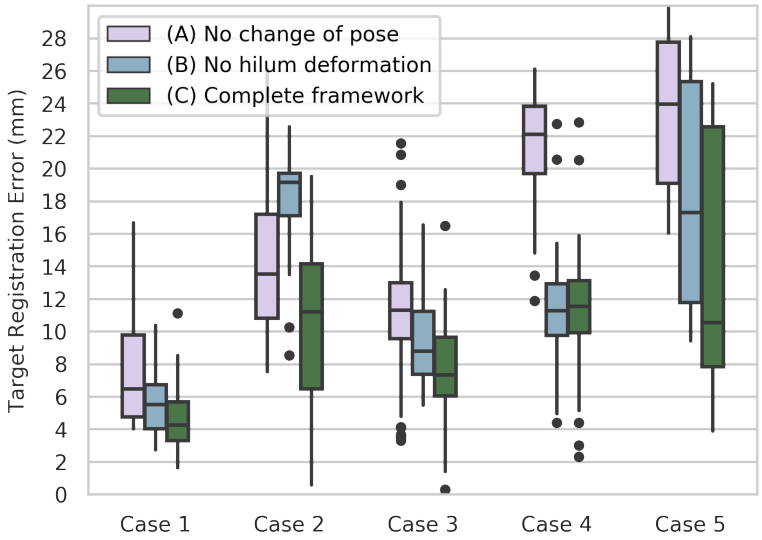

Figure 6.12: TRE distributions for three variants of the proposed lung deformation compensation method.

tact conditions were applied as described in Sec. 6.7.2.

(C) *Complete framework*: This variant corresponds to the implementation of all the methods described in Sec. 6.7.2.

The TRE distributions of each variant are presented in Fig. 6.12. With the exception of Case 2, a significant improvement can be observed of variant (B) over (A) across cases (maximum $p = .006$). Likewise, variant (C) provided better results than variant (B) (maximum $p = .019$), except for Case 4. These results suggest that all processing steps of the complete deformation compensation framework are important. Even though the amount of change of pose and hilum deformation varies among cases, taking these deformations into account allows for a better final estimation.

Influence of the moving diaphragm

Another important element of our deformation compensation framework is the modeling of the diaphragm movement. Its influence was evaluated by comparing the results of the complete framework with and without nullifying the diaphragm movement, *i.e.* fixing $d_{diaph} = 0$ mm. The results are shown in Fig. 6.13. Modeling the diaphragm upward movement significantly reduced TREs for Cases 1, 3, and 4 (maximum $p < .001$). However, the estimation accuracy remained unchanged for Case 5 and actually decreased for Case 2 ($p = .002$). For this complex case, the estimated diaphragm position after the change of pose compensation roughly matched the actual diaphragm position barely visible in the CBCT$_{def}$ image (see Fig. 6.11). Therefore, any positive displacement of the diaphragm (d_{diaph}) would worsen estimation accuracy.

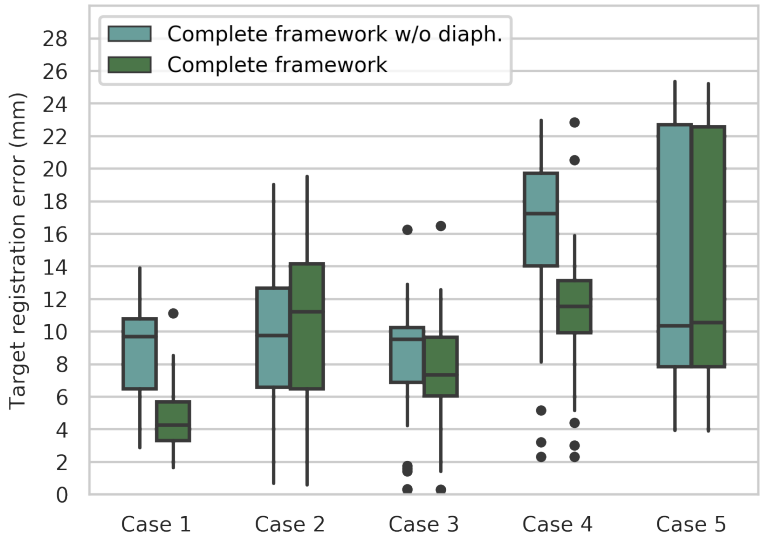

Figure 6.13: TRE distributions for our deformation compensation framework with and without including the upward diaphragm movement.

It should be noted that for all clinical cases except Case 1, the displacement d_{diaph} of the optimal solution was 15 mm, namely the minimum value allowed during the optimization process. However, an observation of the predicted landmark positions with respect to the ground truth landmarks suggests that deformation compensation errors may be partially explained by a miss-prediction of this diaphragm movement. An explanation could reside in the antagonism between a diaphragm upward movement and the cost function of the optimization problem: moving the diaphragm upwards tends to enlarge the lung outwards, in the opposite direction of lung deflation, therefore increasing the surface-to-surface cost function distance.

While the effects of our diaphragm model are still limited in several cases, our results suggest that accounting for the diaphragm movement, even empirically, could allow for a better estimation of the intraoperative deflated lung shape.

6.9 Discussion

Advantages, limits, and perspectives of the main components of the proposed method are discussed in this section.

6.9.1 Hybrid approach to deformation estimation

In this study, we used intensity-based image registration to estimate displacement boundary conditions for FEM lung simulations of change of pose and pneumothorax deformation. This hybrid approach was crucial for the estimation of complex lung deformation that would have been more difficult, if not impossible, using purely intensity-based or FEM strategies. For *Phase 1*, we estimated the change of pose defor-

mation between the preoperative CT and the intraoperative CBCT_{inf} images with an algorithm that accounts for sliding at the lung interface (Wu et al., 2008). We found the magnitude of this deformation to be consistent with values reported in a previous study (Alvarez et al., 2018). For *Phase 2*, the hilum deformation was approximated by registering the main airways of the intraoperative CBCT_{inf} and CBCT_{def} images. Final results suggest that even though approximative, this approach provides better estimations than alternatives not taking into account hilum deformation. To go further, it will be necessary to better capture the non-homogeneous variations of the hilum deformation. This is quite challenging due to the occurrence, to date unpredictable, of very localized atelectasis after pneumothorax. This collapsing of the airways results in severe intensity and textural discrepancies of the CBCT images before and after pneumothorax, which are difficult to cope with using traditional segmentation and registration methods. We believe, however, that these challenges may be overcome thanks to the efforts recently put forward by the community, with registration algorithms not requiring prior segmentation (Heinrich et al., 2016) and/or relying on salient keypoints rather than image intensity (Ruhaak et al., 2017). Incorporating such approaches into our framework could lead to substantial improvements that will be studied in future work.

6.9.2 Modeling choices

For the pneumothorax simulations, we used a poroelastic model of the lung with allowance for air evacuation. This approach follows the principle of effective stress that decomposes the total stress into fluid and solid stresses. This principle permits the macro-scale simulation of airflow-parenchyma interaction in a cost-effective manner. We hypothesized that the solid medium behaves as a homogeneous, linearly-elastic material undergoing small deformations. This assumption was supported by noting that pneumothorax deformation during our simulations was mainly caused by the stress generated from the fluid phase. Also, this simplified model is in principle computationally efficient, which would be important in the future to comply with the time restrictions of clinical practice. However, despite promising preliminary results, the lung deformation can be underestimated, for which several improvements can be investigated. For instance, we envision other constitutive laws for the solid medium, such as the Saint Venant-Kirchhoff model that does not linearize the strain tensor to allow for large displacements (Seyfi Noferest et al., 2018), or more complex hyperelastic non-linear stress-strain relations (Berger et al., 2015). We will also assess the use of heterogeneous material properties estimated from measured lung deformation (Hasse et al., 2018).

In parallel to more adequate constitutive laws and tissue parameters, a major improvement would be expected with a multiple-lobes lung model as opposed to a single-structure lung model. As observed for Case 2, lobes can slide against each

other, the fissures can open widely, or a combination of the two. Modeling such effects will be challenging, as not only they are technically difficult but also very unpredictable.

6.9.3 Inverse formulation approach

The inverse problem formulation based on the poroelastic lung model allowed the compensation of patient-specific and intervention-specific pneumothorax deformation. This was achieved by fitting the deformable lung model to the observed intraoperative surface of the deflated lung, changing tissue porosity (ϕ) and intrabronchi permeability (κ_b) parameters, as well as simulating the upward movement of the diaphragm (d_{diaph}). It should be acknowledged that our inverse problem formulation did not take into account internal lung structural information, which had a clear impact on the correct estimation of the upward moving diaphragm, and possibly the complete lung parenchyma. With improved processing of the CBCT images, it should be possible to include internal lung structures such as vessels (Cazoulat et al., 2016), salient keypoints (Ruhaak et al., 2017), or even the lobe boundaries, in the inverse problem formulation.

Finally, the inverse problem formulation currently minimizes the surface-to-surface distance between the deformable lung model and the intraoperative data in a least-squares sense. Since the proposed model has few degrees of freedom, the deformed lung surface does not exactly fit the intraoperative data. An alternative to this approach would be to use Lagrange multipliers to constrain the deformation so that surface nodes of the FE mesh fit local surface data (Morin et al., 2017).

6.9.4 Diaphragm movement

Clinically, it is known that the diaphragm tends to move upwards due to the surgical setup. This phenomenon was consistently observed on all cases, based on inner-lung landmark measurements. Therefore, a functional approach to model the diaphragm movement was introduced, with the d_{diaph} parameter as part of the optimization process. However, as shown in Sec. 6.8.4, a meaningful estimation of diaphragm movement could be obtained for one case only. Although several factors may be affecting this issue, we believe the definition of the cost function (Eq. (6.15)) to be among the most important. Indeed, currently, it relies on surface data only, which may not be well suited to compensate for longitudinal deformation. Improvements could consist in extracting the diaphragm surface when it is partially visible in the CBCT images (*e.g.* cases 4 and 2), and to include sub-surface information in the computation of the cost function, as mentioned above.

6.9.5 Towards clinical practice: practicability and accuracy

Since the aim of this study was to evaluate the capacity to compensate for lung deformation during VATS, we did not primarily focused on the clinical practicality. Therefore, several processes required limited manual interactions: the initialization of registration or segmentation algorithms, the refinement of segmentation masks, and the extraction of the CBCT_{def} deflated lung surface. However, we are confident that most of these interactions can be avoided with dedicated image processing methods, which we will investigate. Another important factor will be the computational efficiency, especially when considering the methodological improvements previously discussed. It will become necessary to find an equilibrium between accuracy and efficiency, for which deformation atlas (Sun et al., 2014) or learning-based FEM (Mendizabal et al., 2020) approaches will be investigated.

Finally, no standard criteria stands to date regarding the required accuracy and time for an intraoperative nodule localization algorithm. While current results are already significant, our long term objective will be to consistently obtain registration errors under 5 mm, and to limit all intraoperative processes under 15 minutes. These objectives were designed by the clinical investigator of this study.

6.10 Conclusion

To our best knowledge, this is the first study to propose an intraoperative markerless lung nodule localization framework for VATS, which relies on a hybrid method combining intraoperative CBCT imaging, intensity-based image registration, and biomechanical modeling techniques. We proposed to decouple the very challenging problem of intraoperative deformation estimation into two more tractable sub-problems: estimating the change of pose deformation (*Phase 1*) and then estimating the pneumothorax deformation (*Phase 2*). We were able to demonstrate the feasibility of our deformation compensation framework on 5 retrospective clinical cases of patients who underwent a VATS intervention. Average initial errors in the range of 22 to 38 mm were reduced to the range of 4 to 14 mm, which corresponds to a correction of 63 to 85% of the error without compensation (71% in mean).

To improve the methods towards errors consistently under the 5 mm objective, future works will be mostly focused on allowing for lobes separation within the model and taking into account sub-surface lung information to drive the simulations. Another challenge will be to acquire a single CBCT scan instead of two (only CBCT_{def} after lung deflation) to simplify the procedure and limit the radiation dose. Finally, our overall objective aims at overlaying the simulated deformed lung and the nodule position over the CBCT image, and ultimately in real time in the endoscopic view. By removing the need for a preoperative nodule marking localization procedures and its

associated risks, and increasing the resection accuracy, the proposed method could significantly benefit the clinical practice in thoracoscopic surgery.

Acknowledgements

This work was supported by the *Région Bretagne* through its *Allocations de Recherche Doctorale* (ARED) framework; the French National Research Agency (ANR) through the frameworks *Investissements d'Avenir Labex CAMI* (ANR-11-LABX-0004) and *Infrastructure d'Avenir en Biologie et Santé* (ANR-11-INBS-0006); and the National Institutes of Health - NINDS grant R01NS049251.

Additional results and discussion

In the first part of this chapter, a hybrid registration framework for lung deformation compensation during VATS was presented, along with an extensive discussion of the methodology and the results. This second part completes the presentation of qualitative results for the entire clinical dataset, and introduces further discussion elements to compare the study presented in this chapter to the other studies carried out in this thesis.

Additional qualitative results

This section presents qualitative results in the same form used for Fig. 6.11, but for the complete dataset. These results correspond to the supplementary materials submitted with the journal article presented above. The following five figures illustrate coronal slices of the preoperative CT, CBCT$_{inf}$ and CBCT$_{def}$ images, as well as the warped CT after deformation compensation, for the five clinical cases. The CT and CBCT$_{inf}$ images are rigidly registered to the CBCT$_{def}$ image, and the coronal slices are extracted from exactly the same region across all images of a same clinical case. Color contours show the changing shape of the FE lung mesh through the deformation compensation stages: before change of pose (cyan), after change of pose (orange), and after change of pose and pneumothorax (purple).

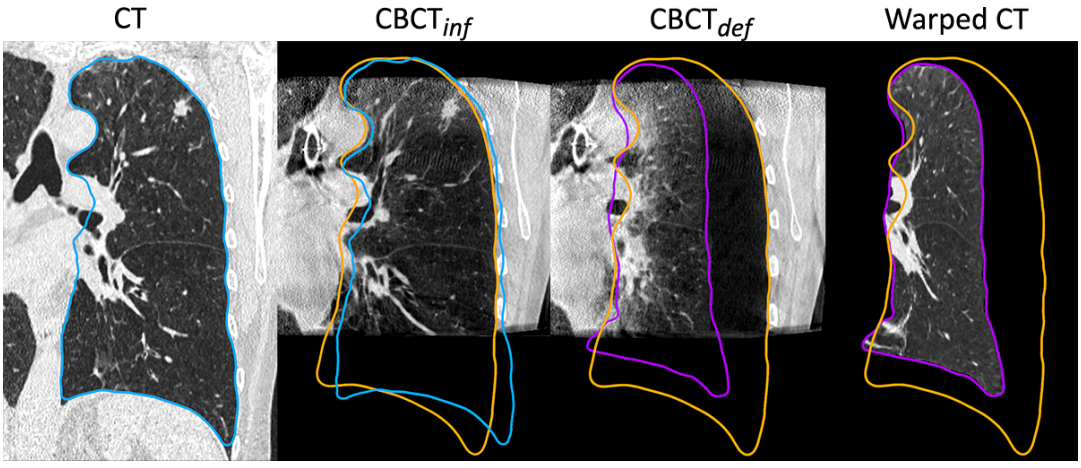

Figure 6.14: Qualitative result of the proposed deformation compensation method in Case 1.

As observed in the Figs. 6.14 to 6.18, the lung deformation varies among clinical cases, and so do the qualitative results. Table 6.4 lists some observations from these qualitative results for each clinical case.

Table 6.4: Observations on qualitative results of the proposed deformation compensation method per clinical case.

Clinical case	Observations
Case 1	– Good alignment of the estimated lung surface. – The oblique fissure moved upwards from CBCT$_{inf}$ to CBCT$_{def}$. – The estimated fissure (in Warped CT) is adequate near the hilum but poorer in the periphery. This unnatural deformation occurred during the elastic registration process during the change of pose deformation estimation.
Case 2	– The FOVs of the CBCT images are offset by several millimeters. – The diaphragm is barely visible in CBCT$_{def}$, putting in evidence the very large change of pose deformation of the diaphragm and an inaccurate estimation of the intraoperative lung's shape. – The three lung lobes deform separately during pneumothorax, whereas the proposed approach currently assumes a single deformable object (first approximation).
Case 3	– Good alignment of the estimated lung surface. – The diaphragm and a large inferior portion of the lung are not visible in the CBCTs images.
Case 4	– An upward movement of both fissures and the diaphragm can be observed from CBCT$_{inf}$ to CBCT$_{def}$. – The estimated upward movement of the diaphragm in CBCT$_{def}$ approaches this observation. – Significant amount of atelectasis. The limits of the lung near the hilum in CBCT$_{def}$ are indistinguishable.
Case 5	– The FOVs of the CBCT images are offset by several millimeters. – Very large deformation at the hilum from CBCT$_{inf}$ to CBCT$_{def}$. It can be observed at and under the main bronchus, through the medial wall of the lung. – During pneumothorax, the two lobes stay attached together but slide one against the other.

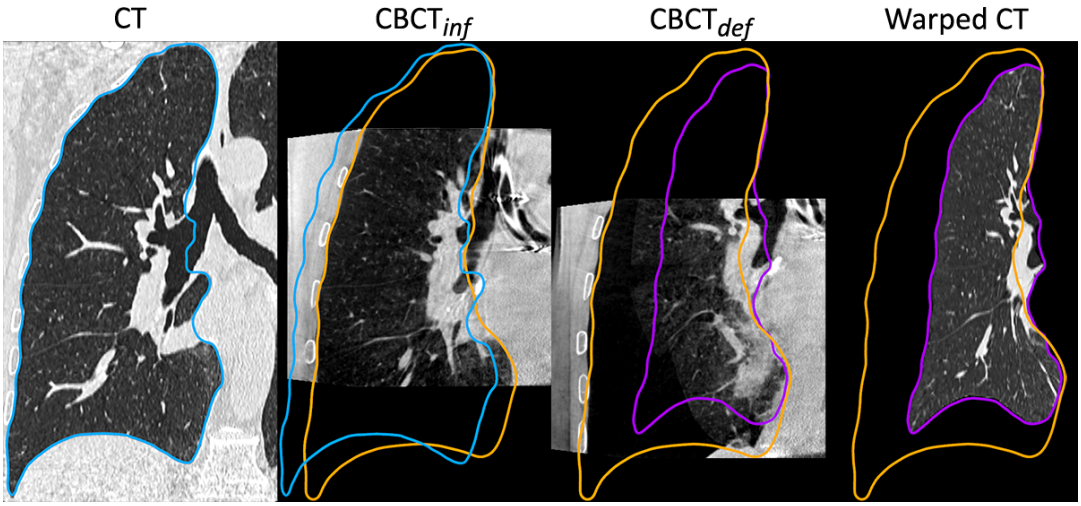

Figure 6.15: Qualitative result of the proposed deformation compensation method in Case 2.

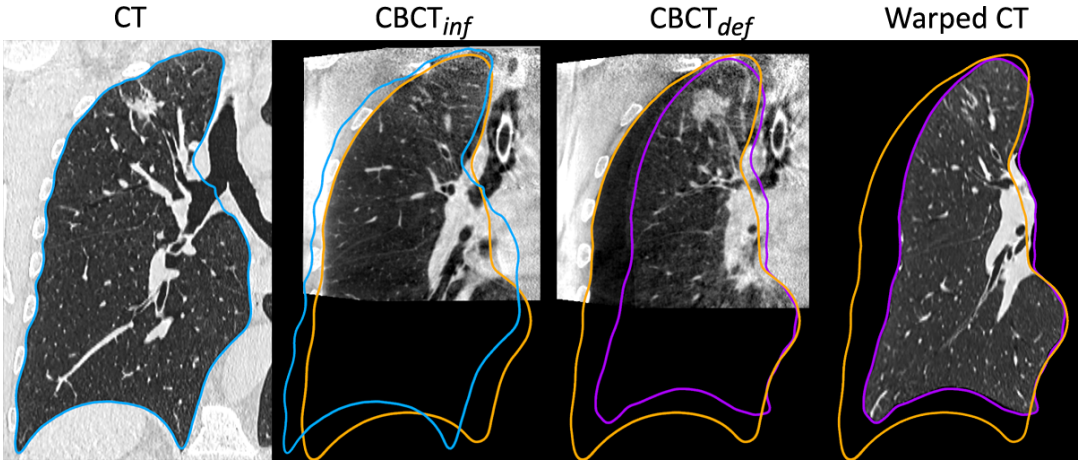

Figure 6.16: Qualitative result of the proposed deformation compensation method in Case 3.

Additional discussion

In addition to the discussion presented in Sec. 6.9, further elements are worth mentioning. On the one hand, the studies presented in Chapter 4, Appendix A and in this chapter share some of the clinical cases considered, and hence are worthy of comparison. On the other hand, some methodological differences between the hybrid registration framework presented in Chapter 5 and that presented in this chapter have not been discussed, mainly because it would require direct comparison of the two frameworks, which was not of interest for the article presented above.

First of all, the intensity-based image registration component of *Phase 1* corresponds to the registration framework presented previously in Chapter 4. As such, the registration results presented in that chapter (Fig. 4.8) and in this one (Fig. 6.7) are the same. However, although Case 6 was taken into account in the deformation char-

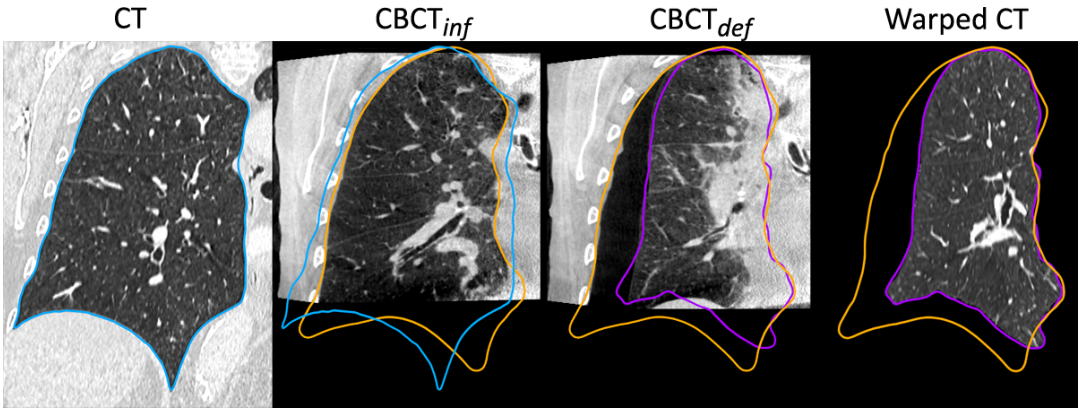

Figure 6.17: Qualitative result of the proposed deformation compensation method in Case 4.

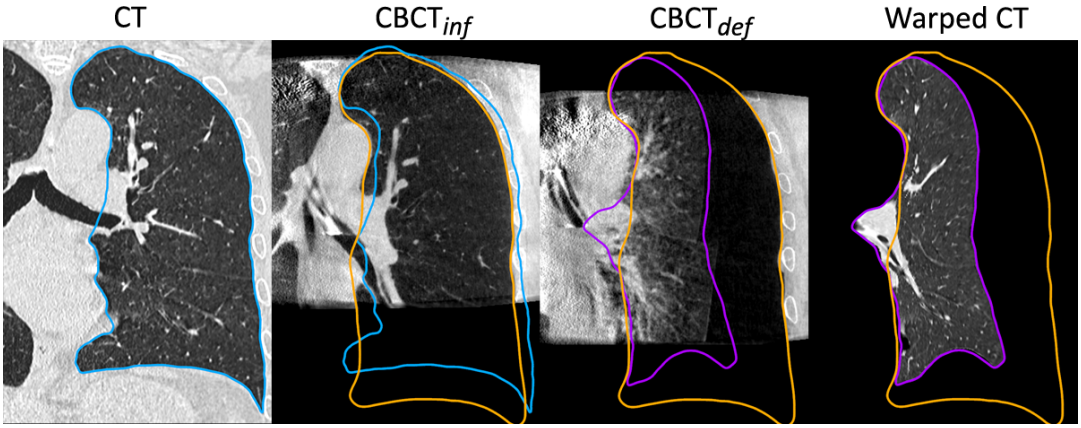

Figure 6.18: Qualitative result of the proposed deformation compensation method in Case 5.

acterization study presented in Chapter 4, it was not included in the current study because no anatomical landmarks were available for the CBCT$_{def}$ image. In fact, the internal lung structures have been so heavily deformed in that case that the surgeon could not identify any meaningful anatomical landmarks in this image.

Also, it should be noted that the registration framework presented in this chapter is one potential solution to the registration problem considered, but other solutions based on other methodological strategies may as well be possible. For the sake of comparison, an initial investigation was carried out to evaluate the feasibility of a registration approach based on image-intensity only as an alternative solution. This intensity-based image registration approach was based on the work presented previously in Chapter 4, and was used to register the preoperative CT image to the intraoperative CBCT$_{def}$ image of Case 1. The details of such study are presented in Appendix A. In comparison to the results presented in this chapter, the average ($\pm$ standard deviation) TRE obtained were 6.3 mm ($\pm$ 3.4 mm) and 4.9 mm ($\pm$ 2.2 mm) for the the intensity-based and hybrid approaches, respectively. The resulting TRE

distributions of both approaches are illustrated in Fig. 6.19.

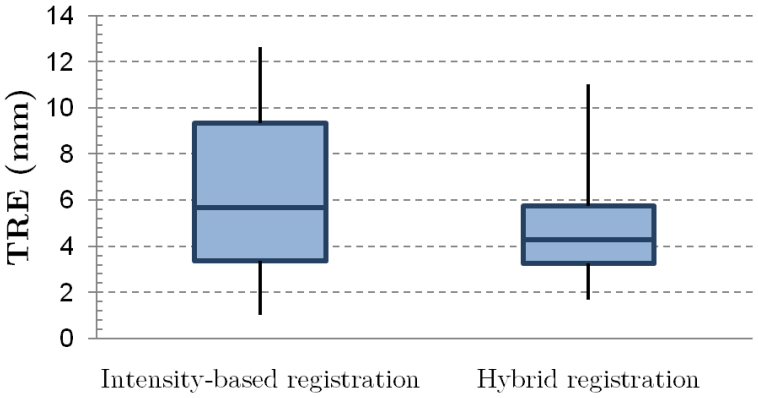

Figure 6.19: TRE distributions of intensity-based registration and hybrid registration frameworks for Case 1.

A comparison of the two registration frameworks shows a significant improvement in favor of the hybrid approach ($p = .021$, non-parametric Wilcoxon signed rank test). However, such improvement could not be verified for the other four clinical cases, as they were not studied using the intensity-based approach (lack of segmentation of the deflated lung). Therefore, a definitive conclusion comparing the two approaches in their current state would require further evaluation. Nonetheless, the same trend should be expected for the other cases as well, especially considering the methodological improvements to the hybrid approach already discussed (see Sec. 6.9 and the Additional results and discussion of Chapter 5).

Finally, the hybrid registration framework presented in this chapter improved in two ways the framework previously presented in Chapter 5. The first improvement corresponds to a change in contact conditions, from nodal/tangential to real small-deformation contact conditions. In comparison with the nodal/tangential conditions, the new contact conditions can be prescribed over all nodes of the lung surface, as their movement will not be restricted in the normal direction if no contact is detected. This not only simplifies the procedure of specifying the contact conditions, but also avoids potential deformation artifacts coming from under- or over-restriction of surface movement. The second improvement involves the extraction of the intraoperative deflated lung surface. In Chapter 5, a manual segmentation was required to generate this surface, which should be avoided as it is incompatible with the surgical workflow. In this chapter, a series of points were used to reconstruct the surface of the deflated lung. Although this process was also manual, it is in principle less time consuming, but more importantly, easier to automate than a manual segmentation. The reason is that manually extracting points of the deflated lung surface does not require dealing with atelectasis, as it happens mostly near the medial face.

General conclusion

In this chapter, the hybrid registration framework previously introduced in Chapter 5 was adapted to the context of a VATS intervention. Methodological changes were necessary for estimating the change of pose deformation with partial intraoperative data, as well as for taking into account hilum and diaphragm deformations. Also, improvements were made with respect to the contact conditions at the lung surface and the extraction of intraoperative data for the inverse problem formulation. The framework was validated using 5 retrospective clinical VATS cases, with varying algorithms that helped to determine the relevance of the main processing steps. Average TRE errors were obtained in a rage from 4.9 mm to 14.3 mm, with average error correction from 63% to 85%. This performance is comparable to that obtained previously in Chapter 5 in the context of transthoracic needle biopsy, but on the more challenging context of VATS. However, further improvements towards better accuracy and clinical compatibility would be necessary, for which potential solutions have been outlined.

7 Summary, perspectives and conclusion

In the context of lung cancer management, the surgical resection of pulmonary nodules through video-assisted thoracoscopic surgery (VATS) is an established diagnostic and treatment tool. During surgery, these pulmonary nodules are generally neither palpable nor visible, especially when they are small, low-dense and/or deep within lung parenchyma. Consequently, adjuvant preoperative/intraoperative pulmonary nodule localization procedures are commonly used in current clinical practice, mostly relying on the placement of various physical markers (*e.g.* hookwires, micro-coils, dyes). However, such localization procedures are not devoid of complications either from the marker placement (*e.g.* pneumothorax, hemothorax, air/dye embolism) or the marker itself (*e.g.* marker migration), and therefore, markerless localization solutions would be preferable. Therefore, an alternative solution based on the delineation of pulmonary nodules within intraoperative CBCT images has been proposed at the Rennes University Hospital, with promising results. The main limitation of this innovative localization strategy is the poor visibility of some pulmonary nodules in the intraoperative CBCT images. The main objective of this thesis was then to propose and evaluate a registration framework accounting for lung deformation during VATS, in order to facilitate the localization of pulmonary nodules within the surgical protocol introduced at the Rennes University Hospital.

An analysis of lung deformation during VATS lead to the interpretation of this deformation as a combination of two primary factors: a change of patient pose, from the preoperative to the intraoperative conditions; followed by a pneumothorax. With the purpose of studying these physical processes independently, the surgical VATS procedure was modified (with the approval of the local ethics committee) in order to include an additional intraoperative CBCT image of the lung before pneumothorax. Accordingly, three structural images were available for a total of 6 VATS clinical cases: a preoperative CT with the patient in supine position, an two intraoperative CBCTs with the patient in lateral decubitus position, before and after pneumothorax, respectively.

Contributions

A first contribution is an analysis of lung deformation after the change of patient pose during VATS. A study was carried out to quantify and characterize this lung deformation for 6 clinical cases. Deformation measurements were extracted from displacement fields that were computed via intensity-based image registration. This study revealed very large displacement (up to 40 mm) and generalized volumetric

contraction of lung tissue. Two primary causes were identified for this deformation: a change in gravity direction with respect to the body, and an upward movement of the diaphragm induced by the muscle relaxants administered for the surgery. A remarkable exception was found for one clinical case, for which a different surgical procedure without muscle relaxants was performed, and therefore, no upward diaphragm movement was observed. This study revealed the change of patient pose as a significant factor causing lung deformation during VATS, which has however been excluded in related works from the literature. This study focused on a phenomenon that has not been addressed in the literature, and contributed to the understanding of lung deformation during VATS.

A second contribution, and the main contribution of this thesis, is a hybrid registration framework accounting for lung deformation during VATS. This registration framework decouples the original registration problem into two smaller, more tractable sub-problems: the first accounting for the change of patient pose deformation, and the second accounting for the pneumothorax deformation. The hybrid approach combines intensity-based image registration and a linear poroelastic model of the lung with allowance for fluid evacuation for the estimation of lung deformation. An initial investigation provided promising results for a clinical case of transthoracic needle biopsy, for which lung deformation was very similar to that of VATS. Then, a follow up investigation with 5 VATS clinical cases (which are considerably more challenging), indicated the feasibility of the proposed approach within the VATS context. These studies constitute a first attempt to compensate for lung deformation for both the change of patient pose and the pneumothorax, using real clinical data.

Finally, a third contribution is a preliminary evaluation of an intensity-based image registration framework as an alternative solution for lung deformation compensation during VATS. This study allowed establishing a baseline method to be compared with the proposed hybrid registration approach. The obtained results in a VATS clinical case suggested better accuracy in favor of the hybrid approach.

Perspectives

The ultimate objective of the registration framework proposed in this thesis is to facilitate the localization of pulmonary nodules during VATS. In order to achieve that goal, various perspectives may be considered.

Assistance to clinical procedure

The image quality currently constitutes an important bottleneck for the interpretation and automatic processing of the intraoperative CBCT images. In this thesis, an artifact-removal post-processing algorithm was used in order to partially account for this problem, but a more appropriate approach for improving image quality would

be the use of state-of-the-art image reconstruction algorithms (Gardner et al., 2019; Schmidgunst et al., 2007). However, this would require access to raw projection-data of the CBCT scanner, which may not be readily accessible in the short term (necessitates an agreement with Siemens, the manufacturer). A more accessible alternative would be to improve image quality by optimizing the scanner acquisition parameters for lung imaging, since these are currently dedicated for heart imaging. This would require a multidisciplinary study involving expert radiologists and engineers.

Also, in order to minimize the radiation dose delivered to the patient, the proposed hybrid registration framework will require adaptation to a surgical protocol with only one intraoperative CBCT image (after pneumothorax) instead of two (before and after pneumothorax). This may be achieved by estimating the change of pose deformation directly from the preoperative CT to the intraoperative CBCT of the deflated lung, using the deformation of the thoracic cavity as guidance. However, this will probably require improvements in modeling lung deformation (see next sections), as well as thorough validation. Also, in the long term, lung deformation compensation strategies accounting for the change of pose and the pneumothorax deformations at once may be investigated.

Finally, an important limitation of the current surgical protocol is the need for fluoroscopy guidance, since it necessitates unavoidable radiation dose to the surgical team and the patient. This limitation may be overcome with the use of augmented reality visualization and real-time tracking techniques, to present guidance information directly into the endoscopic view. The development of such intraoperative guidance tool will constitute an important breakthrough for the localization of pulmonary nodules during VATS.

Image processing aspects

The deformation characterization study performed in this thesis contributed to a better understanding of the change of pose deformation during VATS. Such characterization would also be desirable for the pneumothorax deformation, which is considerably larger and more complex than the change of pose deformation. However, the same methodology will likely be insufficient as image density disparities (tissue densification and atelectasis) and complex deformation (independent lobe movement) present during pneumothorax are currently not being taken into account. Obtaining a dense displacement field is necessary for the characterization of deformation (measures based on the deformation gradient tensor), but it is a real challenge for pneumothorax deformation. As an alternative, the analysis of displacement over a series of anatomical landmarks placed at the interior of the lung would be worth studying, since this would at least provide insight in the amount and direction of displacement during pneumothorax.

Another aspect to consider is the segmentation/delineation of lung structures. Although automatic segmentation algorithms were used for the preoperative CT images, this was not possible for the intraoperative CBCT images because of their reduced image quality. Therefore, semi-automatic or manual methods were used instead. However, some of this segmentations would need to be performed during surgery, and hence, such time consuming manual interactions are to be avoided. The segmentation of lung structures in the CBCT images is a challenging problem that has been poorly addressed in the literature. Future works may include the use of machine learning algorithms in order to perform these automatic segmentations (Pang et al., 2019).

Modeling aspects

Concerning the linear poroelastic model, the first order approximation facilitated the design and implementation of the proposed hybrid registration framework, as well as the evaluation of its feasibility in the context of VATS. However, given the large lung deformation occurring during VATS, this approximation may constitute an important limitation, and hyperelastic constitutive laws for the solid structure would be more appropriate (Berger et al., 2015; Seyfi Noferest et al., 2018). This is expected to improve the accuracy of the deformation estimations with more realistic simulations. However, although various possibilities exist for the hyperelastic law, to date, neither of them has been utilized for simulating lung deformation during VATS, and consequently, comparison studies may be necessary.

In addition, there are two aspects that should be considered with respect to the observed pneumothorax lung deformation. Firstly, the lobes deform as independent structures constrained only at their interfaces. Currently, the single-body assumption considered for the lung parenchyma completely disregards this important aspect. This lobe deformation may be taken into account by modeling each lobe independently, with contact conditions at their interfaces. This, however, would greatly increase the complexity of the simulation (especially if hyperelastic constitutive laws are considered) with consequences in convergence and computation time, which will have to be studied. Secondly, the simulation of lung pneumothorax currently uses a homogeneous value for the intrabronchi permeability parameter. In reality, the presence of localized atelectasis indicates that lung deflation is heterogeneous, with some regions being affected more than others. Although it is difficult to precisely determine these regions, in general, more deflation can be observed near the hilum. As such, using a heterogeneous distribution for intrabronchi permeability that varies with distance to the medial face of the lung may be worth studying, with the intent to reproduce this heterogeneous deflation behavior.

On the inverse problem formulation

The inverse problem formulation used for pneumothorax deformation compensation has various limitations. Firstly, from the available intraoperative information of the deflated lung, only the external surface was integrated into the computation of the cost function. Including internal lung information as well would likely improve the estimation of diaphragm upward movement in the current implementation. Moreover, if heterogeneous material properties are considered (*e.g.* localized deflation or varying tissue elasticity and permeability), this internal lung information may be necessary for converging to meaningful solutions. To improve this aspect, it may be helpful taking into account airway or vessel deformation (Cazoulat et al., 2016; Morin et al., 2017), as well as the inclusion of salient keypoints for deformed internal structures (Ruhaak et al., 2017). Secondly, since no imposed displacements are used at the lung surface, a perfect surface-to-surface match after deformation compensation is very unlikely. To alleviate such misfit error, point-to-surface projection based on shape features could be calculated (Nakao et al., 2019), and incorporated as relaxed imposed displacements to help constrain surface deformation (Morin et al., 2017).

Finally, the current implementation of the inverse problem formulation is not yet compatible with the clinical practice, because it requires many simulations before converging to a solution (after a couple of hours). In order to account for this limitation, model reduction or machine learning approaches may be investigated (Mendizabal et al., 2020), since these are expected to reduce simulation times considerably. Ultimately, a forward problem formulation instead of an inverse problem formulation would be desirable, but this would require deeper understanding of pneumothorax deformation, an improved biomechanical model of lung deformation, and sufficient intraoperative data for guiding such model.

Conclusion

The compensation of lung deformation for the localization of pulmonary nodules during VATS is a challenging problem that has been barely addressed in the literature. In this thesis, a hybrid registration framework combining intensity-based image registration and a linear poroelastic model with allowance for fluid evacuation was proposed in order to account for such deformation. The studies herein performed demonstrated the feasibility of the proposed approach, and provided insights that were useful for the understanding of lung deformation during VATS from a macroscopic perspective. Further research is needed before the proposed approach can be used in the current VATS surgical protocol, but numerous perspectives towards that end were here discussed. Continuing this research has the potential to pave the way for advanced surgical guidance techniques, which may greatly benefit the current clinical practice.

Appendices

A

Image-based registration for lung nodule localization during VATS

Foreword

In order to be compatible with the localization strategy described in Sec. 1.3.3, a deformation compensation algorithm should be able to provide an estimation of the position of the nodule in the CBCT image of the deflated lung. Since structural and positional details are available in the preoperative CT image, a reasonable approach would be to register this preoperative image to the intraoperative image of the deflated lung, and to use the resulting displacement field to estimate the intraoperative position of the pulmonary nodule.

The study presented in this appendix aims at evaluating an intensity-based approach for the registration of the two images. This study introduces an alternative potential solution to be compared with the hybrid approach proposed in this thesis. This intensity-based approach uses the framework previously introduced in Chapter 4, which provided good results for the registration of the preoperative CT image to the intraoperative CBCT image of the inflated lung (*i.e.* change of pose deformation). It should be noted, however, that the two CBCT images contain the lung in considerably different configurations, and the introduction of pneumothorax and atelectasis make the registration problem considerably harder. This initial investigation was carried out in order to compare the intensity-based and hybrid registration approaches.

The first part of this appendix reproduces the investigation that was presented in an international conference:

> **P. Alvarez**, S. Rouzé, M. Chabanas, Y. Payan, and J.-L. Dillenseger. Image-based registration for lung nodule localization during VATS. In *Surgetica 2019*, Rennes, France, 2019

The second part of this appendix further discusses the potential advantages and limitations of the intensity-based registration approach, in comparison to the hybrid approach proposed in this thesis.

Article: Image-based registration for lung nodule localization during VATS

Abstract: Lung nodule localization during Video-Assisted Thoracoscopic Surgery (VATS) is a challenging task for small, low-density nodules. Current preoperative localization techniques are still sub-optimal in some cases. In this work, we studied the use and the limitations of an image-based nonrigid registration approach for nodule localization during VATS. Average target registration errors were of 5.67 mm, meaning an error reduction of 84.36 %.

A.1 Introduction

In clinical practice, early stage lung cancer nodules are prescribed for resection through Video-Assisted Thoracoscopic Surgery (VATS). Because of their typically reduced size and density, these nodules might be difficult to find during surgery. This is caused by the pneumothorax (*i.e.* abnormal presence of air inside the thoracic cage) resultimg from the insertion of the surgical ports. To account for this problem, preoperative nodule localization procedures are typically used. These procedures consist mainly on the placement of hook-wires, dyes or micro-coils in the nodule (Keating and Singhal, 2016). However, studies have found these localization techniques to still be sub-optimal (Park et al., 2017).

Consequently, there is a growing interest towards the development of intraoperative lung localization procedures. In fact, previous studies have proposed the use of intraoperative imaging for nodule localization (Rouzé et al., 2016; Wada et al., 2015). In addition, image processing techniques can also be used in combination with intraoperative imaging for nodule localization. For instance, Uneri *et al.* used intraoperative Cone Beam CT (CBCT) and a hybrid shape-intensity nonrigid registration approach for nodule localization on an animal study (Uneri et al., 2013).

In this preliminary work, we propose to use intraoperative CBCT imaging and nonrigid image registration for lung nodule localization during VATS. Our approach was inspired by Wu *et al.* (Wu et al., 2008), who proposed an algorithm that takes into account sliding effects for registering images of breathing lungs. To the best of our knowledge, this is the first study on human data using intraoperative imaging and nonrigid image registration for nodule localization.

A.2 Materials and Methods

A.2.1 Clinical data

This study used two tomographic images issued from a single clinical case of a VATS intervention performed at the Rennes University Hospital. The first image, a preoperative CT, was taken following current clinical protocol (Fig. A.1 left). The second image, an intraoperative CBCT, was taken after the patient's lung was deflated as result of pneumothorax (Fig. A.1 right). Both images were acquired under the informed consent of the patient and the approval of the local ethics committee.

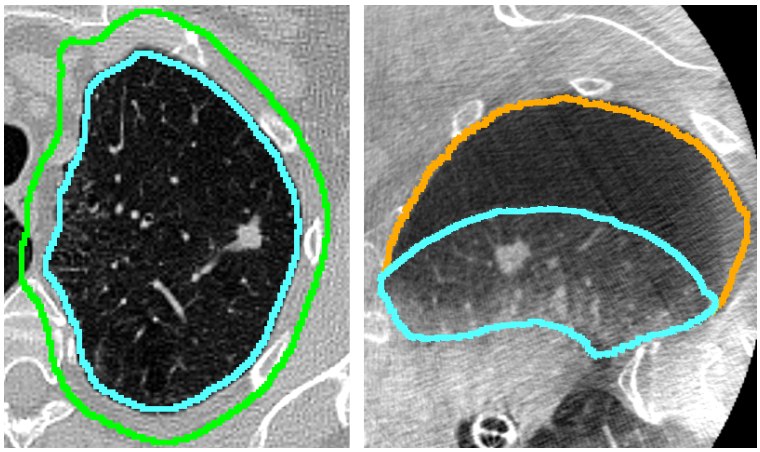

Figure A.1: Left: the preoperative CT with the segmentation of the lung (cyan) and its extension (green). Right: the intraoperative CBCT with the segmentations of the lung (cyan) and the thoracic cage (orange). The pneumothorax is the space between the lung and the thoracic cavity.

A.2.2 Segmentation

Three anatomical structures were manually segmented: the lung in the CT and CBCT images and the thoracic cavity in the CBCT image. The binary masks were post-processed using morphological dilatation to extend the boundaries (Fig. A.1 left).

A.2.3 Nodule localization approach

Our registration approach consists of two steps: a rigid registration for initial alignment followed with image-based nonrigid image registration to account for pneumothorax deformation. Both processes were implemented using Elastix toolbox (Klein et al., 2010).

Rigid registration

We used the thoracic cavity as a reference for aligning the preoperative CT to the intraoperative CBCT images. We performed rigid image registration using the Mutual

Information (MI) similarity metric. The MI computation was filtered to the regions contained in the extended masks of the thoracic cavity. We used discrete probability distributions of a very low resolution for the computation of the MI (*i.e.* the number of bins was only 8). In this way, the strong gradients corresponding to the borders of the thoracic cage and the main airway branches are more likely to drive the registration process than the weak gradients at the interior of the mismatching thoracic cavities. This is important given that the thoracic cavities contain mismatching lungs.

Nonrigid registration

Before nonrigid registration, we performed an intensity assignment procedure. The intensity values of the voxels outside the segmented lungs were assigned with a constant intensity value, while those at the inside were left unchanged. This constant value (-1500 HU) lies outside the range of values inside the lung. A nonrigid registration process was then performed using these intensity-modified images and the extended masks of the lung parenchyma. We accounted for large deformations using a multi-resolution Free Form Deformation (FFD) strategy, with a total of 4 resolutions. At each iteration, the resolution was doubled and the transformation obtained was carried through consecutive iterations. We used BSplines as the transformation model and two intensity-based similarity metrics: Mutual Information (MI) and Normalized Cross Correlation (NCC). The size of the grid for the BSplines was allowed to change with image resolution, reaching 16 mm in the last iteration.

A.3 Results and Discussion

We used a set of 27 paired anatomical landmarks to compute Target Registration Errors (TRE) for validation. These landmarks were manually placed by an expert thoracic surgeon on the tumor and bifurcations of airways and vessels. After rigid registration, these landmarks were at a distance of 40.2 mm (± 1.0 mm).

Nonrigid registration with MI resulted in TREs of 80 mm (± 20.4 mm), which are worse than those of rigid registration. This bad performance may be explained by the fact that the MI similarity metric does not necessarily penalize mismatches of intensity, which makes it is less costly to move the CT-lung voxels out of the CBCT-mask than to move them inside.

However, nonrigid registration with NCC reduced the TREs to 6.23 mm (± 3.4 mm), which corresponds to an error reduction of 84.4 %. In comparison to MI, NCC aims to closely match image intensities, and hence benefits from the usage of the intensity-modified images and the dilated masks. The reason is that the borders of the CT and CBCT lung are forced to match as a result of the strong intensity gradients artificially generated by the intensity assignment procedure.

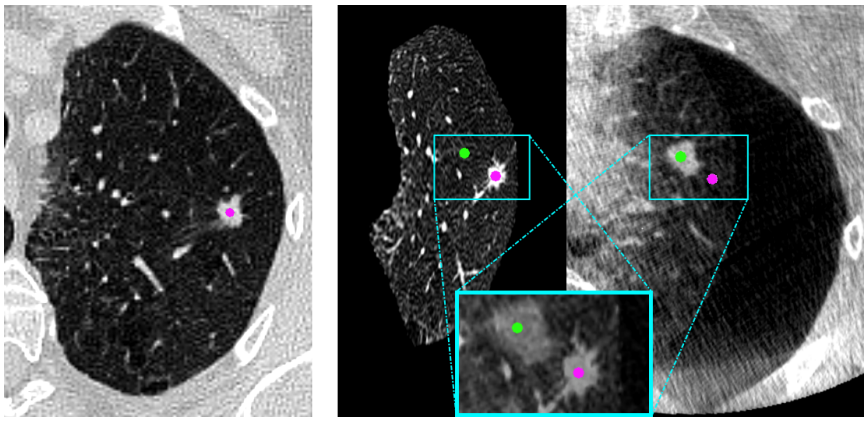

Figure A.2: Result of nonrigid registration with NCC. The preoperative CT is shown to the left. The deformed CT and the CBCT are shown to the right. Colored circles indicate the paired landmarks for the tumor. The image in the window is a closeup of the superposition of the result.

The result of nonrigid registration with NCC is shown in Fig. A.2. A qualitative comparison of the deformed CT and the CBCT reveals large misalignment. This can be seen throughout the lung parenchyma, where several internal structures are visible in only one of the images. In addition, the landmarks placed on the tumor are 11.77 mm apart after registration, which is not within the clinical requirements. The registration problem at hand is a real challenge (*i.e.* very large deformations and low quality images). Although more sophisticated techniques do exist, the use of image intensity only to guide registration is possibly insufficient.

A.4 Conclusion

We have presented a preliminary study that evaluates an intensity-based nonrigid registration approach for nodule localization during VATS. The obtained results show an error correction of 84.36 % when using NCC, which seemed unsatisfactory after a closer qualitative analysis. We believe that intensity-based nonrigid registration techniques are insufficient for nodule localization during VATS. Hence, hybrid approaches combining images and biomechanical models will be explored.

Acknowledgments

This work was supported in part by the *Région Bretagne* through its *Allocations de Recherche Doctorale* (ARED) framework and by the French National Research Agency (ANR) through the frameworks *Investissements d'Avenir Labex CAMI* (ANR-11-LABX-0004) and *Infrastructure d'Avenir en Biologie et Santé* (ANR-11-INBS-0006).

Additional discussion

The work presented in this appendix proposes an intensity-based registration framework for the compensation of lung deformation between the preoperative CT image and the intraoperative CBCT image of the deflated lung during VATS. The framework was adapted from the work presented previously in Chapter 4, as good alignment of internal structures was possible even with very large deformation. The results herein obtained, however, were not as satisfactory. Although the large initial landmark error was reduced by 84.3% in average after registration, the internal structures were clearly misaligned. Indeed, the registration framework used has several limitations.

First of all, the NCC similarity metric assumes that the intensities corresponding to the same structures in both images are linearly related. However, this is clearly not the case, as the lung deflation after pneumothorax not only increases tissue density, but also generates localized atelectasis that completely collapses the parenchyma. Consequently, the image intensity increases significantly and heterogeneously in the CBCT image of the deflated lung, hence invalidating the assumption. The obtained error reduction is then explained notably by the alignment of the lung surfaces, which is achieved by the masking process. In practical terms, the volume of the inflated lung in the preoperative CT image is forced to fit the volume of the deflated lung in the CBCT image. It should be noted that similar results are to be expected with the use of the non-parametric Demons algorithm, as it also relies on intensity similarity of the images (Vercauteren et al., 2007). In order to alleviate this issue, density correction techniques may be used during the registration process (Nithiananthan et al., 2011; Sarrut et al., 2006).

Another limitation is the need of segmenting the lung parenchyma in the images. Indeed, this segmentation is typically required for the registration of lung images, as it helps taking into account sliding motion, restricts the computations to a determined ROI, and provides shape information of lung deformation (Murphy et al., 2011; Uneri et al., 2013; Wu et al., 2008). Although the quality of the CT image allows for this segmentation to be performed automatically, this is considerably harder in the CBCT image, since the contours of the deflated lung may become indistinguishable in the medial and lateral faces of the lung. In the medial face, this is the result of atelectais increasing the density of parenchyma up to a point where it is very close to the density of the mediastinum (see Fig. 3.1). In the lateral face, the parenchyma that is still filled with air can have an intensity very close to that of surrounding air. This issue gets aggravated by the reduced quality of the CBCT image, which may comprise significant image noise and artifacts. The quality of this segmentation is crucial for the performance of the registration framework herein presented and for most lung image registration algorithms. However, a manual procedure cannot be afforded as it is too time consuming for being compatible with the surgical workflow.

General conclusion

This appendix presented an intensity-based registration framework for the compensation of lung deformation during VATS. The framework was based on a classical approach for the registration of lung images in the context of respiratory motion, which allows for sliding motion (Wu et al., 2008). Although a similar framework proved useful for the estimation of the change of pose deformation during VATS (see Chapter 4), the results obtained herein were not satisfactory, which illustrates the complexity of the registration problem at hand. As discussed, only intensity information may not be sufficient to solve such registration problem, and approaches relying less on image information are thus desirable.

List of publications

P. Alvarez, S. Rouzé, M. I. Miga, Y. Payan, J.-L. Dillenseger, and M. Chabanas. A hybrid image registration approach to markerless intraoperative nodule localization during video-assisted thoracoscopic surgery. *Medical Image Analysis*, submitted in April 2020

P. Alvarez, S. Narasimhan, S. Rouzé, J.-L. Dillenseger, Y. Payan, M. I. Miga, and M. Chabanas. Biphasic model of lung deformations for video-assisted thoracoscopic surgery (VATS). In *2019 IEEE 16th International Symposium on Biomedical Imaging (ISBI 2019)*, pages 1367–1371, Venice, Italy, Apr. 2019a. IEEE. ISBN 978-1-5386-3641-1. doi: 10.1109/isbi.2019.8759219

P. Alvarez, S. Rouzé, M. Chabanas, Y. Payan, and J.-L. Dillenseger. Image-based registration for lung nodule localization during VATS. In *Surgetica 2019*, Rennes, France, 2019

P. Alvarez, M. Chabanas, S. Rouzé, M. Castro, Y. Payan, and J.-L. Dillenseger. Lung deformation between preoperative CT and intraoperative CBCT for thoracoscopic surgery: a case study. In *Medical Imaging 2018: Image-Guided Procedures, Robotic Interventions, and Modeling*, page 40, Houston, United States, Mar. 2018. SPIE. ISBN 978-1-5106-1641-7. doi: 10.1117/12.2293938

S. Rouzé, **P. Alvarez**, B. de Latour, E. Flécher, J.-L. Dillenseger, and J.-P. Verhoye. Localisation de nodules pulmonaires en réalité augmentée grâce au cone beam computed tomography (CBCT) en vidéo-thoracoscopie. *Bulletin de l'Académie Nationale de Médecine*, 202(8-9):1897–1908, Nov. 2018. doi: 10.1016/s0001-4079(19)30183-9

S. Rouzé, **P. Alvarez**, M. Castro, Y. Payan, and J.-L. Dillenseger. Développement d'un recalage CT/CBCT avec modélisation biomécanique du poumon pour la localisation de nodules en VATS. In *Journée d'Automne de la Société Française de Chirurgie Thoracique et Cardio-Vasculaire*, Paris, France, 2017

P. Alvarez, S. Rouzé, M. Chabanas, M. Castro, Y. Payan, and J.-L. Dillenseger. Modeling lung deflation during video-assisted thoracoscopy surgery for the localization of small nodules. In EUROMECH Colloquium 595: Biomechanics and computer assisted surgery meets medical reality, Lille, France, 2017

P. Alvarez, S. Rouzé, M. Chabanas, M. Castro, Y. Payan, and J.-L. Dillenseger. A biomechanical model of lung deflation during VATS for the localization of small nodules. In *Surgetica 2017*, Strasbourg, France, 2017

Bibliography

M. Al-Ameri, P. Bergman, A. Franco-Cereceda, and U. Sartipy. Video-assisted thoracoscopic versus open thoracotomy lobectomy: a swedish nationwide cohort study. *Journal of Thoracic Disease*, 10(6):3499–3506, June 2018. doi: 10.21037/jtd.2018.05.177.

A. Al-Mayah, J. Moseley, and K. K. Brock. Contact surface and material nonlinearity modeling of human lungs. *Physics in Medicine and Biology*, 53(1):305–317, 2008. ISSN 0031-9155. doi: 10.1088/0031-9155/53/1/022.

A. Al-Mayah, J. Moseley, M. Velec, and K. K. Brock. Sliding characteristic and material compressibility of human lung: Parametric study and verification. *Medical Physics*, 36(10):4625–4633, 2009. ISSN 0094-2405. doi: 10.1118/1.3218761.

A. Al-Mayah, J. Moseley, M. Velec, S. Hunter, and K. Brock. Deformable image registration of heterogeneous human lung incorporating the bronchial tree. *Medical Physics*, 37(9):4560–4571, 2010. ISSN 0094-2405. doi: 10.1118/1.3471020.

A. Al-Mayah, J. Moseley, M. Velec, and K. Brock. Toward efficient biomechanical-based deformable image registration of lungs for image-guided radiotherapy. *Physics in Medicine and Biology*, 56(15):4701–4713, 2011. ISSN 0031-9155. doi: 10.1088/0031-9155/56/15/005.

P. Alvarez, M. Chabanas, S. Rouzé, M. Castro, Y. Payan, and J.-L. Dillenseger. Lung deformation between preoperative CT and intraoperative CBCT for thoracoscopic surgery: a case study. In R. J. Webster and B. Fei, editors, *Medical Imaging 2018: Image-Guided Procedures, Robotic Interventions, and Modeling*, page 40, Houston, United States, Mar. 2018. SPIE. ISBN 978-1-5106-1641-7 978-1-5106-1642-4. doi: 10.1117/12.2293938.

P. Alvarez, S. Narasimhan, S. Rouzé, J.-L. Dillenseger, Y. Payan, M. I. Miga, and M. Chabanas. Biphasic model of lung deformations for video-assisted thoracoscopic surgery (VATS). In *2019 IEEE 16th International Symposium on Biomedical Imaging (ISBI 2019)*, pages 1367–1371, Venice, Italy, Apr. 2019a. IEEE. ISBN 978-1-5386-3641-1. doi: 10.1109/isbi.2019.8759219.

P. Alvarez, S. Rouzé, M. Chabanas, Y. Payan, and J.-L. Dillenseger. Image-based registration for lung nodule localization during VATS. In *Surgetica 2019*, Rennes, France, 2019b.

R. Amelon, K. Cao, K. Ding, G. E. Christensen, J. M. Reinhardt, and M. L. Raghavan. Three-dimensional characterization of regional lung deformation. *Journal of Biomechanics*, 44(13):2489–2495, 2011. ISSN 0021-9290. doi: 10.1016/j.jbiomech.2011.06.009.

American Joint Committee on Cancer. *AJCC cancer staging manual*. Springer, Switzerland, 2017. ISBN 978-3-319-40617-6.

M. Bendixen, O. D. Jørgensen, C. Kronborg, C. Andersen, and P. B. Licht. Postoperative pain and quality of life after lobectomy via video-assisted thoracoscopic surgery or anterolateral thoracotomy for early stage lung cancer: a randomised controlled trial. *The Lancet Oncology*, 17(6):836–844, June 2016. doi: 10.1016/s1470-2045(16)00173-x.

K. S. Berfield and D. E. Wood. Sublobar resection for stage IA non-small cell lung cancer. *Journal of Thoracic Disease*, 9(S3):S208–S210, Apr. 2017. doi: 10.21037/jtd.2017.03.135.

L. Berger, R. Bordas, K. Burrowes, V. Grau, S. Tavener, and D. Kay. A poroelastic model coupled to a fluid network with applications in lung modelling. *International Journal for Numerical Methods in Biomedical Engineering*, 32(1):n/a–n/a, July 2015. ISSN 2040-7939. doi: 10.1002/cnm.2731.

F. Bernardini, J. Mittleman, H. Rushmeier, C. Silva, and G. Taubin. The ball-pivoting algorithm for surface reconstruction. *IEEE Transactions on Visualization and Computer Graphics*, 5(4):349–359, Oct. 1999. ISSN 1077-2626. doi: 10.1109/2945.817351.

M. A. Biot. General theory of three-dimensional consolidation. *Journal of Applied Physics*, 12(2):155–164, Feb. 1941. ISSN 0021-8979. doi: 10.1063/1.1712886.

M. A. Biot. Theory of elasticity and consolidation for a porous anisotropic solid. *Journal of Applied Physics*, 26(2):182–185, Feb. 1955. ISSN 0021-8979. doi: 10.1063/1.1721956.

Blausen Medical. Medical gallery of Blausen Medical 2014. *WikiJournal of Medicine*, 1(2), 2014. doi: 10.15347/wjm/2014.010.

F. Bray, J. Ferlay, I. Soerjomataram, R. L. Siegel, L. A. Torre, and A. Jemal. Global cancer statistics 2018: GLOBOCAN estimates of incidence and mortality worldwide for 36 cancers in 185 countries. *CA: A Cancer Journal for Clinicians*, 68(6):394–424, 2018. ISSN 0007-9235. doi: 10.3322/caac.21492.

J. D. Brierley, M. K. Gosporadowicz, and C. Wittekind, editors. *TNM Classification of Malignant Tumours, 7th Edition*. Wiley, 2017.

G. Buccheri. Lung cancer: clinical presentation and specialist referral time. *European Respiratory Journal*, 24(6):898–904, Dec. 2004. doi: 10.1183/09031936.04.00113603.

G. Cazoulat, D. Owen, M. M. Matuszak, J. M. Balter, and K. K. Brock. Biomechanical deformable image registration of longitudinal lung CT images using vessel information. *Physics in Medicine and Biology*, 61(13):4826–4839, 2016. ISSN 0031-9155. doi: 10.1088/0031-9155/61/13/4826.

Y.-K. Chao, K.-T. Pan, C.-T. Wen, H.-Y. Fang, and M.-J. Hsieh. A comparison of efficacy and safety of preoperative versus intraoperative computed tomography-guided thoracoscopic lung resection. *The Journal of Thoracic and Cardiovascular Surgery*, 156 (5):1974–1983, Nov. 2018. ISSN 0022-5223. doi: 10.1016/j.jtcvs.2018.06.088.

Y.-K. Chao, O. Q. Y. Leow, C.-T. Wen, and H.-Y. Fang. Image-guided thoracoscopic lung resection using a dual-marker localization technique in a hybrid operating room. *Surgical Endoscopy*, 33(11):3858–3863, 2019. ISSN 0930-2794. doi: 10.1007/s00464-019-06883-y.

I. Chen, A. M. Coffey, S. Ding, P. Dumpuri, B. M. Dawant, R. C. Thompson, and M. I. Miga. Intraoperative Brain Shift Compensation: Accounting for Dural Septa. *IEEE Transactions on Biomedical Engineering*, 58(3):499–508, Mar. 2011. ISSN 0018-9294. doi: 10.1109/TBME.2010.2093896.

Y. Choi and S. Lee. Local injectivity conditions of 2D and 3D uniform cubic B-spline functions. In *Proceedings. Seventh Pacific Conference on Computer Graphics and Applications*, pages 302–311, Seoul, South Korea, 1999. doi: 10.1109/pccga.1999.803374.

P. Cignoni, M. Callieri, M. Corsini, M. Dellepiane, F. Ganovelli, and G. Ranzuglia. Meshlab: an open-source mesh processing tool. In V. Scarano, R. D. Chiara, and U. Erra, editors, *Eurographics Italian Chapter Conference*. The Eurographics Association, 2008. ISBN 978-3-905673-68-5. doi: 10.2312/LocalChapterEvents/ItalChap/ItalianChapConf2008/129-136.

M. Corsini, P. Cignoni, and R. Scopigno. Efficient and flexible sampling with blue noise properties of triangular meshes. *IEEE Transactions on Visualization and Computer Graphics*, 18(6):914–924, 2012. ISSN 1077-2626. doi: 10.1109/tvcg.2012.34.

W. R. Crum, O. Camara, and D. J. Hawkes. Methods for inverting dense displacement fields: Evaluation in brain image registration. In *Medical Image Computing and Computer-Assisted Intervention – MICCAI 2007*, volume 10, pages 900–907, 2007. doi: 10.1007/978-3-540-75757-3_109.

H. J. de Koning, C. M. van der Aalst, P. A. de Jong, E. T. Scholten, K. Nackaerts, M. A. Heuvelmans, J.-W. J. Lammers, C. Weenink, U. Yousaf-Khan, N. Horeweg, S. van 't Westeinde, M. Prokop, W. P. Mali, F. A. A. M. Hoesein, P. M. A. van Ooijen, J. G. J. V.

Aerts, M. A. den Bakker, E. Thunnissen, J. Verschakelen, R. Vliegenthart, J. E. Walter, K. ten Haaf, H. J. M. Groen, and M. Oudkerk. Reduced lung-cancer mortality with volume CT screening in a randomized trial. *New England Journal of Medicine*, 382(6):503–513, Feb. 2020. doi: 10.1056/nejmoa1911793.

V. Delmon, S. Rit, R. Pinho, and D. Sarrut. Registration of sliding objects using direction dependent B-splines decomposition. *Physics in Medicine and Biology*, 58(5): 1303–1314, 2013. ISSN 0031-9155. doi: 10.1088/0031-9155/58/5/1303.

M. Dietel, L. Bubendorf, A.-M. C. Dingemans, C. Dooms, G. Elmberger, R. C. García, K. M. Kerr, E. Lim, F. López-Ríos, E. Thunnissen, P. E. Van Schil, and M. von Laffert. Diagnostic procedures for non-small-cell lung cancer (NSCLC): recommendations of the european expert group. *Thorax*, 71(2):177–184, 2016. ISSN 0040-6376. doi: 10.1136/thoraxjnl-2014-206677.

K. Du, J. E. Bayouth, K. Ding, G. E. Christensen, K. Cao, and J. M. Reinhardt. Reproducibility of intensity-based estimates of lung ventilation. *Medical Physics*, 40 (6Part1):063504, May 2013. doi: 10.1118/1.4805106.

P. Dumpuri, R. C. Thompson, B. M. Dawant, A. Cao, and M. I. Miga. An atlas-based method to compensate for brain shift: Preliminary results. *Medical Image Analysis*, 11(2):128–145, 2007. ISSN 1361-8415. doi: 10.1016/j.media.2006.11.002.

J. Eom, X. G. Xu, S. De, and C. Shi. Predictive modeling of lung motion over the entire respiratory cycle using measured pressure-volume data, 4DCT images, and finite-element analysis. *Medical Physics*, 37(8):4389–4400, 2010. ISSN 0094-2405. doi: 10.1118/1.3455276.

R. S. J. Estepar, J. C. Ross, R. Harmouche, J. Onieva, A. A. Diaz, and G. R. Washko. Chest imaging platform: An open-source library and workstation for quantitative chest imaging. In *C66. Lung Imaging II: New Probes and Emerging Technologies*, 2015. doi: 10.1164/ajrccm-conference.2015.191.1_MeetingAbstracts.A4975.

P.-E. Falcoz, M. Puyraveau, P.-A. Thomas, H. Decaluwe, M. Hürtgen, R. H. Petersen, H. Hansen, and A. Brunelli. Video-assisted thoracoscopic surgery versus open lobectomy for primary non-small-cell lung cancer: a propensity-matched analysis of outcome from the European Society of Thoracic Surgeon database. *European Journal of Cardio-Thoracic Surgery*, 49(2):602–609, Apr. 2015. ISSN 1010-7940. doi: 10.1093/ejcts/ezv154.

B. Fuerst, T. Mansi, F. Carnis, M. Salzle, J. Zhang, J. Declerck, T. Boettger, J. Bayouth, N. Navab, and A. Kamen. Patient-specific biomechanical model for the prediction of lung motion from 4-D CT images. *IEEE Transactions on Medical Imaging*, 34(2): 599–607, 2015. ISSN 0278-0062. doi: 10.1109/tmi.2014.2363611.

S. J. Gardner, W. Mao, C. Liu, I. Aref, M. Elshaikh, J. K. Lee, D. Pradhan, B. Movsas, I. J. Chetty, and F. Siddiqui. Improvements in CBCT image quality using a novel iterative reconstruction algorithm: A clinical evaluation. *Advances in Radiation Oncology*, 4(2):390–400, Apr. 2019. doi: 10.1016/j.adro.2018.12.003.

R. R. Gill, Y. Zheng, J. S. Barlow, J. Jayender, E. E. Girard, P. M. Hartigan, L. R. Chirieac, C. J. Belle-King, K. Murray, C. Sears, J. O. Wee, M. T. Jaklitsch, Y. L. Colson, and R. Bueno. Image-guided video assisted thoracoscopic surgery (iVATS) - phase i-II clinical trial. *Journal of Surgical Oncology*, 112(1):18–25, 2015. ISSN 0022-4790. doi: 10.1002/jso.23941.

M. K. Gould, J. Donington, W. R. Lynch, P. J. Mazzone, D. E. Midthun, D. P. Naidich, and R. S. Wiener. Evaluation of individuals with pulmonary nodules: When is it lung cancer? *Chest*, 143(5):e93S–e120S, 2013. doi: 10.1378/chest.12-2351.

L. Han, H. Dong, J. R. McClelland, L. Han, D. J. Hawkes, and D. C. Barratt. A hybrid patient-specific biomechanical model based image registration method for the motion estimation of lungs. *Medical Image Analysis*, 39:87–100, 2017. ISSN 1361-8415. doi: 10.1016/j.media.2017.04.003.

H. J. Hansen and R. H. Petersen. Video-assisted thoracoscopic lobectomy using a standardized three-port anterior approach - the Copenhagen experience. *Annals of Cardiothoracic Surgery*, 1(1), 2012. ISSN 2225-319X.

T. Hartkens, D. L. G. Hill, A. D. Castellano-Smith, D. J. Hawkes, C. R. Maurer, A. J. Martin, W. A. Hall, H. Liu, and C. L. Truwit. Measurement and analysis of brain deformation during neurosurgery. *IEEE Transactions on Medical Imaging*, 22(1):82–92, 2003. ISSN 0278-0062. doi: 10.1109/TMI.2002.806596.

K. Hasse, D. O'Connell, Y. Min, J. Neylon, D. A. Low, and A. Santhanam. Estimation and validation of patient-specific high-resolution lung elasticity derived from 4DCT. *Medical Physics*, 45(2):666–677, 2018. ISSN 0094-2405. doi: 10.1002/mp.12697.

M. P. Heinrich, I. J. A. Simpson, B. W. Papież, S. M. Brady, and J. A. Schnabel. Deformable image registration by combining uncertainty estimates from supervoxel belief propagation. *Medical Image Analysis*, 27:57–71, 2016. ISSN 1361-8415. doi: 10.1016/j.media.2015.09.005.

C. I. Henschke, D. I. McCauley, D. F. Yankelevitz, D. P. Naidich, G. McGuinness, O. S. Miettinen, D. M. Libby, M. W. Pasmantier, J. Koizumi, N. K. Altorki, and J. P. Smith. Early lung cancer action project: overall design and findings from baseline screening. *The Lancet*, 354(9173):99–105, July 1999. doi: 10.1016/s0140-6736(99)06093-6.

C. I. Henschke, D. P. Naidich, D. F. Yankelevitz, G. McGuinness, D. I. McCauley, J. P. Smith, D. Libby, M. Pasmantier, M. Vazquez, J. Koizumi, D. Flieder, N. Altorki, and O. S. Miettinen. Early lung cancer action project. *Cancer*, 92(1):153–159, July 2001. doi: 10.1002/1097-0142(20010701)92:1<153::aid-cncr1303>3.0.co;2-s.

D. L. G. Hill, P. G. Batchelor, M. Holden, and D. J. Hawkes. Medical image registration. *Physics in Medicine and Biology*, 46(3):R1–R45, Feb. 2001. doi: 10.1088/0031-9155/46/3/201.

O. J. Ilegbusi, Z. Li, B. Seyfi, Y. Min, S. Meeks, P. Kupelian, and A. P. Santhanam. Modeling airflow using subject-specific 4DCT-based deformable volumetric lung models. *International Journal of Biomedical Imaging*, 2012:1–10, 2012. ISSN 1687-4188. doi: 10.1155/2012/350853.

O. J. Ilegbusi, B. Seyfi, and R. Salvin. Patient-specific model of lung deformation using spatially dependent constitutive parameters. *Mathematical and Computer Modelling of Dynamical Systems*, 20(6):546–556, 2014. ISSN 1387-3954. doi: 10.1080/13873954.2013.842927.

International Agency for Research on Cancer. *WHO Classification of Tumours of the Lung, Pleura, Thymus and Heart. Fourth edition*. Medicine Series. International Agency for Research on Cancer, 2015. ISBN 9789283224365.

A. Jemal, F. Bray, M. M. Center, J. Ferlay, E. Ward, and D. Forman. Global cancer statistics. *CA: A Cancer Journal for Clinicians*, 61(2):69–90, Feb. 2011. ISSN 0007-9235. doi: 10.3322/caac.20107.

W. A. Kalender and Y. Kyriakou. Flat-detector computed tomography (FD-CT). *European Radiology*, 17(11):2767–2779, 2007. ISSN 0938-7994. doi: 10.1007/s00330-007-0651-9.

H.-U. Kauczor, L. Bonomo, M. Gaga, K. Nackaerts, N. Peled, M. Prokop, M. Remy-Jardin, O. von Stackelberg, and J.-P. Sculier. ESR/ERS white paper on lung cancer screening. *European Respiratory Journal*, 46(1):28–39, Apr. 2015. doi: 10.1183/09031936.00033015.

J. Keating and S. Singhal. Novel methods of intraoperative localization and margin assessment of pulmonary nodules. *Seminars in Thoracic and Cardiovascular Surgery*, 28(1):127–136, 2016. ISSN 1043-0679. doi: 10.1053/j.semtcvs.2016.01.006.

J. Kim and J. A. Fessler. Intensity-based image registration using robust correlation coefficients. *IEEE Transactions on Medical Imaging*, 23(11):1430–1444, Nov. 2004. ISSN 0278-0062. doi: 10.1109/tmi.2004.835313.

S. Klein, M. Staring, K. Murphy, M. A. Viergever, and J. Pluim. elastix: A toolbox for intensity-based medical image registration. *IEEE Transactions on Medical Imaging*, 29(1):196–205, 2010. ISSN 0278-0062. doi: 10.1109/tmi.2009.2035616.

R. Kondo, K. Yoshida, K. Hamanaka, M. Hashizume, T. Ushiyama, A. Hyogotani, M. Kurai, S. Kawakami, M. Fukushima, and J. Amano. Intraoperative ultrasonographic localization of pulmonary ground-glass opacities. *The Journal of Thoracic and Cardiovascular Surgery*, 138(4):837–842, Oct. 2009. ISSN 0022-5223. doi: 10.1016/j.jtcvs.2009.02.002.

W. Lai. *Introduction to continuum mechanics*. Pergamon Press, Oxford New York, 1993. ISBN 978-0080417004.

J. Lehr. Truncated-view artifacts: clinical importance on CT. *American Journal of Roentgenology*, 141(1):183–191, July 1983. ISSN 0361-803X. doi: 10.2214/ajr.141.1.183.

J. K. Lempel and D. P. Raymond. Intraoperative percutaneous microcoil localization of small peripheral pulmonary nodules using cone-beam CT in a hybrid operating room. *American Journal of Roentgenology*, 213(4):778–781, Oct. 2019. doi: 10.2214/ajr.19.21175.

M. G. Levitzky. *Pulmonary Physiology.* McGraw-Hill Professional Publishing, Blacklick, USA, 2007. ISBN 978-0-07-150874-2. OCLC: 958557642.

P. Li, U. Malsch, and R. Bendl. Combination of intensity-based image registration with 3D simulation in radiation therapy. *Physics in Medicine and Biology*, 53(17):4621–4637, 2008. ISSN 0031-9155. doi: 10.1088/0031-9155/53/17/011.

M.-W. Lin and J.-S. Chen. Image-guided techniques for localizing pulmonary nodules in thoracoscopic surgery. *Journal of Thoracic Disease*, 8(S9):S749–S755, Oct. 2016. doi: 10.21037/jtd.2016.09.71.

J. Lortet-Tieulent, E. Renteria, L. Sharp, E. Weiderpass, H. Comber, P. Baas, F. Bray, J. W. Coebergh, and I. Soerjomataram. Convergence of decreasing male and increasing female incidence rates in major tobacco-related cancers in Europe in 1988–2010. *European Journal of Cancer*, 51(9):1144–1163, June 2015. doi: 10.1016/j.ejca.2013.10.014.

J. B. A. Maintz and M. A. Viergever. A survey of medical image registration. *Medical Image Analysis*, 2(1):1–36, 1998. ISSN 1361-8415. doi: 10.1016/S1361-8415(01)80026-8.

R. Manser, L. B. Irving, C. Stone, G. Byrnes, M. J. Abramson, and D. Campbel. Screening for lung cancer. *Cochrane Database of Systematic Reviews*, (1), 2004. ISSN 1465-1858. doi: 10.1002/14651858.CD001991.pub2.

Y. Mao, C. Chi, F. Yang, J. Zhou, K. He, H. Li, X. Chen, J. Ye, J. Wang, and J. Tian. The identification of sub-centimetre nodules by near-infrared fluorescence thoracoscopic systems in pulmonary resection surgeries. *European Journal of Cardio-Thoracic Surgery*, 52(6):1190–1196, July 2017. ISSN 1010-7940. doi: 10.1093/ejcts/ezx207.

G. Mase. *Continuum Mechanics for Engineers, Third Edition*. CRC Press, Hoboken, 2009. ISBN 978-1420085389.

J. R. McClelland, D. J. Hawkes, T. Schaeffter, and A. P. King. Respiratory motion models: A review. *Medical Image Analysis*, 17(1):19–42, 2013. ISSN 1361-8415. doi: 10.1016/j.media.2012.09.005.

R. J. McKenna and W. V. Houck. New approaches to the minimally invasive treatment of lung cancer. *Current Opinion in Pulmonary Medicine*, 11(4):282–286, 2005. ISSN 1070-5287. doi: 10.1097/01.mcp.0000166589.08880.44.

M. Mehrotra and M. E. Arthur. *Video-Assisted Thoracoscopy (VATS)*. StatPearls Publishing, Treasure Island (FL), 2019.

M. R. Melamed, B. J. Flehinger, M. B. Zaman, R. T. Heelan, W. A. Perchick, and N. Martini. Screening for early lung cancer. *Chest*, 86(1):44–53, July 1984. doi: 10.1378/chest.86.1.44.

A. Mendizabal, P. Márquez-Neila, and S. Cotin. Simulation of hyperelastic materials in real-time using deep learning. *Medical Image Analysis*, 59:101569, 2020. ISSN 1361-8415. doi: 10.1016/j.media.2019.101569.

A. Mesbah, J. Yeung, and F. Gao. Pain after thoracotomy. *BJA Education*, 16(1):1–7, Jan. 2016. doi: 10.1093/bjaceaccp/mkv005.

M. I. Miga, K. D. Paulsen, J. M. Lemery, S. D. Eisner, A. Hartov, F. E. Kennedy, and D. W. Roberts. Model-updated image guidance: initial clinical experiences with gravity-induced brain deformation. *IEEE Transactions on Medical Imaging*, 18(10):866–874, 1999. ISSN 0278-0062. doi: 10.1109/42.811265.

M. I. Miga, K. D. Paulsen, P. J. Hoopes, F. E. Kennedy, A. Hartov, and D. W. Roberts. In vivo modeling of interstitial pressure in the brain under surgical load using finite elements. *Journal of Biomechanical Engineering*, 122(4):354–363, 2000. ISSN 0148-0731. doi: 10.1115/1.1288207.

K. D. Miller, L. Nogueira, A. B. Mariotto, J. H. Rowland, K. R. Yabroff, C. M. Alfano, A. Jemal, J. L. Kramer, and R. L. Siegel. Cancer treatment and survivorship statistics, 2019. *CA: A Cancer Journal for Clinicians*, 69(5):363–385, June 2019. doi: 10.3322/caac.21565.

K. Mohiuddin, S. Haneuse, T. Sofer, R. Gill, M. T. Jaklitsch, Y. L. Colson, J. Wee, R. Bueno, S. J. Mentzer, D. J. Sugarbaker, and S. J. Swanson. Relationship between margin distance and local recurrence among patients undergoing wedge resection for small ($\leq$2 cm) non–small cell lung cancer. *The Journal of Thoracic and Cardiovascular Surgery*, 147(4):1169–1177, Apr. 2014. ISSN 0022-5223. doi: 10.1016/j.jtcvs.2013.11.056.

F. Morin, H. Courtecuisse, I. Reinertsen, F. Le Lann, O. Palombi, Y. Payan, and M. Chabanas. Brain-shift compensation using intraoperative ultrasound and constraint-based biomechanical simulation. *Medical Image Analysis*, 40:133–153, 2017.

K. Murphy, B. van Ginneken, J. M. Reinhardt, S. Kabus, K. Ding, X. Deng, K. Cao, K. Du, G. E. Christensen, V. Garcia, T. Vercauteren, N. Ayache, O. Commowick, G. Malandain, B. Glocker, N. Paragios, N. Navab, V. Gorbunova, J. Sporring, M. de Bruijne, X. Han, M. P. Heinrich, J. A. Schnabel, M. Jenkinson, C. Lorenz, M. Modat, J. R. McClelland, S. Ourselin, S. E. A. Muenzing, M. A. Viergever, D. D. Nigris, D. L. Collins, T. Arbel, M. Peroni, R. Li, G. C. Sharp, A. Schmidt-Richberg, J. Ehrhardt, R. Werner, D. Smeets, D. Loeckx, G. Song, N. Tustison, B. Avants, J. C. Gee, M. Staring, S. Klein, B. C. Stoel, M. Urschler, M. Werlberger, J. Vandemeulebroucke, S. Rit, D. Sarrut, and J. P. W. Pluim. Evaluation of registration methods on thoracic CT: The EMPIRE10 challenge. *IEEE Transactions on Medical Imaging*, 30 (11):1901–1920, Nov. 2011. ISSN 0278-0062. doi: 10.1109/tmi.2011.2158349.

M. Nakamoto, N. Aburaya, Y. Sato, K. Konishi, I. Yoshino, M. Hashizume, and S. Tamura. Thoracoscopic surgical navigation system for cancer localization in collapsed lung based on estimation of lung deformation. In *Medical Image Computing and Computer-Assisted Intervention – MICCAI 2007*, pages 68–76. Springer Berlin Heidelberg, 2007. doi: 10.1007/978-3-540-75759-7_9.

M. Nakao, J. Tokuno, T. Chen-Yoshikawa, H. Date, and T. Matsuda. Surface deformation analysis of collapsed lungs using model-based shape matching. *International Journal of Computer Assisted Radiology and Surgery*, 14(10):1763–1774, June 2019. doi: 10.1007/s11548-019-02013-0.

S. Narasimhan, J. A. Weis, H. F. J. González, R. C. Thompson, and M. I. Miga. In vivo modeling of interstitial pressure in a porcine model: approximation of poroelastic properties and effects of enhanced anatomical structure modeling. *Journal of Medical Imaging*, 5(04):1, Dec. 2018. ISSN 2329-4302. doi: 10.1117/1.JMI.5.4.045002.

S. Nithiananthan, S. Schafer, A. Uneri, D. J. Mirota, J. W. Stayman, W. Zbijewski, K. K. Brock, M. J. Daly, H. Chan, J. C. Irish, and J. H. Siewerdsen. Demons deformable registration of CT and cone-beam CT using an iterative intensity matching approach. *Medical Physics*, 38(4):1785–1798, Mar. 2011. doi: 10.1118/1.3555037.

F. P. M. Oliveira and J. M. R. S. Tavares. Medical image registration: a review. *Computer Methods in Biomechanics and Biomedical Engineering*, 17(2):73–93, Mar. 2012. doi: 10.1080/10255842.2012.670855.

OpenStax. *Anatomy and Physiology*, 2013. URL `https://openstax.org/details/books/anatomy-and-physiology`.

J. Palussière, V. Catena, and X. Buy. Percutaneous thermal ablation of lung tumors – radiofrequency, microwave and cryotherapy: Where are we going? *Diagnostic and Interventional Imaging*, 98(9):619–625, Sept. 2017. doi: 10.1016/j.diii.2017.07.003.

T. Pang, S. G., X. Z., and L. Zhao. Automatic lung segmentation based on texture and deep features of HRCT images with interstitial lung disease. *BioMed Research International*, 2019:1–8, Nov. 2019. doi: 10.1155/2019/2045432.

C. H. Park, K. Han, J. Hur, S. M. Lee, J. W. Lee, S. H. Hwang, J. S. Seo, K. H. Lee, W. Kwon, T. H. Kim, and B. W. Choi. Comparative effectiveness and safety of preoperative lung localization for pulmonary nodules. *Chest*, 151(2):316–328, 2017. ISSN 0012-3692. doi: 10.1016/j.chest.2016.09.017.

T. J. Patton, S. E. Gerard, W. Shao, G. E. Christensen, J. M. Reinhardt, and J. E. Bayouth. Quantifying ventilation change due to radiation therapy using 4dct jacobian calculations. *Medical Physics*, 45(10):4483–4492, Aug. 2018. doi: 10.1002/mp.13105.

S. Paul, A. J. Isaacs, T. Treasure, N. K. Altorki, and A. Sedrakyan. Long term survival with thoracoscopic versus open lobectomy: propensity matched comparative analysis using SEER-medicare database. *British Medical Journal*, 349(oct02 3): g5575–g5575, Oct. 2014. doi: 10.1136/bmj.g5575.

K. D. Paulsen, M. I. Miga, F. E. Kennedy, P. J. Hoopens, A. Hartov, and D. W. Roberts. A computational model for tracking subsurface tissue deformation during stereotactic neurosurgery. *IEEE Transactions on Biomedical Engineering*, 46(2):213–225, 1999. ISSN 0018-9294. doi: 10.1109/10.740884.

R. Pirker. Conquering lung cancer: current status and prospects for the future. *Pulmonology*, Mar. 2020. doi: 10.1016/j.pulmoe.2020.02.005.

J. P. W. Pluim, J. B. A. Maintz, and M. A. Viergever. Mutual-information-based registration of medical images: a survey. *IEEE Transactions on Medical Imaging*, 22(8): 986–1004, Aug. 2003. doi: 10.1109/tmi.2003.815867.

N. Pozin, S. Montesantos, I. Katz, M. Pichelin, I. Vignon-Clementel, and C. Grandmont. A tree-parenchyma coupled model for lung ventilation simulation. *International Journal for Numerical Methods in Biomedical Engineering*, 33(11):e2873, June 2017. doi: 10.1002/cnm.2873.

J. D. Predina, A. Newton, C. Corbett, L. Xia, L. F. Sulyok, M. Shin, C. Deshpande, L. Litzky, E. Barbosa, P. S. Low, J. C. Kucharczuk, and S. Singhal. Localization of pulmonary ground-glass opacities with folate receptor–targeted intraoperative molecular imaging. *Journal of Thoracic Oncology*, 13(7):1028–1036, July 2018. doi: 10.1016/j.jtho.2018.03.023.

V. Puri, A. Patel, K. Majumder, J. M. Bell, T. D. Crabtree, A. S. Krupnick, D. Kreisel, S. R. Broderick, G. A. Patterson, and B. F. Meyers. Intraoperative conversion from video-assisted thoracoscopic surgery lobectomy to open thoracotomy: A study of causes and implications. *The Journal of Thoracic and Cardiovascular Surgery*, 149(1): 55–62, Jan. 2015. doi: 10.1016/j.jtcvs.2014.08.074.

J. N. Reddy. *An introduction to continuum mechanics : with applications*. Cambridge University Press, New York, 2008. ISBN 978-0521870443.

E. Rietzel and G. T. Y. Chen. Deformable registration of 4D computed tomography data. *Medical Physics*, 33(11):4423–4430, Oct. 2006. ISSN 0094-2405. doi: 10.1118/1.2361077.

G. Rocco, M. Cicalese, C. La Manna, A. La Rocca, N. Martucci, and R. Salvi. Ultrasonographic identification of peripheral pulmonary nodules through uniportal video-assisted thoracic surgery. *Annals of Thoracic Surgery*, 92(3):1099–1101, 2011. ISSN 0003-4975. doi: 10.1016/j.athoracsur.2011.03.030.

S. Rouzé, B. de Latour, E. Flécher, J. Guihaire, M. Castro, R. Corre, P. Haigron, and J.-P. Verhoye. Small pulmonary nodule localization with cone beam computed tomography during video-assisted thoracic surgery: a feasibility study. *Interactive CardioVascular and Thoracic Surgery*, 22(6):705–711, Feb. 2016. ISSN 1569-9293. doi: 10.1093/icvts/ivw029.

S. Rouzé, P. Alvarez, B. de Latour, E. Flécher, J.-L. Dillenseger, and J.-P. Verhoye. Localisation de nodules pulmonaires en réalité augmentée grâce au cone beam computed tomography (CBCT) en vidéo-thoracoscopie. *Bulletin de l'Académie Nationale de Médecine*, 202(8-9):1897–1908, Nov. 2018. doi: 10.1016/s0001-4079(19)30183-9.

D. Ruan, S. Esedoglu, and J. A. Fessler. Discriminative sliding preserving regularization in medical image registration. In *2009 IEEE International Symposium on Biomedical Imaging: From Nano to Macro*, pages 430–433, 2009. ISBN 978-1-4244-3931-7. doi: 10.1109/isbi.2009.5193076.

D. Rueckert, L. I. Sonoda, C. Hayes, D. L. G. Hill, M. O. Leach, and D. J. Hawkes. Nonrigid registration using free-form deformations: application to breast MR images. *IEEE Transactions on Medical Imaging*, 18(8):712–721, 1999. ISSN 0278-0062. doi: 10.1109/42.796284.

J. Ruhaak, T. Polzin, S. Heldmann, I. J. A. Simpson, H. Handels, J. Modersitzki, and M. P. Heinrich. Estimation of large motion in lung CT by integrating regularized keypoint correspondences into dense deformable registration. *IEEE Transactions on Medical Imaging*, 36(8):1746–1757, 2017. ISSN 0278-0062. doi: 10.1109/TMI.2017.2691259.

B. F. Sabath and R. F. Casal. Bronchoscopic ablation of peripheral lung tumors. *Journal of Thoracic Disease*, 11(6):2628–2638, June 2019. doi: 10.21037/jtd.2019.01.65.

N. Samavati, M. Velec, and K. Brock. A hybrid biomechanical intensity based deformable image registration of lung 4DCT. *Physics in Medicine and Biology*, 60(8):3359–3373, 2015. ISSN 0031-9155. doi: 10.1088/0031-9155/60/8/3359.

A. P. Santhanam, Y. Min, S. P. Mudur, A. Rastogi, B. H. Ruddy, A. Shah, E. Divo, A. Kassab, J. P. Rolland, and P. Kupelian. An inverse hyper-spherical harmonics-based formulation for reconstructing 3D volumetric lung deformations. *Comptes Rendus Mécanique*, 338(7-8):461–473, July 2010. ISSN 1631-0721. doi: 10.1016/j.crme.2010.07.006.

D. Sarrut, V. Boldea, S. Miguet, and C. Ginestet. Simulation of four-dimensional CT images from deformable registration between inhale and exhale breath-hold CT scans. *Medical Physics*, 33(3):605–617, Feb. 2006. doi: 10.1118/1.2161409.

C. Schmidgunst, D. Ritter, and E. Lang. Calibration model of a dual gain flat panel detector for 2d and 3d x-ray imaging. *Medical Physics*, 34(9):3649–3664, 2007. doi: 10.1118/1.2760024.

A. Schmidt-Richberg, R. Werner, H. Handels, and J. Ehrhardt. Estimation of slipping organ motion by registration with direction-dependent regularization. *Medical Image Analysis*, 16(1):150–159, 2012. ISSN 1361-8415. doi: 10.1016/j.media.2011.06.007.

R. Schulze, U. Heil, D. Groβ, D. D. Bruellmann, E. Dranischnikow, U. Schwanecke, and E. Schoemer. Artefacts in CBCT: a review. *Dentomaxillofacial Radiology*, 40(5):265–273, July 2011. ISSN 0250-832X. doi: 10.1259/dmfr/30642039.

L. A. Schwarz. *Non-rigid Registration Using Free-form Deformations*. PhD thesis, Department of Informatics, Munich, Germany, 2007.

B. Seyfi Noferest, A. P. Santhanam, and O. J. Ilegbusi. Effect of gravity on subject-specific human lung deformation. *Mathematical and Computer Modelling of Dynamical Systems*, 24(1):87–101, 2018. ISSN 1387-3954. doi: 10.1080/13873954.2017.1382537.

R. L. Siegel, K. D. Miller, and A. Jemal. Cancer statistics, 2016. *CA: A Cancer Journal for Clinicians*, 66(1):7–30, 2016. ISSN 0007-9235. doi: 10.3322/caac.21332.

R. L. Siegel, K. D. Miller, and A. Jemal. Cancer statistics, 2020. *CA: A Cancer Journal for Clinicians*, 70(1):7–30, Jan. 2020. doi: 10.3322/caac.21590.

R. A. Smith, D. Manassaram-Baptiste, D. Brooks, M. Doroshenk, S. Fedewa, D. Saslow, O. W. Brawley, and R. Wender. Cancer screening in the united states, 2015: A review of current american cancer society guidelines and current issues in cancer screening. *CA: A Cancer Journal for Clinicians*, 65(1):30–54, Jan. 2015. doi: 10.3322/caac.21261.

A. Sotiras, C. Davatzikos, and N. Paragios. Deformable medical image registration: A survey. *IEEE Transactions on Medical Imaging*, 32(7):1153–1190, July 2013. doi: 10.1109/tmi.2013.2265603.

M. Sperandeo, E. Frongillo, L. M. C. Dimitri, A. Simeone, S. D. Cosmo, M. Taurchini, and C. Cipriani. Video-assisted thoracic surgery ultrasound (VATS-US) in the evaluation of subpleural disease: preliminary report of a systematic study. *Journal of Ultrasound*, 23(1):105–112, Mar. 2019. doi: 10.1007/s40477-019-00374-5.

S. G. Spiro, M. K. Gould, and G. L. Colice. Initial evaluation of the patient with lung cancer: Symptoms, signs, laboratory tests, and paraneoplastic syndromes. *Chest*, 132(3):149S–160S, Sept. 2007. doi: 10.1378/chest.07-1358.

B. W. Stewart and C. P. Wild, editors. *World Cancer Report 2014*. International Agency for Research on Cancer, 2014. ISBN 978-92-832-0429-9 978-92-832-0443-5.

C. Studholme, D. L. G. Hill, and D. J. Hawkes. An overlap invariant entropy measure of 3d medical image alignment. *Pattern Recognition*, 32(1):71–86, Jan. 1999. ISSN 0031-3203. doi: 10.1016/s0031-3203(98)00091-0.

C. Studholme, C. Drapaca, B. Iordanova, and V. Cardenas. Deformation-based mapping of volume change from serial brain MRI in the presence of local tissue contrast change. *IEEE Transactions on Medical Imaging*, 25(5):626–639, May 2006. doi: 10.1109/tmi.2006.872745.

M. Subramanian and V. Puri. Is a complicated VATS lung resection better than no VATS at all?—converting our stance on intraoperative conversions. *Journal of Thoracic Disease*, 11(S9):S1366–S1368, May 2019. doi: 10.21037/jtd.2019.03.87.

K. Suda. Intraoperative molecular imaging—a bright navigator for thoracic surgeons in the era of limited resection. *Translational Lung Cancer Research*, 7(S3):S232–S235, Sept. 2018. doi: 10.21037/tlcr.2018.08.13.

K. Sun, T. S. Pheiffer, A. L. Simpson, J. A. Weis, R. C. Thompson, and M. I. Miga. Near real-time computer assisted surgery for brain shift correction using biomechanical models. *IEEE Journal of Translational Engineering in Health and Medicine*, 2:1–13, 2014. ISSN 2168-2372. doi: 10.1109/JTEHM.2014.2327628.

K. Suzuki, K. Nagai, J. Yoshida, H. Ohmatsu, K. Takahashi, M. Nishimura, and Y. Nishiwaki. Video-assisted thoracoscopic surgery for small indeterminate pulmonary nodules. *Chest*, 115(2):563–568, 1999. ISSN 0012-3692. doi: 10.1378/chest.115.2.563.

L. T. Tanoue, N. T. Tanner, M. K. Gould, and G. A. Silvestri. Lung cancer screening. *American Journal of Respiratory and Critical Care Medicine*, 191(1):19–33, Jan. 2015. doi: 10.1164/rccm.201410-1777ci.

J. N. Tehrani, Y. Yang, R. Werner, W. Lu, D. Low, X. Guo, and J. Wang. Sensitivity of tumor motion simulation accuracy to lung biomechanical modeling approaches and parameters. *Physics in Medicine and Biology*, 60(22):8833–8849, 2015. ISSN 0031-9155. doi: 10.1088/0031-9155/60/22/8833.

The National Lung Screening Trial Research Team. Reduced Lung-Cancer Mortality with Low-Dose Computed Tomographic Screening. *The New England Journal of Medicine*, 365(5):395–409, Aug. 2011. ISSN 1533-4406. doi: 10.1056/NEJMoa1102873.

J.-P. Thirion. Image matching as a diffusion process: an analogy with maxwell's demons. *Medical Image Analysis*, 2(3):243–260, Sept. 1998. doi: 10.1016/s1361-8415(98)80022-4.

C.-K. Toh, F. Gao, W.-T. Lim, S.-S. Leong, K.-W. Fong, S.-P. Yap, A. A. L. Hsu, P. Eng, H.-N. Koong, A. Thirugnanam, and E.-H. Tan. Differences between small-cell lung cancer and non-small-cell lung cancer among tobacco smokers. *Lung Cancer*, 56(2):161–166, May 2007. doi: 10.1016/j.lungcan.2006.12.016.

A. Uneri, S. Nithiananthan, S. Schafer, Y. Otake, J. W. Stayman, G. Kleinszig, M. S. Sussman, J. L. Prince, and J. H. Siewerdsen. Deformable registration of the inflated and deflated lung in cone-beam CT-guided thoracic surgery: Initial investigation of a combined model- and image-driven approach. *Medical Physics*, 40(1):017501, 2013. doi: 10.1118/1.4767757.

A. Vallance, P. Tcherveniakov, C. Bogdan, N. Chaudhuri, R. Milton, and E. Kefaloyannis. The evolution of intraoperative conversion in video assisted thoracoscopic lobectomy. *The Annals of The Royal College of Surgeons of England*, 99(2):129–133, Feb. 2017. doi: 10.1308/rcsann.2016.0253.

J. Vandemeulebroucke, O. Bernard, S. Rit, J. Kybic, P. Clarysse, and D. Sarrut. Automated segmentation of a motion mask to preserve sliding motion in deformable registration of thoracic CT. *Medical Physics*, 39(2):1006–1015, 2012. doi: 10.1118/1.3679009.

M. Velec, J. L. Moseley, S. Svensson, B. Hårdemark, D. A. Jaffray, and K. K. Brock. Validation of biomechanical deformable image registration in the abdomen, thorax, and pelvis in a commercial radiotherapy treatment planning system. *Medical Physics*, 44(7):3407–3417, 2017. ISSN 0094-2405. doi: 10.1002/mp.12307.

T. Vercauteren, X. Pennec, E. Malis, A. Perchant, and N. Ayache. Insight into efficient image registration techniques and the demons algorithm. In *Lecture Notes in Computer Science*, pages 495–506. Springer Berlin Heidelberg, 2007. doi: 10.1007/978-3-540-73273-0_41.

T. Vercauteren, X. Pennec, A. Perchant, and N. Ayache. Diffeomorphic demons: Efficient non-parametric image registration. *NeuroImage*, 45(1):S61–S72, Mar. 2009. doi: 10.1016/j.neuroimage.2008.10.040.

A. Verruijt. *Theory and problems of poroelasticity*. Delft University of Technology, 2013.

H. Wada, T. Anayama, K. Hirohashi, T. Nakajima, T. Kato, T. K. Waddell, S. Keshavjee, I. Yoshino, and K. Yasufuku. Thoracoscopic ultrasonography for localization of subcentimetre lung nodules. *European Journal of Cardio-Thoracic Surgery*, 49(2):690–697, Apr. 2015. ISSN 1010-7940. doi: 10.1093/ejcts/ezv124.

H. Wang, L. Dong, J. O'Daniel, R. Mohan, A. S. Garden, K. K. Ang, D. A. Kuban, M. Bonnen, J. Y. Chang, and R. Cheung. Validation of an accelerated 'demons' algorithm for deformable image registration in radiation therapy. *Physics in Medicine and Biology*, 50(12):2887–2905, June 2005. doi: 10.1088/0031-9155/50/12/011.

R. Werner, J. Ehrhardt, R. Schmidt, and H. Handels. Patient-specific finite element modeling of respiratory lung motion using 4D CT image data. *Medical Physics*, 36 (5):1500–1511, 2009. ISSN 0094-2405. doi: 10.1118/1.3101820.

J. West. *Respiratory physiology : the essentials*. Wolters Kluwer Health/Lippincott Williams & Wilkins, Philadelphia, 2012. ISBN 978-1609136406.

A. S. Wolf, S. J. Swanson, R. Yip, B. Liu, E. S. Tarras, D. F. Yankelevitz, C. I. Henschke, E. Taioli, and R. M. Flores. The impact of margins on outcomes after wedge resection for stage i non-small cell lung cancer. *The Annals of Thoracic Surgery*, 104(4): 1171–1178, Oct. 2017. ISSN 0003-4975. doi: 10.1016/j.athoracsur.2017.04.024.

World Health Organization. *European tobacco use: Trends report 2019*. World Health Organization, 2019.

Z. Wu, E. Rietzel, V. Boldea, D. Sarrut, and G. C. Sharp. Evaluation of deformable registration of patient lung 4DCT with subanatomical region segmentations. *Medical Physics*, 35(2):775–781, 2008. ISSN 0094-2405. doi: 10.1118/1.2828378.

T. D. Yan, D. Black, P. G. Bannon, and B. C. McCaughan. Systematic review and meta-analysis of randomized and nonrandomized trials on safety and efficacy of video-assisted thoracic surgery lobectomy for early-stage non–small-cell lung cancer. *Journal of Clinical Oncology*, 27(15):2553–2562, May 2009. doi: 10.1200/jco.2008.18.2733.

T. D. Yan, C. Cao, T. A. D'Amico, T. L. Demmy, J. He, H. Hansen, S. J. Swanson, W. S. Walker, G. Casali, J. Dunning, M. Shackcloth, R. Shah, S. Stamenkovic, T. Routledge, W. Walker, E. Woo, S. Woolley, J.-M. Baste, D. Gossot, G. Roviaro, L. Solaini, J. Loscertales, D. Gonzalez-Rivas, H. Decaluwe, G. Decker, F. D. Ryck, Y. Sokolow, J. W. Oosterhuis, J. Siebenga, T. Schmid, J. Bodner, H. Dienemann, G. Leschber, D. Schneiter, H. Hansen, P. Licht, R. H. Petersen, C. Piwkowski, T. D'Amico, T. Demmy, C. Deschamps, J. Howington, M. Liptay, R. McKenna, J. Mitchell, B. Meyers, B. Park, S. Swanson, H.-S. Lee, J. He, Y. Li, Z. Liu, N. Wu, A. Yim, W. Yu, T. Kohno, G. Wright, and T. D. Yan. Video-assisted thoracoscopic surgery lobectomy at 20 years: a consensus statement. *European Journal of Cardio-Thoracic Surgery*, 45(4):633–639, Oct. 2013. doi: 10.1093/ejcts/ezt463.

S.-M. Yang, W.-C. Ko, M.-W. Lin, H.-H. Hsu, C.-Y. Chan, I.-H. Wu, Y.-C. Chang, and J.-S. Chen. Image-guided thoracoscopic surgery with dye localization in a hybrid operating room. *Journal of Thoracic Disease*, 8(S9):S681–S689, Oct. 2016. ISSN 2072-1439. doi: 10.21037/jtd.2016.09.55.

T. Zhang, N. P. Orton, T. R. Mackie, and B. R. Paliwal. Technical note: A novel boundary condition using contact elements for finite element based deformable image registration. *Medical Physics*, 31(9):2412–2415, 2004. ISSN 0094-2405. doi: 10.1118/1.1774131.

Z.-R. Zhao, R. W. H. Lau, P. S. Y. Yu, R. H. L. Wong, and C. S. H. Ng. Image-guided localization of small lung nodules in video-assisted thoracic surgery. *Journal of Thoracic Disease*, 8(S9):S731–S737, Oct. 2016. ISSN 2072-1439. doi: 10.21037/jtd.2016.09.47.

UNIVERSITÉ DE RENNES 1

Titre: Estimation des déformations du poumon par une approche hybride image/modèle biomécanique pour la localisation des nodules pulmonaires pendant la vidéo-thoracoscopie

Mot clés: Traitement d'images médicales, recalage d'images, modèle biomécanique, chirurgie assistée par ordinateur, chirurgie thoracique vidéo-assistée, nodules pulmonaires

Résumé: La résection des nodules pulmonaires par chirurgie thoracique vidéo-assistée (VATS) est une intervention de plus en plus utilisée pour le diagnostic et le traitement des cancers du poumon. La localisation de ces nodules pendant la chirurgie étant difficile visuellement et/ou par palpation, de nombreuses techniques d'aide à la localisation sont actuellement utilisées en pratique clinique. Cependant, ces techniques reposent essentiellement sur le placement, avant l'intervention, de marqueurs physiques dans le nodule par des techniques proches de la ponction. Par contre ce placement est souvent sujet à des complications. Pour éviter cela, une nouvelle approche consiste à repérer le nodule pulmonaire sur le scanner X préopératoire puis de localiser sa position sur l'imagerie CBCT peropératoire. Le problème vient du fait que lors de l'intervention, un pneumothorax (déflation du poumon) entraîne des déformations importantes du poumon ainsi qu'un changement des densités tissulaires, ce qui rend impossible la localisation directe du nodule dans le CBCT peropératoire. Les travaux effectués dans cette thèse ont porté sur l'estimation des différentes déformations subies par le poumon pendant la VATS, afin de pouvoir suivre et ainsi reporter sur le CBCT peropératoire la position du nodule repéré dans le scanner X préopératoire. Cela a été fait à l'aide d'une méthode hybride basée sur des techniques de recalage d'images associées à un modèle biomécanique poroélastique du poumon capable de simuler l'évacuation d'air. L'évaluation de cette méthode a été réalisée sur les données de 5 patients par le suivi de points de repère du poumon (bifurcations vasculaires) définis par un chirurgien. Cette évaluation a permis de montrer que l'erreur moyenne de suivie/report de ces points était de l'ordre du centimètre. Ce résultat a prouvé la faisabilité de l'approche proposée qui peut alors être considérée comme une possible solution pour la localisation des nodules pulmonaires pendant la VATS.

Title: Lung deformation estimation using a hybrid image-based/biomechanics-based approach for the localization of pulmonary nodules during video-assisted thoracoscopic surgery

Keywords: Medical image processing, image registration, biomechanical modeling, computer-assisted medical intervention, video-assisted thoracoscopic surgery, pulmonary nodules

Abstract: The resection of lung nodules by video-assisted thoracoscopic surgery (VATS) is an established procedure for the diagnosis and treatment of lung cancer. As the localization of these nodules during surgery is difficult visually and/or by palpation, many adjuvant localization techniques are currently used in clinical practice. Nonetheless, these techniques rely primarily on the placement of physical markers in the nodule before surgery, which has various limitations and may lead to complications. To avoid this, an alternative approach consists in the identification of pulmonary nodules in the preoperative CT image, followed by their intraoperative localization using CBCT imaging. However, during surgery, a pneumothorax (lung deflation) causes significant lung deformation and large tissue density changes that hinder the localization of nodules directly in the intraoperative CBCT. This thesis focused on the compensation of the various lung deformations occurring during VATS as a mechanism for the localization of pulmonary nodules in the intraoperative CBCT image. First, a characterization study allowed to identify the principal factors driving lung deformation during VATS. Then, a hybrid method based on image registration techniques and a poroelastic biomechanical model of the lung was proposed to account for such deformation. A retrospective study comprising 5 clinical VATS cases was performed for the evaluation of the proposed method. The results showed that prediction errors measured at anatomical landmarks were of the order of one centimeter, which suggests the feasibility of the proposed approach as a possible solution for the localization of pulmonary nodules during VATS.